M.L. 2016, Chp. 186, Sec. 2, Subd. 06b Project Abstract
For the Period Ending September 30, 2018

PROJECT TITLE: Developing Membrane Filtration System to Treat Lake Superior Ballast Water
PROJECT MANAGER: Santiago Romero-Vargas Castrillón
AFFILIATION: UMN, Department of Civil, Environmental, and Geo- Engineering
MAILING ADDRESS: 500 Pillsbury Dr. SE
CITY/STATE/ZIP: Minneapolis, MN 55455
PHONE:
E-MAIL: sromerov@umn.edu
WEBSITE: www.cege.umn.edu
FUNDING SOURCE: Environment and Natural Resources Trust Fund
LEGAL CITATION: M.L. 2016, Chp. 186, Sec. 2, Subd. 06b

APPROPRIATION AMOUNT: $151,000
AMOUNT SPENT: $67,862
AMOUNT REMAINING: $83,138

Overall Project Outcome and Results

This project contributed novel membrane materials for water treatment, as well as new fundamental understanding of graphene oxide surface coatings that show potential in membranes for water purification. The materials explored in this work could find application in the treatment of surface water in Minnesota. An account of our work is provided in the Research Addendum that accompanies this workplan, as well as in our recent publication (*Environ. Sci. Technol. Lett.*, 2018, 5 (1), pp 14–19). In summary, our work showed that graphene oxide coatings, covalently tethered to ultrafiltration membranes, inactivate bacteria and thus prevent membrane biofouling. Our work further showed that the nanoscale morphology of GO surface coatings affects membrane interfacial properties; we demonstrated that randomly oriented GO nanosheets are more desirable for membrane applications, since bacteria are less prone to adhere to disordered GO.

Project Results Use and Dissemination

Additional outcomes of this project were promotion of Minnesota's human capital through training of postdoctoral, graduate and undergraduate students (1 postdoc, 2 graduate and one undergraduate student were supported at various points of the project), a M. S. degree to be completed by one of the graduate students supported by the project (expected completion in early 2019), a conference presentation at the 2017 AEESP Research and Education Conference (presented by the postdoc supported by the project), a recent publication in *Environmental Science & Technology Letters,* a premier environmental engineering peer-reviewed journal, and a further manuscript currently under preparation.

In addition, the PM presented three oral presentations reporting the research funded by this project: a conference presentation at the ACS National Meeting in New Orleans on March 18th, 2018 ("Bacterial Adhesion on Surfaces Functionalized with Graphene Oxide: Insights from Single-Cell Force Spectroscopy"); and two invited seminars at the Department of Physics at Hamline University on April 6th, 2018 ("Computational and Experimental Studies of Aqueous Interfaces") and at the Department of Chemical Engineering at University College London on May 9th, 2018 ("Understanding Microbial Adhesion to Aqueous Interfaces using Single-Cell Force Spectroscopy").

Environment and Natural Resources Trust Fund (ENRTF)
M.L. 2016 Work Plan

Date of Report: September 30, 2018

Final Report

Date of Work Plan Approval: June 7, 2016

Project Completion Date: September 30, 2018

Does this submission include an amendment request? No

PROJECT TITLE: Developing Membrane Filtration System to Treat Lake Superior Ballast Water

Project Manager: Santiago Romero-Vargas Castrillón, Ph. D.

Organization: University of Minnesota, Department of Civil, Environmental, and Geo- Engineering

Mailing Address: 500 Pillsbury Dr. SE

City/State/Zip Code: Minneapolis, MN, 55455

Telephone Number: (612)301-1347

Email Address: sromerov@umn.edu

Web Address: www.cege.umn.edu

Location: Cook, Lake, St. Louis.

Total ENRTF Project Budget:		
	ENRTF Appropriation:	**$151,000**
	Amount Spent:	**$67,862.12**
	Balance:	**$83,137.88**

Legal Citation: M.L. 2016, Chp. 186, Sec. 2, Subd. 06b

Appropriation Language:
$151,000 the second year is from the trust fund to the Board of Regents of the University of Minnesota to develop a filtration system utilizing bioactive membrane technologies for use in treating Lake Superior ballast water to remove at least 90 percent of suspended pathogens, invasive species, and contaminants. This appropriation is subject to Minnesota Statutes, section 116P.10. This appropriation is available until June 30, 2019, by which time the project must be completed and final products delivered.

I. PROJECT TITLE: Developing a Membrane Filtration System to Treat Lake Superior Ballast Water

II. PROJECT STATEMENT: The proliferation of invasive species introduced by ballast water discharge is a major threat to marine ecosystems in Minnesota. In the Port of Duluth the discharge of ballast water introduces invasive species of phyto- and zooplankton, bacteria, mollusks and their eggs and larvae; because of their remarkable adaptability, these organisms threaten the biodiversity and disrupt the ecological balance of their new environment. Processes aimed at minimizing the impact of invasive organisms in ballast waters, such as mid-ocean exchange, fail to remove all organisms, while disinfection-based technologies are costly and may produce toxic disinfection byproducts. Membrane filters, in which a polymer film with small pores allows the separation of water from suspended particulates, has shown promise for treatment of wastewaters. In this project, we aim to provide a proof-of-concept demonstration of membrane microfiltration (MF) as a ballast water treatment technology. The proposed effort is structured along two main goals:

- Phase 1: we will develop microfiltration membranes functionalized with graphene oxide, a hydrophilic and bactericidal nanomaterial that will result in a biofouling resistant MF membrane. Our goal is to develop membranes capable of removing >90% of microorganisms and the larvae of invasive species in surface waters sampled in the Port of Duluth-Superior.
- Phase 2: we will develop a pilot-scale unit with a capacity of ~600 gal/day to treat ballast water.

III. OVERALL PROJECT STATUS UPDATES:

Amendment request (9/29/2016)

This amendment affects activities 1 and 2.

As initially budgeted, this project included support for a graduate student research assistant (RA) for 2 years, including stipend, tuition, and fringe benefits. A graduate researcher with the required skill set for the project could not be found, leading the project manager (PM) to hire a qualified postdoctoral research associate, with experience in membrane science, who would be compensated at $36,000 per annum plus fringe benefits (20.1%). In compliance with the Department of Labor's increase of minimum salaries, the University of Minnesota is requiring a salary floor increase for all postdocs to the new minimum of $47,476 per annum (plus fringe benefits at 20.1%). The new minimum salary is effective for all start dates on or after November 14th, 2016; this is the likely start date of the postdoc. As a consequence of the salary increase, the PM requests a budget amendment to support the postdoc at the new minimum salary. Specifically, the PM requests that $18,000 be transferred from "Equipment/tools/supplies/services" to personnel. This will increase the personnel support allocation by $18,000 from $87,395 to $105,395, providing 21 months of support for the postdoc at the new minimum salary. The PM is confident that the postdoc hired for the project will perform at a very high level, and will make more progress in 21 months than a graduate RA would in 24 months. The PM will seek other sources of funds (e.g., NOAA, MN DNR, US EPA) to support the postdoc for the additional 3 months of salary initially budgeted for the project.

To cover the additional personnel costs, the PM requests $18,000 be transferred from the category "Equipment/tools/supplies/services" to "Personnel". The PM expects that the amendment will have little to no impact on the project outcomes, due to the relatively inexpensive reagents that will be used for membrane fabrication. The membranes will be fabricated from commercially available polymers such as polysulfone ($0.67/gram) and polyvinylidene fluoride ($0.94 per gram). The cost of each fabricated membrane ranges from $1 to $2 per membrane, including the price of the solvent. The remaining available funds for chemicals and supplies after the proposed re-budgeting, $10,105, suffices to complete the experiments in Activity 1. The PM will contribute $3,000 from discretionary funds (included in the original "Equipment/tools/supplies/services" allocation) to cover the "services" budget category. A cost-share account will be set up for this purpose.

Amendment approved by LCCMR on 10/5/16

Amendment request (5/18/2017)
An experienced graduate student research assistant (RA) will replace the postdoctoral (PD) associate beginning on May 29th, 2017. The project manager (PM) requests that the PD support be changed to RA, in support of the RA's tuition, salary and fringe benefits through summer 2018 (15 months). The balance remaining for PD salary and fringe benefits is $74,693. RA support for the proposed 15 months is $52,272. The PM requests that the difference ($22,421) be added to the "Equipment/Tools/Supplies" category (split into $11,210 in Activity 1, and $11,211 in Activity 2). These funds will be used for the purchase of reagents and laboratory consumables including polymers for membrane fabrication (polysulfone, polyethersulfone, pvdf), solvents for membrane fabrication (NMP, DMF, acetone, isopropanol), reagents to synthesize graphene oxide and other non-stick coatings, hollow fibers and chemicals to modify hollow fiber membranes, foulants (humic acids, proteins, polysaccharides), supplies for membrane characterization (SEM and AFM sample holders and AFM probes), and analytical equipment user fees.

Amendment approved by LCCMR 6/22/2017

Amendment request (2/15/2018)
In the 1/20/2018 Project Status Update, it was noted that $1965 of the funds for graduate student support from activity 2 were transferred to activity 1, because the salary was slightly overspent for activity 1. The PM requests that this amendment be retroactively approved.

Amendment approved by LCCMR on 2/28/2018

Amendment request (6/30/2018)
The project manager (PM) will be resigning from his position on the faculty at the University of Minnesota on September 30th, 2018. On consultation with Becca Nash, LCCMR director, it was recommended that the project completion date be changed to September 30th, 2018, upon which a final report will be submitted with the project findings. Further, it was recommended that student support be terminated at the end of the summer term (August 26th, 2018); this will allow the two students funded by this project (one part-time graduate student and one part-time undergraduate student) to complete their research and submit relevant findings for publication. To reflect the changes to the project duration, the PM requests that the project completion date be changed to September 30th, 2018. Further, given that an alternate project manager could not be found, the PM requests that Activity 2 be removed from the project. Further, the PM requests that the funds for graduate student support in Activity 1 be increased from $40,005 to $64,254 by transferring $24,249 from Activity 2 (this figure includes $17,739 spent in salary and fringe benefits since 1/30/18, plus $6,510 to fund the undergraduate and graduate student through the end of the summer term, i.e., August 26th, 2018). By continuing funding through the end of the summer, the graduate student currently working on the project will finish the characterization of biofouling propensity of the membranes, thus completing Activity 1. It should be noted that funds for graduate student support allocated for Activity 1 were overspent (hence the request for transfer of $17,139 from Activity 2) due to this activity falling behind schedule, which resulted in the experiments to complete activity 1 extending through the spring and summer semester, i.e., well past the initially projected completion date of January 31st, 2018. The experimental challenges that led to slow progress in Activity 1 have since been overcome, and this activity will be completed by the end of the summer.

Amendment Approved by LCCMR 8/2/2018.

Project Status as of January 30, 2017:
Work on activity 1 began in the fall of 2016. Progress has been made in training of the postdoctoral associate and preliminary fabrication and characterization of membrane materials for ballast water filtration, as explained below.

Project Status as of June 30, 2017: Work on Activity 1 continued. UF membranes and graphene oxide nanomaterials have been synthesized and characterized. Further synthesis and testing of the membrane materials and antifouling coatings is currently underway.

Project Status as of January 30, 2018: Significant progress towards completing Activity 1 has been made. A method to modify UF membranes with graphene oxide was developed. Characterization of the biofouling propensity of graphene oxide coatings was carried out, using bacterial adhesion measurements. Results from this project component were reported in a conference presentation (2017 AIChE National Meeting), and one journal publication. Details are provided in the Dissemination section. Expenses in the accompanying spreadsheet are through 12/31/2017. Please note that $1965 of the funds for graduate student support from activity 2 were transferred to activity 1, because the salary was slightly overspent for activity 1.

Project Status as of June 30, 2018:

The properties of membranes functionalized with graphene oxide (GO), a biocidal nanomaterial, are currently being evaluated. Results from this project were reported in a conference presentation and two invited seminars. Details are provided in the Dissemination section.

Project Status as of January 30, 2019:

Overall Project Outcomes and Results:

This project contributed novel membrane materials for water treatment, as well as new fundamental understanding of graphene oxide surface coatings that show potential in membranes for water purification. The materials explored in this work could find application in the treatment of surface water in Minnesota. An account of our work is provided in the Research Addendum that accompanies this workplan, as well as in our recent publication (*Environ. Sci. Technol. Lett.*, 2018, 5 (1), pp 14–19). In summary, our work showed that graphene oxide coatings, covalently tethered to ultrafiltration membranes, inactivate bacteria and thus prevent membrane biofouling. Our work further showed that the nanoscale morphology of GO surface coatings affects membrane interfacial properties; we demonstrated that randomly oriented GO nanosheets are more desirable for membrane applications, since bacteria are less prone to adhere to disordered GO.

Additional outcomes of this project were promotion of Minnesota's human capital through training of postdoctoral, graduate and undergraduate students (1 postdoc, 2 graduate and one undergraduate student were supported at various points of the project), a M. S. degree to be completed by one of the graduate students supported by the project (expected completion in early 2019), a conference presentation at the 2017 AEESP Research and Education Conference (presented by the postdoc supported by the project), a recent publication in *Environmental Science & Technology Letters,* a premier environmental engineering peer-reviewed journal, and a further manuscript currently under preparation.

In addition, the PM presented three oral presentations reporting the research funded by this project: a conference presentation at the ACS National Meeting in New Orleans on March 18th, 2018 ("Bacterial Adhesion on Surfaces Functionalized with Graphene Oxide: Insights from Single-Cell Force Spectroscopy"); and two invited seminars at the Department of Physics at Hamline University on April 6th, 2018 ("Computational and Experimental Studies of Aqueous Interfaces") and at the Department of Chemical Engineering at University College London on May 9th, 2018 ("Understanding Microbial Adhesion to Aqueous Interfaces using Single-Cell Force Spectroscopy").

Note: the student salary budget in activity 1 was slightly overspent by $1,458; to make up for this shortfall, $1458 were moved from the student support budget of activity 2 to activity 1.

IV. PROJECT ACTIVITIES AND OUTCOMES:

ACTIVITY 1: Development of low-fouling MF membranes showing complete microorganism removal. The first expected outcome of our investigation is a novel MF membrane with improved resistance toward organic fouling and biofouling (i.e., the clogging of membrane pores by dissolved and suspended contaminants, particles and microbes). A hydrophilic, bactericidal nanomaterial known as graphene oxide will be deposited on the membrane to create a fouling- and biofouling-resistant coating on the membrane surface. The benefits of operation with the GO-functionalized membranes (hereinafter designated GO-MF) include pumping energy savings and less frequent membrane backwashing stages between filtration cycles; an added benefit is longer membrane useful life. Since membrane replacement due to fouling or biofouling can amount to 50% of the operating costs of membrane filtration, considerable savings could result from the materials herein proposed. We will aim to develop membranes with a water permeability in excess of 1000 L m^{-2} h^{-1} bar^{-1}, showing complete removal of microorganisms with sizes > 1 μm.

Membranes will be fabricated via the phase inversion technique. MF membranes with pores < 1 μm will be prepared using poly(vinylidene fluoride) (PVDF). Surface functionalization of the MF membranes will be accomplished using a wet adhesive known as polydopamine. Polydopamine creates an adhesive coating on the PVDF surface for the robust attachment of graphene oxide nanosheets. The GO-MF membranes fabricated will be tested in a bench-scale dead-end filtration cell (~5 cm^2 membrane area) to characterize their fouling and biofouling propensity. Ballast waters and Lake Superior water will be used as feed in the fouling experiments. The objective of these small-scale experiments is to identify the membrane fabrication conditions for optimal biofouling resistance and microbe removal.

Summary Budget Information for Activity 1:

ENRTF Budget: $87,027
Amount Spent: $67,862
Balance: $19,165

Outcome	Completion Date
1. Personnel training, assembly of bench-scale setup	January 31, 2017
2. GO synthesis and membranes fabricated	June 30, 2017
3. Characterization of fouling resistance of GO-MF membranes	January 31, 2018

Activity Status as of January 30, 2017:

The postdoctoral associate has been trained in the fabrication, characterization and testing of polymeric microfiltration (MF) and ultrafiltration (UF) membranes. Preliminary membrane materials have been fabricated using polysulfone and other additives such as polyvinylpyrrolidone. The postdoctoral associate has also been trained in the use of various experimental techniques (electron microscopy, contact angle goniometry, zeta potential, IR spectroscopy, and atomic force microscopy) to characterize membrane properties. Flux measurements to obtain the membrane permeability coefficient are currently being performed in a filtration system in the lab of the PI. Work underway involves the modification of the surface of the membranes to confer upon them anti-fouling and anti-microbial properties.

Activity Status as of June 30, 2017: Graphene oxide-based coatings have been characterized by AFM-based force spectroscopy to evaluate their potential as antifouling coatings. A modification method to attach graphene oxide nanosheets to polymeric membranes for ballast water treatment is currently development. This method uses UV-assisted polymerization of acrylic acid to modify the membrane surface with chemical moieties that can subsequently be used to attach graphene oxide nanosheets. The presence of acrylic acid was verified using FTIR

spectroscopy. The next steps include attachment of the graphene oxide sheets to the membrane using amine coupling chemistry, and characterization of the fouling resistance of the GO-modified membranes.

Activity Status as of January 30, 2018: Using amine coupling chemistry, we have successfully modified UF membranes with GO nanosheets. The presence of GO was confirmed by Raman spectroscopy, showing successful functionalization of the membrane surface. The materials are currently being characterized by electron microscopy and contact angle goniometry.

We have also completed and published a detailed investigation on GO-based coatings being used to improve biofouling resistance. Our investigation found that GO sheet spatial orientation is an important design variable in the fabrication of the GO-coatings. We found that bacterial adhesion is weaker (which is beneficial to fouling resistance), when GO nanosheets are edge-tethered to the surface. Insights from this investigation are currently being translated into the fabrication and modification of UF membranes.

Activity Status as of June 30, 2018: The UF membranes modified with graphene oxide (GO) have been characterized in terms of contact angle goniometry, zeta potential, and water permeability. Preliminary experiments show that the GO coating possesses antibacterial activity towards *P. fluorescens*, a biofilm-forming organism that is common in surface waters. Further, we are characterizing the ability of the GO-functionalized membranes using the techniques developed in our recent LCCMR-funded publication (*Environ. Sci. Technol. Lett.* 2018, 5, 14-19).

Final Report Summary: Ultrafiltration membranes functionalized with graphene oxide (GO) where devised, functionalized in the laboratory, and thoroughly characterized by Raman and FTIR spectroscopy, zeta potential, biocidal activity, contact angle, and single-cell force spectroscopy. Detailed experimental protocols are provided in the research addendum that accompanies this workplan. The fabricated membranes show promise for drinking and ballast water treatment given their biocidal activity (i.e., ability to inactivate biofilm-forming bacteria; cf. Figure 6 of the report) and their hydrophilicity (cf. Figure 7 of the report). Ongoing work, supported through non-LCCMR funds, will finalize the characterization of the adhesive properties of the various membranes investigated, using SCFS; preliminary SCFS results are provided in Figures 12 and 13.

Activity 2: Development of a ~600 gal/day pilot-scale microfiltration unit for the treatment of ballast water. In activity 2, a MF pilot-scale unit will be designed and constructed to demonstrate MF as a viable ballast water treatment technology. PVDF hollow fiber membranes will be functionalized with graphene oxide following the protocol developed in Activity 1. The pilot scale unit will consist of an immersed hollow fiber bundle operating in outside-feed mode. Given that typical MF water fluxes are on the order of 1000 L m^{-2} h^{-1}, and considering that the membrane bundle surface area is typically on the order of 0.1 m^2 for pilot-scale units reported in the literature (see Research Addendum), we expect to develop a filtration apparatus capable of processing 100 L/h = ~ 600 gal/day of ballast discharge.

The pilot-scale unit will be demonstrated with waters sampled from Port of Duluth. Permeate quality will be analyzed by total organic carbon and dissolved organic carbon analyses, turbidity, and total suspended solids. Considering that the pore size of the PVDF membranes that will be used in this work is < 1 μm, we expect that the MF pilot-scale unit will achieve >90% removal of suspended pathogens and microscopic larvae.

Summary Budget Information for Activity 2:

ENRTF Budget: $63,973
Amount Spent: $0
Balance: $63,973

Outcome	Completion Date
1. Pilot-scale construction	June 30, 2018
2. Pilot-scale testing	June 30, 2019

Activity status as of January 30, 2017: this activity has not begun

Activity status as of June 30, 2017: this activity has not begun

Activity status as of January 30, 2018: this activity has not begun

Activity Status as of June 30, 2018: no activity to report. Due to the circumstances discussed in the June 30, 2018 amendment request, this activity will not continue and the funds will be returned to the ENRTF after project close-out.

V. DISSEMINATION:

Description: Results will be disseminated via publication in peer-reviewed journals such as The Journal of Membrane Science, Water Research, and Environmental Science & Technology. Results will also be communicated through oral and poster presentations at local, regional and national conferences on water technology.

Status as of January 30, 2017: no activity to report

Status as of June, 30 2017: an oral presentation was delivered by the postdoctoral associate executing the project. The presentation reported on our characterization of the antifouling potential of graphene oxide-based coatings. The talk was delivered on 6/21/17 at the 2017 AEESP Research & Education conference in Ann Arbor, MI.

Status as of January 30, 2018: an invited oral presentation was delivered by the PI on cell adhesion to GO-based coatings at the 1st Pan American Nanotechnology Conference in Guarujá, Brazil, on November 28, 2017. The title of the talk was:
"The interaction of bacterial cells with model graphene oxide surfaces: insights from single-cell force spectroscopy."

In addition, the PI delivered a talk on the same topic at the 2017 AIChE National Meeting in Minneapolis, on October 31, 2017. The title of the talk was:
"Initial Adhesion of Bacterial Cells on Surfaces Functionalized with Graphene Oxide: Insights from AFM-Based Single-Cell Force Spectroscopy."

A publication on our findings regarding GO-functionalized interfaces recently appeared in *Environmental Science & Technology Letters.* The complete reference is:
J. Xue, S. BinAhmed, Z. Wang, N. G. Karp, B. L. Stottrup, S. Romero-Vargas Castrillón, Bacterial adhesion to graphene oxide (GO)-functionalized interfaces is determined by hydrophobicity and GO sheet spatial orientation, Environ. Sci. Technol. Lett. 2018, 5, 14-19
DOI: 10.1021/acs.estlett.7b00509

Status as of June 30 2018:

The PM presented three oral presentations reporting the research funded by this project: a conference presentation at the ACS National Meeting in New Orleans on March 18th, 2018 ("Bacterial Adhesion on Surfaces Functionalized with Graphene Oxide: Insights from Single-Cell Force Spectroscopy"); and two invited seminars at the Department of Physics at Hamline University on April 6th, 2018 ("Computational and Experimental Studies of Aqueous Interfaces") and at the Department of Chemical Engineering at University College London on May 9th, 2018 ("Understanding Microbial Adhesion to Aqueous Interfaces using Single-Cell Force Spectroscopy").

Final Report Summary:

As detailed above, results from this project were disseminated in multiple conference presentations by both the students and the PM, as well as a journal publication in *Environ. Sci. Technol. Lett.* A further manuscript, to be submitted for publication in the upcoming months, is currently under preparation.

VI. PROJECT BUDGET SUMMARY:

A. ENRTF Budget Overview:

Budget Category	$ Amount	Overview Explanation
Graduate and undergraduate student support. Past support for postdoc (through May 2017), undergraduate researcher support (through December 2017)	$82,974	Current support is for graduate research assistant (25% time during summer term, fringe benefits 10% of cost) and undergraduate student researcher ($18.11/hr for 67 days in the summer (9.57 weeks)).
Professional/Technical/Service Contracts:	$ N/A	
Equipment/Tools/Supplies: reagents, chemicals, consumables, analytical services	$32,526	Reagents and laboratory consumables including, but not limited to, polymers for membrane fabrication (polysulfone, polyethersulfone, pvdf), solvents for membrane fabrication (NMP, DMF, acetone, isopropanol), reagents to synthesize graphene oxide, membrane casting equipment (PET fabric, thin film applicator, glass plates), hollow fibers and chemicals to modify hollow fiber membranes, foulants (humic acids, proteins, polysaccharides), supplies for membrane characterization (SEM and AFM sample holders and AFM probes), analytical equipment user fees. Stirred filtration cell with data logger.
Capital Expenditures over $5,000: MF pilot-scale unit	$ 34,500	Construction of a pilot-scale MF unit.
Travel Expenses in MN:	$ 1,000	Travel in Minnesota for ballast and surface water collection from Lake Superior. Mileage will be reimbursed at $0.55 per mile or current UMN compensation plan.
TOTAL ENRTF BUDGET:	**$ 151,000**	

Explanation of Use of Classified Staff:

Explanation of Capital Expenditures Greater Than $5,000:

MF pilot scale unit: custom-made hollow fiber membrane module, pump and motor assembly, valves, fittings, tubing, flow meters and pressure gauges, data acquisition and logging computer, heater/chiller.

Number of Full-time Equivalents (FTE) Directly Funded with this ENRTF Appropriation:
A full-time graduate student researcher will be employed with this appropriation for 15 months. This results in a total of 1 FTE for the total project.

Number of Full-time Equivalents (FTE) Estimated to Be Funded through Contracts with this ENRTF Appropriation: N/A

B. Other Funds:

Source of Funds	$ Amount Proposed	$ Amount Spent	Use of Other Funds
Non-state	N/A	N/A	N/A
University of Minnesota	$3,000	$0	Analytical services
State	N/A	N/A	N/A
	$	$	
TOTAL OTHER FUNDS:	**$3,000**	**$0**	

VII. PROJECT STRATEGY:

A. Project Partners:

The project manager will be Professor Santiago Romero-Vargas Castrillón (U. of Minnesota), who will supervise a graduate student in the execution of the proposed work. Romero-Vargas has expertise in the development, characterization, and testing of membrane materials for water purification, and membrane-based processes for water production.

B. Project Impact and Long-Term Strategy:

The proposed work will result in membrane materials and processes for the treatment of ballast water discharges in Minnesota. This project therefore directly addresses one of the main vectors for invasive species in the State. We expect this project to lead to further applications in drinking water treatment and, also, to patentable technology.

C. Funding History:

Funding Source and Use of Funds	Funding Timeframe	$ Amount
United States Geological Survey. Project title: "Improving the (Bio)fouling and Mechanical Resistance of Ultrafiltration Membranes for Drinking Water Production". The project proposed in this work plan partially builds on results and expertise developed during the USGS-sponsored project.	3/1/2015 – 2/28/2016	$30,000
Matching funds from UMN for the abovementioned USGS project.	3/1/2015 – 2/28/2016	$60,000

VIII. FEE TITLE ACQUISITION/CONSERVATION EASEMENT/RESTORATION REQUIREMENTS:

A. Parcel List: N/A

B. Acquisition/Restoration Information: N/A

IX. VISUAL COMPONENT or MAP(S):

See attached graphic.

X. RESEARCH ADDENDUM:

See attached research addendum.

XI. REPORTING REQUIREMENTS:

Periodic work plan status update reports will be submitted no later than January 30, 2017, June 30, 2017, January 30, 2018, and June 30, 2018. A final report will be submitted by September 30, 2018.

Environment and Natural Resources Trust Fund
M.L. 2016 Project Budget

Project Title: Developing Membrane Filtration System to Treat Lake Superior Ballast Water
Legal Citation: M.L. 2016, Chp. 186, Sec. 2, Subd. 06b
Project Manager: Santiago Romero-Vargas Castrillón
Organization: University of Minnesota - Twin Cities
M.L. 2016 ENRTF Appropriation: $151,000
Project Length and Completion Date: September 30, 2018
Date of Report: 9/30/2018 (expenses reported through 9/12/18)

ENVIRONMENT AND NATURAL RESOURCES TRUST FUND BUDGET	Activity 1 Budget (6/30/18)	Amount Spent	Activity 1 Balance	Activity 2 Budget	Amount Spent	Activity 2 Balance	TOTAL BUDGET	TOTAL BALANCE
BUDGET ITEM								
Personnel (Wages and Benefits)								
Graduate research assistant, postdoc and undergraduate researcher support. Current support is for graduate research assistant (50% time per year for 15 months, salary 57% of cost, tuition 33% of cost, fringe benefits 10% of cost)	$65,712	$65,712	$0	$17,262	$0	$17,262	$82,974	$17,262
Equipment/Tools/Supplies								
Reagents and laboratory consumables including, but not limited to, Polymers for membrane fabrication (polysulfone, polyethersulfone, pvdf), solvents for membrane fabrication (NMP, DMF, acetone, isopropanol), reagents to synthesize graphene oxide, membrane casting equipment (PET fabric, thin film applicator, glass plates), hollow fibers and chemicals to modify hollow fiber membranes, foulants (humic acids, proteins, polysaccharides, supplies for membrane characterization (SEM and AFM sample holders and AFM probes), analytical equipment user fees.	$21,315	$2,150	$19,165	$11,211	$0	$11,211	$32,526	$30,376
Analytical services ($3,000 **cost-shared by UMN, please see workplan, section B other funds**)	$0	$0	$0	$0	$0	$0	$0	$0

Capital Expenditures Over $5,000								
Construction of a pilot-scale MF unit: custom-made hollow fiber membrane module, pump and motor assembly, valves, fittings, tubing, flow meters and pressure gauges, data acquisition and logging computer, heater/chiller.	$0	$0	$0	$34,500	$0	$34,500	$34,500	$34,500
Travel expenses in Minnesota								
Mileage and lodging. To collect water samples within Minnesota. Mileage will be reimbursed @ $0.55 per mile or current U of M compensation plan.	$0	$0	$0	$1,000	$0	$1,000	$1,000	$1,000
COLUMN TOTAL	**$87,027**	**$67,862**	**$19,165**	**$63,973**	**$0**	**$63,973**	**$151,000**	**$83,138**

Developing Membrane Filtration System to Treat Lake Superior Ballast Water

(M.L. 2016, Chp. 186, Sec. 2, Subd. 06b)

Final Report Research Addendum

30th September, 2018

Contents

Materials and Methods

Membrane Modification

Membrane Preparation

Polyethersulfone (PES) membranes with 30 kDA molecular weight cutoffs (MWCO) were purchased from Synder filtration. PES membranes were soaked in 50% glycerin solution and stored at 4^{o}C. Prior to use, membranes were rinsed with ultrapure (UP) water, soaked in 25% isopropanol 75% ultrapure solution for 24hrs, and thoroughly rinsed again with UP water to remove any residual preservatives.

Acrylic Acid Modification procedure

It has been shown that polysulfone and Polyethersulfone membranes have the unique ability to generate free radicals when exposed to ultraviolet light which can be used to induce graft polymerization of monomers to the surface of the membranes to alter their properties. [1], [2]. Past works have focused on modifying the surface of PS and PES membranes with various monomers to improve their fouling and filtration capabilities, including the grafting of acrylic acid monomers [3], [4]. In this work, we build on the modification procedures for grafting acrylic acid with the intention of further modification with graphene oxide.

A 10% acrylic acid (AA) solution was prepared by diluting 99% AA from Sigma Aldrich with ultrapure water. Dilution was carried out in 500mL covered flasks under 125rpm of stirring for 30 minutes. PES membranes were fixed to a Teflon frame with the active area facing up. The membranes and the AA solution were brought to a glove box, where oxygen had been purged to less than 500ppm. The solution and the membranes were left in the glove box for 15 minutes to remove any dissolved oxygen.

From here, a modified dip coating method was performed. Dip coating is often used for coating membranes with monomer solutions prior to irradiation to increase the UV penetration to the membrane surface. This will in turn increase the free radicals generated on the membrane surface, not in the monomer solution, and increase grafting to the membrane. 10 percent acrylic acid solution was poured over the membrane surface and allowed to sit for 15 minutes. After 15 minutes, all excess acrylic acid monomer solution was poured into a collection vessel. This was done to ensure an even thin layer of AA monomer over the membrane surface. A Spectroline Model EF-160C 120V 60Hz 0.2amp UV lamp was positioned approximately 2cm above the membrane surface. The membranes were then irradiated for 10 seconds. After irradiation, the membranes were rinsed thoroughly and soaked in UP water for 24 hours to remove any unreacted monomer. FTIR Spectroscopy was performed on the unmodified and AA modified PES membranes to test the validity of the AA grafting step.

Preparation of Graphene Oxide solution

A 2mg/mL stock solution of graphene oxide was prepared by dissolving 100mg of GO in 50mL of ultrapure water. Dissolution was carried out in a sealed 250mL flask. The flask was submerged in a bath sonicater and the GO suspension was sonicated for 24 hours to disperse GO particles until colloidally stable.

GO Modification Procedure

PES membranes were functionalized with GO by adapting the procedure developed by Perrault et al. (2013) [5] for polyamide membranes, illustrated in Figure 1. The modification procedure utilized the EDC/NHS coupling reaction in and MES buffer. Instead of the carboxylic acid groups from the polyamide, carboxylic acids groups from the acrylic acid grafted to the membrane surface were activated to amine-reactive esters with a 4 mM 1-ethyl-3-[3-(dimethylamino) propyl]carbodiimide hydro-chloride (EDC, 98%, Sigma) and 10 mM N-hydroxysuccinimide (NHS, 98%, Sigma), buffered by 10 mM MES monohydrate (BioXtra, Sigma) with 0.5 M NaCl, at pH 5 [6]. The membranes were reacted for 60 minutes under ambient conditions while on a shaker table set to 30 rpm. Membranes were then rinsed gently with UP water. The amine reactive esters (NHS) were contacted with 10mM ethylenediamine (ED, BioXtra, Sigma) solution buffered buffered by 19 mM HEPES (99.5%, Sigma) with 0.15 mM NaCl, at pH 7.5, for 30 minutes to replace the esters with ED amino groups on the membrane surface.

The GO sheets were then activated in a similar manner to the membranes. The carboxylic acid groups on the GO nanosheets were substituted for the amine reactive esters (NHS) following a similar procedure. The 2 mg mL^{-1} GO stock solution was diluted to 250 µg mL^{-1}. The following components were then mixed together as follows: 10 parts of 250 mg mL^{-1} GO suspension mixed with 2 parts 100 mM MES buffer, followed with 1.75 parts 20 mM EDC in 10 mM MES buffer, followed by 1.75 parts 50 mM NHS in 10 mM MES buffer. The pH of the solution was then lowered to 5.5 and allowed to react for 15 minutes to ensure the esters were stable while being formed. The pH was then raised to 7.2. The membrane modified with ED groups was then contacted with the activated GO solution for 60 minutes under ambient conditions and 30rpm shaking. This resulted in a covalent linkage between the ED on the membrane surface and the GO nanosheets in suspension. Membranes were then gently rinsed and sonicated for 5 minutes to remove non-covalently bound GO. Following the modification procedure, all membranes were stored in ultrapure water (4^{o}C) prior to use.

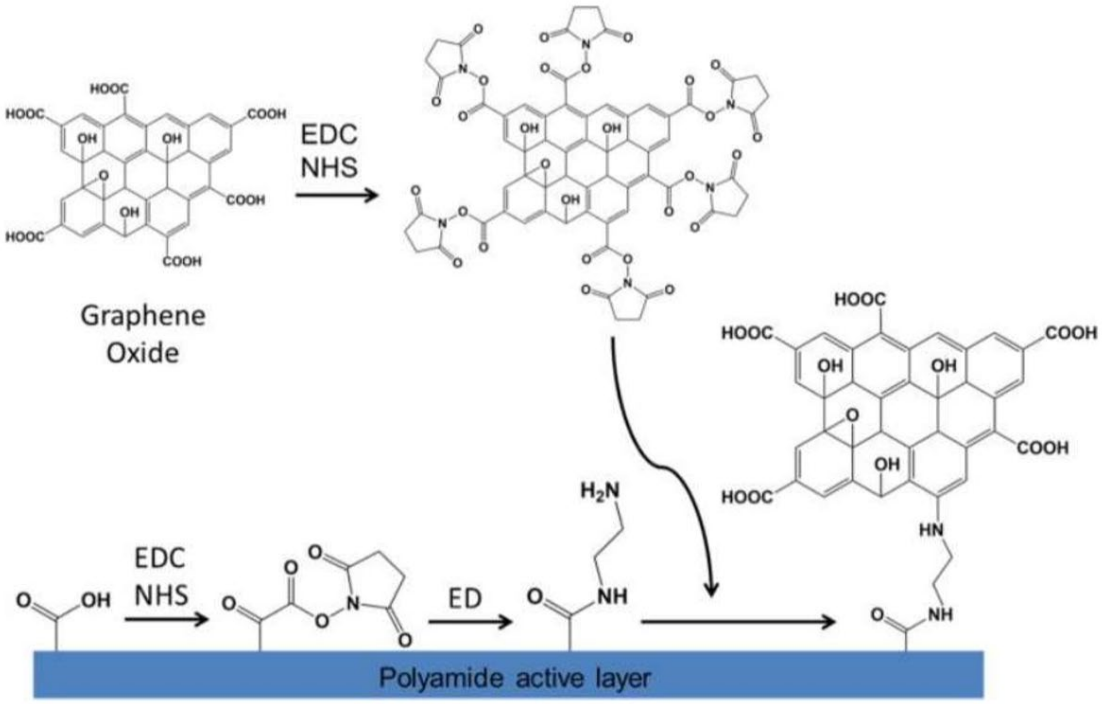

Figure 1 Membrane Modification Procedure with Graphene Oxide [5]

Membrane Characterization Techniques

There were several techniques that were used to characterize the unmodified and modified membranes. Each of the techniques, including the instruments and their respective procedures, are discussed in detail below.

Fourier-Transform Infrared Spectrometer (FTIR)

Attenuated total reflectance (ATR) FTIR was utilized to characterize the functional groups covering the membrane surfaces throughout the modification procedure. Membrane samples were dried overnight in a desiccator to remove any residual water that might appear on the FTIR spectrums. A Nicolet Series II Magna-IR System 750 Fourier-Transform Infrared Spectrometer was then used to irradiate the dried membrane surfaces.

Raman Spectroscopy

Raman spectroscopy irradiates a sample with a laser (either green or red) and measures the scattered light off the sample to yield information about the structural makeup of the surface being irradiated. Different functional groups will yield different characteristic peaks in the Raman spectrum. For this project, membrane samples were tested by first drying them overnight in a desiccator. An Alpha300R Confocal Raman Microscope (Witec) was used to carry out the Raman measurements. For each membrane tested, 20x20 µm area Raman maps at a 0.5 µm resolution were created for randomly chosen sections of the membranes. These maps were used to determine the two dimensional coverage of GO on the membrane surfaces. In addition, an average Raman spectrum was created for each membrane to give information regarding the average coverage of GO.

Contact Angle

Membrane hydrophobicity was characterized using both the water droplet in air and the captive bubble technique. For the captive bubble technique, the contact angle between droplets of n-decane and the membrane were measured in a submerged aqueous environment using a goniometer (Ramé-Hart, Model 200) and DROP Image software (Ramé-Hart). Membranes were inverted and suspended such that their active face was pointing down. The membranes were then submerged in ultrapure water. A J-shaped needle was used to inject n-decane droplets of roughly 10µL onto the membrane surface. The droplet sizes were kept at this volume for each measurement to reduce the skewing effect on the contact angle by increased buoyant forces of larger bubbles. At least 8 angles were measured across three separately functionalized membranes for each membrane type.

For the water droplet in air technique, droplets of ultra pure water were deposited on the membranes and the contact angles between the membrane and the water droplets were measured. Prior to conducting measurements, membranes were dried overnight in a desiccator. Droplets of roughly 5µL were then deposited on the membrane surfaces using a needle. The contact angles were then measured using the same equipment as the captive bubble technique described previously. At least 8 angles were measured across three separately functionalized membranes for each membrane type.

While drying out the membranes for this technique can change the surface properties [7], it also allowed for more consistent, smaller droplet sizes in comparison to the captive bubble technique. This meant that the contact angles were less prone to skewing and spreading from the increased gravitational forces associated with larger droplets.

Zeta potential

Streaming potential of the membrane surface was measured using a SurPASS electrokinetic analyzer (Anton-Paar). Streaming potential was measured over a pH range of 4-10 in 1 mM KCl solution. The pH was initially set at 10 and sequentially reduced to 4 using varying aliquots of 0.05mM HCl. An adjustable gap cell with a set distance of 120µm was used. At least two measurements were carried out for the AA and GO functionalized PES membranes. The pristine PES membrane will need measurements performed.

Biocidal Plate Assay

A biocidal plate assay was performed on the PES, AA, and GO membranes using the colony counting technique. Pseudomonas fluorescens ATCC 13525 bacteria were prepared in an overnight culture in 50mL of autoclaved LB broth under constant 125rpm stirring at 30^{o}C in an incubator. Bacteria were diluted three hours prior to the bioassay in 50mL of fresh LB broth. Stirring was increased to 175rpm for approximately three hours. The colony density in solution was characterized by measuring the OD using a spectrometer. Bacterial dilutions were used when the OD was approximately 0.6nm. 1.5mL of bacterial suspension was washed by centrifuging at 5,000G, dumping the supernatant, rinsing the bacteria with 1mL of fresh sterile PBS saline solution, vertexing, and repeating three times. The bacterial cells were then diluted with 10mL of PBS and applied to 1x1cm membrane coupons for 1 hour. Membranes were then removed, gently rinsed with PBS, and placed in 10mL of fresh PBS in 50mL falcon tubes, where they were bath sonicated for 10 minutes. The resulting solutions were then sequentially diluted in 10:100:1000 ratios. Add 50 µL of each dilution were added to agar plates and speared evenly over the surface with a glass stick. The plates were then incubated overnight at 30^{o}C and the colonies were counted after 24hrs.

Single Cell Force spectroscopy (SCFS)

Single cell force spectroscopy is used to measure the adhesion forces of bacterial cells on surfaces. This is done by adhering single bacterial cells to calibrated AFM tips, followed by contacting the surface and measuring the repulsive and attractive forces associated with pulling the bacteria back off the surface. In this experiment, Pseudomonas fluorescens ATCC 13525 was used for all singlecell force spectroscopy (SCFS) experiments due to its high biodhesion and biofilm formation potential [8]. Cells were grown in an identical manner as those used for the biocidal assays detailed previously. Individual P. fluorescens cells were adhered to the AFM cantilever tips with a polydopamine (PDA) solution used as an adhesive. An MFP-3D-Bio AFM (Asylum Research) integrated to a Zeiss Axio Observer A.1 inverted optical microscope was used for single-cell force measurements carried out under ambient conditions. Force curves were generated with extension and retraction cycles carried out with a cantilever speed of 400

nm/s, force distance of at least 3 µm or longer depending whether long-range interactions were observed, and trigger force of 600 pN. For each membrane type, 100 force curves were to be generated. Currently, all force curves for PES and the AA modified PES membranes have been gathered with about 66 curves for the GO modified membranes. Force curves were acquired at randomly chosen sites on the membrane surfaces. At each randomly chosen location, up to three force curves were performed. This was done to minimize deposition of extracellular polymeric substances.

For each membrane type, at least three individual cells cultured from three different colonies were used to collect the force curves. In addition, at least three separately functionalized membranes of each type were used as well. The cantilever deflection versus piezo Z position curves were converted into force−separation curves. Maximum adhesion forces (FAd) and rupture separation distances (LR) (the separation at which surface forces vanish) for each curve were calculated. After each experiment, the cell viability (alive or dead) using the live/dead assay (Baclight). Only data collected with a live cell that remained at its initial location were reported.

Membrane Characterization

Several of the previously mentioned techniques were used to characterize the membranes throughout the membrane modification procedure to verify the efficacy of the modifications.

Fourier-Transform Infrared Spectroscopy

FTIR Spectroscopy was used primarily to determine the if carboxylic acid groups were present on the surface of the PES membranes after the acrylic acid functionalization step. The primary peak attributed with carboxylic acid groups is a sharp band roughly at 1720cm^{-1} of the IR spectrum and a broad increase in the 2500-3500cm^{-1} region. The sharp band at 1720cm^{-1} comes from the C=O double bond stretching while the broad band roughly around ~3000cm^{-1} comes from the O-H stretching.

As described earlier, PES membranes undergo free radical polymerization upon direct radiation with UV light. In the presence of acrylic acid monomers, these free radicals polymerize the vinyl double bond on the acrylic acid, causing the formation of polyacrylic acid chains covalently bonded to the surface of the membrane. The degree of grafting (i.e. the amount of acrylic acid polymerized to the surface of the membranes) has been shown to be proportional to the time under UV radiation [9]. In addition, it has been shown that the intensity of the UV light increases the rate of polymerization and degree of grafting.

As described in the experimental section, the PES membranes used were irradiated for difference periods of time under the same UV intensity. The UV intensity was set by fixing the distance between the membrane surface and UV light source at ~ 2.5cm. Membranes were irradiated for 10, 20, 40, and 60 seconds with a thin layer of 10 wt% AA solution on top of the membrane. The FTIR results for each membrane are shown in Figure 2. FTIR was performed three times per membrane to account for any spatial deviation with respect to AA grafting. As shown in Figure 2, there is a sharp increase at 1723cm^{-1} and a broad increase in the 2500-3500cm^{-1} for each membrane relative to the control. In addition, the % reflectance for these peaks increased with radiation time. These results are indicative of the increasing presence of carboxylic acid on the surface of the membrane, thus concluding that acrylic acid was successfully grafted onto the membrane surface.

It was decided that only 10s of irradiation time was to be used for subsequent GO modification. This decision was based primarily off the fact that increased irradiation time resulted in damage to the membrane structure. Because PES membranes are reactive to UV light, the polymerization of AA to the surface of PES via free radical polymerization of the PES chains results in irreversible change to the membrane surface structure. Poor collapse is often a side effect of this modification mechanism, resulting in decreased permeability of the membrane. This was not a desired result. As such, the irradiation time was kept to a minimum (10s) to limit the loss in permeability as much as possible. GO was then grafted onto these membranes as described earlier. The results of FTIR of the PES, PES-AA and PES-GO membranes are shown below in Figure 3. This figure shows that both the GO and the acrylic acid membranes display the C=O stretching peak around 1720cm^{-1}. In addition, the GO FTIR spectrum shows increased reflectance for several peaks around 2900cm^{-1}. These peaks are known to be associated with GO and are consistent with other GO FTIR spectrum results.

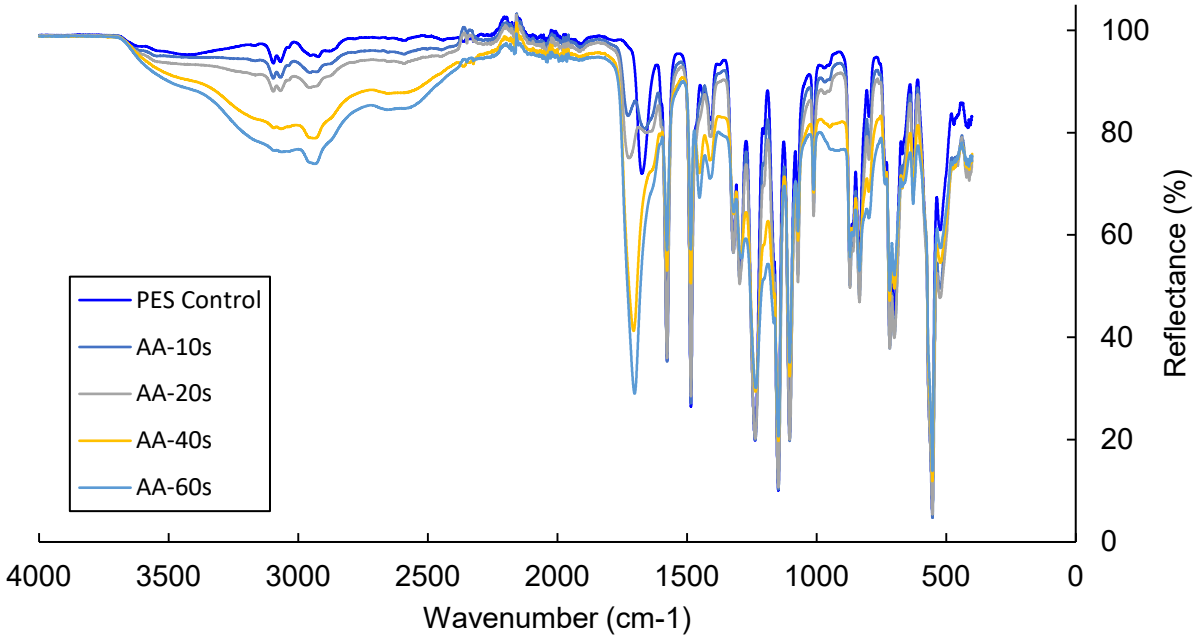

Figure 2 FTIR Results for Varied UV Irradiation Time with 10% AA Solution.

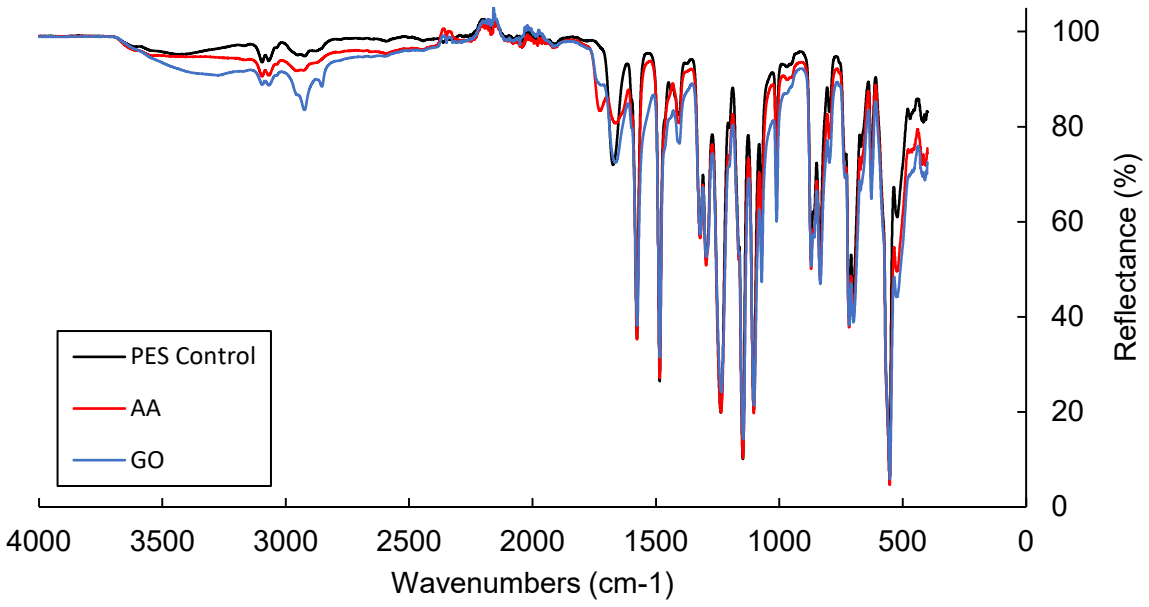

Figure 3 FTIR Results for PES, PES-AA, and PES-GO Membranes

Raman Spectroscopy

The presence of graphene oxide on the modified membrane surfaces was confirmed using Raman spectroscopy. Raman spectroscopy was performed on all three membranes (the pristine PES membrane, the AA functionalized intermediated, and the GO modified membranes) to ensure that the presence of acrylic acid or other functional groups was not mistaken for GO. Three peaks were analyzed to determine if GO was present. The first peak, labeled PES, is inherent to the PES membranes which is the result of symmetric C-O-C stretching of polyether sulfone. The second and third peaks, labeled D and G, respectively, are the characteristic D (~1350 cm^{-1}) and G (~1590 cm^{-1}) bands of GO [10]. In addition, the third (G) peak, is shared by the PES membrane [5]. Figure 4 shows the spectrums of the three membrane types (unmodified PES, AA modified PES, and GO modified PES) averaged over the 20x20um area.

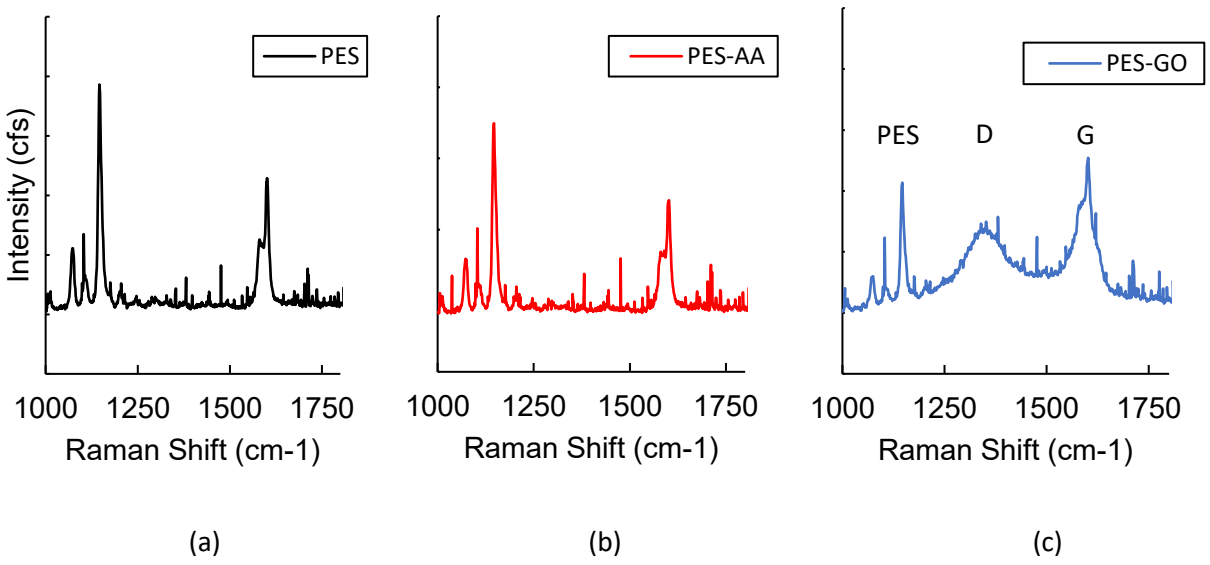

(a) (b) (c)

Figure 4 Raman Results for Pristine PES (a), AA Modified PES (b), and GO Modified PES (b) Membranes.

Figure 5 shows the three spatial Raman spectrums of the modified, AA modified, and GO modified membranes. The unmodified PES membrane and the AA modified membrane shows no evidence of graphene oxide nanoparticles adhered to the surface. The GO modified membranes shows substantial GO coverage across the entire membrane surface.

At each of the scanned points in the spatial Raman maps, the ratio of the GO D peaks to the membrane PES peaks was taken to illustrate the coverage of graphene oxide. The increased intensity of GO to PES is displayed by increased brightness. As expected, the pristine PES and the AA modified membranes showed no apparent GO binding as exhibited by the darker image. The GO modified membrane showed significant coverage throughout the tested area as seen with the brighter intensity of the Raman maps. This confirms the hypothesis that the modification procedure was successful.

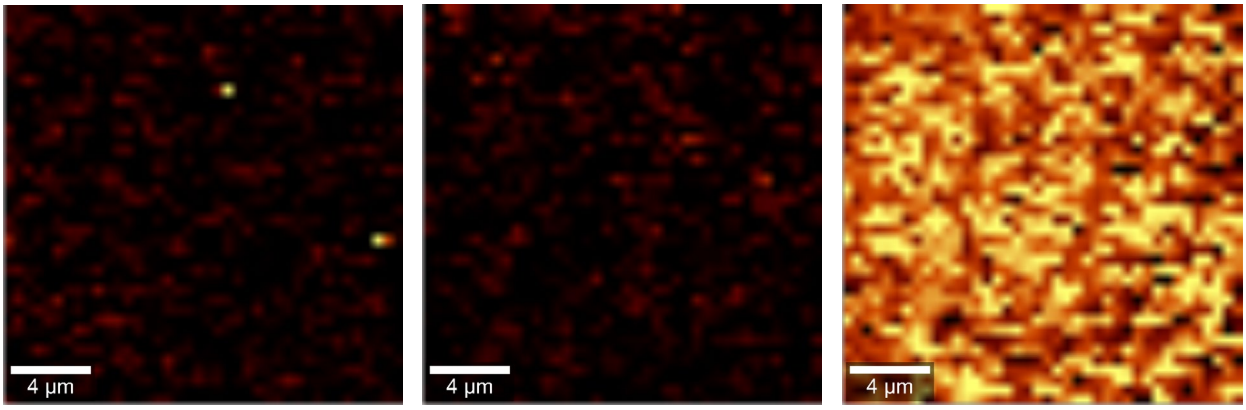

(a) (b) (c)

Figure 5 Spatial Raman Maps for Pristine PES (a), AA Modified PES (b), and GO Modified PES (b) Membranes.

Biocidal Assay

Biocidal assays were performed on all three membranes using the techniques described previously. Three separate assays were performed. In each case, the 1:100 dilution was used for counting since the colonies were both distinctive and numerous enough to count after spreading. For each assay, the number of colonies for the AA and GO membranes were normalized to that of PES. The results for the three assays are shown in Figure 6. Both the AA and GO modified membranes showed signs of biocidal activity as seen in the reduction of viable colonies in Figure 6. The GO membranes showed the strongest reduction in colonies, indicating the greatest biocidal effects of the three membranes. The increased biocidal nature of the GO membranes is consistent with previous literature.

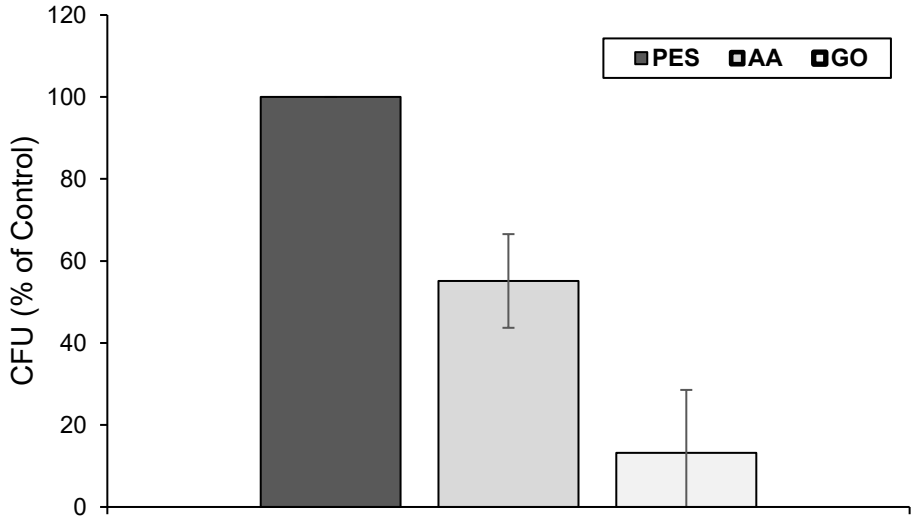

Figure 6 Biocidal Assay Results for Pristine and AA and GO Modified PES Membranes

Contact Angle

Measurements for contact angles were performed using n-decane droplets in water via the captive bubble technique. At least angles were measured for each of the three membrane types. Due to the hydrophilic nature of the membranes (particularly the GO and AA membranes), large droplets of n-decane were required. Efforts were made to keep the droplet size consistent across all three membrane types to minimize. The results for submerged contact angles are shown in Figure 7. The average contact angle for the AA membranes, 20.6°, was slightly higher than that of the GO membranes, 19.6°. Both the GO and AA average contact angles were significantly lower than for the unmodified PES membranes which had an average contact angle of 43.1°.

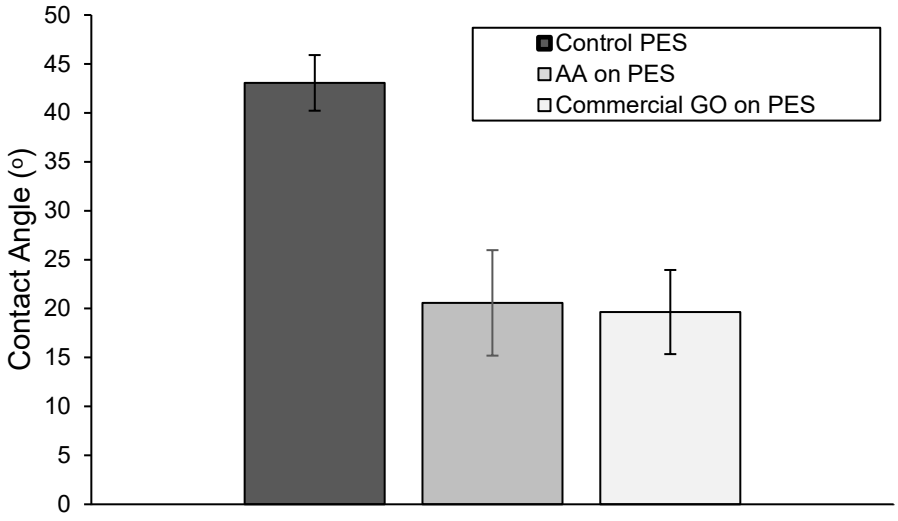

Figure 7 Captive Bubble Contact Angle Results

Contact angles were also measured using the water droplet in air method. For this, a 1uL droplet was deposited on the surface of the dried membranes. The contact angle was immediately measured to minimize the effects of spreading. At least separate angles were used for each membrane. The results are shown in Figure 8. These results show that the unmodified and GO modified PES membranes had similar hydrophilicity when measured in air, while the acrylic acid modified membrane showed significantly higher hydrophilicity.

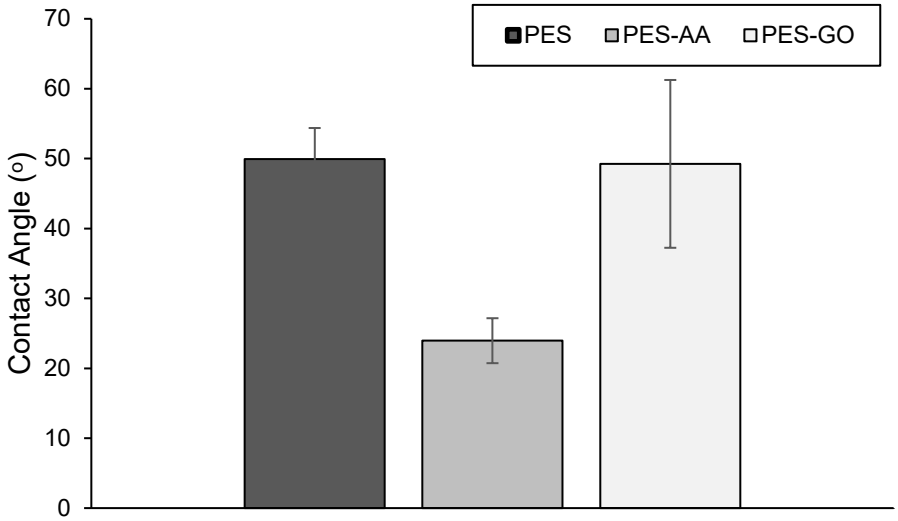

Figure 8 Water Droplet in Air Contact Angle Results

Zeta potential

Zeta potential measurements were taken for three pristine PES membranes, three AA membranes, and three GO membranes. The resulting curves for each membrane are in Figure 9. The acrylic acid modified membranes had a consistent streaming potential of roughly -30mV which was maintained from a pH of 10 to a pH of around 6.5. At higher acidic conditions, the potential dropped to nearly -40mV at a pH around 5 and then gradually increased as the pH was increased to 4. This dip in the potential could have been associated with the presence of carboxylic acid groups on the membrane surface. All three GO membranes followed a consistent trend of increasing in zeta potential initially at a pH of 10, plateauing until a pH of 6.5 and then sharply increasing through a pH of 4. In general, the GO membranes had a lower potential than the acrylic acid membranes until a pH of 6. This more negatively charged surface could be explained by the increase in carboxylic acid density from the GO nanosheets. The generally lower zeta potential (seen in the typical operating conditions of a pH of 6-8) could result in more better rejection due to Donnan exclusion. In addition, this lower charge should cause both the GO and acrylic acid modified membranes to have a lower propensity for bacterial fouling.

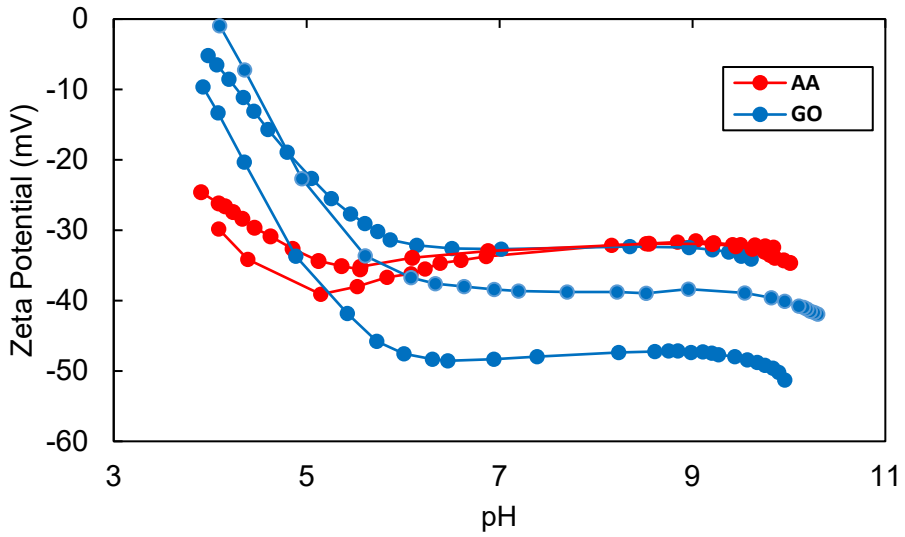

Figure 9 Zeta Potential Results for PES-AA and PES-GO Membranes

Single Cell Force Spectroscopy

A total of roughly 100 force curves were collected from at least three separately functionalized membranes for each of the three membrane types. A single Pseudomonas genus, P. fluorescens bacterium was immobilized on a calibrated cantilever tip. Extension−retraction cycles were performed at a cantilever speed of 400 nm/s, force distance of 2 μm or longer, and trigger force of 600 pN. For each force curve generated, the rupture separation distance and the adhesive forces of the bacteria were calculated. Figures 1-4 represent the data for adhesion force and rupture separation for PES membranes and PES-AA membranes. GO membrane data collection will need to be finished and worked up prior to analysis.

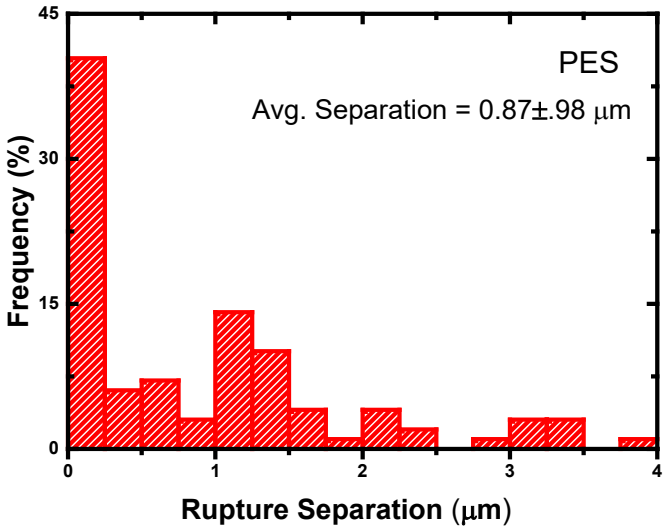

Figure 10: Rupture Separation Data Over PES Membrane

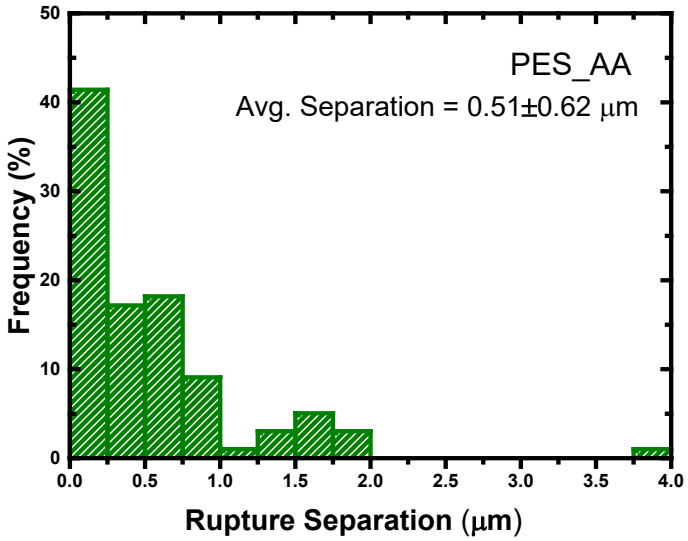

Figure 11: Rupture Separation Data Over PES-AA Membrane

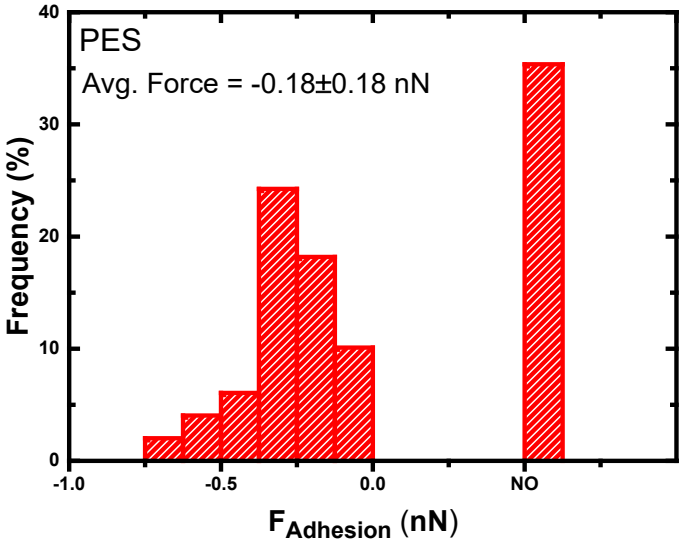

Figure 12: Adhesion Force Data Over PES Membrane

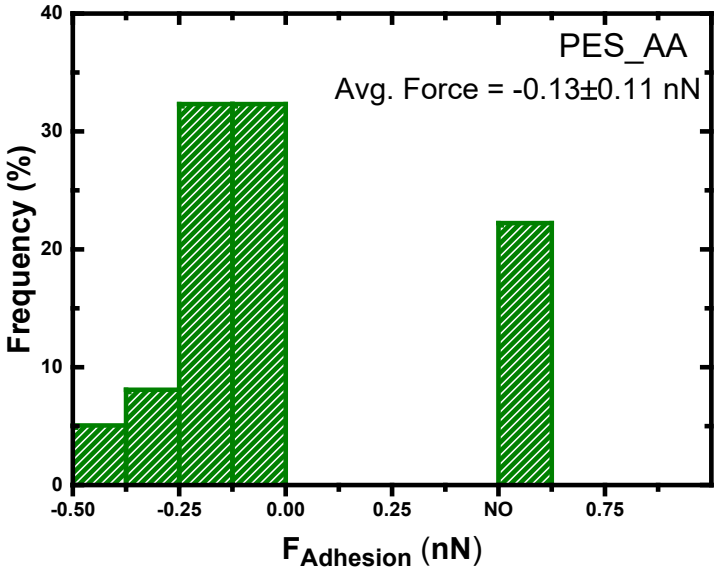

Figure 13: Adhesion Force Data Over PES-AA Membrane

The PES membrane SCFS experiments consist of 99 force curves using three different bacteria cells with an intact cell membrane. The PES-AA membrane SCFS experiments consist of 99 force curves using three different bacteria cells with an intact cell membrane, as well. Future work will consist of obtaining 99 force curves over the GO functionalized membranes for comparison.

Works Cited

[1] M. Homayoonfal, A. Akbari, and M. R. Mehrnia, “Preparation of polysulfone nanofiltration membranes by UV-assisted grafting polymerization for water softening,” *Desalination*, vol. 263, no. 1–3, pp. 217–225, 2010.

[2] E. Igbinigun, Y. Fennell, R. Malaisamy, K. L. Jones, and V. Morris, “Graphene oxide functionalized polyethersulfone membrane to reduce organic fouling,” *J. Memb. Sci.*, vol. 514, pp. 518–526, 2016.

[3] A. Rahimpour, “UV photo-grafting of hydrophilic monomers onto the surface of nano-porous PES membranes for improving surface properties,” *DES*, vol. 265, no. 1–3, pp. 93–101, 2011.

[4] M. Taniguchi, J. E. Kilduff, and G. Belfort, “Low fouling synthetic membranes by UV-assisted graft polymerization: Monomer selection to mitigate fouling by natural organic matter,” *J. Memb. Sci.*, vol. 222, no. 1–2, pp. 59–70, 2003.

[5] F. Perreault, M. E. Tousley, and M. Elimelech, “Thin-Film Composite Polyamide Membranes Functionalized with Biocidal Graphene Oxide Nanosheets,” *Environ. Sci. Technol. Lett.*, vol. 1, no. 1, pp. 71–76, 2013.

[6] R. Avazzadeh and E. V. Masoud, “Synthesis and application of magnetite dextran-spermine nanoparticles in breast cancer hyperthermia,” *Prog. Biomater.*, vol. 6, no. 3, pp. 75–84, 2017.

[7] T. He, M. Frank, M. H. V. Mulder, and M. Wessling, “Preparation and characterization of nanofiltration membranes by coating polyethersulfone hollow fibers with sulfonated poly(ether ether ketone) (SPEEK),” *J. Memb. Sci.*, vol. 307, no. 1, pp. 62–72, 2008.

[8] S. P. Singh, Y. Li, J. Zhang, J. M. Tour, and C. J. Arnusch, “Sulfur-Doped Laser-Induced Porous Graphene Derived from Polysulfone-Class Polymers and Membranes,” *ACS Nano*, vol. 12, no. 1, pp. 289–297, 2018.

[9] H. Ma, R. H. Davis, and C. N. Bowman, “Novel sequential photoinduced living graft polymerization,” *Macromolecules*, vol. 33, no. 2, pp. 331–335, 2000.

[10] W.A. Mitch, J.O. Sharp, R.R. Trussell, R.L. Valentine, L. Alvarez-Cohen, D.L. Sedlak, NNitrosodimethylamine (NDMA) as a Drinking Water Contaminant: A Review, Environ. Eng. Sci. 20 (2003) 389–404. doi:10.1089/109287503768335896.

Environmental Science & Technology Letters

Letter

Cite This: Environ. Sci. Technol. Lett. XXXX, XXX, XXX−XXX

pubs.acs.org/journal/estlcu

Bacterial Adhesion to Graphene Oxide (GO)-Functionalized Interfaces Is Determined by Hydrophobicity and GO Sheet Spatial Orientation

Jinkai Xue,*[,†,♦] Sara BinAhmed,[†,♦] Zhaoxing Wang,[†] Nathan G. Karp,[†] Benjamin L. Stottrup,[‡] and Santiago Romero-Vargas Castrillón*[,†]

[†]Department of Civil, Environmental, and Geo-Engineering, University of Minnesota, Twin Cities, 500 Pillsbury Dr. SE, Minneapolis, Minnesota 55455, United States

[‡]Department of Physics, Augsburg University, Minneapolis, Minnesota 55454, United States

Supporting Information

ABSTRACT: The potential of graphene oxide (GO) in environmental applications, such as the development of antimicrobial materials and low-fouling membranes, has thus far been hindered by an incomplete understanding of bioadhesion mechanisms on GO interfaces. Using atomic force microscopy (AFM)-based single-cell force spectroscopy, we investigate the adhesion of single *Pseudomonas fluorescens* cells on GO-functionalized interfaces possessing distinct morphologies. Specifically, we investigate Si-GO surfaces, in which Langmuir−Blodgett GO films are transferred to Si wafers by dip-coating, forming an immobilized layer of horizontally arranged GO nanosheets, and PLL-GO surfaces, where GO nanosheets, edge-tethered to poly-L-lysine, form an interface characterized by morphological and conformational disorder. We observe strong adhesion forces on both Si-GO and PLL-GO surfaces; analysis of the pull-off forces in terms of the worm-like chain model reveals that adhesion is driven by hydrophobic interactions between proteinaceous adhesins on *P. fluorescens* and graphenic basal planes. We further show that adhesion forces are significantly stronger on Si-GO surfaces that facilitate interactions with graphenic planes, compared to PLL-GO surfaces, which show weaker adhesion due to steric and electrostatic repulsion. These results therefore demonstrate that the spatial orientation and conformational disorder of GO nanosheets are key factors governing the interfacial properties of graphene nanomaterials.

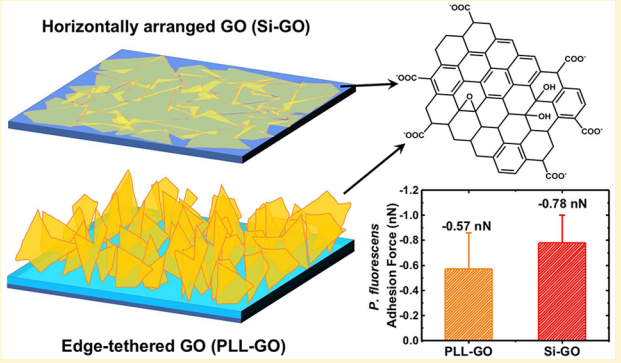

1. INTRODUCTION

The significant interest in graphene nanomaterials is motivated by their unique physical and chemical properties. Graphene is the thinnest, strongest material ever developed.[1] As a 2-D nanomaterial with metallic properties, it is finding applications in electronic and photovoltaic devices.[2] The high surface area and photocatalytic-enhancing properties of graphene hold promise in environmental remediation, adsorption, degradation of organic contaminants, and the development of water purification membranes.[2,3] Furthermore, graphene and graphene oxide (GO) exhibit wide-spectrum antibacterial activity,[4−9] opening new avenues for the development of biocidal materials and interfaces, such a low-biofouling membranes.[10,11] Nonetheless, further deployment of graphene-based biocidal materials has been hindered by an incomplete understanding of the adhesion mechanisms of bacteria on graphenic interfaces. Previous studies have attempted to explain the interactions between cells and individual graphenic sheets in suspension, with contradictory conclusions documented by different investigators. Li et al.[12] and Tu et al.,[13] using a combination of microscopy and simulation, proposed that graphene[12,13] and GO sheets[13] pierce lipid bilayers via sheet asperities or edges; a mechanism for bilayer piercing was provided based on molecular dynamics simulation, which showed spontaneous piercing of the cell membrane when graphene and GO sheets translocate orthogonally to the cell.[12,13] On the other hand, AFM-based force spectroscopy measurements showed that the interactions of a GO-coated AFM probe with *E. coli* cell membranes were predominantly repulsive, possibly due to negatively charged GO sheet edges, which result in electrostatic repulsive forces as the nanosheets impinge on the cell membrane edge-first.[12,14] These studies suggest that GO sheet spatial orientation plays an important role in determining the behavior of interfaces functionalized with GO. The relevance of nanosheet configuration is underscored by reports that nanosheet edge-bacteria contact is a determinant of biocidal activity,[9,15] with a recent

Received: November 12, 2017
Revised: December 7, 2017
Accepted: December 13, 2017
Published: December 13, 2017

DOI: 10.1021/acs.estlett.7b00509
Environ. Sci. Technol. Lett. XXXX, XXX, XXX−XXX

study reporting higher biocidal activity in GO films comprising, edge-exposed, vertically aligned nanosheets,[16] though this view remains contentious.[17−19] Nonetheless, direct, real-time experimental measurements examining the adhesion forces of bacteria on GO surfaces and the possible role played by GO sheet orientation in GO-cell adhesion forces are still lacking. In this work, we use atomic force microscopy (AFM)-based force spectroscopy to quantitatively evaluate the interactions of single *P. fluorescens* cells, a biofilm forming,[20,21] environmentally relevant bacterium found in soil and drinking water,[22,23] with substrates possessing horizontally oriented or randomly oriented GO surface coatings. We find strong bacterial adhesion on GO-functionalized surfaces, driven by hydrophobic interactions between proteinaceous adhesins and graphenic basal planes in GO. Further, we demonstrate that *P. fluorescens* adhesion is stronger on "flat" GO surface coatings as compared to randomly oriented surface coatings, demonstrating the importance of spatial orientation of GO as a design variable in GO surface coatings.

2. MATERIALS AND METHODS

2.1. Preparation of GO and GO Model Surfaces. GO was prepared following a modification of Hummers' method, as explained in the Supporting Information (SI).[24] Confocal Raman spectroscopy, AFM, and scanning electron microscopy (SEM) were performed to characterize the GO sheets. The characteristic D (∼1350 cm^{-1}) and G (∼1590 cm^{-1}) bands[25] of GO were identified in the Raman spectrum (Figure S1(a)). GO sheets showed an average sheet size (Figure S1(b)) of ∼0.08 μm (SEM images were analyzed with Fiji[26]) and sheet thickness (Figure S1(c, d)) of ∼1 nm, in agreement with previous reports.[14] Zeta potential measurements of GO in aqueous dispersion (Figure S1(e)) showed that the nanosheets are negatively charged, due to deprotonation of carboxylic acid groups at the sheet edges.[27,28]

Two model GO surfaces (i.e., randomly oriented GO sheets and horizontally oriented GO sheets) were prepared. The first class (denoted as PLL-GO surfaces) was prepared by covalently tethering GO sheets to poly-L-lysine (PLL)-coated glass (Poly-Prep slides, Sigma-Aldrich) via amine coupling chemistry.[29] The second class of surfaces (designated Si-GO) was prepared by transferring a GO Langmuir−Blodgett (LB) film[17] to a P-type silicon (Si) wafer via dip-coating.[30] Details on the preparation of GO surfaces can be found in the SI. GO immobilized on the PLL-GO and Si-GO surfaces was confirmed by Raman spectroscopy. Surface roughness, hydrophobicity, and zeta potential were evaluated using AFM, captive bubble contact angle, and streaming current measurements, respectively, as described in the SI.

2.2. AFM-Based Single Cell Force Spectroscopy. *Pseudomonas fluorescens* ATCC 13525 was used in all single-cell force spectroscopy (SCFS) experiments. As in other bacteria of the *Pseudomonas* genus, *P. fluorescens* has high biodhesion and biofilm formation potential, owing to an array of adhesins,[31] including flagella, pili, lipopolysaccharides (LPS), and outer membrane proteins (OMP) that influence its motility and adhesiveness.[32−35] Single *P. fluorescens* cells were adhered to the cantilever using a polydopamine (PDA) wet adhesive.[36,37] Details of the bacterial growth conditions and preparation of bacterial cell AFM probes are given in our recent publication[38] and summarized in the SI.

An MFP-3D-Bio AFM (Asylum Research) integrated to a Zeiss Axio Observer A.1 inverted optical microscope was used for single-cell force measurements at room temperature (25 °C). Extension−retraction cycles were performed at a cantilever speed of 400 nm/s, force distance of 2 μm (longer force distances were used whenever long-range interactions were observed), and trigger force of 600 pN. Force curves were acquired at randomly chosen sites on the specimen surface; only three replicate force curves were recorded over each site to minimize deposition of extracellular polymeric substances. For each model surface, at least three individual cells (from three independent cell cultures) were used to collect a total of ≈100 curves. Raw data (i.e., cantilever deflection versus piezo Z position) were converted into force−separation curves, recording from each pull-off curve the maximum adhesion force (F_{Ad}) and rupture separation (L_R) (i.e., the separation at which surface forces vanish). Cell viability was checked after each experiment by a live/dead assay (Baclight). Only data collected with a live cell that remained at its initial location (such as that shown in Figure S12) are reported and discussed.

3. RESULTS AND DISCUSSION

3.1. Characterization of the Surfaces. Raman spectroscopy maps and AFM topographic images (collected in PBS buffer, pH 7.4) of the GO surfaces are provided in Figure 1.

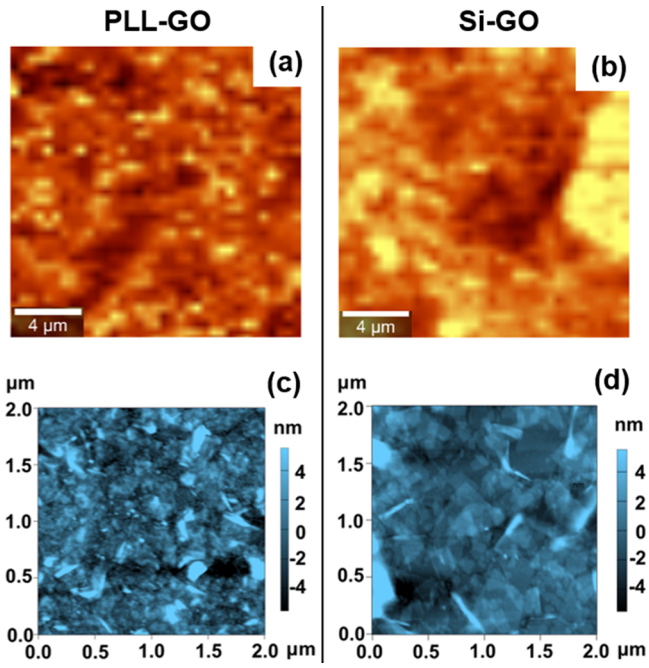

Figure 1. Surface characterization of PLL-GO (left column) and Si-GO surfaces (right column). (a, b) Raman spectroscopy maps of PLL-GO (a) and Si-GO (b) substrates. (c, d) Tapping mode AFM images of PLL-GO (c) and Si-GO (d) substrates. AFM imaging was conducted in PBS buffer, pH 7.4.

The Raman maps (Figure 1(a, b) and Figure S3(a, b)) show regions of high brightness (proportional to the intensity of the D and G peaks of GO), albeit with dissimilar spatial distribution: small (typically <1 μm) regions of high brightness were observed on the PLL-GO surface (Figure 1(a)), whereas the Si-GO surface exhibited larger GO domains (≥1 μm), suggesting the presence of horizontally arranged GO (Figure 1(b)). In control surfaces (GO-free PLL and Si), Raman intensity is significantly attenuated (Figures S3(c, d)). The morphological features of Figure 1(a, b) are consistent with the

DOI: 10.1021/acs.estlett.7b00509
Environ. Sci. Technol. Lett. XXXX, XXX, XXX−XXX

AFM images (Figure 1(c, d)), showing that two different spatial orientations are realized by these surfaces: GO nanosheets in Si-GO surfaces are stacked horizontally on the Si substrate (Figure 1(d) and Figure S2(b)), whereas a significantly more disordered interface is obtained when GO is tethered to flexible PLL chains (cf. PLL-GO, Figure 1(c) and Figure S2(a)), where horizontally oriented sheets on the substrate are not observed. In accord with the morphological features described in Figure 1, the root-mean-square roughness (R_{RMS}, Figure S4(a)) of PLL-GO (R_{RMS} = 2.78 nm) is higher than that of Si-GO (R_{RMS} = 1.62 nm, which suggests a GO film 1−2 sheets thick on Si). Figure S4(a) further shows that the presence of GO increases the roughness of the unmodified control substrates (note the lower surface roughness of bare PLL and Si surfaces). The orientational disorder of GO nanosheets in PLL-GO is partially due to the roughness of the underlying PLL, and it is also a consequence of bonding GO to primary amines in PLL, which allows edge-tethered solvated nanosheets to undergo thermal agitation. The zeta potential values showed that the four surfaces were negatively charged, exhibiting similar surface potentials (−60 to −90 mV) at pH 7.4 (Figure S4(b)).

The wettability of the surfaces, characterized by the contact angle of captive *n*-decane droplets in PBS (pH 7.4), is presented in Figure S5. Low contact angles (i.e., low *n*-decane wettability) are observed in all surfaces; H-bonding functional groups present in PLL (primary amine groups) and PLL-GO (epoxide, hydroxyl, and carboxylic groups that decorate the GO sheet edges[27,39]) explain the poor wettability with *n*-decane. The similarity of contact angle values observed in Si and Si-GO is consistent with the wetting translucency[40] of graphene films. Given its ultrathin-sheet geometry, a significant fraction of the *n*-decane-Si van der Waals interactions are transmitted through the graphenic planes, resulting in wetting behavior that is relatively unaffected by the graphene coating.[41,42]

3.2. GO Nanosheet Spatial Orientation and Hydrophobicity Are Determining Factors of Bacterial Adhesion. Figure 2(a) presents the mean maximum adhesion force ($\langle F_{Ad} \rangle$, where F_{Ad} is defined in the inset) observed on control and GO surfaces; adhesion force histograms for each system are given in Figure S6. GO functionalization has a significant effect on cell adhesion, as shown by the doubling of $\langle F_{Ad} \rangle$ in PLL-GO compared to PLL substrates and the order-of-magnitude increase in $\langle F_{Ad} \rangle$ observed in Si-GO surfaces compared to the Si control. The mean adhesion forces presented in Figure 2(a) increase as Si (−0.01 nN) < PLL (−0.28 nN) < PLL-GO (−0.57 nN) < Si-GO (−0.78 nN) ($p < 0.01$ from two-sided unpaired *t*-tests); these reflect cell−substrate adhesion forces, as demonstrated by the significantly weaker forces observed in control measurements with bacterium-free PDA-coated cantilevers (Figure S7, $p < 0.01$ except Si, on which weak adhesions are observed with and without cell). To explain the results shown in Figure 2(a), we note that bacterial adhesion is determined by a variety of cell-surface structures, such as pili and outer membrane proteins,[34,35,43] which, owing to the high content of hydrophobic amino acids (in e.g., pilin proteins[43]), mediate attachment to hydrophobic substrates via hydrophobic interactions.[44,45] At the micro- and nanoscales both PLL-GO and Si-GO surfaces present hydrophobic regions embedded in the graphenic planes of the nanosheets,[27,46] which are known to serve as adsorption sites for hydrophobic molecules.[27,47−49] Consequently, the significant increase in $\langle F_{Ad} \rangle$ observed over Si-GO and PLL-GO is ascribed to hydrophobic association of cell-surface adhesins with hydrophobic domains in GO sheets.

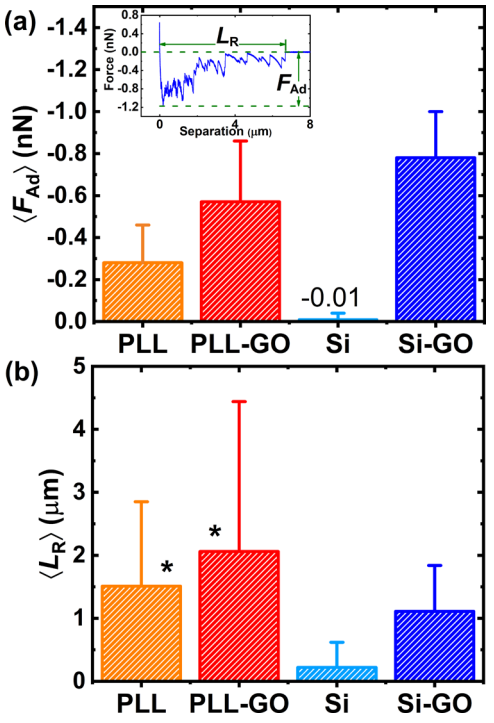

Figure 2. Results of single-cell force spectroscopy. (a) Average maximum adhesion force ($\langle F_{Ad} \rangle$) of *P. fluorescens* cells on the various surfaces. A representative pull-off force curve showing the definition of F_{Ad} and L_R is shown in the inset of panel (a). (b) Mean rupture separation ($\langle L_R \rangle$, the separation at which adhesion forces vanish). All experiments were performed in PBS buffer (pH 7.4). The histograms from which the reported means were computed are given in Figures S6 and S8; $p < 0.01$ (two-tailed unpaired *t*-test) for all pairwise comparisons except when indicated by ∗.

The determining role of hydrophobicity in *P. fluorescens* attachment is underscored by the weak adhesion (∼10 pN, cf. Figure 2(a)) observed on Si substrates, the most hydrophilic surface investigated in this work (cf. Figure S5). Furthermore, we observe stronger ($p < 0.01$) $\langle F_{Ad} \rangle$ over Si-GO than PLL-GO (−0.78 nN vs −0.57 nN, respectively, cf. Figure 2(a)). The different adhesiveness demonstrated by PLL-GO and Si-GO is derived from their respective morphologies. Si-GO surfaces, as shown in Figure 1(d), exhibit horizontally arranged GO sheets, whereas GO sheets tethered to PLL form a rougher and more disordered PLL-GO interface (Figure 1(c) and Figure S4(a)). The flat GO sheet orientation in Si-GO surfaces therefore maximizes the surface area of graphenic planes with which cell biopolymers interact, thereby facilitating bacterial attachment. Low roughness of Si-GO (Figure S4(a)) may also enable bacterial attachment, as observed with pyrolytic graphite.[15] Conversely, bacteria adhering on PLL-GO face negatively charged GO sheet edges,[28] which weaken bacterial attachment due to electrostatic repulsive forces.[14] In addition, GO sheets edge-tethered to PLL create a steric barrier against microbial deposition, akin to that formed by solvated polymers.[50−52] As a bacterium adheres on PLL-GO, GO nanosheets are compressed, the resulting loss of conformational entropy opposing cell adhesion.[50] These data thus demonstrate that nanosheet spatial arrangement (i.e., flat vs randomly oriented) and conformational degrees of freedom play key roles in determining the GO-bacterial cell adhesion forces.

To gain insight into the cell-surface structures mediating adhesion, we analyzed the rupture distance (L_R), defined in

DOI: 10.1021/acs.estlett.7b00509
Environ. Sci. Technol. Lett. XXXX, XXX, XXX−XXX

Figure 2(a) (inset). The values of the mean rupture distance ($\langle L_R \rangle$) are presented in Figure 2(b), and the distributions of L_R appear in Figure S8. Apart from the Si control, over which no significant adhesion is observed, mean L_R values reported by PLL, PLL-GO, and Si-GO surfaces (1−2 μm) are consistent with bioadhesion mediated by membrane proteins (contour length ≈2 μm[34,35]); a fraction of measurements showing L_R > 2 μm (Figure S8 for PLL, PLL-GO, and Si-GO) is likely due to pili-mediated adhesion, which can extend to several micrometers.[53,54] Long L_R values may also be attributed to stretching of PLL chains on the glass substrates, as shown by the longer-ranged forces exhibited by PLL and PLL-GO compared to Si-GO substrates (Figure 2(b)).

3.3. Proteinaceous Adhesins Mediate *P. fluorescens* Attachment to GO-Functionalized Interfaces. In a subset (~20%) of the pull-off force−separation profiles recorded on PLL, PLL-GO, and Si-GO, we observed the sawtooth pattern (Figure 3(a)) that is associated with force unfolding of protein domains.[44,55] As shown in the inset of Figure 3(a), the peaks are well fitted by the worm-like chain (WLC) model of polymer elasticity[56,57] which describes the force F necessary to unravel a random coil as $F(x) = k_BT/L_P[0.25(1 - x/L_C)^{-2} + x/L_C - 0.25]$, where x is separation, k_B is the Boltzmann constant, T is the absolute temperature (298 K), L_P is the persistence length (a measure of polymer rigidity), and L_C is the contour length (the length of the unfolded macromolecule). Quantitative analysis of the pull-off force curves in terms of the WLC model yielded values of L_P and L_C (in fitting the WLC model, we discarded nonspecific adhesion peaks at short separation, as well as peaks yielding L_P < 0.15 nm, the length of a C−C bond[58]). We find that best-fit L_P values were narrowly distributed with means in the 0.23−0.28 nm range (Figure 3(b) and Figure S9), close to the persistence length of proteins (~0.4−1 nm[34,55,59,60]), and observed that the mean peak force (F_{Unf}, defined in Figure 3(a)) was consistent with the unfolding force of membrane proteins (~300 pN, cf. Figure 3(c) and Figure S10).[34,55] The values of L_P and F_{Unf} suggest that adhesion of *P. fluorescens* is mediated by proteinaceous hydrophobic adhesins, likely to be membrane proteins that interact with hydrophobic graphenic planes in GO nanosheets, and lysyl side chains in PLL. The hydrophobic character of adhesin proteins is manifested by the absence of the sawtooth pattern in all force curves recorded over hydrophilic Si substrates. ΔL_C, the difference in contour lengths between consecutive sawtooth peaks, revealed the length scale of the unfolded domains. As shown in Figures S11(b, c), ΔL_C values for PLL-GO and Si-GO were distributed around means of 66.4 and 80.6 nm, respectively, which suggest that each sawtooth peak is due to unfolding of more than one protein domain (whose repeats are ~30−40 nm for membrane proteins[35] and ~50−60 nm in pilin proteins[53]). The broader distribution of ΔL_C observed over PLL (Figure S11(a)) suggests that adhesins undergo surface-induced unfolding over this substrate.[34]

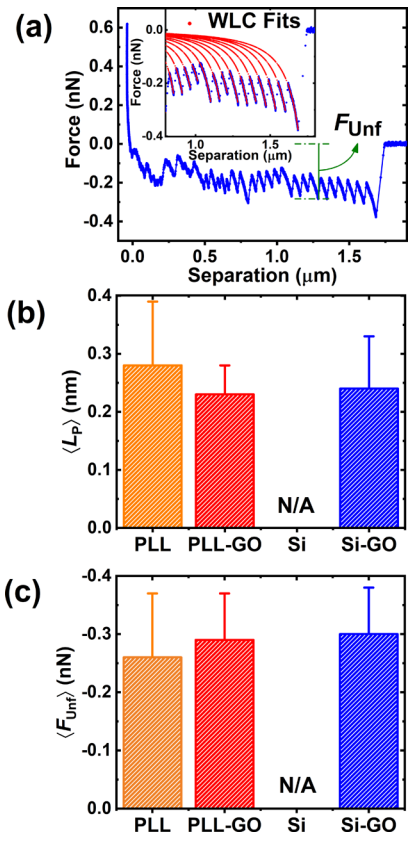

Figure 3. Signatures of macromolecular unfolding observed over different model surfaces. (a) Representative force curve exhibiting the sawtooth pattern characteristic of force-unfolding of macromolecular domains. Representative fits of the worm-like chain (WLC) model to the sawtooth patterns are shown in the inset. (b) Mean persistence length ($\langle L_P \rangle$) obtained from WLC model fits to the pull-off force curve of single *P. fluorescens* cells. (c) Mean unfolding force ($\langle F_{Unf} \rangle$). The definition of F_{Unf} is shown in panel (a). The histograms from which the means in panels (b) and (c) were computed are given in Figures S9 and S10. N/A for Si indicates that no signatures of macromolecular unfolding were observed on this substrate.

In closing, we have demonstrated that the hydrophobic interactions that drive *P. fluorescens* adhesion are stronger in GO interfaces assembled from horizontally arranged nanosheets, as compared to edge-tethered GO sheets where electrostatic and steric repulsion weaken adhesion forces. Our results emphasize the importance of nanosheet hydrophobicity, spatial arrangement, and conformational disorder in determining the interfacial behavior of GO-functionalized substrates, pointing out possible directions for future inquiry. Reactive oxygen species (ROS)-mediated cell oxidation[6,14] is likely to modify cell bioadhesion due to breakdown of the outer membrane. Experiments isolating the competing effect of ROS pose interesting questions that warrant future investigations. Further investigations should also aim to elucidate the mechanism of adhesion of hydrophilic bacteria[61] to graphenic surfaces, perhaps using adhesin-knockout mutants.

■ ASSOCIATED CONTENT

Supporting Information

The Supporting Information is available free of charge on the ACS Publications website at DOI: 10.1021/acs.estlett.7b00509.

Further information on materials and methods (GO synthesis and characterization, preparation and characterization of PLL-GO and Si-GO surfaces, and functionalization of AFM probes with bacterial cells). Results of GO characterization (Figure S1); AFM imaging, Raman spectroscopy images, AFM surface roughness, zeta potential, and contact angle measurements for all surfaces (Figures S2−S5); histograms of adhesion forces (Figures S6 and S7), rupture separations (Figure S8), persistence lengths (Figure S9), unfolding forces (Figure

DOI: 10.1021/acs.estlett.7b00509
Environ. Sci. Technol. Lett. XXXX, XXX, XXX−XXX

S10), contour lengths (Figure S11); and digital image of bacterial cell AFM probe (Figure S12). (PDF)

AUTHOR INFORMATION

Corresponding Authors

*E-mail: xuexx145@umn.edu. Tel: +1 (226) 505-0458 (Jinkai Xue).

*E-mail: sromerov@umn.edu. Tel: +1 (612) 301-1347 (Santiago Romero-Vargas Castrillón).

ORCID

Santiago Romero-Vargas Castrillón: 0000-0003-3339-7692

Author Contributions

♦J. X. and S. BA. were equal contributors to this work.

Notes

The authors declare no competing financial interest.

ACKNOWLEDGMENTS

This work was supported by grants to S.R.-V.C. from the United States Geological Survey (MN WRC 2015MN362B), 3M Co. (Non-Tenured Faculty Award), and the Environment and Natural Resources Trust Fund, as recommended by the Legislative-Citizen Commission on Minnesota Resources. Portions of this work were carried out in the Characterization Facility and Minnesota Nano Center, University of Minnesota, which receive partial support from NSF through the MRSEC and NNIN programs, respectively. Work at Augsburg University was supported by NSF MRI 1040126.

REFERENCES

(1) Lee, C.; Wei, X.; Kysar, J. W.; Hone, J. Measurement of the elastic properties and intrinsic strength of monolayer graphene. *Science (Washington, DC, U. S.)* **2008**, *321* (5887), 385−388.

(2) Zhu, Y.; Murali, S.; Cai, W.; Li, X.; Suk, J. W.; Potts, J. R.; Ruoff, R. S. Graphene and graphene oxide: Synthesis, properties, and applications. *Adv. Mater.* **2010**, *22* (35), 3906−3924.

(3) Hu, M.; Mi, B. Enabling graphene oxide nanosheets as water separation membranes. *Environ. Sci. Technol.* **2013**, *47* (8), 3715−3723.

(4) Chen, J.; Peng, H.; Wang, X.; Shao, F.; Yuan, Z.; Han, H. Graphene oxide exhibits broad-spectrum antimicrobial activity against bacterial phytopathogens and fungal conidia by intertwining and membrane perturbation. *Nanoscale* **2014**, *6* (3), 1879−1889.

(5) Hu, W.; Peng, C.; Luo, W.; Lv, M.; Li, X.; Li, D.; Huang, Q.; Fan, C. Graphene-based antibacterial paper. *ACS Nano* **2010**, *4* (7), 4317−4323.

(6) Perreault, F.; De Faria, A. F.; Nejati, S.; Elimelech, M. Antimicrobial properties of graphene oxide nanosheets: Why size matters. *ACS Nano* **2015**, *9* (7), 7226−7236.

(7) Gurunathan, S.; Han, J. W.; Dayem, A. A.; Eppakayala, V.; Kim, J. H. Oxidative stress-mediated antibacterial activity of graphene oxide and reduced graphene oxide in *Pseudomonas aeruginosa*. *Int. J. Nanomed.* **2012**, *7*, 5901−5914.

(8) Chen, J.; Wang, X.; Han, H. A new function of graphene oxide emerges: Inactivating phytopathogenic bacterium. *J. Nanopart. Res.* **2013**, *15* (5), 1−14.

(9) Akhavan, O.; Ghaderi, E. Toxicity of graphene and graphene oxide nanowalls against bacteria. *ACS Nano* **2010**, *4* (10), 5731−5736.

(10) Soroush, A.; Ma, W.; Cyr, M.; Rahaman, M. S.; Asadishad, B.; Tufenkji, N. In situ silver decoration on graphene oxide-treated thin film composite forward osmosis membranes: Biocidal properties and regeneration potential. *Environ. Sci. Technol. Lett.* **2016**, *3* (1), 13−18.

(11) Perreault, F.; Jaramillo, H.; Xie, M.; Ude, M.; Nghiem, L. D.; Elimelech, M. Biofouling mitigation in forward osmosis using graphene oxide functionalized thin-film composite membranes. *Environ. Sci. Technol.* **2016**, *50* (11), 5840−5848.

(12) Li, Y.; Yuan, H.; von dem Bussche, A.; Creighton, M.; Hurt, R. H.; Kane, A. B.; Gao, H. Graphene microsheets enter cells through spontaneous membrane penetration at edge asperities and corner sites. *Proc. Natl. Acad. Sci. U. S. A.* **2013**, *110* (30), 12295−12300.

(13) Tu, Y.; Lv, M.; Xiu, P.; Huynh, T.; Zhang, M.; Castelli, M.; Liu, Z.; Huang, Q.; Fan, C.; Fang, H.; et al. Destructive extraction of phospholipids from Escherichia coli membranes by graphene nanosheets. *Nat. Nanotechnol.* **2013**, *8* (8), 594−601.

(14) Romero-Vargas Castrillón, S.; Perreault, F.; De Faria, A. F.; Elimelech, M. Interaction of graphene oxide with bacterial cell membranes: Insights from force spectroscopy. *Environ. Sci. Technol. Lett.* **2015**, *2* (4), 112−117.

(15) Pham, V. T. H.; Truong, V. K.; Quinn, M. D. J.; Notley, S. M.; Guo, Y.; Baulin, V. A.; Al Kobaisi, M.; Crawford, R. J.; Ivanova, E. P. Graphene induces formation of pores that kill spherical and rod-shaped bacteria. *ACS Nano* **2015**, *9* (8), 8458−8467.

(16) Lu, X.; Feng, X.; Werber, J. R.; Chu, C.; Zucker, I.; Kim, J.-H.; Osuji, C. O.; Elimelech, M. Enhanced antibacterial activity through the controlled alignment of graphene oxide nanosheets. *Proc. Natl. Acad. Sci. U. S. A.* **2017**, *114*, E9793.

(17) Mangadlao, J. D.; Santos, C. M.; Felipe, M. J. L.; de Leon, A. C. C.; Rodrigues, D. F.; Advincula, R. C. On the antibacterial mechanism of graphene oxide (GO) Langmuir−Blodgett films. *Chem. Commun.* **2015**, *51* (14), 2886−2889.

(18) Hui, L.; Piao, J. G.; Auletta, J.; Hu, K.; Zhu, Y.; Meyer, T.; Liu, H.; Yang, L. Availability of the basal planes of graphene oxide determines whether it is antibacterial. *ACS Appl. Mater. Interfaces* **2014**, *6* (15), 13183−13190.

(19) Zucker, I.; Werber, J. R.; Fishman, Z. S.; Hashmi, S. M.; Gabinet, U. R.; Lu, X.; Osuji, C. O.; Pfefferle, L. D.; Elimelech, M. Loss of phospholipid membrane integrity induced by two-dimensional nanomaterials. *Environ. Sci. Technol. Lett.* **2017**, *4* (10), 404−409.

(20) O'Toole, G. A.; Kolter, R. Initiation of biofilm formation in *Pseudomonas fluorescens* WCS365 proceeds via multiple, convergent signalling pathways: A genetic analysis. *Mol. Microbiol.* **1998**, *28* (3), 449−461.

(21) Spiers, A. J.; Rainey, P. B. The *Pseudomonas fluorescens* SBW25 wrinkly spreader biofilm requires attachment factor, cellulose fibre and LPS interactions to maintain strength and integrity. *Microbiology* **2005**, *151* (9), 2829−2839.

(22) Haas, D.; Défago, G. Biological control of soil-borne pathogens by fluorescent pseudomonads. *Nat. Rev. Microbiol.* **2005**, *3* (4), 307−319.

(23) Hardalo, C.; Edberg, S. C. *Pseudomonas aeruginosa*: assessment of risk from drinking water. *Crit. Rev. Microbiol.* **1997**, *23* (1), 47−75.

(24) Tung, V. C.; Allen, M. J.; Yang, Y.; Kaner, R. B. High-throughput solution processing of large-scale graphene. *Nat. Nanotechnol.* **2009**, *4* (1), 25−29.

(25) Kudin, K. N.; Ozbas, B.; Schniepp, H. C.; Prud'homme, R. K.; Aksay, I. A.; Car, R. Raman spectra of graphite oxide and functionalized graphene sheets. *Nano Lett.* **2008**, *8* (1), 36−41.

(26) Schindelin, J.; Arganda-Carreras, I.; Frise, E.; Kaynig, V.; Longair, M.; Pietzsch, T.; Preibisch, S.; Rueden, C.; Saalfeld, S.; Schmid, B.; et al. Fiji: an open-source platform for biological-image analysis. *Nat. Methods* **2012**, *9* (7), 676−682.

(27) Sanchez, V. C.; Jachak, A.; Hurt, R. H.; Kane, A. B. Biological interactions of graphene-family nanomaterials: An interdisciplinary review. *Chem. Res. Toxicol.* **2012**, *25*, 15−34.

(28) Li, D.; Müller, M. B.; Gilje, S.; Kaner, R. B.; Wallace, G. G. Processable aqueous dispersions of graphene nanosheets. *Nat. Nanotechnol.* **2008**, *3* (2), 101−105.

(29) Grabarek, Z.; Gergely, J. Zero-length crosslinking procedure with the use of active esters. *Anal. Biochem.* **1990**, *185* (1), 131−135.

(30) Cote, L. J.; Kim, F.; Huang, J. Langmuir-Blodgett assembly of graphite oxide single layers. *J. Am. Chem. Soc.* **2009**, *131* (3), 1043−1049.

(31) Tamber, S.; Hancock, R. E. W. The outer membranes of *Pseudomonas*. In *Pseudomonas*; Ramos, J. L., Ed.; Springer, 2004; pp 575−601.

DOI: 10.1021/acs.estlett.7b00509
Environ. Sci. Technol. Lett. XXXX, XXX, XXX−XXX

(32) Dasgupta, N.; Arora, S.; Ramphal, R. The flagellar system of *Pseudomonas aeruginosa*. In *Pseudomonas*; Ramos, J. L., Ed.; 2004; Springer, pp 675−698.
(33) Tolker-Nielsen, T.; Molin, S. The biofilm lifestyle of *Pseudomonas*. In *Pseudomonas*; Ramos, J. L., Ed.; Springer, 2004; pp 547−571.
(34) El-Kirat-Chatel, S.; Boyd, C. D.; O'Toole, G. A.; Dufrene, Y. F. Single-molecule analysis of *Pseudomonas fluorescens* footprints. *ACS Nano* **2014**, *8* (2), 1690−1698.
(35) El-Kirat-Chatel, S.; Beaussart, A.; Boyd, C. D.; O'Toole, G. A.; Dufrene, Y. F. Single-cell and single-molecule analysis deciphers the localization, adhesion, and mechanics of the biofilm adhesin LapA. *ACS Chem. Biol.* **2014**, *9* (2), 485−494.
(36) Lee, H.; Dellatore, S. M.; Miller, W. M.; Messersmith, P. B. Mussel-inspired surface chemistry for multifunctional coatings. *Science (Washington, DC, U. S.)* **2007**, *318* (5849), 426−430.
(37) Kang, S.; Elimelech, M. Bioinspired single bacterial cell force spectroscopy. *Langmuir* **2009**, *25* (17), 9656−9659.
(38) BinAhmed, S.; Hasane, A.; Wang, Z.; Mansurov, A.; Romero-Vargas Castrillón, S. Bacterial adhesion to ultrafiltration membranes: Role of hydrophilicity, natural organic matter, and cell-surface macromolecules. *Environ. Sci. Technol.* **2017**, DOI: 10.1021/acs.est.7b03682.
(39) Park, S.; An, J.; Jung, I.; Piner, R. D.; An, S. J.; Li, X.; Velamakanni, A.; Ruoff, R. S. Colloidal suspensions of highly reduced graphene oxide in a wide variety of organic solvents. *Nano Lett.* **2009**, *9* (4), 1593−1597.
(40) Rafiee, J.; Mi, X.; Gullapalli, H.; Thomas, A. V.; Yavari, F.; Shi, Y.; Ajayan, P. M.; Koratkar, N. A. Wetting transparency of graphene. *Nat. Mater.* **2012**, *11* (3), 217−222.
(41) Shih, C.-J.; Strano, M. S.; Blankschtein, D. Wetting translucency of graphene. *Nat. Mater.* **2013**, *12* (10), 866−869.
(42) Shih, C. J.; Wang, Q. H.; Lin, S.; Park, K. C.; Jin, Z.; Strano, M. S.; Blankschtein, D. Breakdown in the wetting transparency of graphene. *Phys. Rev. Lett.* **2012**, *109* (17), 176101.
(43) Vesper, S. J. Production of pili (fimbriae) by *Pseudomonas fluorescens* and correlation with attachment to corn roots. *Appl. Environ. Microbiol.* **1987**, *53* (7), 1397−1405.
(44) Dufrene, Y. F. Sticky microbes: Forces in microbial cell adhesion. *Trends Microbiol.* **2015**, *23*, 376−382.
(45) Ong, Y. L.; Razatos, A.; Georgiou, G.; Sharma, M. M. Adhesion forces between *E. coli* bacteria and biomaterial surfaces. *Langmuir* **1999**, *15* (8), 2719−2725.
(46) Erickson, K.; Erni, R.; Lee, Z.; Alem, N.; Gannett, W.; Zettl, A. Determination of the local chemical structure of graphene oxide and reduced graphene oxide. *Adv. Mater.* **2010**, *22* (40), 4467−4472.
(47) Cote, L. J.; Kim, J.; Tung, V. C.; Luo, J.; Kim, F.; Huang, J. Graphene oxide as surfactant sheets. *Pure Appl. Chem.* **2010**, *83* (1), 95−110.
(48) Kim, J.; Cote, L. J.; Kim, F.; Yuan, W.; Shull, K. R.; Huang, J. Graphene oxide sheets at interfaces. *J. Am. Chem. Soc.* **2010**, *132* (23), 8180−8186.
(49) Liu, Z.; Robinson, J. T.; Sun, X.; Dai, H. PEGylated nanographene oxide for delivery of water-insoluble cancer drugs. *J. Am. Chem. Soc.* **2008**, *130* (33), 10876−10877.
(50) Prime, K. L.; Whitesides, G. M. Adsorption of proteins onto surfaces containing end-attached oligo(ethylene oxide): A model system using self-assembled monolayers. *J. Am. Chem. Soc.* **1993**, *115* (23), 10714−10721.
(51) Prime, K.; Whitesides, G. Self-assembled organic monolayers: model systems for studying adsorption of proteins at surfaces. *Science (Washington, DC, U. S.)* **1991**, *252* (5009), 1164−1167.
(52) Gon, S.; Kumar, K. N.; Nüsslein, K.; Santore, M. M. How bacteria adhere to brushy PEG surfaces: Clinging to flaws and compressing the brush. *Macromolecules* **2012**, *45* (20), 8373−8381.
(53) Filloux, A.; de Bentzmann, S.; Aurouze, M.; Lazdunski, A.; Vallet, I. Fimbrial genes in *Pseudomonas aeruginosa* and *Pseudomonas putida*. In *Pseudomonas*; Ramos, J. L., Ed.; Springer, 2004; pp 721−748.
(54) Whitechurch, C. B. Biogenesis and function of type IV pili in *Pseudomonas* species. In *Pseudomonas*; Ramos, J. L., Ed.; Springer, 2006; pp 139−188.
(55) Rief, M.; Gautel, M.; Oesterhelt, F.; Fernandez, J. M.; Gaub, H. E. Reversible unfolding of individual titin immunoglobulin domains by AFM. *Science (Washington, DC, U. S.)* **1997**, *276* (5315), 1109−1112.
(56) Bustamante, C.; Marko, J.; Siggia, E.; Smith, S. Entropic elasticity of lambda-phage DNA. *Science (Washington, DC, U. S.)* **1994**, *265* (5178), 1599−1600.
(57) Israelachvili, J. N. *Intermolecular and Surface Forces*, Third ed., Academic Press, 2011.
(58) Abu-Lail, N. I.; Camesano, T. A. Elasticity of *Pseudomonas putida* KT2442 surface polymers probed with single-molecule force microscopy. *Langmuir* **2002**, *18* (10), 4071−4081.
(59) Walther, K. A.; Grater, F.; Dougan, L.; Badilla, C. L.; Berne, B. J.; Fernandez, J. M. Signatures of hydrophobic collapse in extended proteins captured with force spectroscopy. *Proc. Natl. Acad. Sci. U. S. A.* **2007**, *104* (19), 7916−7921.
(60) Stirnemann, G.; Giganti, D.; Fernandez, J. M.; Berne, B. J. Elasticity, structure, and relaxation of extended proteins under force. *Proc. Natl. Acad. Sci. U. S. A.* **2013**, *110* (10), 3847−3852.
(61) Krasowska, A.; Sigler, K. How microorganisms use hydrophobicity and what does this mean for human needs? *Front. Cell. Infect. Microbiol.* **2014**, *4*, 1−7.

DOI: 10.1021/acs.estlett.7b00509
Environ. Sci. Technol. Lett. XXXX, XXX, XXX−XXX

Supporting Information

Bacterial Adhesion to Graphene Oxide (GO)-Functionalized Interfaces is Determined by Hydrophobicity and GO Sheet Spatial Orientation

Jinkai Xue[1,*,♦], Sara BinAhmed[1,♦], Zhaoxing Wang[1], Nathan G. Karp[1], Benjamin L. Stottrup[2], Santiago Romero-Vargas Castrillón[1,*]

Environ. Sci. Technol. Lett.

[1] Department of Civil, Environmental, and Geo- Engineering, University of Minnesota, Twin Cities, Minneapolis, MN 55455, USA

[2] Department of Physics, Augsburg University, Minneapolis, MN 55454

♦J. X. and S. BA. were equal contributors to this work

Contents: 17 pages and 12 figures

*Corresponding authors: Jinkai Xue. Email: xuexx145@umn.edu. Tel: +1 (226) 505-0458. Santiago Romero-Vargas Castrillón. Email: sromerov@umn.edu. Tel: +1 (612) 301-1347.

Supporting Materials and Methods

Synthesis of GO

Graphene oxide (GO) was prepared *via* chemical exfoliation of graphite (Bay Carbon, SP-1, 325 mesh) using a modified Hummers method.[1] First, 2.0 g of graphite was placed in 5 mL of concentrated sulfuric acid at 80 °C. Next, 2.0 g each of $K_2S_2O_8$ and P_2O_5 were added and the suspension was allowed to react at 80 °C for 4.5 hours. After reaction, the mixture was transferred into 320 mL of ultrapure water (18.2 MΩ cm, Barnstead, Thermo Fisher) and allowed to settle overnight. The mixture was subsequently vacuum filtered using PTFE membranes (0.45 μm, Whatman TE 36) and dried overnight at room temperature. Next, the obtained black solid was mixed with 80 mL of concentrated sulfuric acid over an ice bath, and 10.0 g of $KMnO_4$ was slowly added so that the temperature of the mixture did not exceed 10 °C. The mixture was then slowly heated to 35 °C over a period of 2.5 hours. Next, 154 mL of ultrapure water was slowly added, preventing the suspension temperature from exceeding 50 °C, and reacted for 2 hours at room temperature. Lastly, the mixture was transferred to 480 mL of ultrapure water, and 8.4 mL of 30% H_2O_2 was added, causing the mixture to acquire a yellowish-brown color. The suspension was allowed to settle for 2 days, and the precipitate was subsequently recovered by multiple centrifugation steps (12,000 × g, 30 min), initially re-suspending the product in 10% HCl to remove chemical residues and finishing with resuspension in water until the supernatant reached a pH of about 3.5. Finally, the suspended product was purified *via* dialysis (3.5 kDa membranes, Spectrum Labs) for 4 days and lyophilized for 4 days.

Preparation of PLL-GO Surfaces

GO sheets were covalently tethered to poly-L-lysine (PLL, MW = 150-300 kDa) immobilized on glass surfaces (Poly-Prep slides, Sigma Aldrich) *via* amine coupling[2] mediated by EDC (1-ethyl-3-(3-dimethylaminopropyl)carbodiimide hydrochloride) and NHS (*N*-hydroxysuccinimide), following established protocols.[2,3] MES buffer (2-(*N*-morpholino)ethanesulfonic acid, 100 mM, pH 6.0) was mixed with GO aqueous dispersion (250 μg L^{-1}) at a 1:5 volume ratio. Next, EDC (20 mM) and NHS (50 mM) solutions prepared in 10 mM MES buffer were sequentially mixed with the GO suspension. During this step, carboxylic acid groups in GO are converted to amine-reactive esters. The reaction proceeded for 15 min at pH ~5.5. The pH of the suspension was subsequently adjusted to ~7.2 before immersing in the suspension a PLL-coated glass coupon. The suspension was placed on a shaker table (~30 rpm) for 1 h, after which the coupon was rinsed with ultrapure water, and bath-sonicated for ~10 min to remove unbound GO sheets. Prepared PLL-GO coupons were stored in ultrapure water at 4 °C until use.

Preparation of Si-GO Surfaces

Si-GO substrates were prepared *via* dip coating of Langmuir-Blodgett (LB) GO films on P-type silicon wafers (100 orientation, single side polished, test grade, 500-μm thickness). The bare silicon substrate was first soaked in acetone for 15 min, rinsed with copious amounts of ultrapure water, and washed with isopropyl alcohol to eliminate water residues. After air drying, the wafer was placed in a UV/O_3 cleaner for 20 min to eliminate organic residues (ProCleaner™ Plus, Bioforce Nanosciences). The cleaned wafer was stored in a nitrogen-purged desiccator before use.

The LB trough (effective area = 172 cm^2) was cleaned with Alconox solution followed by thorough rinsing with ultrapure water. Thereafter the trough was filled with a sublayer consisting of HCl solution, pH 1.0. The Si wafer was then dipped vertically into the trough well with the upper end clamped on the dipper. Surface pressure was monitored using a Wilhelmy plate positioned parallel to the Si substrate. A mixture of GO dispersion (2 mg mL^{-1}) and methanol (v/v = 1/5) was added to the acidic water sublayer dropwise in 0.5-mL aliquots to a total of 2.5 mL. Five min was allowed between aliquot additions. The setup was left overnight for methanol to completely evaporate. Finally, the Si substrate was pulled up at a constant speed of 0.03 mm/s with a surface pressure of 5 mN/m. More information on GO LB film preparation is documented elsewhere.[4–6]

Confocal Raman Microscopy

Confocal Raman Microscopy (Witec Alpha300R) was performed in the study to confirm the two characteristic bands of GO materials and GO coverage on the model surfaces. Sample surfaces were scanned using a Nikon 100× objective, 532-nm laser excitation and 1800 grooves/mm grating.

The optimal depth for mapping was determined by performing an x-z scan over a 20 × 8 μm^2 (length × depth) cross-section. Next, the x-y Raman map was generated over a 20 × 20 μm^2 scan area at the determined depth, with a resolution of 1 μm. Two spectra were measured per micron. The sum of the area under the D and G peaks of GO (found at ~1350 cm^{-1} and ~1590 cm^{-1}, respectively[7]) was used to generate the signal intensity maps.

AFM Topography and Surface Roughness

An MFP-3D-Bio atomic force microscope (Asylum Research) was used to image the surfaces and measure their nanoscale roughness using tapping (AC) mode AFM in phosphate buffered saline (PBS, pH 7.4). Bruker SNL probes were used (cantilever C, nominal k = 0.24 N/m). Surface images were collected at 0.5 Hz over areas of 20 × 20 μm^2, 5 × 5 μm^2, and 2 × 2 μm^2, on each surface type. Root-mean-square (RMS) roughness was calculated from three randomly selected spots (0.5 μm × 0.5 μm) on each surface type.

Contact Angle Goniometry

Contact angle measurements were performed with a Model 200 contact angle goniometer (Ramé-Hart) equipped with a fluid cell for captive bubble measurements. *n*-Decane drops (2 μL) were injected into the fluid cell (filled with PBS, pH 7.4) and deposited on the surface using a syringe fitted with a J-shaped needle (Type 304 stainless steel, 22 gauge). The left and right contact angles were recorded after 60 s from digital images using the DROPImage Standard software (Ramé-Hart). For each surface, 4 replicate specimens were measured for a total of ~10 deposited droplets.

Surface Charge (ζ-Potential)

The ζ-potential of the surfaces was determined from streaming current measurements using an electrokinetic analyzer (SurPASS, Anton Paar). Two 10 × 20 mm^2 specimen coupons were attached to sample holders using double-sided tape; sample holders were subsequently mounted in an adjustable gap cell, setting the gap size to ≈ 110 μm. The streaming current was measured by flowing the electrolyte solution (1 mM KCl) through the gap (i.e., parallel to the specimen coupons) as the pressure difference was increased to 400 mbar. A linear dependence of the streaming current with the pressure difference was observed, in accordance with the Helmholtz-Smoluchowski equation,[8] and the ζ-potential was determined from the slope. Streaming potential measurements were performed at pH ~5.5 – 10 adding aliquots of 0.05 M NaOH. Two independently prepared samples of each surface type were characterized.

Bacterial Culture Conditions

The as-received freeze-dried bacterial culture powder (*P. fluorescens* ATCC 13525) was used to inoculate 6 mL of LB broth (Miller, Sigma-Aldrich). Following incubation for 2 hours at 30 °C, agar plates were streaked and incubated at 30 °C overnight to grow bacterial colonies. Bacterial suspensions were prepared by transferring a colony with a pipette tip to 50 mL of LB medium. The suspension was incubated overnight at 30 °C and 125 RPM shaking speed, and diluted (1:25) with fresh LB broth. After further incubation for ~3 hours at 30 °C and 175 RPM, cells were harvested in mid-exponential phase ($OD_{600\ nm}$ ≈ 0.4 – 0.6), centrifuged at 5000 × g for 1 min, and re-suspended in PBS, pH 7.4. This step was repeated thrice. All materials and reagents used in cell culture were autoclaved before use.

Sample Preparation and Cantilever Functionalization

A specimen of sample surface with a dimension of ~1 × 0.5 cm^2 was adhered using epoxy (3M Quick Set Epoxy Adhesive) to a piranha- and UV/O_3-cleaned 35-mm circular glass disc (Asylum Research). After a 15-min epoxy curing step, a 20-μL droplet of bacterial suspension was placed on the glass disc beside the specimen. The droplet was let to stand for 30 min to permit bacterial deposition on the glass surface. Afterward, 4 mL of PBS was used to rinse off excess unattached cells, avoiding contact between the specimen surface and the bacterial suspension. The glass disc

was mounted in the AFM fluid cell (Fluid Cell Lite, Asylum Research), which was then filled with 2 mL of PBS buffer (pH 7.4).

Tipless silicon nitride cantilevers with nominal k = 0.01 N/m (Bruker MLCT-O10 probe "C") were used in force spectroscopy experiments. Cantilevers were cleaned in a UV/O_3 chamber for 25 min before use. A self-adherent polydopamine (PDA) coating[9,10] was deposited on the AFM probe to enable attachment of a bacterial cell to the end of the cantilever. PDA deposition was conducted for 15 min (65 RPM shaking speed) from a solution containing 4 mg of dopamine hydrochloride (Sigma-Aldrich) per milliliter of Trizma buffer (10 mM, BioReagent, Sigma-Aldrich) buffered to pH 8.5. Following deposition, the probe was rinsed with ultrapure water and dried in a nitrogen-purged desiccator for 5 min. Prior to bacterial attachment, the cantilever optical lever sensitivity was measured over the bare glass surface, and the spring constant (k) was calibrated using the thermal noise method[11] (the values of k were within the range specified by the manufacturer). The AFM probe was mounted onto the AFM probe holder, and the AFM head was thereafter lowered into the fluid cell, allowing ~40 min for the cantilever deflection signal to reach a stable value. To prepare a single-cell AFM probe, the PDA-coated cantilever was engaged at a 1 nN loading force on a single bacterial cell identified using the 63× objective of the inverted optical microscope (Zeiss Axio Observer A.1). After 5 min, the cantilever (functionalized with the bacterial cell) was withdrawn.

Supporting Results

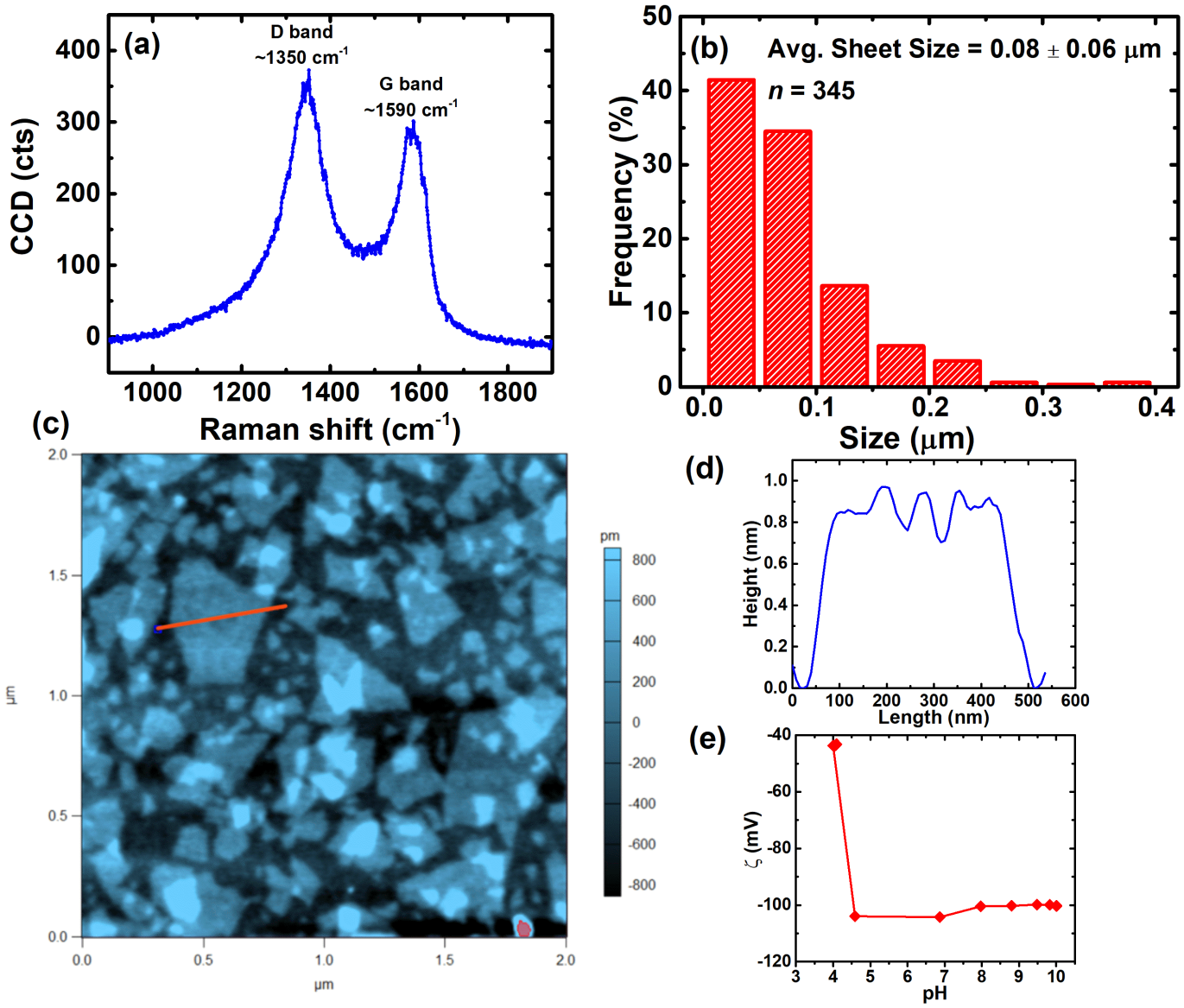

Figure S1: Characterization of graphene oxide (GO): (a) Raman spectrum; (b) sheet size (equivalent radius) distribution; (c) tapping mode AFM image of GO sheets deposited on silicon; (d) GO sheet height profile (determined along the red line in panel c); (e) zeta potential of GO in aqueous dispersion at a concentration of 250 µg mL^{-1}.

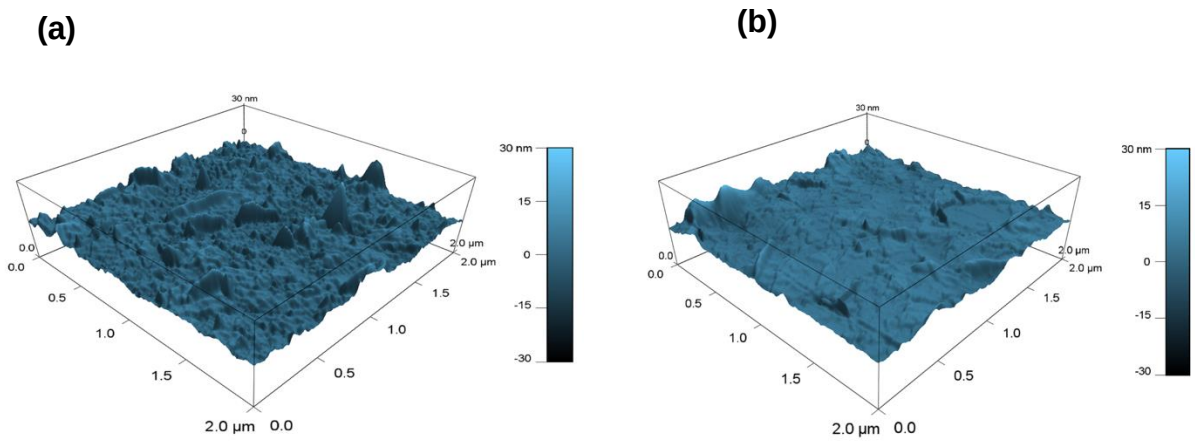

Figure S2: Surface topography visualized by tapping mode AFM: (a) PLL-GO and (b) Si-GO.

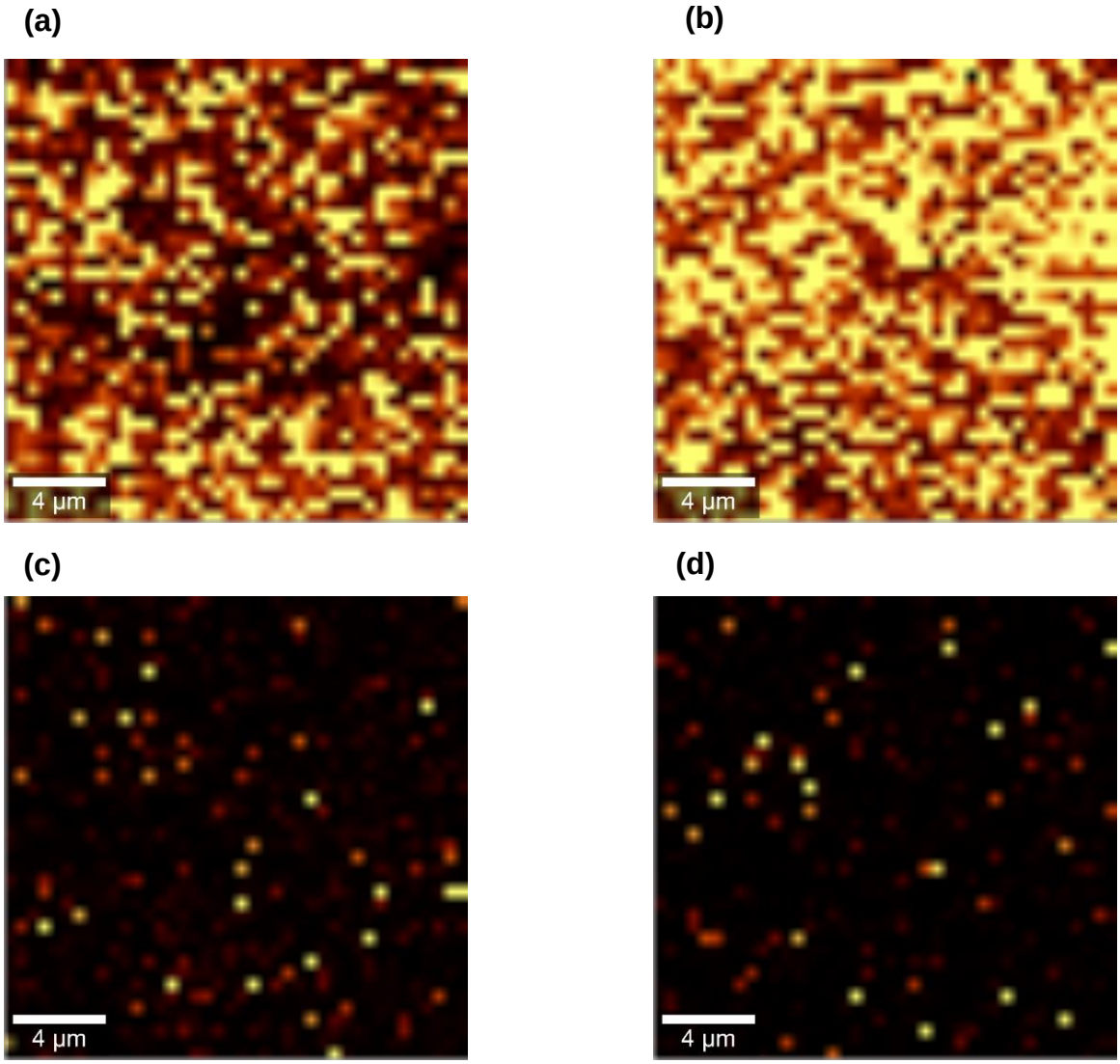

Figure S3: Raman spectroscopy images of (a) PLL-GO, (b) Si-GO, (c) PLL, and (d) Si surfaces.

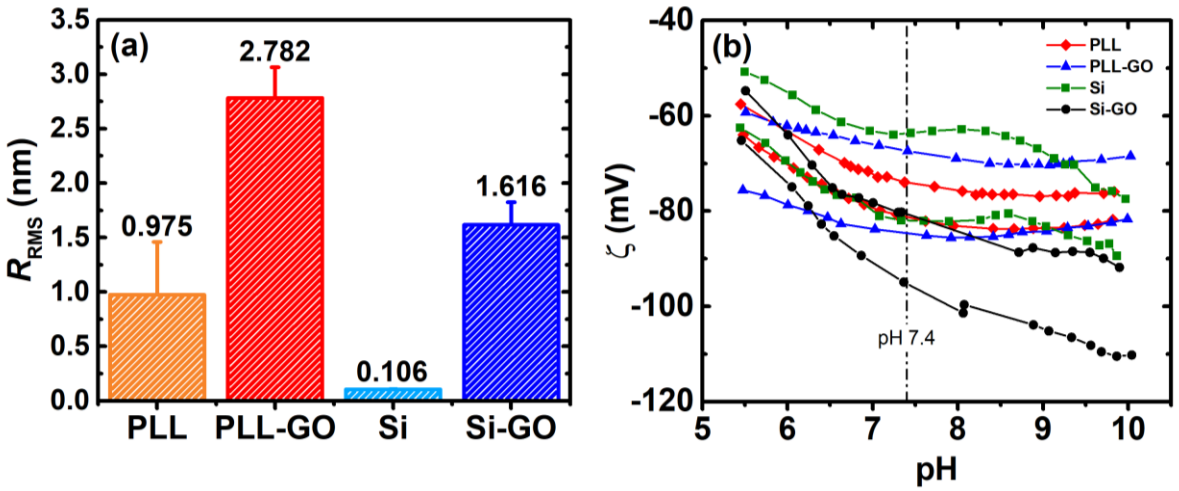

Figure S4: RMS roughness values (a) and ζ-potential as a function of pH (b) for the different surfaces.

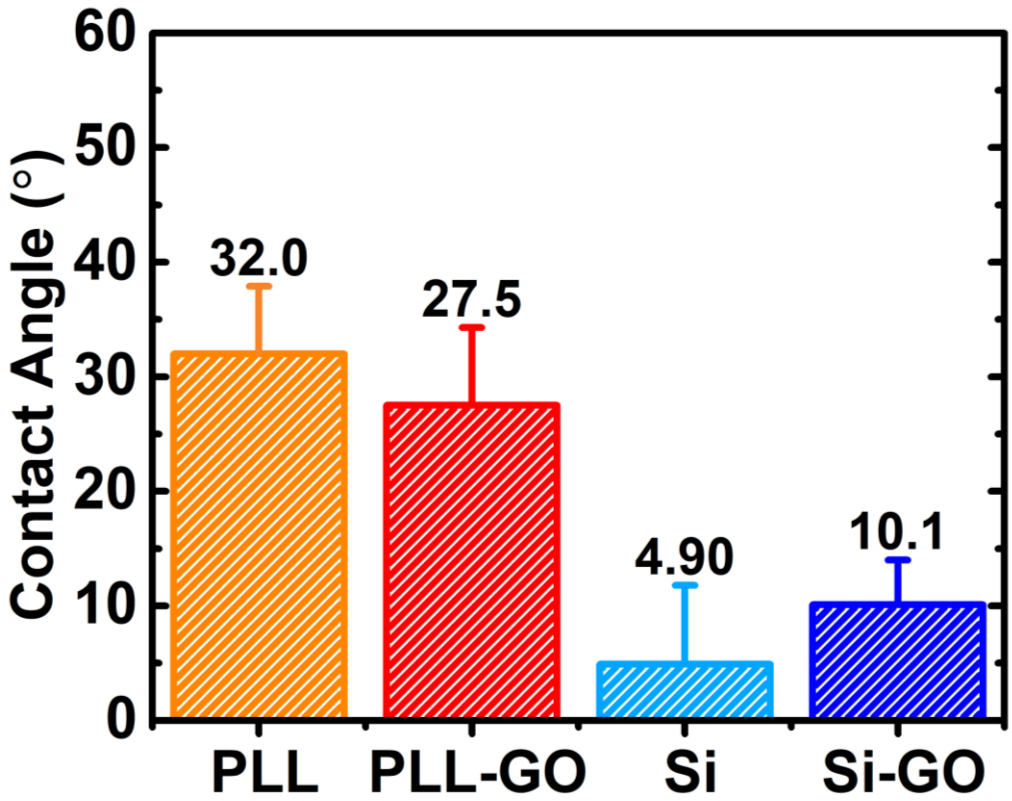

Figure S5: Contact angles obtained through the captive bubble method using *n*-decane droplets in PBS buffer (pH 7.4).

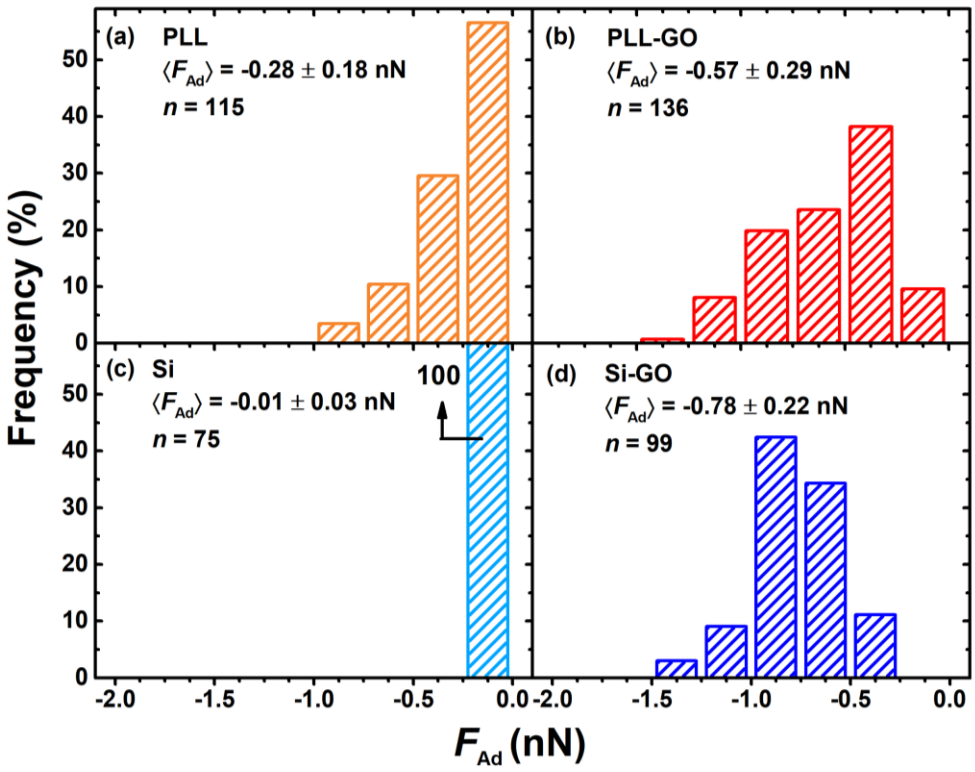

Figure S6: Distribution of maximum adhesion forces (F_{Ad}) of single *P. fluorescens* cells on: (a) poly-L-lysine-coated glass (PLL); (b) graphene oxide (GO)-functionalized PLL surfaces (PLL-GO); (c) Si wafers; (d) Langmuir-Blodgett GO films deposited on Si wafers by dip-coating (Si-GO). The inset shows the histogram average ($\langle F_{Ad} \rangle$), standard deviation, and number of measurements (n). Measurements were performed in PBS buffer (pH 7.4).

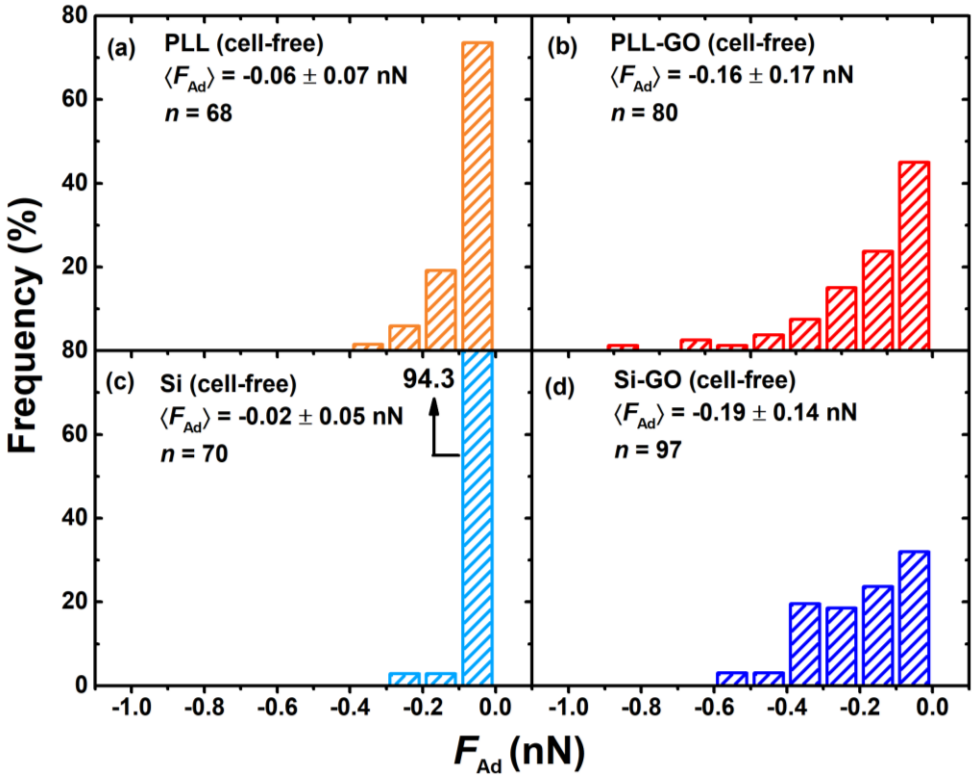

Figure S7: Distribution of maximum adhesion forces (F_{Ad}) of cell-free polydopamine-coated cantilevers on: (a) poly-L-lysine-coated glass (PLL); (b) graphene oxide (GO)-functionalized PLL surfaces (PLL-GO); (c) Si wafers; (d) Langmuir-Blodgett GO films deposited on Si wafers by dip-coating (Si-GO). The inset shows the histogram average ($\langle F_{Ad} \rangle$), standard deviation, and number of measurements (n). Experiments were performed in PBS buffer (pH 7.4).

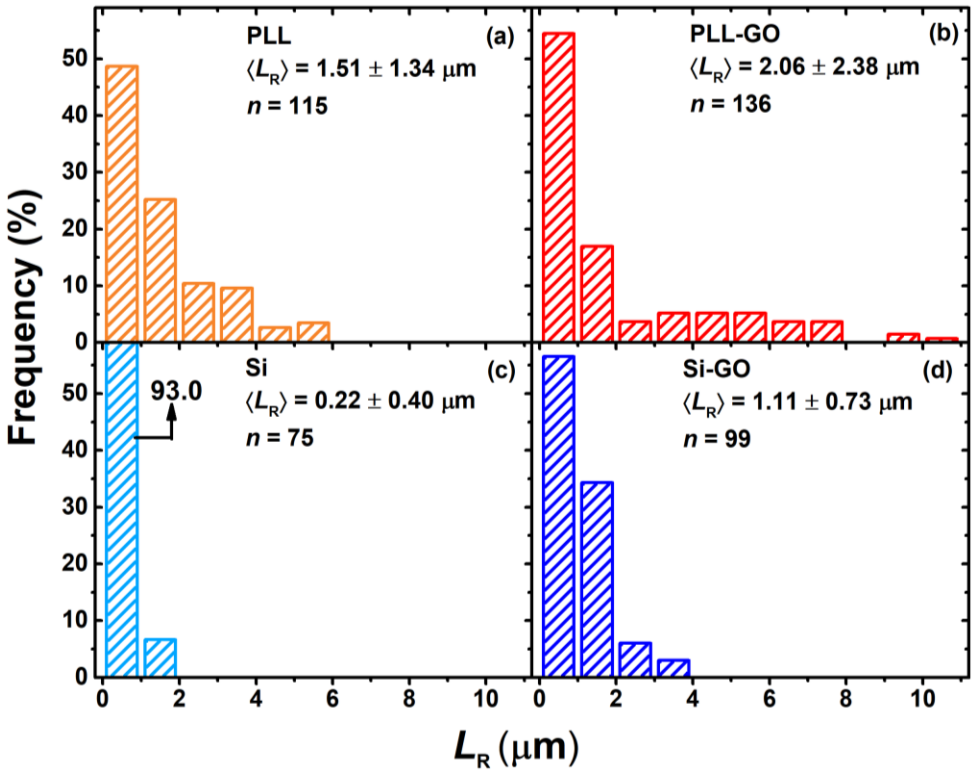

Figure S8: Distribution of rupture separation (L_R: distance from the surface at which adhesion forces vanish) for single *P. fluorescens* cells on: (a) poly-L-lysine-coated glass (PLL); (b) graphene oxide (GO)-functionalized PLL surfaces (PLL-GO); (c) Si wafers; (d) Langmuir-Blodgett GO films deposited on Si wafers by dip-coating (Si-GO). The inset shows the histogram average ($\langle L_R \rangle$), standard deviation, and number of measurements (n). Experiments were performed in PBS buffer (pH 7.4).

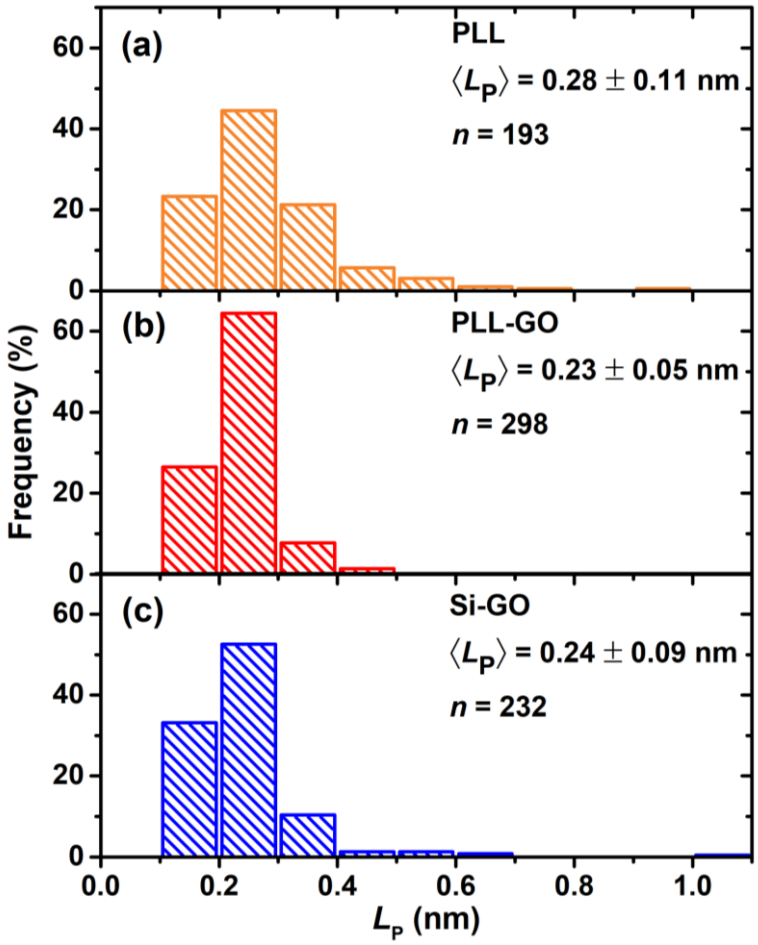

Figure S9: Distribution of best-fit persistence length values (L_P), obtained from WLC model fits to the pull-off force curve of single *P. fluorescens* cells on: (a) poly-L-lysine-coated glass (PLL); (b) graphene oxide (GO)-functionalized PLL surfaces (PLL-GO); (c) Langmuir-Blodgett GO films deposited on Si wafers by dip-coating (Si-GO). The inset shows the histogram average (⟨L_P⟩), standard deviation, and number of measurements (n). Experiments were performed in PBS buffer (pH 7.4).

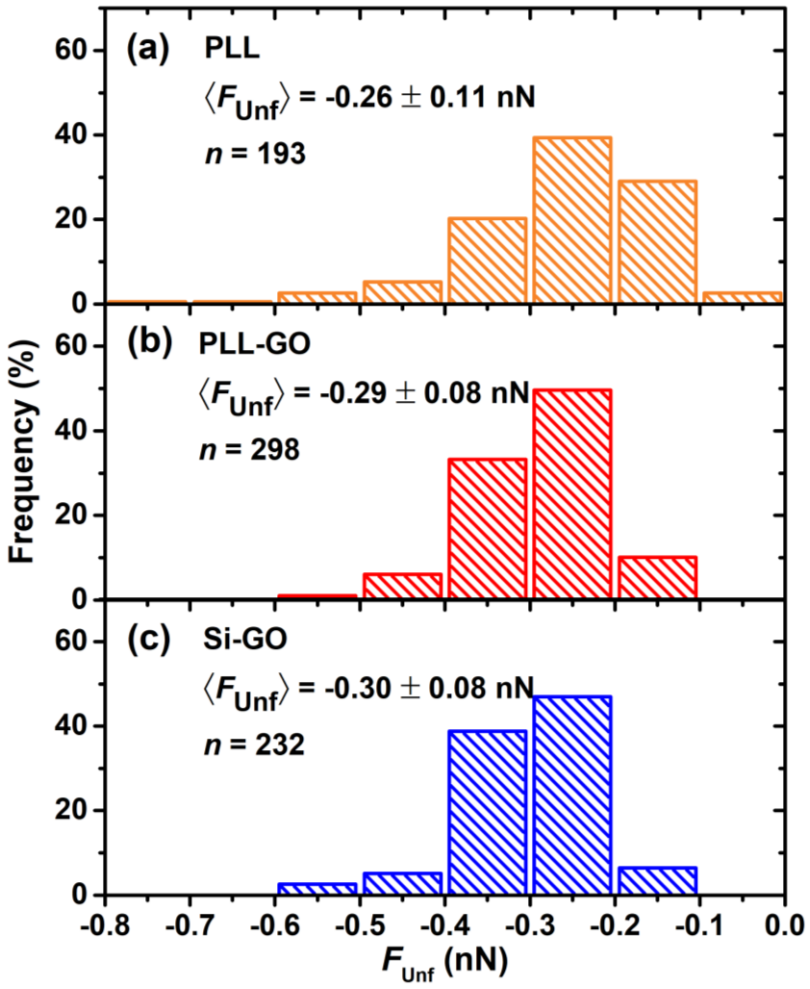

Figure S10: Distribution of the unfolding forces (F_{Unf}, the force measured at the sawtooth peak, cf. Figure 3(a)), obtained from the pull-off force curve of single *P. fluorescens* cells on: (a) poly-L-lysine-coated glass (PLL); (b) graphene oxide (GO)-functionalized PLL surfaces (PLL-GO); (c) Langmuir-Blodgett GO films deposited on Si wafers by dip-coating (Si-GO). The inset shows the histogram average ($\langle F_{Unf} \rangle$), standard deviation, and number of measurements (n). Experiments were performed in PBS buffer (pH 7.4).

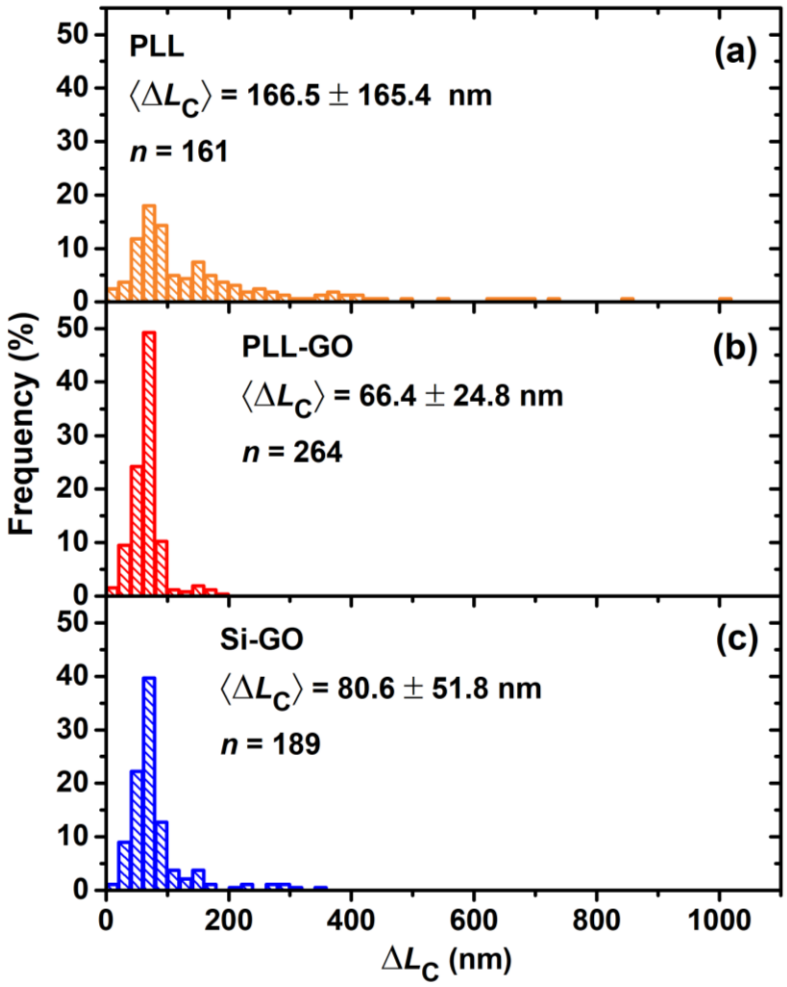

Figure S11: Distribution of ΔL_C (the difference in contour length between two consecutive sawtooth peaks), obtained from the pull-off force curve of single *P. fluorescens* cells on: (a) poly-L-lysine-coated glass (PLL); (b) graphene oxide (GO)-functionalized PLL surfaces (PLL-GO); (c) Langmuir-Blodgett GO films deposited on Si wafers by dip-coating (Si-GO). The inset shows the histogram average ($\langle \Delta L_C \rangle$), standard deviation, and number of measurements (n). Experiments were performed in PBS buffer (pH 7.4).

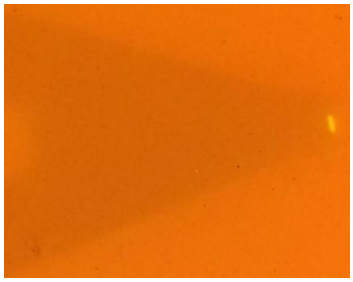

Figure S12: Bacterial cell probe imaged after force measurements. The bacterial cell (*P. fluorescens*) was attached to the front edge of a tipless AFM cantilever using polydopamine wet adhesive. The observed green fluorescence indicates that the cell remained viable throughout the experiment.

Supporting References

(1) Tung, V. C.; Allen, M. J.; Yang, Y.; Kaner, R. B. High-throughput solution processing of large-scale graphene. *Nat. Nanotechnol.* **2009**, *4* (1), 25–29.

(2) Grabarek, Z.; Gergely, J. Zero-length crosslinking procedure with the use of active esters. *Anal. Biochem.* **1990**, *185* (1), 131–135.

(3) Hermanson, G. T. *Bioconjugate Techniques: Third Edition*; 2013, 259–266.

(4) Valtierrez-Gaytan, C.; Ismail, I.; Macosko, C.; Stottrup, B. L. Interfacial activity of graphene oxide. *Colloids Surfaces A Physicochem. Eng. Asp.* **2017**, *529*, 434–442.

(5) Cote, L. J.; Kim, F.; Huang, J. Langmuir-Blodgett assembly of graphite oxide single layers. *J. Am. Chem. Soc.* **2009**, *131* (3), 1043–1049.

(6) Kim, F.; Cote, L. J.; Huang, J. Graphene oxide: Surface activity and two-dimensional assembly. *Adv. Mater.* **2010**, *22* (17), 1954–1958.

(7) Kudin, K. N.; Ozbas, B.; Schniepp, H. C.; Prud'homme, R. K.; Aksay, I. A.; Car, R. Raman spectra of graphite oxide and functionalized graphene sheets. *Nano Lett.* **2008**, *8* (1), 36–41.

(8) Werner, C.; Körber, H.; Zimmermann, R.; Dukhin, S.; Jacobasch, H. Extended electrokinetic characterization of flat solid surfaces. *J. Colloid Interface Sci.* **1998**, *208* (1), 329–346.

(9) Lee, H.; Dellatore, S. M.; Miller, W. M.; Messersmith, P. B. Mussel-inspired surface chemistry for multifunctional coatings. *Science (80-.).* **2007**, *318* (5849), 426–430.

(10) Kang, S.; Elimelech, M. Bioinspired single bacterial cell force spectroscopy. *Langmuir* **2009**, *25* (17), 9656–9659.

(11) Hutter, J. L.; Bechhoefer, J. Calibration of atomic-force microscope tips. *Rev. Sci. Instrum.* **1993**, *64* (7), 1868–1873.

ACS ES&T Engineering

pubs.acs.org/estengg

Article

Feed Temperature Effects on Organic Fouling of Reverse Osmosis Membranes: Competition of Interfacial and Transport Properties

Sara BinAhmed, Raymond M. Hozalski, and Santiago Romero-Vargas Castrillón*

Cite This: https://dx.doi.org/10.1021/acsestengg.0c00258

Read Online

ACCESS | Metrics & More | Article Recommendations | Supporting Information

ABSTRACT: We investigated the effect of feedwater temperature on the organic fouling of reverse osmosis (RO) membranes. Experiments were conducted over the range $27 \leq T \leq 40$ °C, relevant to feed temperatures in arid, near-equatorial latitudes. Fouling by alginate, a major component of extracellular polymeric substances, was investigated at the nanoscale by means of AFM-based temperature-controlled colloidal-probe force spectroscopy (CPFS). The CPFS results, complemented by interfacial property characterization (contact angle, surface roughness, and charge) conducted under temperature-controlled conditions, enabled us to rationalize the observed fouling kinetics in cross-flow fouling experiments. We observed less severe flux loss at 35 °C ($J/J_0 = 75\%$, $t = 24$ h) compared to 27 °C ($J/J_0 = 65\%$), which is due to weaker adhesion forces with rising temperature. The observed variation in the magnitude of adhesion forces is consistent with the temperature dependence of hydrophobic interactions. At 40 °C, the observed flux loss ($J/J_0 = 68\%$) was similar to that at 27 °C, despite the fact that adhesion forces are relatively weak (and similar to those at 35 °C). Analysis using a series-resistance model shows that the foulant layer hydraulic resistance is equal at 35 and 40 °C, consistent with the CPFS results. More severe fouling was observed at 40 °C compared to 35 °C, however, due to the higher water permeance at 40 °C, which resulted in a greater flux of foulant to the membrane. Our experiments further show that the fouling layer develops within ~2 h, during which the flux sharply decreases by 26% at 27 °C, 19% at 35 °C, and 22% at 40 °C; thereafter, flux losses are small and temperature independent. CPFS experiments show that this behavior is due to the foulant layer, which results in weak, often repulsive, and T-independent foulant–foulant interactions, which hinder further foulant deposition.

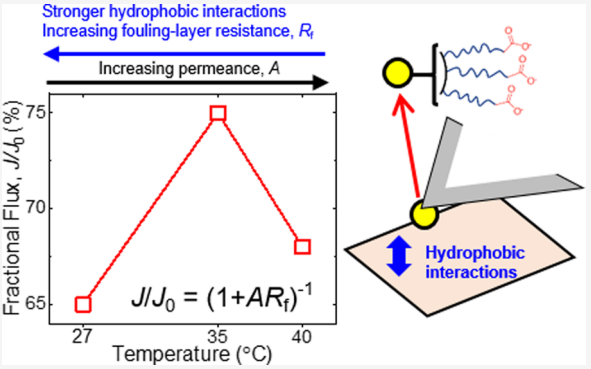

KEYWORDS: *reverse osmosis, hydrophobic interactions, fouling, wastewater reuse*

1. INTRODUCTION

Population growth and climate change are exerting enormous pressure on the world's water resources.[1−3] Over 2.4 billion people inhabit highly water stressed areas (defined as those with a water scarcity index > 0.4), many of which are in densely populated urban agglomerations in which water demand exceeds the watershed capacity.[4] In addition to increased population, urbanization, and industrialization,[5] climate change is expected to increase water stress through prolonged heatwaves that diminish surface and groundwater supplies.[6] There is thus an urgent need to tap into unconventional water sources (e.g., brackish water, seawater, and wastewater) to expand the water inventory.[2,7−9] Water recovered from secondary and tertiary municipal wastewater effluents can supplement water resources[10] through indirect use in agricultural and urban irrigation, cooling towers, and recharge of groundwater aquifers.[11] Desalination and advanced wastewater treatment by reverse osmosis (RO) have been instrumental in sustainably extracting potable water from unconventional water sources. Nonetheless, membrane fouling in its various forms (organic, inorganic, colloidal, biological) remains a key obstacle,[12−14] resulting in lower permeability and contaminant rejection,[1,12,14,15] ultimately increasing energy comsumption.[12]

Research over the past two decades has improved our understanding of the link between fouling propensity and RO membrane interfacial properties. Within the context of organic fouling of polyamide RO membranes, low roughness,[16] more hydrophilic,[17,18] and more negatively charged[19] membranes exhibit less pronounced flux losses.[16−19] Studies on the effect of feedwater quality have shown that Ca^{2+} causes more severe organic fouling (compared to Mg^{2+} and Na^{+}) with proteins (bovine serum albumin) and alginate,[20,21] likely due to the

Received: December 23, 2020
Revised: February 1, 2021
Accepted: February 9, 2021

calcium-mediated gelation of foulants[21−23] and Ca^{2+} bridging of carboxyl groups on the membrane and foulant.[20] A higher ionic strength results in compression of the electrical double layer and shielding of the surface charge of both the membrane and the foulants, resulting in a higher fouling rate due to a reduced electrostatic repulsion.[3,20,21] The effect of pH is more pronounced around the isoelectric point (IEP) of the foulant, such that foulant−membrane electrostatic repulsion is reduced and fouling rate increases at a pH equal to or less than the IEP of the foulant.[3,20,24] The presence of organic matter in water contributes to the formation of an organic fouling layer on the surface of the membrane, which can provide nutrients to bacteria and facilitate bacterial adhesion to the surface.[25−28] Therefore, minimizing organic fouling can help delay biofouling by mitigating initial bacterial adhesion to the surface of RO membranes.[29,30]

The influence of the feedwater temperature on membrane performance and fouling has attracted far less attention. Only a few studies have been devoted to this subject,[20,31−33] despite the increasing use of membrane-based desalination and wastewater reuse in arid, near-equatorial latitudes[34] where seawater temperatures can reach 35.5 °C.[35] Previous work on the connection between RO membrane transport properties and the feed temperature has shown that water permeability[32,36] increases with increasing temperature, due to lower water viscosity[37,38] and higher water diffusivity.[31,32] As a result of increasing temperature, permeate recovery increases[36,38−40] and energy consumption decreases due to lower pressure requirements.[39−41] Similarly, the salt permeability coefficient, B_s, is directly proportional to the solute diffusivity, D_s, and partition (solubility) coefficient K_s,[31,42,43] both of which increase with temperature, leading to a higher salt flux and lower salt rejection.[36,39,40,44] In one study, Goosen et al.[32] observed an increase in the permeate flux at a fixed applied pressure as the temperature was increased from 20 to 40 °C for NaCl concentrations ranging from 0 to 5% (w/v) NaCl, suggesting that the membrane undergoes morphological changes such as an increase in the polymer free void volume.[32] Sharma and Chellam[45] observed that the network pore size of nanofiltration (NF) membranes increased with increasing temperature (5−41 °C). In another study, Goosen et al.[33] found that correcting for viscosity changes of water with increasing temperature did not totally account for the increase in water permeance with increasing temperature. The researchers suggested an interplay between the feed temperature and the applied pressure that affected the membrane void volume. Francis and Pashley[38] observed that water recovery and permeate flow increased, while salt rejection decreased, with increasing temperature (20 to 30 °C) when treating seawater (0.5 M NaCl) and brackish water (0.2 M NaCl) with thin-film composite (TFC) RO membranes. Jin et al.[31] attributed the lower rejection of humic acid as total organic carbon (TOC) with increasing temperature (T = 15 to 35 °C) to increased swelling of the polymer network voids. The rates of fouling were similar at 25 and 35 °C while the highest flux decline occurred at 15 °C. The higher applied pressure and the larger size of humic acid aggregates at lower temperatures resulted in a higher resistance of the fouling layer at these temperatures.[31] On the other hand, Mo et al.[20] reported an increased rate of protein fouling (50 mg L^{-1} bovine serum albumin) of RO membranes at higher temperatures (18 to 35 °C) and for pH values 4.9 and 7. Baghdadi et al.[46] simulated the performance of two TFC RO membranes with increasing temperature (15−45 °C) and observed an increase in the salt mass transfer coefficient and a decrease in salt rejection when treating a 35 g L^{-1} NaCl feedwater at a constant hydraulic pressure (800 psi).

Current investigations of the effect of feedwater temperature on membrane performance are limited to bench-scale experiments, which describe thermal effects on membrane transport parameters and flux loss but offer little mechanistic insight.[20,31−33,46] To explain the connection between the feed temperature and the observed fouling kinetics, it is necessary to understand the thermal response of interfacial properties such as membrane hydrophobicity, roughness, and charge. As a step in this direction, we used colloidal probe atomic force microscopy (AFM) measurements to probe the effects of temperature on membrane−foulant and foulant−foulant interactions. We then explored how the temperature dependence of the interfacial properties manifests itself in RO membrane fouling experiments using alginate, a polysaccharide that is abundant in wastewater[47,48] and in bacterial biofilms,[49,50] as a model foulant. Our results show that weaker hydrophobic interactions with increasing feed temperature (from 27 to 35 °C) initially decrease membrane fouling, but further increases in feed temperature exacerbate fouling due to an increase in the water permeance of the membrane. Consequently, variation of the feed temperature reveals that fouling is determined by a competition between membrane interfacial and transport properties.

This paper is structured as follows. In Section 2, we describe the experimental protocols for the colloidal-probe AFM and dynamic fouling experiments. We discuss our results in Section 3, beginning with the effect of temperature (T) on interfacial properties (Section 3.1); the effect of T on foulant−membrane and foulant−foulant interactions, as determined by AFM, is discussed in Section 3.2; and Sections 3.3 and 3.4 present the results of membrane transport and fouling experiments, drawing connections to the interfacial and nanoscale adhesion properties. Concluding remarks are given in Section 4.

2. MATERIALS AND METHODS

2.1. Reverse Osmosis (RO) Membrane. All experiments were carried out with ESPA2-LD membranes (Hydranautics, Oceanside, CA), a low pressure aromatic polyamide RO membrane commonly employed in wastewater recycling.[10,51] Membrane coupons (~15 × 9 cm^2) were cut out from a 10 cm diameter spiral wound element (membrane area 7.43 m^2), rinsed in ultrapure water (UP) (18.2 MΩ cm, Barnstead), and stored at 5 °C in UP water. The hydraulic resistance and water permeance of the membranes were determined with a UP water feed at 25 °C. For quality assurance purposes, only membranes with A values within the range specified by the manufacturer (3.5−5.1 L m^{-2} h^{-1} bar^{-1}) were used for dynamic fouling experiments. Further details on the determination of membrane transport properties are provided in Section S.1 of the Supporting Information (SI).

The hydrophilicity and roughness of ESPA2-LD membranes were characterized at T = 27, 35, and 40 °C. Hydrophilicity was quantified in terms of water contact angle measurements in a temperature-controlled goniometer (DSA30S, Krüss). Both the temperature-controlled goniometer chamber and liquid dispenser were set to the same temperature, so that the droplet and substrate were in thermal equilibrium throughout the measurement. Root-mean-squared roughness (R_{RMS}) was measured in a temperature-controlled fluid cell using an atomic

https://dx.doi.org/10.1021/acsestengg.0c00258
ACS EST Engg. XXXX, XXX, XXX−XXX

force microscope (MFP-3D-Bio, Asylum Research) in tapping mode. The zeta potential of the membrane was determined from streaming potential measurements using an electrokinetic analyzer (SurPass, Anton Paar). Streaming potential measurements were performed at 27 and 35 °C only (40 °C exceeded the maximum operating temperature of the instrument). Further details on membrane surface characterization are found in Section S.2 of the SI.

2.2. Organic Foulant and Feed Solution Chemistry. We used alginate, a polysaccharide,[52] as a model foulant representative of extracellular polymeric substances (EPS)[53−56] in secondary wastewater effluent.[55−57] A 6 g L^{-1} sodium alginate (SA) (A2033, Millipore Sigma, St Louis, MO) stock solution was prepared in UP water before each dynamic fouling experiment by stirring the solution for 24 h. Alginate was dosed at a concentration of 250 mg L^{-1} to a feed solution containing 0.45 mM KH_2PO_4, 0.935 mM NH_4Cl, 0.5 mM $CaCl_2$, 0.5 mM $NaHCO_3$, 9.20 mM NaCl, and 0.61 mM $MgSO_4$ at pH 7.4. The inorganic composition of the synthetic wastewater used in all fouling experiments is representative of the inorganic fraction of secondary wastewater effluent from certain wastewater treatment plants in California.[50,58] The ionic strength of foulant-free synthetic wastewater was 14.7 mM (MinTEQ 3.1). The alginate concentration used (250 mg L^{-1}) is much higher than concentrations in real systems (in which TOC concentrations are in the 5−20 mg L^{-1} range[59−62]). An elevated concentration was used to accelerate fouling and ensure fouling can be observed within 24 h.

2.3. Dynamic Fouling Experiments. A bench-scale crossflow system (see Section S.1) was used for fouling, with each experiment comprising the following stages: (1) Membrane compaction at 500−580 psi with UP water at 25 °C until a steady-state permeate flux was achieved. (2) Stabilization of the permeate flux at J = 20 ± 1 L m^{-2} h^{-1} (LMH) for 1 h at 25 °C to validate the water permeance of the membrane (the manufacturer-specified water permeance for ESPA2-LD membranes is 3.5−5.1 LMH bar^{-1}). (3) Adjustment of the temperature of the UP feedwater to 27, 35, or 40 °C by means of a heater/chiller (6500 series, Polyscience) followed by overnight stabilization of the permeate flux at J = 20 ± 1 LMH (this stage was used to calculate the A at each temperature). (4) Dosing of alginate-free synthetic wastewater into the feed tank, followed by system stabilization at the desired temperature (27, 35, or 40 °C) at J = 20 ± 1 LMH; this stage typically required stabilization for 4−6 days, and included sampling of the feed and permeate conductivity to determine conductivity rejection before fouling. (5) Dosing of 250 mg L^{-1} alginate into the synthetic wastewater feed and initiation of dynamic fouling at an initial flux J_0 = 20 L m^{-2} h^{-1}; the flux loss during fouling was measured over 24 h accompanied by sampling of the feed and permeate conductivity and TOC content (2 and 24 h after initiation of fouling) to calculate conductivity and TOC rejection, respectively. The permeate flow rate was recorded every 0.2 s at all phases (except compaction) with a digital flow meter (SLI-2000, Sensirion, Stäfa, Switzerland) and logged to a computer. Further details on the experimental apparatus and fouling experiments can be found in the SI.

2.4. Colloidal Probe AFM Force Spectroscopy. *2.4.1. Colloidal Probes.* Carboxyl-modified latex (CML) colloidal particles with a nominal diameter of 4 μm were used in all AFM measurements. These polystyrene microspheres have a surface rich in carboxylic acid functional groups,[56,63] which are commonly found in alginate and other foulants.[56,64] According to the product specifications (ThermoFisher Scientific, C37253), the CML particles are hydrophobic at low pH and somewhat hydrophilic at high pH. However, other studies have characterized similar CML particles as hydrophobic.[65] CML particles were received as a 4% (w/v) suspension in deionized water and were stored at 5 °C until use.

2.4.2. Preparation of Colloidal Probes. The protocol for preparing the colloidal probes was adapted from those reported by others.[3,63,66] A 20 μL aliquot of CML particle suspension (2500× dilution) was deposited on a UV/O_3-cleaned[67] glass slide and dried overnight in a desiccator. An inverted optical microscope (Zeiss Axio Observer A.1) integrated into the AFM was used to guide a tipless AFM cantilever (MLCT-O10 cantilever "A", nominal k = 0.07 N/m, Bruker) first toward a small amount of UV-curable glue (Norland 86, Norland optical, Cranbury, NJ) deposited on the glass slide and then toward the CML to be adhered to the cantilever. The prepared AFM colloidal probes were then cured in a solar simulator (xenon lamp, wavelength > 290 nm, 350 W/m^2) for 30 min.

2.4.3. Experimental Conditions. The measurement of interfacial interactions between the CML probes and the surface of pristine and alginate-fouled ESPA2-LD membranes was performed using an atomic force microscope (MFP-3D-Bio, Asylum Research) equipped with a temperature-controlled fluid cell. Force measurements were conducted at T = 27 °C, 35 °C, and 40 °C in two different systems: pristine membranes in 20 mg L^{-1} alginate in synthetic wastewater (a concentration representative of the TOC levels of 5−20 mg L^{-1}[55,59] in wastewater effluent) and alginate-fouled membranes in synthetic wastewater supplemented with 20 mg L^{-1} alginate. The former investigates the temperature dependence of foulant−membrane interactions, which determine the initial adhesion of foulant at the early stages of fouling, while the latter measurements investigate foulant−foulant interactions in the subsequent stages, once a foulant layer has formed on the membrane surface.[3,63,68] Synthetic wastewater supplemented with 20 mg L^{-1} alginate was freshly prepared prior to each experiment as described in Section 2.2. The alginate-fouled membrane substrate was prepared as described in the SI (see Section S.1). To distinguish between real CML microsphere adhesion and artifacts resulting from particles contaminated with glue, control measurements were performed using a particle-free cantilever on which we deposited a small amount of cured glue. These measurements (performed in phosphate buffered saline at pH 7.4 on pristine membranes) resulted in distinctly sharp adhesion peaks compared to those of clean CML particles. Probes suspected of glue contamination were discarded. Only data collected with CML particles unaffected by glue artifacts are presented and discussed.

For individual coupons, force measurements were collected at 27 °C, then 35 °C, and finally 40 °C by ramping up the temperature at a rate of 1 °C/min. After allowing 30 min for the cantilever to reach thermal equilibrium, at each set-point temperature the inverse optical lever sensitivity and spring constant were determined (the latter according to the thermal noise method[69]). Measurements at the three temperatures were repeated in triplicate (i.e., with three different membrane coupons) with three independently functionalized AFM cantilevers. A total of ≥105 force curves were collected at each temperature. To account for membrane surface

https://dx.doi.org/10.1021/acsestengg.0c00258
ACS EST Engg. XXXX, XXX, XXX−XXX

heterogeneity,[70] adhesion forces were measured at each temperature over at least 11 randomly selected spots (collecting three force curves per spot) located at least 6 μm apart from one another. The AFM probe was checked at the end of every experiment to verify that the CML particle was not dislocated and that it had remained at its original position during force measurements.

Force curves were recorded at a 200 nm/s approach−retraction speed, a cycle speed that results in negligible dissipative friction on the CML particle.[71] The CML probe engaged the membrane substrate with a trigger force ($F_{trigger}$; defined in Figure S3 of the SI) of 2 nN, while remaining in contact with the surface of the pristine or fouled membrane for a dwell time of 5 s. A constant force was maintained between the CML particle and membrane surface during the dwell time by setting the feedback channel to deflection. AFM experiments were performed in open-loop mode to minimize the noise in the collected forces. The choice of trigger force was based on calculations of the permeation drag force exerted on a 4-μm diameter particle experiencing a flux of 20 LMH, typical of RO operation (see Section S.3). For data analysis, the minimum measurable force—30 pN—was determined by measuring the noise in the free end of several force curves at each temperature. Parameters collected from the force curves are identified in Figure S3. From the extension force curve, the snap-in force (F_{snap}) is defined as the adhesion force observed as the colloidal probe approaches the membrane substrate;[72−74] snap-in separation (R_{snap}) is identified as the distance at which the snap-in event occurs.[75,76] From the retraction force curve, the peak adhesion force (F_{peak}) is defined as the maximum adhesion force observed as the colloidal probe is pulled away from the membrane; the rupture separation (R) is the distance at which interactions between the probe and the membrane surface vanish.[77]

2.5. Statistical Analysis. Unpaired two-sided homoscedastic (equal variance) t-tests were used to determine the statistical significance of the results.

3. RESULTS AND DISCUSSION

3.1. Characterization of the RO Membrane. The contact angle of sessile water droplets (θ_w) reflects membrane hydrophilicity[78−80] and depends on membrane properties (surface roughness, surface charge, and surface functional groups)[78,80−82] as well as on external conditions such as the water temperature[78,83] and salt concentration.[78,84] The effect of temperature on θ_w and the root-mean-squared roughness (R_{RMS}) of pristine RO membranes is shown in Figure 1. The measured θ_w at 27 °C (53.5 ± 2.5°) is similar to that reported by other studies (43°−55°)[10,85] on ESPA2 membranes at room temperature. The contact angle at 27 °C was significantly higher than that at 35 °C (38.5 ± 2.8°; $p < 0.01$) and at 40 °C (36.7 ± 3.5°; $p < 0.01$), but the θ_w values at 35 and 40 °C were similar ($p = 0.078$). The decrease in the contact angle with increasing temperature is a manifestation of a general surface phenomenon: as first postulated by Zisman[86] and Petke and Ray,[87] θ_w decreases with rising T for common liquids whose surface tension decreases with increasing T. It is expected that the membrane would swell more at higher temperatures, as has been observed with polyamide membranes,[31,88] due to the increasing wettability of the membrane by water. Consistent with this expectation, we observed (Figure 1) an increase in R_{RMS} of the pristine RO membrane with increasing temperature (representative AFM scans at each T are given in Figure S1). R_{RMS} increased from 91.8 ± 12.3 nm at 27 °C to 113.7 ± 15.7 nm at 35 °C ($p < 0.01$) and 102.8 ± 14.5 nm at 40 °C ($p < 0.05$), while the R_{RMS} values at 35 and 40 °C were similar ($p = 0.0562$).

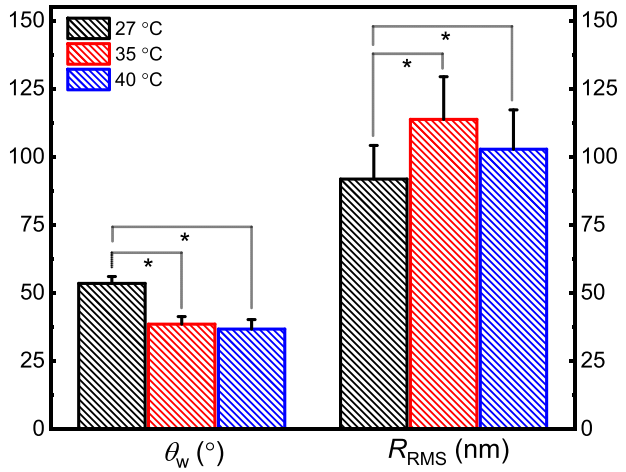

Figure 1. Sessile water drop contact angle (θ_w) and root-mean-squared roughness (R_{RMS}) measurements of pristine ESPA2-LD membranes at T = 27, 35, and 40 °C (* denotes a significant difference between the indicated samples, $p < 0.05$).

The zeta potential (ζ) of ESPA2-LD membranes at 27 °C (Figure S2) varied from −7 mV to −35 mV as the pH was increased from 4 to 10 with $\zeta \approx -30$ mV at pH = 7.4. The negative charge of polyamide is due to the deprotonation of carboxylic acid groups on the membrane surface[84] and presumably to the adsorption of hydroxide ions on uncharged hydrophobic regions on polyamide. Hydroxide ion adsorption is posited as the cause of the negative charge of many hydrophobic surfaces.[89,90] At 27 and 35 °C we observe a similar charging behavior at pH < 7, while a less negative ζ is observed at a basic pH at 35 °C. We ascribe this behavior to a lower extent of adsorption of hydroxide ions resulting from the decreasing hydrophobicity of the interface at 35 °C (cf. Figure 1).

3.2. Effect of Temperature on Adhesion Forces. In this section, we investigate the T dependence of membrane surface forces using AFM-based force spectroscopy measurements with a carboxylated colloidal probe (a mimic of alginate). We considered pristine membranes as well as alginate-fouled membranes (prepared as explained in the SI) to investigate the T dependence of foulant−membrane and foulant−foulant interactions. Previous work has used AFM to relate foulant−membrane interactions to the rate of fouling, finding a strong correlation between the fouling propensity and the strength of adhesion forces determined by AFM.[56,63] On the other hand, the effect of temperature, investigated below, has hitherto been overlooked. We analyzed both the approach and the retraction segments of the force curves. The approach segment provides information about the mechanism of the adhesion of foulant molecules as they first encounter the membrane interface, i.e., whether foulants experience repulsive or attractive forces during initial adhesion (and the strength of such interactions). The retraction segment quantifies the force necessary to detach adhered foulants.

Before discussing the force spectroscopy data quantitatively (Figures 2, 3, and S6−S9), a few qualitative features of the force curves are noteworthy. Figures S3 and S4 show

https://dx.doi.org/10.1021/acsestengg.0c00258
ACS EST Engg. XXXX, XXX, XXX−XXX

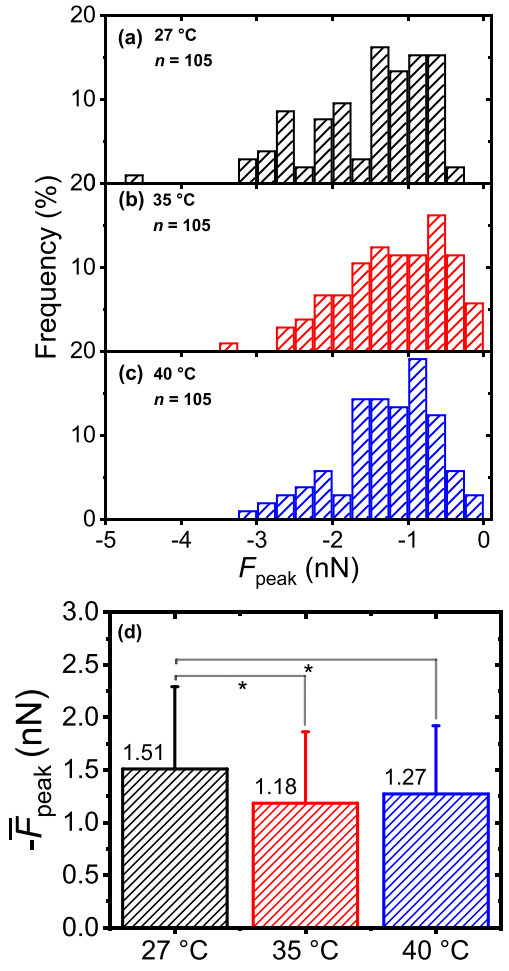

Figure 2. (a–c) Distribution of peak adhesion forces (F_{peak}) of CML colloidal probes on pristine ESPA2-LD membranes for each indicated temperature (given in the inset along with the number of force measurements, n). (d) Average peak adhesion force ($\bar{F}_{peak}$) at each temperature calculated from (a)–(c) (* denotes statistical significance with $p < 0.05$). Error bars denote one standard deviation. Data were collected in synthetic wastewater supplemented with 20 mg L^{-1} sodium alginate ($t_{contact}$ = 5 s; $F_{trigger}$ = 2 nN; pH 7.4; I = 14.7 mM).

representative force–distance curves, including the approach segment as the inset, collected over pristine and alginate-fouled membranes, respectively. The CML microsphere experiences a small repulsive force (F_{rep} ~ 43–50 pN; see Figure S3) as it approaches the surface of the pristine membranes; this repulsion is likely steric as it is observed at separations (8–9 nm) greater than the Debye length (2.5 nm at I = 14.7 mM). At shorter separations, the polystyrene chains on the microsphere surface eventually encounter the surface, and the microsphere experiences a sudden attractive force known as a "snap-in" or "jump-to-contact" spring instability:[91,92] at the snap-in point, the gradient of the particle–membrane force exceeds the cantilever spring constant, the cantilever becomes unstable (i.e., the particle–surface force and the cantilever elastic force are no longer in balance), and jump-to-contact occurs. This jump-to-contact force has been attributed to the van der Waals attractive force between the tip and the surface.[72−74] The snap-in force is not observed in the approach force curves recorded over alginate-fouled membranes (inset in Figure S4a,b); instead, the force is repulsive throughout the contact region, but the gradual increase in the loading force is consistent with compression of the soft alginate layer by the colloidal microsphere.[76] The retraction force curves over pristine membranes display sharp (often multiple) adhesion peaks (Figure S3), presumed to be due to the stretching of polystyrene chains upon probe pull-off. In some cases, we observe tethering events (Figure S5a,b), which are likely due to the detachment of alginate molecules bridging (with the aid of Ca^{2+}) the CML probe and the membrane surface[93] or desorption[94] of alginate molecules from the membrane. Over alginate-fouled membranes, we observe adhesion peaks, likely due to alginate desorption (Figure S4a). In addition, a fraction of the force curves (quantified below) are repulsive during retraction (Figure S4b), indicating that the alginate layer prevented the adhesion events that are otherwise observed in pristine membranes.

Next, we discuss quantitatively the force spectroscopy data in terms of the distribution of peak adhesion, snap-in forces, and rupture separations (defined in Section 2.4.3 and in Figure S3). The data are plotted as histograms in Figures 2, 3, and S6–S9. The distribution of snap-in forces (F_{snap}) and snap-in separations (R_{snap}) on pristine membranes is shown in Figures S6 and S7. As shown in Figure S6d, the attraction is strongest at 27 °C when the membrane is least hydrophilic and smoothest (see Figure 1), with an average snap-in force ($\bar{F}_{snap}$) of 115 pN compared to 81 pN at 35 °C (p = 0.039) and 92 pN at 40 °C (p = 0.138). The force curves that do not display a snap-in force (i.e., purely repulsive approach curves tallied as the "NO" column in Figures S6a–c), representing between 31.4% and 45.7% of the forces, were assigned F_{snap} = 0 when calculating the average in Figure S6d. A similar trend—decreasing $\bar{F}_{snap}$ with rising T —is observed when the average excluded the nonadhesive approaches, Figure S6e. The probability with which snap-in events occurred (ranging between 54.3% and 68.6%) and the distance at which snap-in is established (R_{snap}, Figure S7), ~8–9 nm on average, showed no discernible T dependence.

Figure 2a–c shows the peak adhesion force (F_{peak}) distribution (defined in Figure S3) of the CML probes collected over pristine membranes at T = 27, 35, and 40 °C. The distribution of the F_{peak} at 27 °C shows more frequent strong adhesion events (−3 nN < F_{peak} < −2 nN) compared to higher temperatures. Moreover, Figure 2d shows that the average adhesion force at 27 °C ($\bar{F}_{peak}$ = −1.51 ± 0.78 nN) is stronger than those at 35 °C ($\bar{F}_{peak}$ = −1.18 ± 0.68 nN; p = 0.0015) and 40 °C ($\bar{F}_{peak}$ = −1.27 ± 0.65 nN; p = 0.0174). Adhesion forces at 35 and 40 °C were similar (p = 0.339), which is consistent with the invariant contact angle and surface roughness at these same temperatures (cf. Figure 1). We expect adhesion forces to decrease at T > 40 °C, as observed by other studies.[95,96] Such a range, however, is not environmentally relevant and was therefore not studied in our work. The distribution of rupture separations (R) over pristine membranes (Figure S8), ranging between 120 and 150 nm, was not dependent on T.

The decreasing adhesion force with increasing temperature observed during approach (F_{snap}; Figure S6) and retraction (F_{peak}; Figure 2) followed the same trend with T as the hydrophobic interactions, suggesting that the T dependence of organic foulant adhesion shows close resemblance to hydrophobic hydration phenomena. Weakening of hydrophobic adhesion forces with rising T agree with previous force spectroscopic experiments.[95,96] The decreasing magnitude of adhesion forces is also consistent with theoretical inves-

https://dx.doi.org/10.1021/acsestengg.0c00258
ACS EST Engg. XXXX, XXX, XXX–XXX

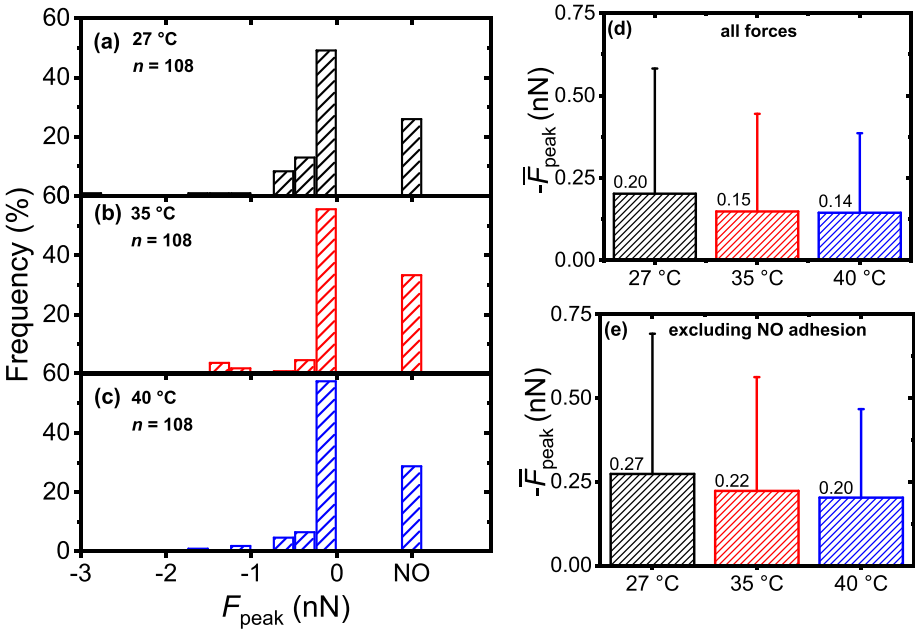

Figure 3. (a–c) Distribution of peak adhesion forces (F_{peak}) of CML colloidal probes on alginate-fouled ESPA2-LD membranes for each indicated temperature (given in the inset along with the number of force measurements, n). Force curves in which $|F_{peak}| < 30$ pN are tallied as the "NO" column (30 pN is the magnitude of the noise observed in the free end of force curves). (d) Average peak adhesion force ($\bar{F}_{peak}$) at each temperature calculated from (a)–(c) including the nonadhesive events as $\bar{F}_{peak} = 0$. (e) Average peak adhesion force ($\bar{F}_{peak}$) at each temperature calculated from (a)–(c) excluding the nonadhesive events. Error bars denote one standard deviation. Data were collected in synthetic wastewater supplemented with 20 mg L^{-1} sodium alginate ($t_{contact}$ = 5 s; $F_{trigger}$ = 2 nN; pH 7.4; I = 14.7 mM).

tigations showing that macroscopic surfaces become less hydrophobic with rising T.[97] As first envisaged by Stillinger,[98] hydration of large hydrophobes requires the formation of a water-depleted interface around the solute, akin to a liquid–vapor interface. Building on these ideas, Chandler and coworkers showed that the free energy of hydrophobic solvation scales with the liquid–vapor surface tension of water (γ) as $\Delta G \sim 4\pi\gamma R^2$ (where R is the hydrophobic solute radius).[99] Accordingly, the temperature dependence of ΔG approaches that of γ (i.e., it decreases with rising temperature), with hydrophobic hydration becoming more energetically favorable at higher T.[97]

While hydrophobic interactions appear to be the main driving force of foulant–membrane adhesion, we cannot rule out the possibility that adhesion is aided by Ca^{2+}-mediated[13,63] bridging interactions between the deprotonated carboxylic groups on the CML particle and the surface of the membrane. Both the membrane (Figure S2) and alginate are negatively charged at pH > 6 because most of the carboxylic groups are deprotonated[93] (pK_a = 3.5–4.7[3,16,100]). The presence of deprotonated carboxylic acid groups is suggested by the negative charge of both the membrane (Figure S2) and alginate.[16,93]

Substantially different surface forces dominate the interactions between the colloidal particle and the alginate-fouled membrane. These results are presented in Figure 3a–c for T = 27, 35, and 40 °C, respectively. As mentioned previously, snap-in events are absent in measurements with fouled membranes; we observe instead repulsive forces during approach at any temperature (see Figure S4). Repulsive forces are also observed in 25.9–33.3% of the retraction force curves (denoted by the "NO" column in Figure 3a–c). These repulsive forces can be attributed to strong electrostatic repulsion between the CML particle and the more negative membrane surface in the presence of the alginate fouling layer.[101] Wang et al.[68] also attributed weaker alginate–alginate adhesion forces to electrostatic repulsive forces resulting from the more negative charge of alginate compared to other foulants (bovine serum albumin and effluent organic matter). In contrast to the pristine membrane, the average peak adhesion force ($\bar{F}_{peak}$) over fouled membranes is significantly weaker in magnitude and less sensitive to temperature (p > 0.05 for all pairwise comparisons) irrespective of whether repulsive forces curves are included in the average (Figure 3d) or not (Figure 3e).

The distribution of rupture separations (R) of CML particles over fouled membranes at T = 27, 35, and 40 °C is shown in Figure S9. Although $\bar{R}$ is similar for all the temperatures investigated (p > 0.05 for all pairwise comparisons), $\bar{R}$ has a larger value (≈ 0.6 μm) on the fouled membranes than on pristine membranes (compare Figure S9 with Figure S8). Longer rupture separations are likely due to desorption of alginate molecules from the membrane surface during probe retraction.

3.3. Effect of Temperature on Membrane Transport Parameters. Having established the T-dependence of membrane adhesive properties, we next examine the impact of T on transport and selectivity during membrane filtration. The effect of temperature on the membrane permeance to water and conductivity rejection of ESPA2-LD thin-film composite membranes is shown in Figure 4.

In agreement with previous experiments (5 °C < T < 60 °C),[32,39,102] A increases with the feed temperature (Figure 4) from 3.8 ± 0.3 LMH bar^{-1} at 27 °C to 4.9 ± 0.4 and 6.7 ± 0.8 LMH bar^{-1} at 35 and 40 °C, respectively. The change in permeance with temperature is due to the dependence of A on water viscosity and diffusivity:[31,39] $A \propto \frac{D_{w,m}}{T}$ ($D_{w,m}$ is the water

https://dx.doi.org/10.1021/acsestengg.0c00258
ACS EST Engg. XXXX, XXX, XXX–XXX

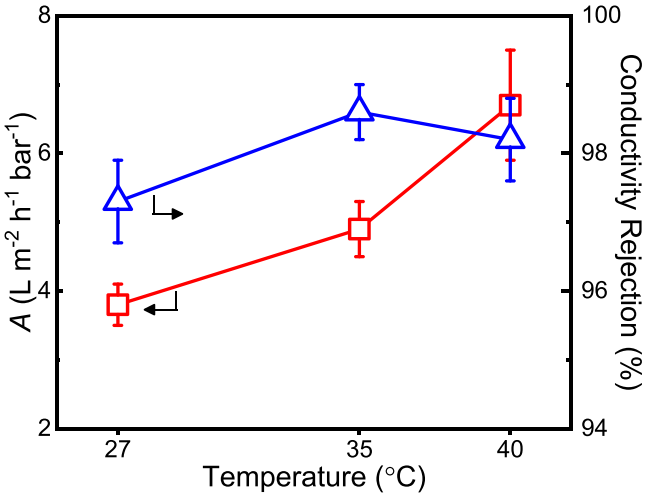

Figure 4. Effect of temperature on the permeance to water (A) and conductivity rejection (right y-axis) of ESPA2-LD membranes at T = 27, 35, and 40 °C. The error bars denote one standard deviation. Alginate-free synthetic wastewater feed was used to determine conductivity rejection (number of measurements n = 6 at 27 °C, n = 6 at 35 °C, and n = 8 at 40 °C). All data determined at a permeate flux J = 20 ± 1 LMH.

diffusivity in the membrane) and $D_{w,m} \propto \frac{T}{\mu}$ (μ is the dynamic water viscosity).[31] As a result, A will be inversely proportional to μ which, in turn, varies inversely with temperature.[36,102,103] Another possible factor contributing to the increase in A is the thermal expansion of the polyamide network:[31] the increase in surface roughness with T (Figure 1) is presumably due to thermal expansion of the polyamide active layer.[31] In addition, the increase in roughness observed between 27 and 35 °C (Figure 1)—resulting in a larger effective permeable area[104]—may also be responsible for the increase in A[105] observed between 27 and 35 °C.

Conductivity rejection was found to be weakly dependent on T, ranging from 97.3 ± 0.6% at 27 °C to 98.6 ± 0.4% and 98.2 ± 0.6% at 35 and 40 °C, respectively. While these observations are at odds with the expected temperature dependence of the solute diffusivity, D_s, and solubility, K_s, in the membrane (both D_s and K_s increase with increasing temperature),[31,39,106] the results in Figure 4 appear to be in agreement with other studies showing negligible temperature dependence of the reflection coefficient over a similar temperature range.[32]

3.4. Effect of Temperature on Organic Fouling. The effect of temperature on alginate fouling is investigated in Figure 5a, showing the normalized permeate flux, J/J_0, as a function of time. The time dependence of the permeate flux exhibits common features at all temperatures, indicative of a transition of fouling dominated by foulant−membrane interactions to a regime determined by foulant−foulant interactions.[107] A steep flux loss (26% at 27 °C, 19% at 35 °C, and 22% at 40 °C) within the first 2 h is followed by slow flux decline at longer times (Figure 5a). This behavior is consistent with our colloidal AFM data: at short time scales, fouling is dominated by strong foulant−clean membrane interactions (Figures 2 and S6), leading to the rapid formation of a foulant layer and significant flux loss. At longer times scales ($t \gtrsim 2$ h), weakly adhesive or repulsive foulant−foulant interactions (Figure 3) cause J/J_0 to decrease at a much slower rate. On the other hand, the extent of the flux loss is different

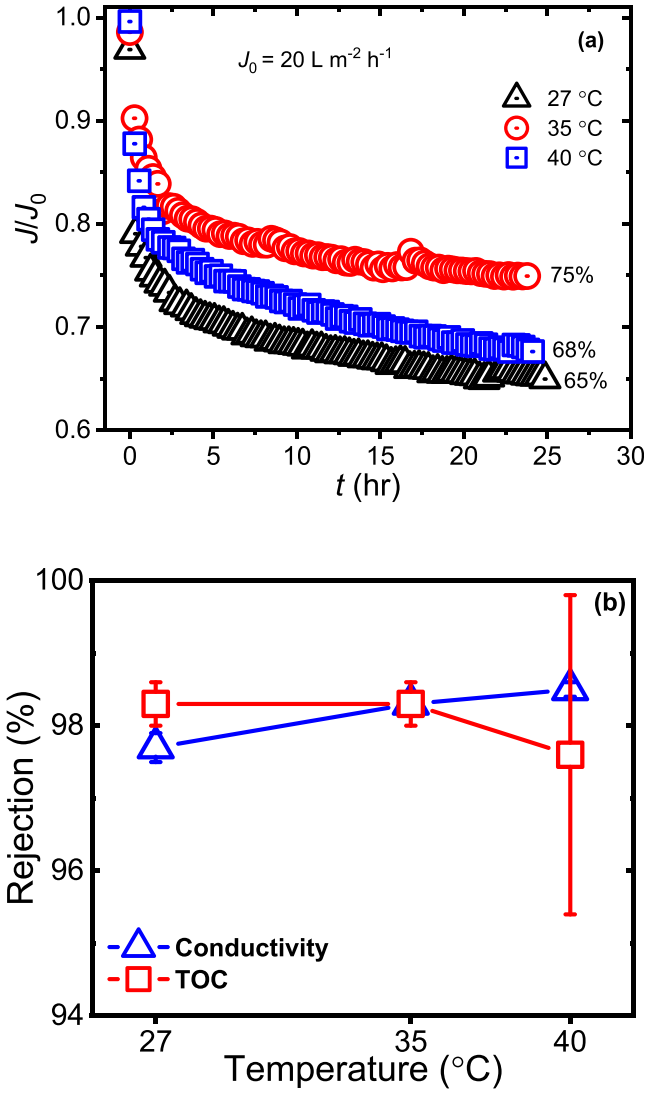

Figure 5. Effect of temperature on the performance of ESPA2-LD membranes during alginate fouling: (a) flux decline of ESPA2-LD membranes over 24 h during accelerated fouling with 250 mg L^{-1} sodium alginate for each indicated feed temperature given in the inset. Due to the noise underlying the permeate flow rate measurements, flux data was smoothed using a locally estimated scatterplot smoothing algorithm (loess) implemented in Origin 2018 (Northampton, MA). (b) Average conductivity and TOC rejection after initiation of fouling. Error bars denote one standard deviation. Experimental conditions: initial permeate flux J_0 = 20 LMH; synthetic wastewater feed (I = 14.7 mM) at pH = 7.4 supplemented with 250 mg L^{-1} sodium alginate; crossflow velocity = 15.8 cm s^{-1}.

at each temperature. Fouling is most severe at 27 °C, with a flux loss of 35% after 24 h compared to 25% at 35 °C and 32% at 40 °C. The more significant fouling at 27 °C is consistent with the stronger hydrophobic interactions at this temperature (cf. Figure 2). However, at 35 and 40 °C different fouling propensity does not reflect the similar adhesion forces observed in Figure 2. Thus, interfacial behavior alone does not explain the observed fouling behavior.

To reconcile the fouling experiments in Figure 5a with the interfacial behavior presented in Figure 2, we quantified the resistance contributed by the foulant layer to water transport using a resistance-in-series model.[108,109] Within this approach, the overall transport resistance of the fouled membrane is

https://dx.doi.org/10.1021/acsestengg.0c00258
ACS EST Engg. XXXX, XXX, XXX−XXX

given by the sum of the individual hydraulic resistances of the polyamide (A^{-1}) and a (time-dependent) hydraulic resistance due to the foulant layer, $A_f(t)^{-1}$. The resulting expression for the time-dependent flux through the fouled membrane is

$$J(t) = \frac{1}{A^{-1} + A_f(t)^{-1}}(\Delta p - \Delta\pi) \quad (1)$$

where $\Delta\pi$ is the osmotic pressure difference between the feed and the permeate. Dividing eq 1 by the steady-state water flux through the clean membrane [$J_0 = A(\Delta p - \Delta\pi)$] yields

$$\frac{J(t)}{J_0} = \frac{1}{1 + \frac{A}{A_f(t)}} = \frac{1}{1 + R_f(t)A} \quad (2)$$

where the inverse of the permeability of the foulant layer is expressed as a hydraulic resistance, $R_f(t) = A_f(t)^{-1}$. Equation 1 shows that two mechanisms could contribute to flux loss: fouling, which increases $R_f(t)$ as the foulant layer develops, and increasing water permeance (e.g., due to T), which will also lower J/J_0 due to the increased convective flux of foulant to the membrane. Based on the characterization results, we speculate that the smaller flux loss at 35 °C compared to 27 °C is primarily due to the effect of the interfacial properties on the foulant layer: a lower R_f value at 35 °C results from a thinner foulant layer due to a more hydrophilic membrane (Figure 1) and weaker hydrophobic interactions (Figure 2) at 35 °C versus 27 °C. The smaller R_f mitigates the effect of a larger value of A at 35 °C compared to 27 °C (Figure 4), with the net effect being a smaller flux loss at 35 °C. Conversely, raising T from 35 to 40 °C brings about a negligible change in interfacial properties and R_f (similar hydrophilicity and adhesion forces, cf. Figures 1 and 2), but a significant increase in A (Figure 4) that results in more severe flux loss at 40 °C compared to 35 °C.

These arguments are supported by the experimental data. Solving for R_f using eq 2 with data from Figures 4 and 5 ($A_{35°C}$ = 4.9 LMH bar^{-1}, $A_{40°C}$ = 6.7 LMH bar^{-1}, $(J(t = 24\ \text{h})/J_0)_{35°C}$ = 0.75 and $(J(t = 24\ \text{h})/J_0)_{40°C}$ = 0.68) yields $R_{f,35°C}$ = 0.07 bar LMH^{-1} = $R_{f,40°C}$, i.e., similar foulant layer resistances consistent with the AFM results (Figure 2); thus, the greater flux loss at 40 °C compared to 35 °C stems from $A_{40°C} > A_{35°C}$ (Figure 4). On the other hand, $R_{f,27°C}$ = 0.14 bar LMH^{-1}, a significantly higher resistance (due to stronger adhesion at 27 °C) that causes a more pronounced flux loss compared to experiments at higher T. As we elaborate in Section S.4 (SI), we estimate the thickness of the foulant layer at $O(10\ \mu m)$ and the fraction of foulant adhered to the membrane at ca. 3% of the total mass of alginate. Thus, we can neglect the contribution to the slowdown of the fouling rate resulting from a lower concentration of alginate in the feed.

Finally, the results of conductivity and TOC rejection at each temperature are summarized in Figure 5b. These data are derived from measurements at t = 2 and 24 h after initiation of the fouling experiment and are reported as a single average as they were similar (within 1%) to one another at each temperature. Conductivity rejection remained approximately constant with increasing temperature, exhibiting values similar to those of the clean membrane (see Figure 4). Similarly, TOC rejection shown in Figure 5b is independent of temperature. Although increased passage of dissolved alginate could be expected with rising temperature on account of membrane swelling,[31] the high TOC rejection suggests that alginate (likely found as Ca^{2+}-complexed aggregates) is large enough (>1 nm,[110] compared to subnanometer voids in polyamide[1,105]) to deposit on the surface of the membrane as a fouling layer. The TOC passage observed (1.7−2.4%) is likely due to low molecular weight impurities in alginate (e.g., polyphenols and proteins[111]). A similar TOC passage has been observed by previous studies with humic acid.[31]

4. CONCLUSION

We have shown that membrane interfacial and transport properties play competing roles during alginate fouling of reverse osmosis membranes at different temperatures. Colloidal probe force spectroscopy (CPFS) measurements show that foulant−membrane interactions are markedly temperature-dependent (Figure 2). Rising temperature *weakens* foulant adhesion, given that foulant−membrane hydrophobic interactions, which become weaker with increasing temperature, drive adhesion onto clean membranes. Conversely, the monotonic increase in water permeance with temperature (Figure 4) worsens fouling, which suggests that lower operating pressures (and hence lower fluxes) will be needed during extreme temperature conditions (e.g., heat waves) to avoid exposing the membrane to excessive fouling. Interestingly, our results suggest that membrane hydrophilicity, a key interfacial property in membrane development, becomes less relevant at high feed temperatures, since membranes become *ipso facto* less hydrophobic at higher temperatures (Figures 1 and 2). CPFS measurements further show that the alginate layer is self-limiting: once an adlayer of a critical thickness is formed, deposition of additional foulant molecules is hindered by weak (or repulsive) foulant−foulant interactions (Figure 3), which appear to be temperature independent. Our results also suggest possible lines for future inquiry. Understanding of the process conditions that lead to the formation of the critical foulant layer is crucial for effective fouling management. Given the preeminent role of hydrophobic interactions in alginate fouling, experiments at lower temperatures (which strengthen foulant−membrane hydrophobic interactions) should be conducted to understand fouling under feed conditions relevant to temperate and cold climates. These experiments would also be useful in the formulation of cleaning-in-place formulations tailored to specific feedwater temperatures.

■ ASSOCIATED CONTENT

Supporting Information

The Supporting Information is available free of charge at https://pubs.acs.org/doi/10.1021/acsestengg.0c00258.

Additional materials and methods (Sections S.1 and S.2); calculation of the permeate drag force exerted on a colloidal particle (Section S.3); estimation of the foulant layer thickness and adsorbed mass (Section S.4); tapping-mode AFM images of polyamide membranes at various temperatures (Figure S1); ζ-potential of polyamide membranes at various temperature and pH conditions (Figure S2); representative force curves over pristine and alginate-fouled membranes (Figures S3−S5); snap-in forces (Figure S6) and snap-in distances (Figure S7) on pristine membranes; and rupture separations over pristine (Figure S8) and alginate-fouled (Figure S9) membranes (PDF)

https://dx.doi.org/10.1021/acsestengg.0c00258
ACS EST Engg. XXXX, XXX, XXX−XXX

AUTHOR INFORMATION

Corresponding Author

Santiago Romero-Vargas Castrillón − *Department of Civil, Environmental, and Geo- Engineering, University of Minnesota, Minneapolis, Minnesota 55455, United States; Institute for Infrastructure and Environment, School of Engineering and Institute for Materials and Processes, School of Engineering, The University of Edinburgh, Edinburgh EH9 3FG, United Kingdom;* orcid.org/0000-0003-3339-7692; Phone: +44(0)131 651 3567; Email: santiago@ed.ac.uk, sromerov@umn.edu

Authors

Sara BinAhmed − *Department of Civil, Environmental, and Geo- Engineering, University of Minnesota, Minneapolis, Minnesota 55455, United States*

Raymond M. Hozalski − *Department of Civil, Environmental, and Geo- Engineering, University of Minnesota, Minneapolis, Minnesota 55455, United States;* orcid.org/0000-0002-7541-0165

Complete contact information is available at: https://pubs.acs.org/10.1021/acsestengg.0c00258

Notes

The authors declare no competing financial interest.

ACKNOWLEDGMENTS

This work was supported by grants to S.R.-V.C. from 3M Co. (Non-Tenured Faculty Award) and the Environment and Natural Resources Trust Fund, as recommended by the Legislative-Citizen Commission on Minnesota Resources. We thank Hydranautics (Oceanside, CA) for supplying the membranes used in the initial stages of this investigation. The technical assistance of Wieslaw J. Suszynski (Coating Process Fundamentals Visualization Laboratory, University of Minnesota) with contact angle measurements is gratefully acknowledged. S.B.-A. acknowledges support from the Graduate School at the University of Minnesota through a Doctoral Dissertation Fellowship. S.R.-V.C. is grateful to Dr. Steve Jons (Dupont Water Solutions) for useful comments regarding the series-resistance model.

REFERENCES

(1) Werber, J. R.; Osuji, C. O.; Elimelech, M. Materials for Next-Generation Desalination and Water Purification Membranes. *Nat. Rev. Mater.* **2016**, *1*, 1−15.

(2) Jjemba, P. K.; Weinrich, L. A.; Cheng, W.; Giraldo, E.; LeChevallier, M. W. Regrowth of Potential Opportunistic Pathogens and Algae in Reclaimed-Water Distribution Systems. *Appl. Environ. Microbiol.* **2010**, *76* (13), 4169−4178.

(3) Ang, W. S.; Elimelech, M. Protein (BSA) Fouling of Reverse Osmosis Membranes: Implications for Wastewater Reclamation. *J. Membr. Sci.* **2007**, *296* (1−2), 83−92.

(4) Oki, T.; Kanae, S. Global Hydrological Cycles and World Water Resources. *Science (Washington, DC, U. S.)* **2006**, *313* (5790), 1068−1072.

(5) Gullinkala, T.; Escobar, I. C. Membranes for Water Treatment Applications - An Overview. *ACS Symp. Ser.* **2011**, *1078*, 155−170.

(6) Kelley, C. P.; Mohtadi, S.; Cane, M. A.; Seager, R.; Kushnir, Y. Climate Change in the Fertile Crescent and Implications of the Recent Syrian Drought. *Proc. Natl. Acad. Sci. U. S. A.* **2015**, *112* (11), 3241−3246.

(7) Alvarez, P. J. J.; Chan, C. K.; Elimelech, M.; Halas, N. J.; Villagrán, D. Emerging Opportunities for Nanotechnology to Enhance Water Security. *Nat. Nanotechnol.* **2018**, *13* (8), 634−641.

(8) Elimelech, M.; Phillip, W. A. The Future of Seawater Desalination: Energy, Technology, and the Environment. *Science (Washington, DC, U. S.)* **2011**, *333* (6043), 712−717.

(9) Jarusutthirak, C.; Amy, G. Membrane Filtration of Wastewater Effluents for Reuse: Effluent Organic Matter Rejection and Fouling. *Water Sci. Technol.* **2001**, *43* (10), 225−232.

(10) Fujioka, T.; Khan, S. J.; McDonald, J. A.; Henderson, R. K.; Poussade, Y.; Drewes, J. E.; Nghiem, L. D. Effects of Membrane Fouling on N-Nitrosamine Rejection by Nanofiltration and Reverse Osmosis Membranes. *J. Membr. Sci.* **2013**, *427*, 311−319.

(11) Petala, M.; Tsiridis, V.; Samaras, P.; Zouboulis, A.; Sakellaropoulos, G. P. Wastewater Reclamation by Advanced Treatment of Secondary Effluents. *Desalination* **2006**, *195*, 109−118.

(12) Doederer, K.; Farré, M. J.; Pidou, M.; Weinberg, H. S.; Gernjak, W. Rejection of Disinfection By-Products by RO and NF Membranes: Influence of Solute Properties and Operational Parameters. *J. Membr. Sci.* **2014**, *467*, 195−205.

(13) Wu, J.; Contreras, A. E.; Li, Q. Studying the Impact of RO Membrane Surface Functional Groups on Alginate Fouling in Seawater Desalination. *J. Membr. Sci.* **2014**, *458*, 120−127.

(14) Kang, G.; Cao, Y. Development of Antifouling Reverse Osmosis Membranes for Water Treatment: A Review. *Water Res.* **2012**, *46* (3), 584−600.

(15) Varin, K. J.; Lin, N. H.; Cohen, Y. Biofouling and Cleaning Effectiveness of Surface Nanostructured Reverse Osmosis Membranes. *J. Membr. Sci.* **2013**, *446*, 472−481.

(16) Li, Q.; Xu, Z.; Pinnau, I. Fouling of Reverse Osmosis Membranes by Biopolymers in Wastewater Secondary Effluent: Role of Membrane Surface Properties and Initial Permeate Flux. *J. Membr. Sci.* **2007**, *290* (1−2), 173−181.

(17) Xu, P.; Drewes, J. E.; Kim, T.-U.; Bellona, C.; Amy, G. Effect of Membrane Fouling on Transport of Organic Contaminants in NF/RO Membrane Applications. *J. Membr. Sci.* **2006**, *279* (1−2), 165−175.

(18) Zou, L.; Vidalis, I.; Steele, D.; Michelmore, A.; Low, S. P.; Verberk, J. Q. J. C. Surface Hydrophilic Modification of RO Membranes by Plasma Polymerization for Low Organic Fouling. *J. Membr. Sci.* **2011**, *369* (1−2), 420−428.

(19) Ghanbari, M.; Emadzadeh, D.; Lau, W. J.; Matsuura, T.; Ismail, A. F. Synthesis and Characterization of Novel Thin Film Nanocomposite Reverse Osmosis Membranes with Improved Organic Fouling Properties for Water Desalination. *RSC Adv.* **2015**, *5* (27), 21268−21276.

(20) Mo, H.; Tay, K. G.; Ng, H. Y. Fouling of Reverse Osmosis Membrane by Protein (BSA): Effects of PH, Calcium, Magnesium, Ionic Strength and Temperature. *J. Membr. Sci.* **2008**, *315*, 28−35.

(21) Lee, S.; Ang, W. S.; Elimelech, M. Fouling of Reverse Osmosis Membranes by Hydrophilic Organic Matter: Implications for Water Reuse. *Desalination* **2006**, *187*, 313−321.

(22) Ang, W. S.; Lee, S.; Elimelech, M. Chemical and Physical Aspects of Cleaning of Organic-Fouled Reverse Osmosis Membranes. *J. Membr. Sci.* **2006**, *272* (1−2), 198−210.

(23) Katsoufidou, K.; Yiantsios, S. G.; Karabelas, A. J. An Experimental Study of UF Membrane Fouling by Humic Acid and Sodium Alginate Solutions: The Effect of Backwashing on Flux Recovery. *Desalination* **2008**, *220* (1−3), 214−227.

(24) Jones, K. L.; O'Melia, C. R. Ultrafiltration of Protein and Humic Substances: Effect of Solution Chemistry on Fouling and Flux Decline. *J. Membr. Sci.* **2001**, *193* (2), 163−173.

(25) Bazaka, K.; Jacob, M. V.; Crawford, R. J.; Ivanova, E. P. Efficient Surface Modification of Biomaterial to Prevent Biofilm Formation and the Attachment of Microorganisms. *Appl. Microbiol. Biotechnol.* **2012**, *95* (2), 299−311.

(26) Friedlander, R. S.; Vogel, N.; Aizenberg, J. Role of Flagella in Adhesion of *Escherichia Coli* to Abiotic Surfaces. *Langmuir* **2015**, *31* (22), 6137−6144.

(27) Garrett, T. R.; Bhakoo, M.; Zhang, Z. Bacterial Adhesion and Biofilms on Surfaces. *Prog. Nat. Sci.* **2008**, *18* (9), 1049−1056.
(28) Araújo, E. A.; de Andrade, N. J.; da Silva, L. H. M.; de Carvalho, A. F.; de Sá Silva, C. A.; Ramos, A. M. Control of Microbial Adhesion as a Strategy for Food and Bioprocess Technology. *Food Bioprocess Technol.* **2010**, *3* (3), 321−332.
(29) Baek, Y.; Yu, J.; Kim, S.-H.; Lee, S.; Yoon, J. Effect of Surface Properties of Reverse Osmosis Membranes on Biofouling Occurrence under Filtration Conditions. *J. Membr. Sci.* **2011**, *382* (1−2), 91−99.
(30) Suwarno, S. R.; Hanada, S.; Chong, T. H.; Goto, S.; Henmi, M.; Fane, A. G. The Effect of Different Surface Conditioning Layers on Bacterial Adhesion on Reverse Osmosis Membranes. *Desalination* **2016**, *387*, 1−13.
(31) Jin, X.; Jawor, A.; Kim, S.; Hoek, E. M. V. V. Effects of Feed Water Temperature on Separation Performance and Organic Fouling of Brackish Water RO Membranes. *Desalination* **2009**, *239* (1−3), 346−359.
(32) Goosen, M. F. A.; Sablani, S. S.; Al-Maskari, S. S.; Al-Belushi, R. H.; Wilf, M. Effect of Feed Temperature on Permeate Flux and Mass Transfer Coefficient in Spiral-Wound Reverse Osmosis Systems. *Desalination* **2002**, *144* (1−3), 367−372.
(33) Goosen, M. F. A. A.; Sablani, S.; Cin, M. D.; Wilf, M. Effect of Cyclic Changes in Temperature and Pressure on Permeation Properties of Composite Polyamide Seawater Reverse Osmosis Membranes. *Sep. Sci. Technol.* **2010**, *46* (1), 14−26.
(34) Kim, S.; Lee, S.; Lee, E.; Sarper, S.; Kim, C. H.; Cho, J. Enhanced or Reduced Concentration Polarization by Membrane Fouling in Seawater Reverse Osmosis (SWRO) Processes. *Desalination* **2009**, *247* (1−3), 162−168.
(35) John, V. C.; Coles, S. L.; Abozed, A. I. Seasonal Cycles of Temperature, Salinity and Water Masses of the Western Arabian Gulf. *Oceanol. Acta* **1990**, *13* (3), 273−282.
(36) Agashichev, S. P.; Lootahb, K. N. Influence of Temperature and Permeate Recovery on Energy Consumption of a Reverse Osmosis System. *Desalination* **2003**, *154* (3), 253−266.
(37) Schaep, J.; Van Der Bruggen, B.; Uytterhoeven, S.; Croux, R.; Vandecasteele, C.; Wilms, D.; Van Houtte, E.; Vanlerberghe, F. Remvoal of Hardness from Groundwater by Nanofiltration. *Desalination* **1998**, *119* (1−3), 295−301.
(38) Francis, M. J. J.; Pashley, R. M. M. The Effects of Feed Water Temperature and Dissolved Gases on Permeate Flow Rate and Permeate Conductivity in a Pilot Scale Reverse Osmosis Desalination Unit. *Desalin. Water Treat.* **2011**, *36* (1−3), 363−373.
(39) Jawor, A.; Hoek, E. M. V. Effects of Feed Water Temperature on Inorganic Fouling of Brackish Water RO Membranes. *Desalination* **2009**, *235* (1−3), 44−57.
(40) Al-Mutaz, I. S.; Al-Ghunaimi, M. A. Performance of Reverse Osmosis Units at High Temperatures. Presented at *IDA World Congress on Desalination and Water Reuse*, 2001.
(41) Wilf, M.; Bartels, C. Optimization of Seawater RO Systems Design. *Desalination* **2005**, *173* (1), 1−12.
(42) Geise, G. M.; Park, H. B.; Sagle, A. C.; Freeman, B. D.; McGrath, J. E. Water Permeability and Water/Salt Selectivity Tradeoff in Polymers for Desalination. *J. Membr. Sci.* **2011**, *369* (1−2), 130−138.
(43) Geise, G. M.; Paul, D. R.; Freeman, B. D. Fundamental Water and Salt Transport Properties of Polymeric Materials. *Prog. Polym. Sci.* **2014**, *39*, 1−24.
(44) Ormanci-Acar, T.; Celebi, F.; Keskin, B.; Mutlu-Salmanlı, O.; Agtas, M.; Turken, T.; Tufani, A.; Imer, D. Y.; Ince, G. O.; Demir, T. U.; et al. Fabrication and Characterization of Temperature and PH Resistant Thin Film Nanocomposite Membranes Embedded with Halloysite Nanotubes for Dye Rejection. *Desalination* **2018**, *429*, 20−32.
(45) Sharma, R. R.; Chellam, S. Temperature Effects on the Morphology of Porous Thin Film Composite Nanofiltration Membranes. *Environ. Sci. Technol.* **2005**, *39* (13), 5022−5030.
(46) Baghdadi, Y. N.; Alnouri, S. Y.; Matsuura, T.; Tarboush, B. J. A. Temperature Effects on Concentration Polarization Thickness in Thin-Film Composite Reverse Osmosis Membranes. *Chem. Eng. Technol.* **2018**, *41* (10), 1905−1912.
(47) Listiarini, K.; Chun, W.; Sun, D. D.; Leckie, J. O. Fouling Mechanism and Resistance Analyses of Systems Containing Sodium Alginate, Calcium, Alum and Their Combination in Dead-End Fouling of Nanofiltration Membranes. *J. Membr. Sci.* **2009**, *344* (1−2), 244−251.
(48) Romero-Vargas Castrillón, S.; Lu, X.; Shaffer, D. L.; Elimelech, M. Amine Enrichment and Poly(Ethylene Glycol) (PEG) Surface Modification of Thin-Film Composite Forward Osmosis Membranes for Organic Fouling Control. *J. Membr. Sci.* **2014**, *450*, 331−339.
(49) Boyd, A.; Chakrabarty, A. M. Pseudomonas Aeruginosa Biofilms: Role of the Alginate Exopolysaccharide. *J. Ind. Microbiol.* **1995**, *15* (3), 162−168.
(50) Herzberg, M.; Elimelech, M. Biofouling of Reverse Osmosis Membranes: Role of Biofilm-Enhanced Osmotic Pressure. *J. Membr. Sci.* **2007**, *295* (1−2), 11−20.
(51) Bellona, C.; Heil, D.; Yu, C.; Fu, P.; Drewes, J. E. The Pros and Cons of Using Nanofiltration in Lieu of Reverse Osmosis for Indirect Potable Reuse Applications. *Sep. Purif. Technol.* **2012**, *85*, 69−76.
(52) Ci, S. X.; Huynh, T. H.; Louie, L. W.; Yang, A.; Beals, B. J.; Ron, N.; Tsang, W.-G.; Soon-Shiong, P.; Desai, N. P. Molecular Mass Distribution of Sodium Alginate by High-Performance Size-Exclusion Chromatography. *J. Chromatogr. A* **1999**, *864* (2), 199−210.
(53) Ye, Y.; Le Clech, P.; Chen, V.; Fane, A. G.; Jefferson, B. Fouling Mechanisms of Alginate Solutions as Model Extracellular Polymeric Substances. *Desalination* **2005**, *175* (1), 7−20.
(54) Matin, A.; Shafi, H.; Wang, M.; Khan, Z.; Gleason, K.; Rahman, F. Reverse Osmosis Membranes Surface-Modified Using an Initiated Chemical Vapor Deposition Technique Show Resistance to Alginate Fouling under Cross-Flow Conditions: Filtration & Subsequent Characterization. *Desalination* **2016**, *379*, 108−117.
(55) Katsoufidou, K.; Yiantsios, S. G.; Karabelas, A. J. Experimental Study of Ultrafiltration Membrane Fouling by Sodium Alginate and Flux Recovery by Backwashing. *J. Membr. Sci.* **2007**, *300* (1−2), 137−146.
(56) Lu, X.; Romero-Vargas Castrillón, S.; Shaffer, D. L.; Ma, J.; Elimelech, M. In Situ Surface Chemical Modification of Thin-Film Composite Forward Osmosis Membranes for Enhanced Organic Fouling Resistance. *Environ. Sci. Technol.* **2013**, *47* (21), 12219.
(57) Ang, W. S.; Yip, N. Y.; Tiraferri, A.; Elimelech, M. Chemical Cleaning of RO Membranes Fouled by Wastewater Effluent: Achieving Higher Efficiency with Dual-Step Cleaning. *J. Membr. Sci.* **2011**, *382* (1−2), 100−106.
(58) Tiraferri, A.; Kang, Y.; Giannelis, E. P.; Elimelech, M. Superhydrophilic Thin-Film Composite Forward Osmosis Membranes for Organic Fouling Control: Fouling Behavior and Antifouling Mechanisms. *Environ. Sci. Technol.* **2012**, *46* (20), 11135−11144.
(59) Bartels, C. R.; Wilf, M.; Andes, K.; Iong, J. Design Considerations for Wastewater Treatment by Reverse Osmosis. *Water Sci. Technol.* **2005**, *51* (6−7), 473−482.
(60) Khan, M. T.; Busch, M.; Molina, V. G.; Emwas, A.-H.; Aubry, C.; Croue, J.-P. How Different Is the Composition of the Fouling Layer of Wastewater Reuse and Seawater Desalination RO Membranes? *Water Res.* **2014**, *59*, 271−282.
(61) Kim, H.-C.; Dempsey, B. A. Comparison of Two Fractionation Strategies for Characterization of Wastewater Effluent Organic Matter and Diagnosis of Membrane Fouling. *Water Res.* **2012**, *46* (11), 3714−3722.
(62) Michael-Kordatou, I.; Michael, C.; Duan, X.; He, X.; Dionysiou, D. D.; Mills, M. A.; Fatta-Kassinos, D. Dissolved Effluent Organic Matter: Characteristics and Potential Implications in Wastewater Treatment and Reuse Applications. *Water Res.* **2015**, *77*, 213−248.
(63) Li, Q.; Elimelech, M. Organic Fouling and Chemical Cleaning of Nanofiltration Membranes: Measurements and Mechanisms. *Environ. Sci. Technol.* **2004**, *38* (17), 4683−4693.
(64) Mi, B.; Elimelech, M. Organic Fouling of Forward Osmosis Membranes: Fouling Reversibility and Cleaning without Chemical Reagents. *J. Membr. Sci.* **2010**, *348* (1−2), 337−345.

https://dx.doi.org/10.1021/acsestengg.0c00258
ACS EST Engg. XXXX, XXX, XXX−XXX

(65) Behrens, S. H.; Christl, D. I.; Emmerzael, R.; Schurtenberger, P.; Borkovec, M. Charging and Aggregation Properties of Carboxyl Latex Particles: Experiments versus DLVO Theory. *Langmuir* **2000**, *16* (6), 2566−2575.
(66) Beaussart, A.; El-Kirat-Chatel, S.; Sullan, R. M. A.; Alsteens, D.; Herman, P.; Derclaye, S.; Dufrêne, Y. F. Quantifying the Forces Guiding Microbial Cell Adhesion Using Single-Cell Force Spectroscopy. *Nat. Protoc.* **2014**, *9* (5), 1049−1055.
(67) Zhang, X. H.; Quinn, A.; Ducker, W. A. Nanobubbles at the Interface between Water and a Hydrophobic Solid. *Langmuir* **2008**, *24* (9), 4756−4764.
(68) Wang, L.; Miao, R.; Wang, X.; Lv, Y.; Meng, X.; Yang, Y.; Huang, D.; Feng, L.; Liu, Z.; Ju, K. Fouling Behavior of Typical Organic Foulants in Polyvinylidene Fluoride Ultrafiltration Membranes: Characterization from Microforces. *Environ. Sci. Technol.* **2013**, *47* (8), 3708−3714.
(69) Hutter, J. L.; Bechhoefer, J. Calibration of Atomic-Force Microscope Tips. *Rev. Sci. Instrum.* **1993**, *64* (7), 1868−1873.
(70) Allen, A.; Semião, A. J. C.; Habimana, O.; Heffernan, R.; Safari, A.; Casey, E. Nanofiltration and Reverse Osmosis Surface Topographical Heterogeneities: Do They Matter for Initial Bacterial Adhesion? *J. Membr. Sci.* **2015**, *486*, 10−20.
(71) Lo, Y.-S.; Simons, J.; Beebe, T. P. Temperature Dependence of the Biotin-Avidin Bond-Rupture Force Studied by Atomic Force Microscopy. *J. Phys. Chem. B* **2002**, *106* (38), 9847−9852.
(72) Heinz, W. F.; Hoh, J. H. Getting Physical with Your Chemistry: Mechanically Investigating Local Structure and Properties of Surfaces with the Atomic Force Microscope. *J. Chem. Educ.* **2005**, *82* (5), 695−703.
(73) Heinz, W. F.; Hoh, J. H. Spatially Resolved Force Spectroscopy of Biological Surfaces Using the Atomic Force Microscope. *Trends Biotechnol.* **1999**, *17* (4), 143−150.
(74) Erts, D.; Lõhmus, A.; Lõhmus, R.; Olin, H.; Pokropivny, A. V.; Ryen, L.; Svensson, K. Force Interactions and Adhesion of Gold Contacts Using a Combined Atomic Force Microscope and Transmission Electron Microscope. *Appl. Surf. Sci.* **2002**, *188* (3−4), 460−466.
(75) Thewes, N.; Loskill, P.; Jung, P.; Peisker, H.; Bischoff, M.; Herrmann, M.; Jacobs, K. Hydrophobic Interaction Governs Unspecific Adhesion of Staphylococci: A Single Cell Force Spectroscopy Study. *Beilstein J. Nanotechnol.* **2014**, *5*, 1501−1512.
(76) Butt, H.-J.; Cappella, B.; Kappl, M. Force Measurements with the Atomic Force Microscope: Technique, Interpretation and Applications. *Surf. Sci. Rep.* **2005**, *59* (1), 1−152.
(77) Binahmed, S.; Hasane, A.; Wang, Z.; Mansurov, A.; Romero-Vargas Castrillón, S. Bacterial Adhesion to Ultrafiltration Membranes: Role of Hydrophilicity, Natural Organic Matter, and Cell-Surface Macromolecules. *Environ. Sci. Technol.* **2018**, *52* (1), 162−172.
(78) Li, Q.; Pan, X.; Qu, Z.; Zhao, X.; Jin, Y.; Dai, H.; Yang, B.; Wang, X. Understanding the Dependence of Contact Angles of Commercially RO Membranes on External Conditions and Surface Features. *Desalination* **2013**, *309*, 38−45.
(79) Akin, O.; Temelli, F. Probing the Hydrophobicity of Commercial Reverse Osmosis Membranes Produced by Interfacial Polymerization Using Contact Angle, XPS, FTIR, FE-SEM and AFM. *Desalination* **2011**, *278* (1−3), 387−396.
(80) Miller, D. J.; Dreyer, D. R.; Bielawski, C. W.; Paul, D. R.; Freeman, B. D. Surface Modification of Water Purification Membranes. *Angew. Chem., Int. Ed.* **2017**, *56* (17), 4662−4711.
(81) Andrade, J. D.; Smith, L. M.; Gregonis, D. E. The Contact Angle and Interface Energetics. In *Surface and Interfacial Aspects of Biomedical Polymers*; Springer US: Boston, MA, 1985; Vol. *1*, pp 249−292; DOI: 10.1007/978-1-4684-8610-0_7.
(82) Surawanvijit, S.; Rahardianto, A.; Cohen, Y. An Integrated Approach for Characterization of Polyamide Reverse Osmosis Membrane Degradation Due to Exposure to Free Chlorine. *J. Membr. Sci.* **2016**, *510*, 164−173.
(83) Diaz, M. E.; Savage, M. D.; Cerro, R. L. The Effect of Temperature on Contact Angles and Wetting Transitions for N-Alkanes on PTFE. *J. Colloid Interface Sci.* **2017**, *503*, 159−167.
(84) Yang, J.; Lee, S.; Lee, E.; Lee, J.; Hong, S. Effect of Solution Chemistry on the Surface Property of Reverse Osmosis Membranes under Seawater Conditions. *Desalination* **2009**, *247* (1−3), 148−161.
(85) Tu, K. L.; Chivas, A. R.; Nghiem, L. D. Effects of Chemical Preservation on Flux and Solute Rejection by Reverse Osmosis Membranes. *J. Membr. Sci.* **2014**, *472*, 202−209.
(86) Zisman, W. A. Relation of the Equilibrium Contact Angle to Liquid and Solid Constitution. *Adv. Chem. Ser.* **1964**, *43*, 1−51.
(87) Petke, D. F.; Ray, R. B. Temperature Dependence of Contact Angles of Liquids on Polymeric Solids. *J. Colloid Interface Sci.* **1969**, *31* (2), 216−227.
(88) Nilsson, M.; Trägårdh, G.; Östergren, K. The Influence of PH, Salt and Temperature on Nanofiltration Performance. *J. Membr. Sci.* **2008**, *312* (1−2), 97−106.
(89) Kasemset, S.; He, Z.; Miller, D. J.; Freeman, B. D.; Sharma, M. M. Effect of Polydopamine Deposition Conditions on Polysulfone Ultrafiltration Membrane Properties and Threshold Flux during Oil/Water Emulsion Filtration. *Polymer* **2016**, *97*, 247−257.
(90) Kudin, K. N.; Car, R. Why Are Water-Hydrophobic Interfaces Charged? *J. Am. Chem. Soc.* **2008**, *130* (12), 3915−3919.
(91) Seo, Y.; Jhe, W. Atomic Force Microscopy and Spectroscopy. *Rep. Prog. Phys.* **2008**, *71* (1), 016101.
(92) Thewes, N.; Thewes, A.; Loskill, P.; Peisker, H.; Bischoff, M.; Herrmann, M.; Santen, L.; Jacobs, K. Stochastic Binding of Staphylococcus Aureus to Hydrophobic Surfaces. *Soft Matter* **2015**, *11* (46), 8913−8919.
(93) Lee, S.; Elimelech, M. Relating Organic Fouling of Reverse Osmosis Membranes to Intermolecular Adhesion Forces. *Environ. Sci. Technol.* **2006**, *40* (3), 980−987.
(94) Kocun, M.; Grandbois, M.; Cuccia, L. A. Single Molecule Atomic Force Microscopy and Force Spectroscopy of Chitosan. *Colloids Surf., B* **2011**, *82* (2), 470−476.
(95) Stock, P.; Utzig, T.; Valtiner, M. Direct and Quantitative AFM Measurements of the Concentration and Temperature Dependence of the Hydrophobic Force Law at Nanoscopic Contacts. *J. Colloid Interface Sci.* **2015**, *446*, 244−251.
(96) Dallin, B. C.; Yeon, H.; Ostwalt, A. R.; Abbott, N. L.; Van Lehn, R. C. Molecular Order Affects Interfacial Water Structure and Temperature-Dependent Hydrophobic Interactions between Nonpolar Self-Assembled Monolayers. *Langmuir* **2019**, *35* (6), 2078−2088.
(97) Huang, D. M.; Chandler, D. Temperature and Length Scale Dependence of Hydrophobic Effects and Their Possible Implications for Protein Folding. *Proc. Natl. Acad. Sci. U. S. A.* **2000**, *97* (15), 8324−8327.
(98) Stillinger, F. H. Structure in Aqueous Solutions of Nonpolar Solutes from the Standpoint of Scaled-Particle Theory. *J. Solution Chem.* **1973**, *2* (2−3), 141−158.
(99) Huang, D. M.; Geissler, P. L.; Chandler, D. Scaling of Hydrophobic Solvation Free Energies. *J. Phys. Chem. B* **2001**, *105* (28), 6704−6709.
(100) Elimelech, M.; Childress, A. E. *Zeta Potential of Reverse Osmosis Membranes: Implications for Membrane Performance*; National Technical Reports Library: 1996.
(101) Jermann, D.; Pronk, W.; Meylan, S.; Boller, M. Interplay of Different NOM Fouling Mechanisms during Ultrafiltration for Drinking Water Production. *Water Res.* **2007**, *41* (8), 1713−1722.
(102) Mehdizadeh, H.; Dickson, J. M.; Eriksson, P. K. Temperature Effects on the Performance of Thin-Film Composite, Aromatic Polyamide Membranes. *Ind. Eng. Chem. Res.* **1989**, *28* (6), 814−824.
(103) Madaeni, S. S.; Mansourpanah, Y. Chemical Cleaning of Reverse Osmosis Membranes Fouled by Whey. *Desalination* **2004**, *161* (1), 13−24.
(104) Karan, S.; Jiang, Z.; Livingston, A. G. Sub-10 Nm Polyamide Nanofilms with Ultrafast Solvent Transport for Molecular Separation. *Science (Washington, DC, U. S.)* **2015**, *348* (6241), 1347−1351.

https://dx.doi.org/10.1021/acsestengg.0c00258
ACS EST Engg. XXXX, XXX, XXX−XXX

(105) Fujioka, T.; Oshima, N.; Suzuki, R.; Price, W. E.; Nghiem, L. D. Probing the Internal Structure of Reverse Osmosis Membranes by Positron Annihilation Spectroscopy: Gaining More Insight into the Transport of Water and Small Solutes. *J. Membr. Sci.* **2015**, *486*, 106−118.
(106) Goh, P. S.; Lau, W. J.; Othman, M. H. D.; Ismail, A. F. Membrane Fouling in Desalination and Its Mitigation Strategies. *Desalination* **2018**, *425*, 130−155.
(107) Liu, J.; Huang, T.; Ji, R.; Wang, Z.; Tang, C. Y.; Leckie, J. O. Stochastic Collision-Attachment-Based Monte Carlo Simulation of Colloidal Fouling: Transition from Foulant-Clean-Membrane Interaction to Foulant-Fouled-Membrane Interaction. *Environ. Sci. Technol.* **2020**, *54* (19), 12703−12712.
(108) Henis, J. M. S.; Tripodi, M. K. Composite Hollow Fiber Membranes for Gas Separation: The Resistance Model Approach. *J. Membr. Sci.* **1981**, *8* (3), 233−246.
(109) Sagle, A. C.; Van Wagner, E. M.; Ju, H.; McCloskey, B. D.; Freeman, B. D.; Sharma, M. M. PEG-Coated Reverse Osmosis Membranes: Desalination Properties and Fouling Resistance. *J. Membr. Sci.* **2009**, *340*, 92.
(110) Ang, W. S.; Tiraferri, A.; Chen, K. L.; Elimelech, M. Fouling and Cleaning of RO Membranes Fouled by Mixtures of Organic Foulants Simulating Wastewater Effluent. *J. Membr. Sci.* **2011**, *376* (1−2), 196−206.
(111) Torres, M. L.; Fernandez, J. M.; Dellatorre, F. G.; Cortizo, A. M.; Oberti, T. G. Purification of Alginate Improves Its Biocompatibility and Eliminates Cytotoxicity in Matrix for Bone Tissue Engineering. *Algal Res.* **2019**, *40*, 101499.

https://dx.doi.org/10.1021/acsestengg.0c00258
ACS EST Engg. XXXX, XXX, XXX−XXX

Feed Temperature Effects on Organic Fouling of Reverse Osmosis Membranes: Competition of Interfacial and Transport Properties

Supporting Information

Sara BinAhmed[1], Raymond M. Hozalski[1], Santiago Romero-Vargas Castrillón[1,2,3,*]

Journal: ACS ES&T Engineering

[1] Department of Civil, Environmental, and Geo- Engineering, University of Minnesota, Minneapolis, MN 55455, USA

[2] Institute for Infrastructure and Environment, School of Engineering, The University of Edinburgh, William Rankine Building, Thomas Bayes Road, Edinburgh EH9 3FG United Kingdom

[3] Institute for Materials and Processes, School of Engineering, The University of Edinburgh, Sanderson Building, Robert Stevenson Road, Edinburgh EH9 3FB United Kingdom

Contents: 17 pages, including 9 figures and 1 table

*Corresponding author:
Santiago@ed.ac.uk, sromerov@umn.edu. Tel: +44(0)131 651 3567

Supporting Materials and Methods

S.1. Reverse osmosis setup, membrane transport properties and fouling experiments

Reverse osmosis setup. We conducted fouling experiments in a laboratory-scale membrane filtration system comprising a crossflow cell (CF042D, Sterlitech, Kent, WA) with 42-cm^2 active membrane area and a 20-L stainless steel feed tank. The feed temperature was set by a portable chiller (6500 series, Polyscience) equipped with a heat exchange coil immersed in the feed tank. A high-pressure pump (HydraCell M-03S, Wanner Engineering, Minneapolis, MN) circulated the feed solution. The permeate flowrate was recorded with a digital flow meter (SLI-2000, Sensirion, Stäfa, Switzerland) and logged to a computer every 0.2 s. The system was operated in closed-loop mode, recycling the permeate and retentate streams to the feed tank.

Determination of membrane permeance to water. Membranes were compacted with an ultrapure (UP) water (18.2 MΩ cm, Barnstead) feed at 500-580 psi and 25 ˚C until a steady-state permeate flux was observed (typically within ~60 hours). Next, the transmembrane pressure difference was adjusted so that the permeate flux was 20 ± 1 L m^{-2} h^{-1} (LMH), typical of wastewater reclamation by RO,[1,2] at 15.8 cm s^{-1} crossflow velocity. At this stage, the water permeance at 25 °C ($A_{w,25}$) was calculated. Next, the chiller settings were adjusted to maintain the feed at the desired temperature, T = 27, 35, or 40 ˚C, and the pressure difference ($\Delta p_{w,T}$) was reduced to maintain a pure water flux of $J_{w,T}$ = 20 ± 1 LMH at the corresponding temperature T. The system was run overnight to reach steady-state operation at T, after which the water permeance at T ($A_{w,T}$) was calculated using $A_{w,T} = J_{w,T} / \Delta p_{w,T}$.

Fouling experiments. To begin the fouling experiment, the pure water feed was replaced with foulant-free synthetic wastewater (SWW) with the following composition: 0.45 mM KH_2PO_4, 0.935 mM NH_4Cl, 0.5 mM $CaCl_2$, 0.5 mM $NaHCO_3$, 9.20 mM NaCl, and 0.61 mM $MgSO_4$.[3,4] This synthetic wastewater recipe is representative of secondary effluent in certain wastewater treatment plants in California. The system was again allowed to reach steady state at feed temperature T = 27, 35, or 40 ˚C and a baseline permeate flux J = 20 ± 1 LMH. The conductivity of feed and permeate was measured using a conductivity meter with automatic temperature compensation (WD-35604-00, Con 6+ Meter, Oakton) to determine the conductivity rejection coefficient.[4] Finally, the synthetic wastewater feed was supplemented with sodium alginate (SA) foulant solution to initiate the accelerated fouling experiment at an alginate feed concentration of 250 mg L^{-1} while recording the permetate flow for 24 hours. Feed and permeate samples were collected 2 and 24 hours after the addition of alginate to determine conductivity and total organic carbon (TOC) rejection. TOC was measured using a Sievers 900 portable TOC analyzer (GE Analytical Instruments, Boulder, CO) that uses the 5310C National Environmental Methods Index (NEMI) standard method.[5] The feed was diluted 20× before analysis while the permeate was analyzed without dilution.

Fouling of Reverse Osmosis Membranes for Colloidal-Probe AFM. To perform adhesion force measurements over a fouled membrane, an alginate layer was deposited on a pristine membrane using a dead-end filtration cell (Amicon stirred cell 8010, Millipore). To this end, 3 mL of synthetic wastewater (SWW) prepared as described above, supplemented with 50 mg L^{-1} sodium alginate, was filtered through the membrane at 60 psi for 45 minutes.

S.2. Characterization of membrane interfacial properties

Contact angle: The wettability of pristine ESPA2-LD membranes as a function of temperature was evaluated in terms of water contact angle measurements using the sessile drop method. Desiccator-dried membrane coupons were attached to a glass slide using two-sided tape (Scotch®, 3M). A goniometer (DSA30S, Krüss) equipped with a temperature-controlled chamber (TC30) and temperature-controlled liquid dispenser (TC 3212) was used to measure the contact angle of 2-µL water droplets deposited on the membrane substrate. Right-hand-side and left-hand-side angles were determined from digital images using the proprietary ADVANCE software of the instrument for a total of 20 contact angle measurements at each temperature. Measurements were collected at least 15 minutes after both the chamber and UP water reached the set-point temperature (T = 27, 35, and 40 ºC). Contact angles were immediately recorded after the 2-µL water drop was deposited.

Roughness: The nanoscale surface roughness of pristine membranes was measured by tapping mode AFM in aqueous solution using an atomic force microscope (MFP-3D-Bio, Asylum Research) equipped with a temperature-controlled fluid cell. AFM scanning was performed in foulant-free synthetic wastewater (I = 14.7 mM, see section S.1 or 2.2) at 27, 35, and 40 ºC using SNL-10 probes (cantilever "C", nominal k = 0.24 N/m, f = 56 kHz, Bruker). The temperature of the fluid cell was increased from ambient to the target temperature T = 27, 35, or 40 °C (± 0.2 °C) at a rate of 1 ºC/min. After allowing the AFM to equilibrate at the target temperature for at least an hour, the cantilever resonance frequency was calibrated. Three 5 × 5-µm^2 scans were collected at each temperature at a 0.25 Hz scan rate, after which the root-mean-square (RMS) roughness (R_{RMS}) of 5 random 1 × 1-µm^2 subareas on each image were computed for a total of 15 R_{RMS} values.

Surface charge: An electrokinetic analyzer (SurPASS, Anton Paar) was used to measure the streaming potential of ESPA2 membranes in a 1 mM KCl background electrolyte solution. Two 10 × 20-mm^2 membrane coupons were attached to sample holders of an adjustable gap cell. The electrolyte solution was maintained at a constant temperature (monitored using a thermocouple connected to the electrokinetic analyzer) by placing the solution on a heating stir plate. The zeta potential was calculated from the streaming potential using the Smoluchowski-Helmholtz equation. Prior to the measurements, an instrument validation run was carried out using a cotton cloth (~ 4 × 4 cm^2) following a protocol provided by the manufacturer. Streaming potential data were collected over the pH range 4-10 by addition of aliquots of 0.05 mM NaOH or HCl. Duplicates at each temperature were analyzed. Additional details of zeta potential measurements can be found in our previous work.[6–8]

S.3. Calculation of permeate drag force

The approach loading force (also known as trigger force, Figure S3) exerted on the colloidal probe during AFM force measurements was set to a value representative of the drag force (F_D) exerted on a colloidal particle during membrane filtration. The permeate drag force (F_D) was calculated following the analysis by Goren[9], where the resistance to the approach of a sphere is affected by the permeability of the membrane (considered as a permeable wall).

Goren's analysis[9] leads to the following expression for the permeate drag force,

$$F_D = -6\pi\mu a_p J \Phi_H \qquad \text{(S.1)}$$

where F_D is the permeate drag force (N), and the negative sign indicates that the force is normal to and directed toward the surface of the membrane[10]; μ is the dynamic viscosity of water (kg m^{-1} s^{-1}); a_p is the colloidal probe radius (m); J is the permeate water flux (m s^{-1}); and Φ_H is a hydrodynamic correction factor to Stokes drag force.[9,10]

The hydrodynamic resistance to the particle motion toward the membrane decreases with increasing permeability. When the particle is in contact with the permeable wall, the hydrodynamic correction factor is given by Goren[9] as,

$$\Phi_H = \left(\frac{2R_m a_p}{3}\right)^{\frac{1}{2}} \qquad \text{(S.2)}$$

where $R_m = \frac{\Delta p}{\mu J}$ is the membrane hydraulic resistance (m^{-1}), and Δp is the transmembrane pressure difference (Pa),

The value of R_m of ESPA2-LD RO membranes was determined experimentally in a laboratory-scale crossflow RO setup operating at a pure water flux $J = 20 \pm 1$ LMH and 25 ˚C. Three membrane specimens were thus characterized. Flux and corresponding transmembrane pressure values are shown in Table S1. R_m was calculated for each membrane specimen; the resulting values were within the range of typical RO resistance values (5×10^{13} - 1×10^{15} m^{-1}).[11] Using a_p = 2 μm (the radius of the CML particle), Φ_H was calculated using equation S.2 and used to find the drag force from S.1.

Table S1: Experimentally determined pure water flux (J_w), calculated membrane resistance (R_m) and permeate drag force (F_D).

Δp (bar)	**J_w (LMH)**	**R_m (m^{-1})**	**Hydrodynamic Correction Factor Φ_H**	**F_D (nN)**
4.34	20.1	8.73×10^{13}	1.08×10^{4}	2.02
4.83	20.0	9.77×10^{13}	1.14×10^{4}	2.13
4.27	19.6	8.81×10^{13}	1.08×10^{4}	1.98
Average				2.04

S.4. Estimation of the foulant layer thickness and mass of adsorbed alginate

We computed an order-of-magnitude estimate of the mass of alginate adsorbed on the polyamide layer as follows.

The hydraulic resistance due to the foulant (R_f) calculated from our experimental data at 27 °C, under which the most severe fouling is observed, is 0.14 bar L^{-1} m^2 h (140 bar m^{-1} h). This is related to the permeability (P_f) and thickness (l_f) of the alginate film through[12]

$$R_f = \frac{l_f}{P_f} \qquad \text{(R.1)}$$

Olivas et al.[13] reported values of $P_f \sim O(10^{-9})$ g m^{-1} s^{-1} Pa^{-1} = $O(10^{-7})$ m^2 h^{-1} bar^{-1} for the permeability of water vapor in alginate films. Using this value to solve for l_f we obtain,

l_f = (140 bar m^{-1} h)(10^{-7} m^2 h^{-1} bar^{-1}) ~ $O(10^{-5})$ m = 10 μm

This estimate agrees with the thickness of alginate foulant layers ($O(10)$ μm) following RO filtration reported by Xie et al.[14]

Finally, we can estimate the mass of adsorbed alginate (m_f) using the value reported by Kube et al.[15] for the density of alginate (ρ_f = 0.8755 g cm^{-3}),

$m_f = \rho_f l_f A_f \approx$ (0.8755 g cm^{-3})(10^{-3} cm)(42 cm^2) = 0.037 g = 37 mg

, where A_f was assumed to be equal to the projected surface area of the membrane (i.e., we assumed complete coverage of the membrane coupon by alginate). Xie et al.[14] reported a *surface* density of alginate foulant layers on RO membranes of ≈ 0.7 mg cm^{-2}; using the same surface area as in our system, this yields an adsorbed mass of alginate of ≈ 30 mg, in good agreement with our estimate based on l_f and ρ_f.

These calculations show that the mass of adsorbed alginate is ca. 3% of the mass of alginate available in the bulk solution (i.e., 0.25 g L^{-1} × 4 L = 1 g). We therefore conclude that the slow-down of the rate of fouling is not due to a lower concentration of foulant in the feed. Rather, the decreasing rate of flux loss results from weakly adhesive or repulsive foulant-foulant interactions (Figure 3).

Supporting Results

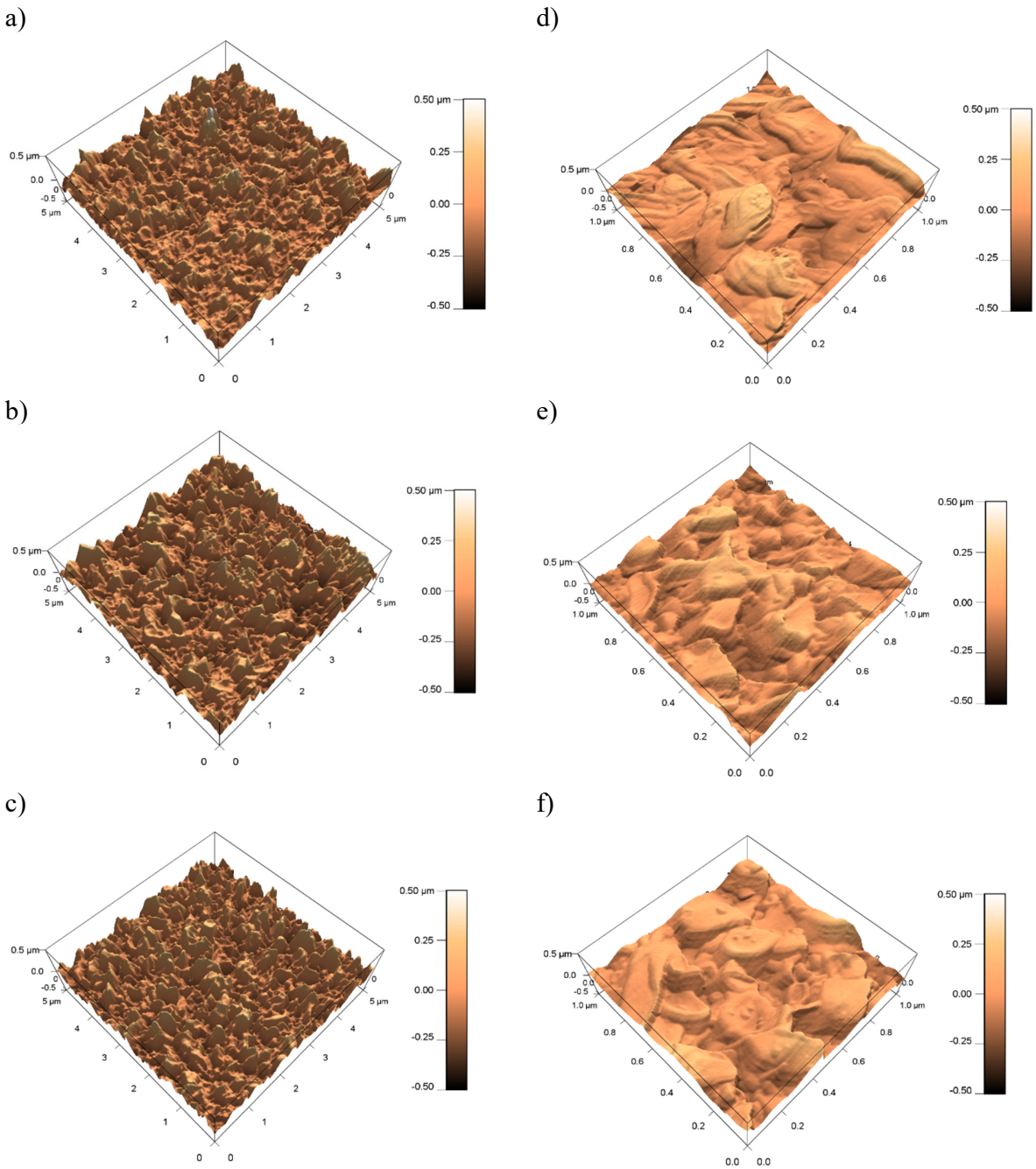

Figure S1: Tapping mode AFM images of pristine ESPA2-LD membranes scanned in foulant-free synthetic wastewater (pH 7.4; I = 14.7 mM) at 27 °C (a, d), 35 °C (b, e), and 40 °C (c, f). Left column: 5 × 5 µm^2 scan area. Right column: 1 × 1 µm^2 scan area.

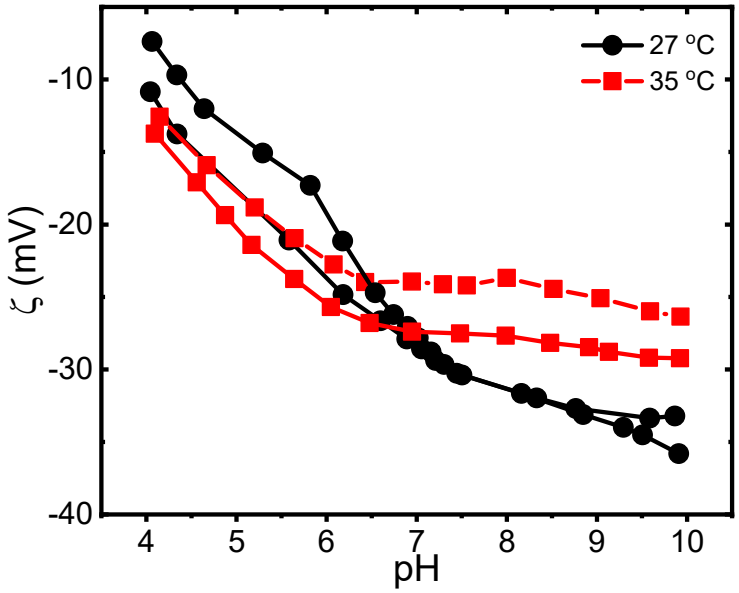

Figure S2: Zeta potential (ζ) of pristine ESPA2-LD membranes at 27 °C and 35 °C determined in 1 mM KCl solution. Duplicates are shown at each temperature.

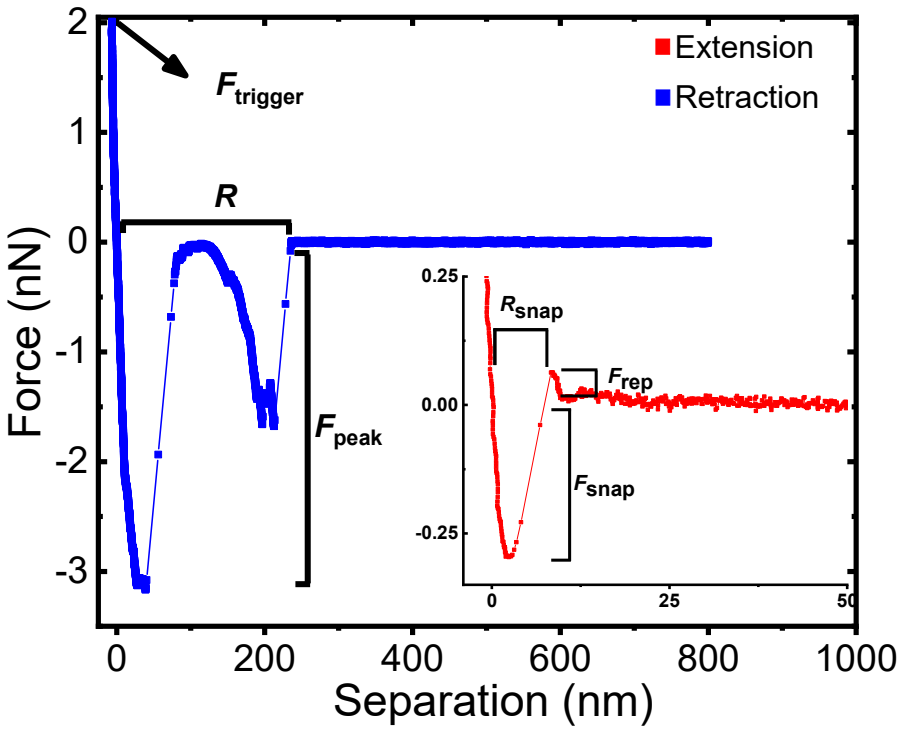

Figure S3: Representative retraction force curve and approach force curve (shown in the inset) of a CML colloidal probe on a pristine ESPA2-LD membrane at 27 °C. Data were collected in synthetic wastewater supplemented with 20 mg L^{-1} sodium alginate ($t_{contact}$ = 5 s; $F_{trigger}$ = 2 nN; pH 7.4; I = 14.7 mM). The curve shows the definition of the peak adhesion force (F_{peak}), snap-in force (F_{snap}), trigger force ($F_{trigger}$), rupture separation (R), snap-in separation (R_{snap}), and repulsive force (F_{rep}). The units of the x- and y-axes in the inset are nm and nN, respectively.

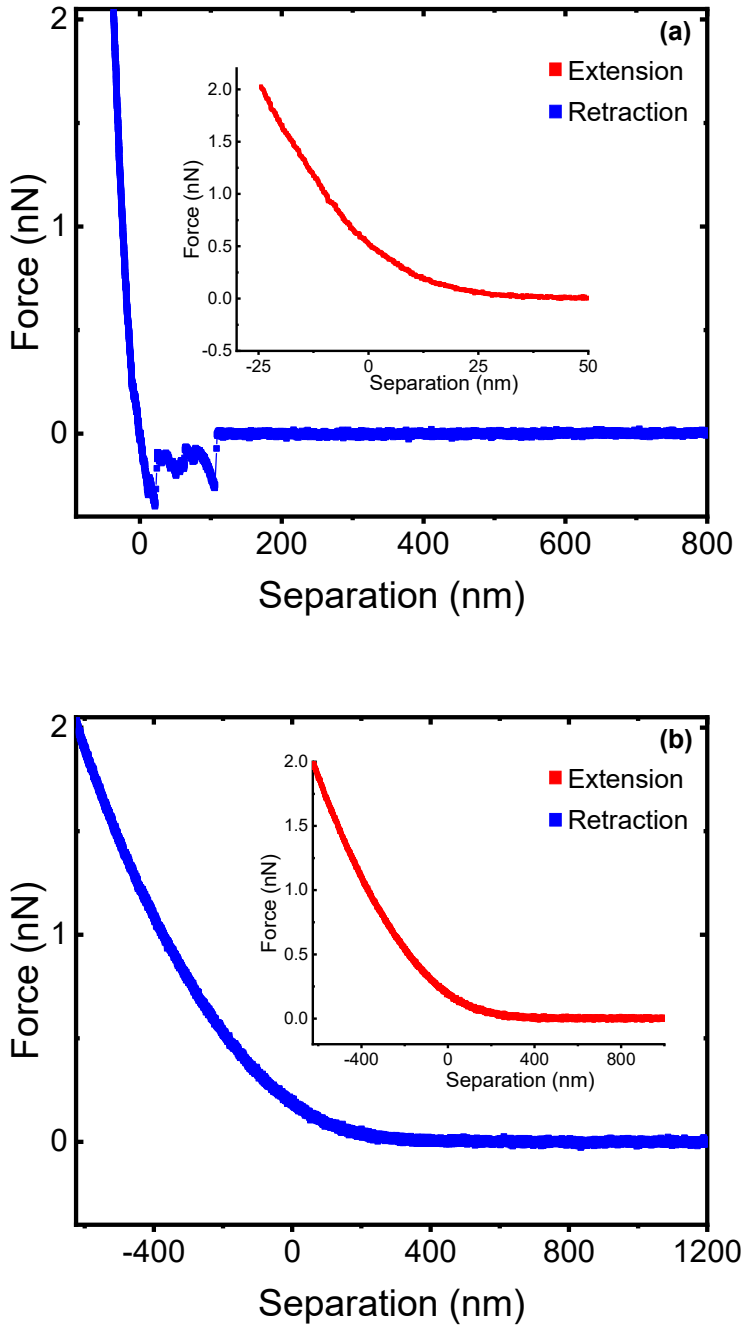

Figure S4: Representative retraction and approach force curves (the latter shown in the inset) of a CML colloidal probe on an alginate-fouled ESPA2-LD membrane at 27 °C. Panel (a) shows a typical force curve exhibiting repulsive interactions during extension, and weak adhesion during retraction. Panel (b) shows the case of repulsive interactions during extension and retraction. Data were collected in synthetic wastewater supplemented with 20 mg L^{-1} sodium alginate ($t_{contact}$ = 5 s; $F_{trigger}$ = 2 nN; pH 7.4; I = 14.7 mM).

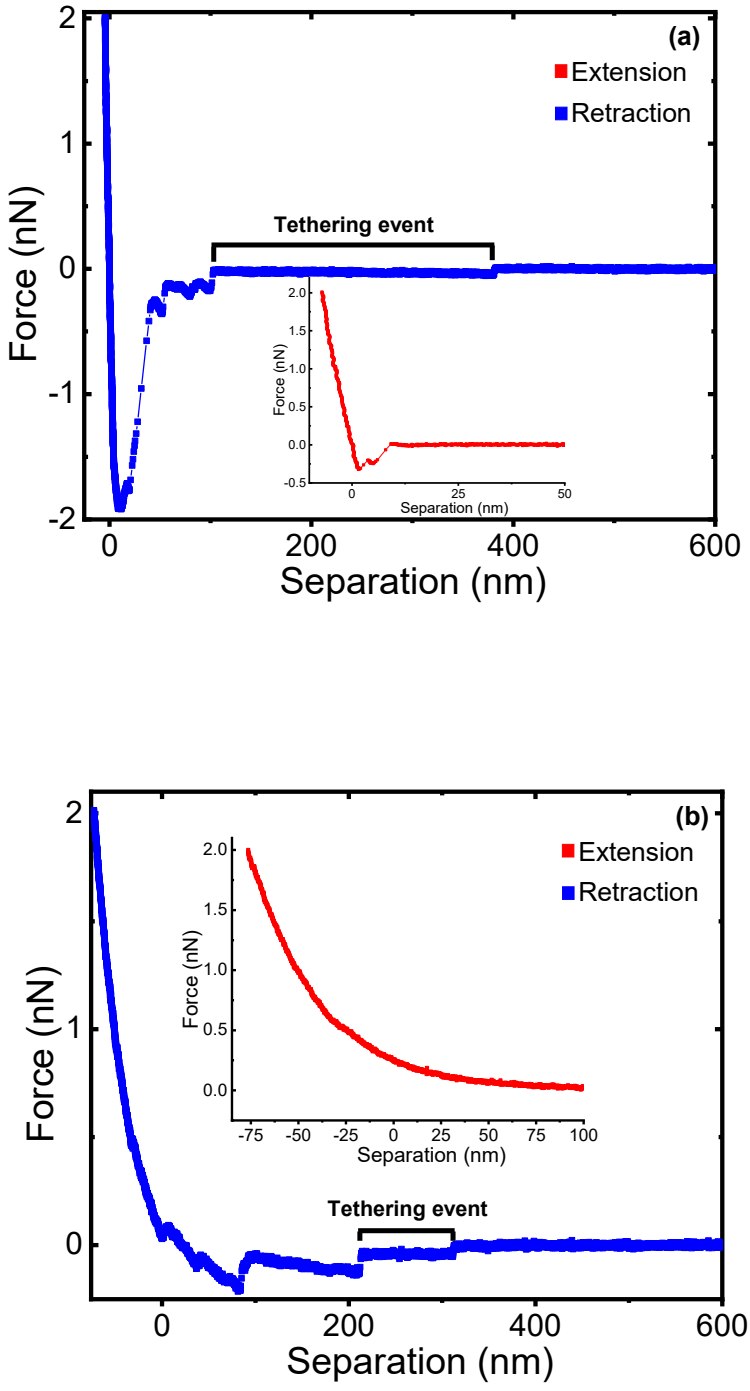

Figure S5: Representative retraction force curve exhibiting a tethering event during adhesion of a CML colloidal probe at 27 °C on an ESPA2-LD (a) pristine and (b) alginate-fouled membrane (approach force curves shown in the inset). Data were collected in synthetic wastewater supplemented with 20 mg L^{-1} sodium alginate ($t_{contact}$ = 5 s; $F_{trigger}$ = 2 nN; pH 7.4; I = 14.7 mM).

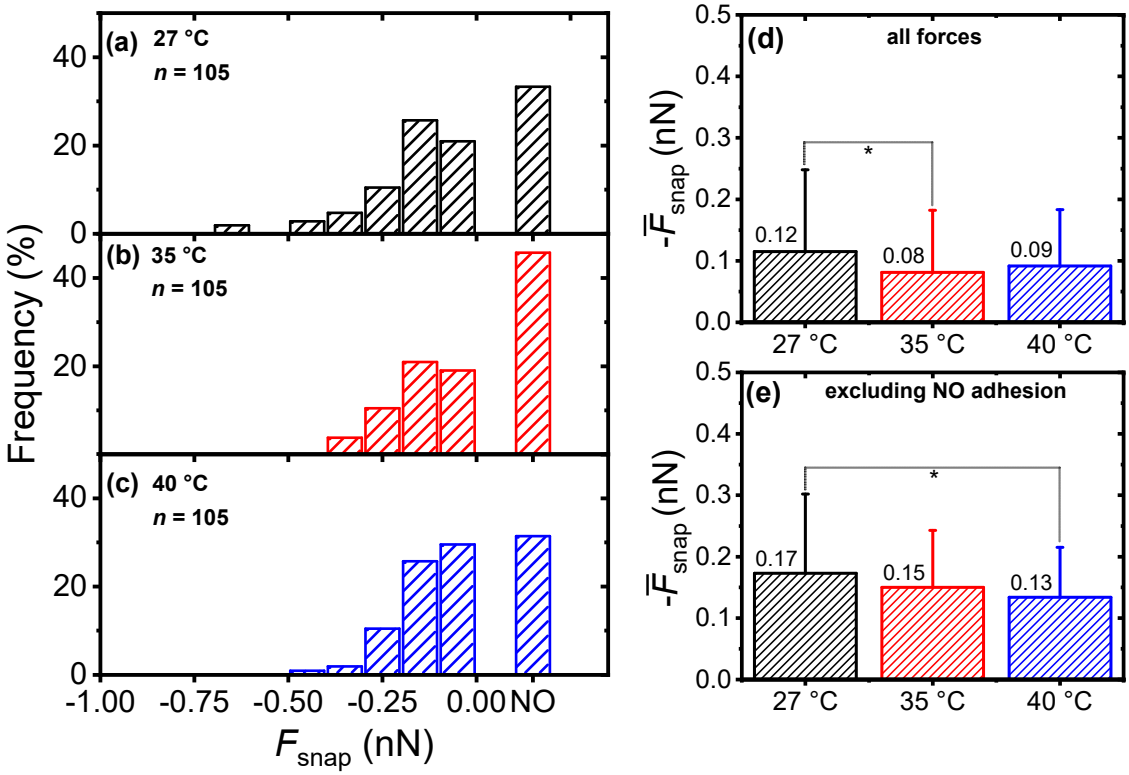

Figure S6: (a-c) Distribution of snap-in forces during adhesion of a CML colloidal probe to pristine ESPA2-LD membranes for each indicated temperature (given in the inset along with the number of force measurements, *n*). Force curves in which snap-in events were not detected are tallied as the "NO" column. (d) Average snap-in force ($\bar{F}_{snap}$) at each temperature calculated from (a-c) including the non-adhesive (i.e., purely repulsive approach) events as $\bar{F}_{snap} = 0$ (* denotes statistical significance with $p < 0.05$). (e) Average snap-in force ($\bar{F}_{snap}$) at each temperature calculated from (a-c) excluding the non-adhesive events (* denotes statistical significance with $p < 0.05$). Error bars denote one standard deviation. Data were collected in synthetic wastewater supplemented with 20 mg L^{-1} sodium alginate ($t_{contact}$ = 5 s; $F_{trigger}$ = 2 nN; pH 7.4; I = 14.7 mM).

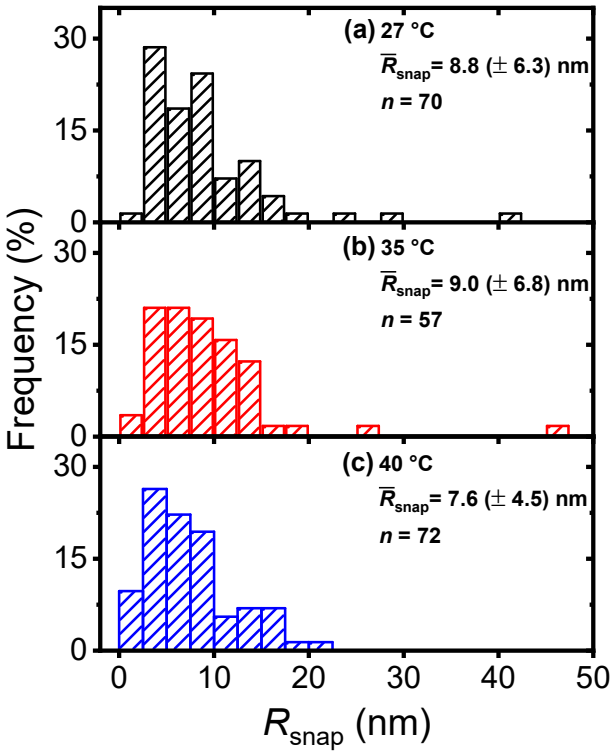

Figure S7: Distribution of snap-in distances (R_{snap}) during adhesion of a CML colloidal probe to pristine ESPA2-LD membranes. Data were collected in synthetic wastewater supplemented with 20 mg L^{-1} sodium alginate at each indicated temperature (given in the inset along with the number of measurements (n) and average snap-in distance $\bar{R}_{snap}$ (± standard deviation)). Other experimental details: $t_{contact}$ = 5 s; $F_{trigger}$ = 2 nN; pH 7.4; I =14.7 mM. Average snap-in distances are similar at all temperatures ($p > 0.05$ for all pairwise comparisons).

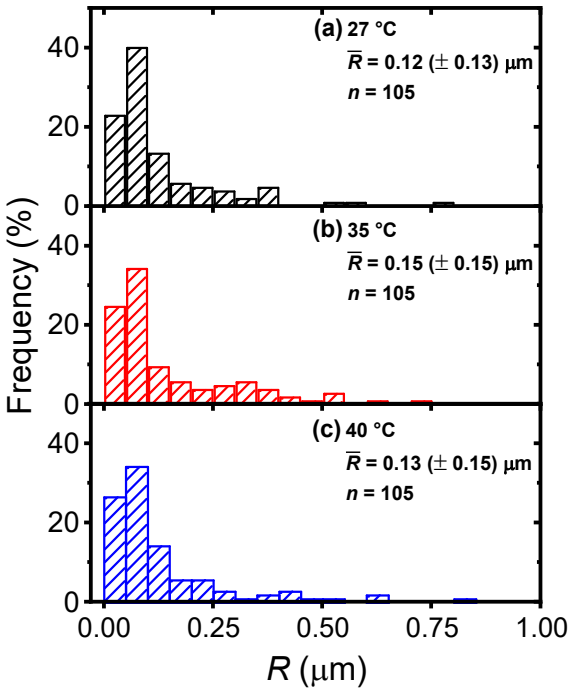

Figure S8: Distribution of rupture separations (R) during adhesion of a CML colloidal probe to pristine ESPA2-LD membranes. Data were collected in synthetic wastewater supplemented with 20 mg L^{-1} sodium alginate at each indicated temperature (given in the inset along with the number of measurements (n) and average rupture separation $\bar{R}$ (± standard deviation)). Other experimental details: $t_{contact}$ = 5 s; $F_{trigger}$ = 2 nN; pH 7.4; I =14.7 mM. Average rupture separations are similar at all temperatures ($p > 0.05$ for all pairwise comparisons).

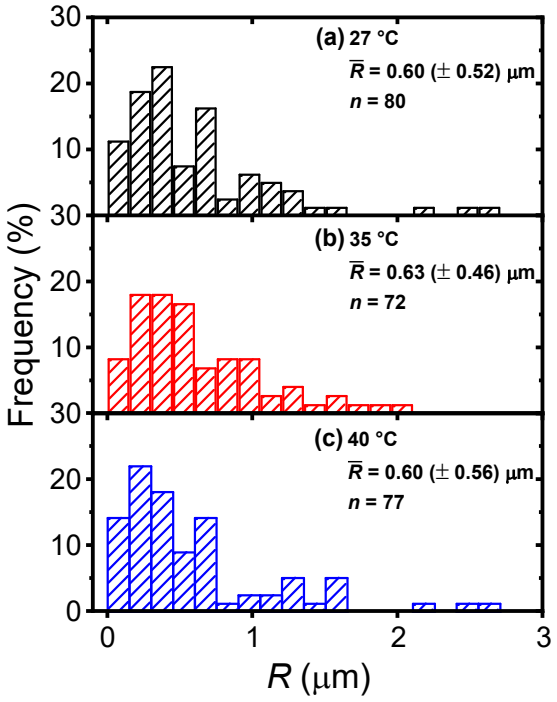

Figure S9: Distribution of rupture separations (R) during adhesion of a CML colloidal probe to alginate-fouled ESPA2-LD membranes. Data were collected in synthetic wastewater supplemented with 20 mg L^{-1} sodium alginate at each indicated temperature (given in the inset along with the number of measurements (n) and average rupture separation $\bar{R}$ (± standard deviation)). Other experimental details: $t_{contact}$ = 5 s; $F_{trigger}$ = 2 nN; pH 7.4; I =14.7 mM. Average rupture separations are similar at all temperatures ($p > 0.05$ for all pairwise comparisons).

References

(1) Fujioka, T.; Khan, S. J.; McDonald, J. A.; Henderson, R. K.; Poussade, Y.; Drewes, J. E.; Nghiem, L. D. Effects of Membrane Fouling on N-Nitrosamine Rejection by Nanofiltration and Reverse Osmosis Membranes. *J. Memb. Sci.* **2013**, *427*, 311–319. https://doi.org/10.1016/j.memsci.2012.09.055.

(2) Fujioka, T.; Khan, S. J.; McDonald, J. A.; Roux, A.; Poussade, Y.; Drewes, J. E.; Nghiem, L. D. N-Nitrosamine Rejection by Reverse Osmosis: Effects of Membrane Exposure to Chemical Cleaning Reagents. *Desalination* **2014**, *343*, 60–66. https://doi.org/10.1016/j.desal.2013.10.032.

(3) Tiraferri, A.; Kang, Y.; Giannelis, E. P.; Elimelech, M. Superhydrophilic Thin-Film Composite Forward Osmosis Membranes for Organic Fouling Control: Fouling Behavior and Antifouling Mechanisms. *Environ. Sci. Technol.* **2012**, *46* (20), 11135–11144. https://doi.org/10.1021/es3028617.

(4) Herzberg, M.; Elimelech, M. Biofouling of Reverse Osmosis Membranes: Role of Biofilm-Enhanced Osmotic Pressure. *J. Memb. Sci.* **2007**, *295* (1–2), 11–20. https://doi.org/10.1016/j.memsci.2007.02.024.

(5) *Standard Methods for the Examination of Water and Wastewater*, 22nd ed.; Rice, E. W., Baird, R. B., Eaton, A. D., Clesceri, L. S., Eds.; American Public Health Association, American Water Works Association, Water Environment Federation, 2012.

(6) Xue, J.; BinAhmed, S.; Wang, Z.; Karp, N. G.; Stottrup, B. L.; Romero-Vargas Castrillón, S. Bacterial Adhesion to Graphene Oxide (GO)-Functionalized Interfaces Is Determined by Hydrophobicity and GO Sheet Spatial Orientation. *Environ. Sci. Technol. Lett.* **2018**, *5* (1), 14–19. https://doi.org/10.1021/acs.estlett.7b00509.

(7) Binahmed, S.; Hasane, A.; Wang, Z.; Mansurov, A.; Romero-Vargas Castrillón, S. Bacterial Adhesion to Ultrafiltration Membranes: Role of Hydrophilicity, Natural Organic Matter, and Cell-Surface Macromolecules. *Environ. Sci. Technol.* **2018**, *52* (1), 162–172. https://doi.org/10.1021/acs.est.7b03682.

(8) Wuolo-Journey, K.; Binahmed, S.; Linna, E.; Romero-Vargas Castrillón, S. Do Graphene Oxide Nanostructured Coatings Mitigate Bacterial Adhesion? *Environ. Sci. Nano* **2019**, *6* (9), 2863–2875. https://doi.org/10.1039/c9en00499h.

(9) Goren, S. L. The Hydrodynamic Force Resisting the Approach of a Sphere to a Plane Permeable Wall. *Colloid Interface Sci.* **1979**, *69* (1), 78–85.

(10) Kang, S.; Subramani, A.; Hoek, E.; Deshusses, M.; Matsumoto, M. Direct Observation of Biofouling in Cross-Flow Microfiltration: Mechanisms of Deposition and Release. *J. Memb. Sci.* **2004**, *244* (1–2), 151–165. https://doi.org/10.1016/j.memsci.2004.07.011.

(11) Benjamin, M. M.; Lawler, D. F. Membrane Processes. In *Water Quality Engineering Physical/Chemical Treatment Processes*; John Wiley & Sons, Inc.: Hoboken, NJ, 2013; pp 731–845.

(12) Sagle, A. C.; Van Wagner, E. M.; Ju, H.; McCloskey, B. D.; Freeman, B. D.; Sharma, M. M. PEG-Coated Reverse Osmosis Membranes: Desalination Properties and Fouling Resistance. *J. Memb. Sci.* **2009**. https://doi.org/10.1016/j.memsci.2009.05.013.

(13) Olivas, G. I.; Barbosa-Cánovas, G. V. Alginate-Calcium Films: Water Vapor Permeability and Mechanical Properties as Affected by Plasticizer and Relative Humidity. *LWT - Food Sci. Technol.* **2008**, *41* (2), 359–366. https://doi.org/10.1016/j.lwt.2007.02.015.

(14) Xie, M.; Lee, J.; Nghiem, L. D.; Elimelech, M. Role of Pressure in Organic Fouling in Forward Osmosis and Reverse Osmosis. *J. Memb. Sci.* **2015**, *493*, 748–754.

https://doi.org/10.1016/j.memsci.2015.07.033.
(15) Kube, M.; Mohseni, A.; Fan, L.; Roddick, F. Impact of Alginate Selection for Wastewater Treatment by Immobilised Chlorella Vulgaris. *Chem. Eng. J.* **2019**, *358*, 1601–1609. https://doi.org/10.1016/j.cej.2018.10.065.

Environmental Science Nano

PAPER

View Article Online
View Journal | View Issue

Cite this: *Environ. Sci.: Nano*, 2019, **6**, 2863

Do graphene oxide nanostructured coatings mitigate bacterial adhesion?†

Karl Wuolo-Journey,‡[a] Sara BinAhmed, ‡[a] Elise Linna[a] and Santiago Romero-Vargas Castrillón *[abc]

Given its potent biocidal properties, graphene oxide (GO) holds promise as a building block of antimicrobial surfaces, with numerous potential environmental applications. Nonetheless, the extent to which GO-based coatings decrease bacterial adhesion propensity, a necessary requirement of low-fouling surfaces, remains unclear. Here we use AFM-based single-cell force spectroscopy (SCFS) to show that coatings comprising GO nanosheets bonded to a hydrophilic polymer brush mitigate adhesion of *Pseudomonas fluorescens* cells. We demonstrate low-adhesion GO coatings by grafting poly(acrylic acid) (PAA) to polyethersulfone (PES) substrates *via* self-initiated UV polymerization, followed by edge-tethering of GO to the PAA chains through amine coupling. We characterize the chemistry and interfacial properties of the unmodified PES, PAA-modified (PES–PAA), and GO-modified (PES–GO) substrates using ATR-FTIR, Raman spectroscopy, contact angle goniometry, and AFM to confirm the presence of PAA and covalently bonded GO on the substrates. Using SCFS we show that peak adhesion force distributions for PES–PAA (with mean adhesion force $\bar{F}_{Peak}$ = −0.13 nN) and PES–GO ($\bar{F}_{Peak}$ = −0.11 nN) substrates are skewed towards weaker values compared to the PES control ($\bar{F}_{Peak}$ = −0.18 nN). Our results show that weaker adhesion on PES–GO is due to a higher incidence of non-adhesive (repulsive) forces (45.9% compared to 22.2% over PES–PAA and 32.3% over PES), which result from steric repulsion afforded by the brush-like GO–PAA interface. Lastly, we show that attachment to the various substrates is due to interactions of proteinaceous adhesins whose force response is well described by the worm-like chain model of polymer elasticity.

Received 2nd May 2019,
Accepted 25th July 2019

DOI: 10.1039/c9en00499h

rsc.li/es-nano

Environmental significance

While surface functionalization with graphene oxide (GO) is effective in bacterial inactivation, the modification of interfacial properties due to the nanomaterial coating may in fact increase the bioadhesion (and biofouling) propensity of a substrate. GO is biocidal; is it also anti-adhesive? Here we address this question using AFM-based bacterial adhesion force measurements. We show that coatings displaying low-bioadhesion properties can be formed by binding GO nanosheets to a hydrophilic polymer brush. Our work indicates that the underlying polymer layer enables a brush-like GO coating, which mitigates bacterial adhesion through steric repulsive forces. Conformational disorder (afforded by the polymer brush) is thus an important design variable for environmental interfaces (membranes, sorbents) seeking to exploit the antimicrobial properties of GO.

1. Introduction

The discovery of graphenic nanomaterials (GNMs, such as graphene, graphene oxide and reduced graphene oxide)[1] in 2004 unleashed a scientific revolution due to their unique physical and chemical properties, leading to numerous potential applications in water treatment and wastewater reuse.[2] The high specific surface area (~2630 $m^2\ g^{-1}$)[3] and single-atom-thickness of GNMs could enable them as membrane materials[4–6] and adsorbents for the removal of water contaminants.[7] Moreover, the thermal properties displayed by graphene (*i.e.*, its ability to harvest sunlight and increase the local temperature above the boiling point of water[8]), and graphene's high electron mobility (up to 2×10^5 $cm^2\ V^{-1}\ s^{-1}$),[3] could enable electrochemical and solar-driven water purification and disinfection.

The specific application addressed by the present work concerns graphene oxide (GO)-based biocidal coatings.[9,10] Given their wide-spectrum antimicrobial activity,[11–14] GO nanosheets are being explored as building blocks of

[a] *Department of Civil, Environmental, and Geo- Engineering, University of Minnesota, 500 Pillsbury Dr. SE, Minneapolis, MN 55455, USA. E-mail: Santiago@ed.ac.uk, sromerov@umn.edu; Tel: +44(0)131 651 3567*
[b] *Institute for Infrastructure and Environment, School of Engineering, The University of Edinburgh, William Rankine Building, Thomas Bayes Road, Edinburgh, EH9 3FG UK*
[c] *Institute for Materials and Processes, School of Engineering, The University of Edinburgh, Sanderson Building, Robert Stevenson Road, Edinburgh, EH9 3FB UK*

† Electronic supplementary information (ESI) available. See DOI: 10.1039/c9en00499h

‡ These authors contributed equally to this work.

antimicrobial surfaces, aiming to inactivate water-borne bacteria and mitigate biofilm formation. In recent studies, GO has been incorporated into the polymeric matrix of polyamide membranes,[15–18] or covalently bonded to membrane surfaces.[19,20] Nevertheless, the underlying mechanism of bacterial adhesion to GO-functionalized interfaces—the crucial first step of biofilm formation[21]—continues to be poorly understood. Moreover, recent studies have observed that GO functionalization of inorganic and polymeric substrates can increase their bio-adhesiveness.[22,23] The possible adverse modification of interfacial properties challenges the notion of GO films as anti-biofouling coatings. This question needs to be addressed since the effectiveness of GO as a biocidal nanomaterial will be compromised if it increases the adhesiveness of a given substrate *vis-à-vis* bacterial cells.

In a recent study,[22] we reported that the nanoscale morphology of GO coatings significantly influences bacterial adhesion, with edge-tethered GO showing weaker adhesion forces compared to immobilized layers of horizontally arranged GO nanosheets; spatial arrangement and conformational disorder of the GO building blocks thus seem essential to realize both biocidal activity and low adhesion propensity. Here, we investigate the extent to which GO coatings, comprising GO nanosheets edge-tethered to a polymer brush, are capable of mitigating bacterial adhesion. We surmise that the combination of hydrophilicity and conformational disorder afforded by the GO-functionalized polymer brush is essential to mitigate bioadhesion. To test this hypothesis, we use self-initiated UV polymerization of acrylic acid to graft poly(acrylic acid) (PAA) to polyethersulfone (PES) substrates, tethering GO nanosheets to the PAA chains. We then explore the interfacial properties of the GO coatings using atomic force microscopy (AFM)-based single-cell force spectroscopy,[24] whereby a single *Pseudomonas fluorescens* cell (a Gram-negative, biofilm-forming bacterium[25,26]) is immobilized on an AFM cantilever, enabling investigation of bacterial adhesion with nanoscale resolution. We show that microbial adhesion to GO-functionalized substrates is weakened compared to the GO-free control substrates. Consistent with our AFM results, bacterial deposition experiments show that GO-functionalized substrates mitigate adhesion under dynamic conditions. Characterization of the surface interfacial properties suggests that weaker adhesion on GO-modified substrates is a consequence of steric repulsive forces derived from the GO layer, edge-tethered to PAA brushes.

This paper is organized as follows. In section 2 we describe the substrate modification protocols, and the techniques employed to characterize interfacial properties. Results and discussion are given in section 3. We close with concluding remarks in section 4.

2. Materials and methods

GO functionalization

Substrates. All coatings investigated were formed on polyethersulfone (PES) substrates. To this end, commercially available PES ultrafiltration (UF) membranes were used (30 kDa molecular weight cutoff; Synder Filtration, Vacaville, USA). PES substrates were soaked in 50% glycerin solution and stored at 4 °C. Prior to use, substrates were rinsed with ultrapure (UP) water (18.2 MΩ cm, Barnstead, Thermo Fisher), soaked in 25 vol% aqueous isopropanol for 24 hours, and thoroughly rinsed again with UP water to remove residual preservatives.

Poly(acrylic acid) grafting. We used self-initiated UV graft polymerization to grow poly(acrylic acid) (PAA) on PES.[27–31] PAA chains were subsequently used to functionalize substrates with GO. A schematic diagram of the surface modification protocol is given in Fig. 1. An aqueous acrylic acid (AA) solution (10 vol%) was prepared from a 99% AA stock solution (Sigma Aldrich) with UP water. PES coupons (9 × 14 cm^2) were attached to PTFE frames with a holding volume of 112 mL. The PES substrates and the AA solution were brought to a glove box, from which oxygen had been purged to a concentration < 500 ppm. The solution and the substrates were left to equilibrate with the atmosphere inside the glove box for 15 minutes to lower the dissolved oxygen concentration in the AA monomer solution. Next, 10 vol% AA solution was poured over the PES (affixed to the PTFE frame) and allowed to soak the PES substrate. After 15 minutes, excess AA solution was removed, leaving a thin liquid film of AA monomer solution on the surface (Fig. 1 (a)). Ensuring that the monomer solution is cast as a thin film increases UV penetration depth, thus accelerating the polymerization kinetics on the substrate. Subsequently, the AA-soaked PES surface was irradiated with a UV lamp (Spectroline Model EF-160C) positioned ~2 cm above the substrate for times ranging from 10 to 60 seconds. After irradiation, the substrate was rinsed thoroughly and soaked in UP water for 24 hours to remove unreacted monomers. This step resulted in PAA-functionalized PES substrates (Fig. 1 (b)), which hereinafter we designate as PES–PAA.

Substrate functionalization with GO. Single-layer graphene oxide (GO) was purchased from Cheap Tubes (Grafton, VT, USA). Characterization by AC mode AFM revealed an average nanosheet thickness of 0.8 ± 0.1 nm, consistent with single sheets,[22] and sub-micron lateral dimensions (Fig. S1 (a) and (b)†) in agreement with the manufacturer's specifications (*i.e.*, 300–800 nm). A negative zeta potential was observed over the pH range ~1.5–9 for GO in aqueous dispersion (Fig. S1 (c)†) (consistent with previous work[32]), indicative of deprotonation of carboxylic acid groups in the nanosheet edges.[10] The oxygen content of GO was 35–45%, per the manufacturer's specifications. The Raman spectrum of GO nanosheets deposited on a silicon wafer (Fig. S1 (d)†) exhibited the D (~1350 cm^{-1}) and G (~1590 cm^{-1}) bands characteristic of GO.[33] Substrates were functionalized with 250 μg mL^{-1} GO dispersions prepared from 2 mg mL^{-1} stock dispersions, which were rendered colloidally stable through bath sonication for 24 hours. PES–PAA substrates were functionalized with GO by adapting the procedure developed by Perreault *et al.*,[19] which is based on amine coupling.[34] Carboxylic acid

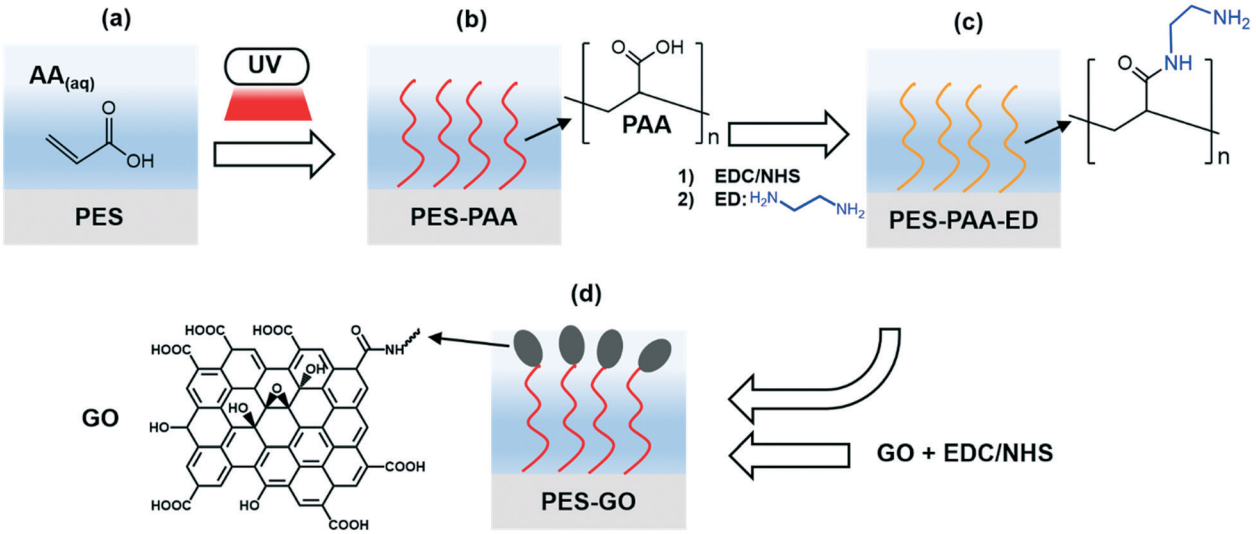

Fig. 1 Schematic diagram of polyethersulfone (PES) surface modification with graphene oxide (GO). (a and b) Self-initiated UV polymerization results in growth of poly(acrylic acid) (PAA) chains from acrylic acid (AA) monomers in aqueous solution, yielding PES–PAA substrates. (c) EDC/NHS-mediated amine coupling binds ethylenediamine (ED) linkers to the PAA chains, resulting in PES–PAA–ED substrates. (d) EDC/NHS-activated GO nanosheets react with primary amines in the ED linker to covalently tether GO to the substrates (yielding PES–GO substrates).

functional groups in the grafted PAA chains were activated to amine-reactive esters with 4 mM 1-ethyl-3-(3-dimethylaminopropyl)carbodiimide hydrochloride (EDC, 98%, Sigma) and 10 mM *N*-hydroxysuccinimide (NHS, 98%, Sigma), buffered at pH 5 with 10 mM MES (BioXtra, Sigma) supplemented with 0.5 M NaCl. The EDC–NHS activation step was carried out for 60 minutes under ambient conditions on a benchtop shaker at 30 rpm. Substrates were then rinsed gently with UP water. The amine reactive esters on the PES–PAA surface were subsequently contacted with 10 mM ethylenediamine solution (ED, BioXtra, Sigma) buffered at pH 7.5 by 10 mM HEPES (99.5%, Sigma) with 0.15 mM NaCl. The ED amine coupling step proceeded for 30 minutes, resulting in PES–PAA–ED substrates, as shown schematically in Fig. 1 (c). Next, the carboxylic acid functional groups decorating the GO nanosheet edges[10] were activated to amine reactive esters in a similar way. A GO dispersion (10 parts, 250 μg mL^{-1}) was mixed with 2 parts 100 mM MES buffer, followed by 1.75 parts 20 mM EDC in 10 mM MES buffer, and 1.75 parts 50 mM NHS in 10 mM MES buffer. The pH of the solution was then lowered to 5.5 by addition of 1 M HCl dropwise (to minimize flocculation of GO nanosheets), and allowed to react for 15 minutes. Subsequently, the pH was raised to 7.2 by addition of 1 M NaOH dropwise. The GO dispersion was poured over the ED-functionalized surface (PES–PAA–ED), covered, and allowed to react for 1 hour on a benchtop shaker at 30 rpm. Reaction between the amine-reactive esters in GO and the primary amine groups on the surface of the ED-modified substrate resulted in covalent linkage of the GO nanosheets to produce PES–GO substrates (Fig. 1 (d)). Finally, PES–GO samples were thoroughly rinsed and sonicated for 5 minutes to remove non-covalently bonded GO. All substrate samples were stored in ultrapure water at 4 °C for up to 3 weeks until use.

Interfacial characterization techniques

Raman and Fourier-transform infrared spectroscopy (FTIR). Attenuated total reflectance (ATR) FTIR was used to characterize the surface chemistry of the substrates. Spectra of desiccator-dried specimens of each substrate type were acquired in an FTIR spectrometer (Nicolet Series II Magna-IR System 750) equipped with an ATR cell. The spectra were collected in terms of % reflectance at a resolution of 0.241 cm^{-1}. Raman spectra were obtained with an Alpha300R Raman microscope (Witec). For each specimen, we acquired 20 × 20 μm^2 Raman scans at a 0.5 μm resolution, on randomly chosen sections of the substrates. At each point in the 2D scan, we computed the ratio of the area under the D band of GO (observed at 1350 cm^{-1})[33] and the area under a prominent PES peak (observed at 1146 cm^{-1}) to generate maps characterizing the spatial distribution of GO nanosheets. In addition, a mean Raman spectrum was generated by averaging the spectra collected at each point on the 2D scan.

Contact angle, surface charge, and nanoscale roughness. Substrate hydrophobicity was characterized in terms of oil-in-water contact angle measurements using the captive bubble technique. We performed measurements with a Ramé-Hart Model 200 goniometer; images were analyzed with the DROP Image software (Ramé-Hart). For captive bubble measurements, substrates were affixed to a surface with the functionalized side facing a liquid cell containing ultrapure water. A J-shaped needle was used to inject *n*-decane droplets (~10 μL). We performed ≥14 contact angle measurements across three independently functionalized specimens of each substrate type. The surface charge of the substrates was characterized *via* streaming potential measurements using an electrokinetic analyzer (SurPass, Anton-Paar) equipped with an adjustable gap cell at a gap size of 120 μm. Streaming

potential was measured from pH 10 to pH 4 in 1 mM KCl solution, and the zeta potential was determined from the streaming potential using the Smoluchowski–Helmholtz equation.[35] Three specimens of each substrate type were characterized. The nanoscale roughness of the substrates was investigated with an MFP-3D-Bio AFM (Asylum Research) equipped with a liquid cell. AC mode AFM scans (5 × 5 μm^2, scan rate = 0.25 Hz) of two specimens of each substrate type were obtained in phosphate-buffered saline (PBS) at pH 7.4 using a silicon nitride cantilever (SNL probe "C", nominal k = 0.24 N m^{-1}, Bruker). Surface topography was quantified in terms of the root-mean-squared roughness (R_{RMS}) determined in 1 × 1 μm^2 areas of each of the AFM scans for a total of 8 roughness calculations for each substrate type.

Single-cell force spectroscopy (SCFS). The adhesion of *P. fluorescens* cells to the surface of control and functionalized substrates was quantitatively investigated using single-cell force spectroscopy (SCFS). Bacterial cells were grown and cultivated following the protocol provided in the ESI.† The experimental procedure of SCFS, outlined below, is provided in detail in our recent publication.[36] An individual *P. fluorescens* (ATCC 13525) cell was adhered to a tip-less AFM cantilever (MLCT-O10 probe "C", nominal k = 0.01 N m^{-1}, Bruker) on which a polydopamine wet adhesive layer had been deposited from a dopamine hydrochloride solution (4 mg of dopamine hydrochloride per milliliter of Trizma buffer, pH 8.5) shortly before adhering the cell. The cell was adhered with its long axis parallel to the leading edge of the cantilever, an orientation that maximizes adhesion contact area. Bacterium orientations probing adhesion *via* the flagellar pole were not studied, due to the risk of cell detachment during force collection. An MFP-3D-Bio AFM (Asylum Research) integrated to a Zeiss Axio Observer A1 inverted optical microscope was used to perform cell adhesion force measurements. All forces were determined at room temperature (25 °C) in a liquid cell filled with PBS, pH 7.4. Force curves, comprising extension–retraction cycles, were carried out at a cantilever speed of 400 nm s^{-1}, a piezo dynamic range of at least 3 μm, a trigger force (the maximum force applied to the cell as it contacts the substrate) of 600 pN, and a dwell time of 0 s (*i.e.*, the bacterial cell was immediately retracted from the substrate upon reaching the trigger force). For each substrate type, a total of ≥98 force curves were collected with at least 2 independently cultivated bacterial cells, on ≥2 different substrate specimens of each type. Force curves were acquired at randomly chosen sites on the substrate. At each randomly chosen location, up to three force curves were collected to minimize deposition of extracellular polymeric substances on the substrate. After each experiment, the cell viability was determined using a live/dead assay (BacLight, Thermofisher). Only data collected with a live cell that remained at its initial location were reported.

Statistical analysis. Unless stated otherwise, two-sided unpaired *t*-tests, presuming unknown but equal population variances (*i.e.*, assuming homoscedasticity), were conducted to determine the statistical significance of the results.

3. Results and discussion

Interfacial characterization

We used an array of surface analytical techniques to characterize the chemistry and morphology of the various substrates.

Surface chemistry. Given the prominent IR bands present in the AA monomer, we used FTIR spectroscopy to assess the efficacy of PAA grafting. AA polymerizes on the substrate due to UV-generated free radicals formed on the PES surface, which react with the vinyl double bond of the AA molecule, leading to the formation of PAA chains covalently bonded to the substrate.[29] The degree of grafting (*i.e.*, the extent of AA polymerization on the PES substrate), and the kinetics of polymerization, are influenced by the UV irradiation time and UV wavelength.[29,37] PES substrates soaked with a thin liquid film of 10 vol% AA solution were exposed to UV light for 10–60 seconds. The FTIR results for the PES control and PES–PAA substrates are shown in Fig. 2. The peak at 1580 cm^{-1}, observed in all samples, is due to vibration of the aromatic rings in PES.[38] In addition, we observe IR bands resulting from carboxylic acid groups in PAA, namely a peak at 1700–1730 cm^{-1} due to C=O stretching vibration,[39] and multiple bands in the 2500–3300 cm^{-1} range due to COO–H stretching.[39] These peaks increase monotonically with irradiation time, in line with increasing degree of PAA grafting.[37] In the remainder of the study we focus on substrates fabricated with a 10 s UV irradiation step, which resulted in materials with nanofiltration-like water permeability coefficient and divalent ion rejection (see ESI† for methods and results). Irradiation times > 10 s resulted in a dense PAA layer and a steep loss in water permeability.

The FTIR spectra of the PES, PES–PAA (10 s UV irradiation) and PES–GO substrates are presented in Fig. 3. The spectrum corresponding to PES–GO shows an increase in the COO–H stretching band at 3300 cm^{-1} relative to PES–PAA, which can be attributed to carboxylic acid functional groups present in the GO nanosheet edges.[10] In addition, PES–GO presents a peak at ~2900 cm^{-1} absent in the other substrates,

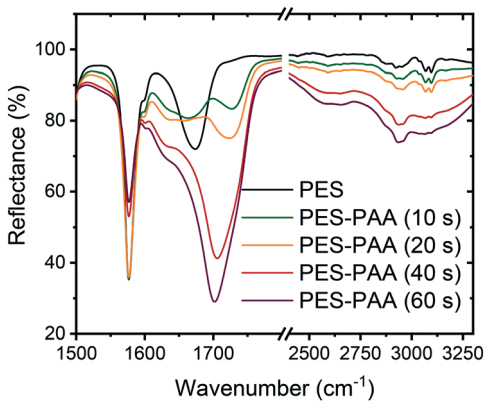

Fig. 2 FTIR spectra of PES and poly(acrylic acid) (PAA)-functionalized PES substrates (PES–PAA, prepared with different UV irradiation times noted in the caption).

which is likely an N–H stretching vibration band (typically observed at 3100–3500 cm^{-1} [39]) due to primary amines that remain unreacted after GO modification.

We confirmed the presence of graphene oxide on the PES–GO substrates using Raman spectroscopy. The average of 1600 spectra scanned over a 20 × 20 μm^2 area of each specimen is presented in Fig. 4. The PES–GO substrate prominently shows the G and D bands of graphene oxide,[33] thus confirming functionalization of PES with GO. All substrates show similar chemical signatures due to polyethersulfone, *e.g.*, peaks at 790, 1070, 1107, 1146, 1580 and 1601 cm^{-1}.[40]

We used confocal Raman mapping to assess the spatial distribution of GO on the PES–GO substrates. The results are presented in Fig. 5. The PES–GO map (Fig. 5 (c)) exhibits high brightness regions indicative of the presence of GO nanosheets throughout the scanned area (the intensity of each pixel is proportional to the ratio of the area under the D peak of GO to that under the polyethersulfone peak at 1146 cm^{-1}). Conversely, neither the PES nor the PES–PAA Raman maps (Fig. 5 (a and b)) exhibit signatures of GO. The data in Fig. 5 consequently show that the modification protocol enables the formation of uniform layers of tethered GO nanosheets on the PES substrates.

Interfacial properties. We investigated the interfacial properties which are known to influence biofouling propensity: hydrophobicity, nanoscale roughness and surface charge.[41,42] To characterize the hydrophobicity of each substrate type, we measured the contact angle of *n*-decane droplets in aqueous suspension using the captive bubble technique. The angles shown below are measured from the substrate, through the aqueous phase, to the *n*-decane interface, so that smaller values indicate poor wetting of the substrate by the *n*-decane droplet (*i.e.*, greater hydrophilicity). The results, presented in Fig. 6 (a), show that PES–PAA ($\theta_{n\text{-Decane}}$ = 20.6 ± 4.3°) and PES–GO samples ($\theta_{n\text{-Decane}}$ = 19.7 ± 5.4°) are significantly more hydrophilic ($p < 0.01$) than the control PES substrate ($\theta_{n\text{-Decane}}$ = 53.1 ± 3.9°). PES–PAA and PES–GO showed approximately equal contact angles ($p = 0.6$). We attribute the low wettability of PES–PAA and PES–GO surfaces by a hydrophobic liquid (*n*-decane) to the abundance of H-bonding functional groups in PAA- and GO-functionalized surfaces (*i.e.*, –COOH groups in PES–PAA; hydroxyl, and –COOH groups in GO,[10] all of which are absent in PES).

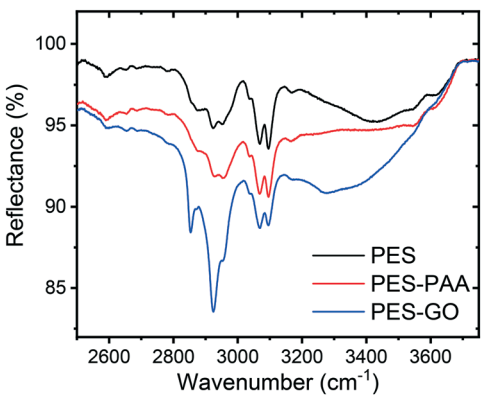

Fig. 3 FTIR spectra of control (PES), poly(acrylic acid) (PAA)-functionalized PES (PES–PAA, 10 s UV irradiation), and GO-functionalized (PES–GO) substrates.

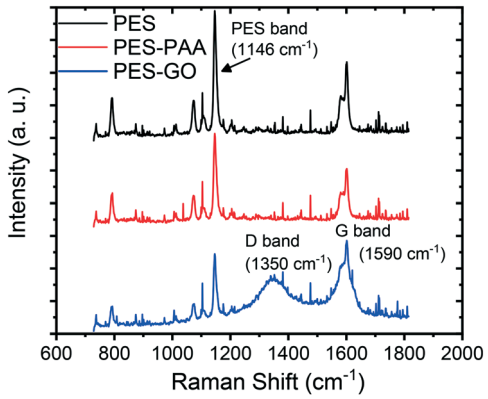

Fig. 4 Raman spectra of pristine PES, poly(acrylic acid) (PAA)-functionalized PES (PES–PAA), and GO-modified PES (PES–GO) substrates.

We characterized the surface charge of the substrates in terms of the ζ-potential as a function of pH. The results are presented in Fig. 6 (b). All substrates (including pristine PES[43]) exhibited negative zeta potentials over the pH range investigated. At pH 7.4, (*i.e.*, the condition at which we characterized other interfacial properties such as surface roughness, and microbial adhesion), all specimens show a similar zeta potential value of ~−30 to −40 mV, suggesting that surface functionalization does not significantly modify the charge of the interface at this pH. PES–PAA and PES–GO samples are negatively charged primarily due to deprotonation of carboxylic acid groups with increasing pH.[10,32] While PES does not have acidic functional groups, its negative zeta potential is due to adsorption of hydroxyl ions.[44]

Surface roughness influences fouling, with rougher substrates exhibiting greater biofouling and colloidal fouling propensity.[45–48] We determined the RMS roughness (R_{RMS}) of the hydrated substrates using AFM. Representative 2 × 2 μm^2 AFM scans along with average R_{RMS} values are shown in Fig. 7. We observed a relatively smooth interface in the PES substrate with low surface roughness (R_{RMS} = 2.51 ± 0.49 nm, *cf.* Fig. 7 (a)). On the other hand, the grafted PAA chains increase the R_{RMS} of the PES–PAA substrate (R_{RMS} = 5.74 ± 2.18 nm, *cf.* Fig. 7 (b)) compared to the PES control ($p < 0.01$). The negatively charged tethered PAA chains exist in a collapsed (*i.e.*, non-extended) conformation given that the high ionic strength of PBS (162 mM) results in screening of electrostatic repulsions.[49] PAA chain collapse yields the rough, peak-and-valley interfacial structure shown in Fig. 7 (b). Upon edge-tethering GO nanosheets to the PAA surface, we observe an interface with lower R_{RMS} (R_{RMS} = 3.63 ± 1.17 nm, *cf.* Fig. 7 (c)) compared to PES–PAA ($p = 0.03$). GO nanosheets appear to cover the rougher PAA interfacial features, thus decreasing R_{RMS}. This "smoothing over" is possibly caused by GO nanosheets tethered to the PAA layer

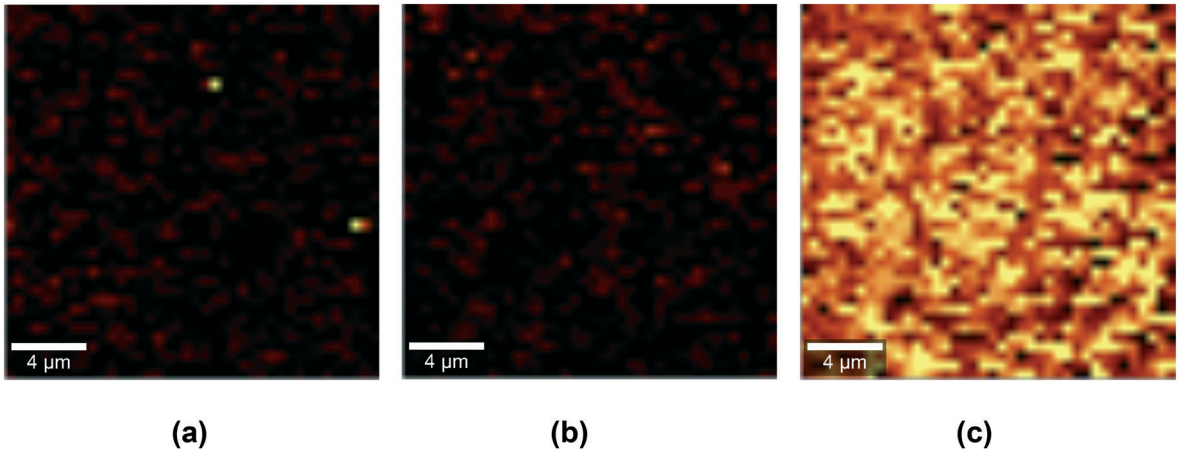

Fig. 5 Raman spectroscopy maps of (a) pristine PES, (b) poly(acrylic acid) (PAA)-modified PES (PES–PAA), and (c) GO-modified PES (PES–GO) substrates.

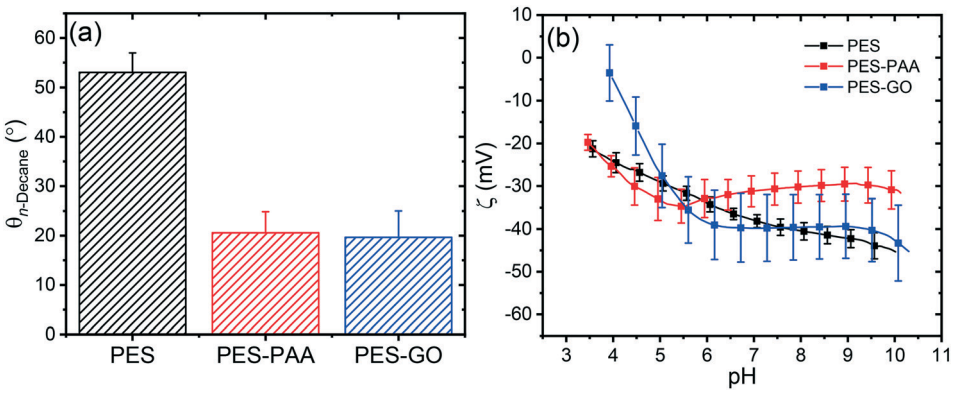

Fig. 6 (a) Contact angles of *n*-decane droplets ($\theta_{n\text{-Decane}}$) on the various substrates, determined in ultrapure water *via* the captive bubble technique. Error bars denote one standard deviation ($n \geq 14$). (b) ζ-Potential as a function of pH of pristine PES, poly(acrylic acid) (PAA)-modified PES (PES–PAA), and GO-modified PES (PES–GO) substrates. The ζ-potential results shown for each substrate type are the average of three independently modified specimens (error bars indicate one standard deviation).

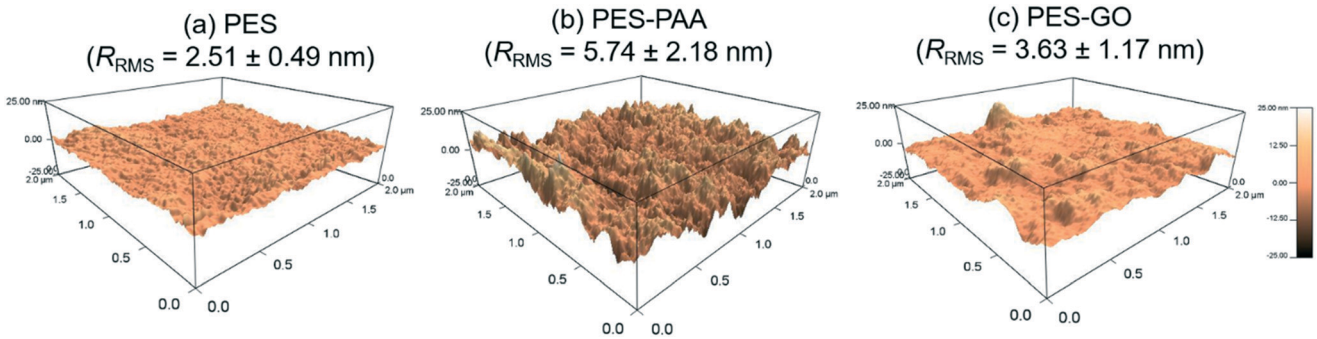

Fig. 7 AC mode AFM images of (a) pristine PES, (b) poly(acrylic acid) (PAA)-modified PES (PES–PAA), and (c) GO-modified PES (PES–GO) substrates. The caption denotes the root-mean-squared roughness (R_{RMS}) computed from eight 1×1 μm^2 sections sampled over two different 5×5 μm^2 scans of each substrate type. AFM scans and R_{RMS} were obtained in PBS (pH 7.4).

through multiple sites along the sheet periphery (effectively acting as a crosslinker of PAA chains).

Bacterial adhesion. We now investigate bacterial adhesion onto GO-functionalized substrates. Our aim is to examine whether GO substrate functionalization mitigates bacterial adhesion, the first step in biofouling. GO coatings that are both biocidal and anti-adhesive are preferable to those that afford only bacterial inactivation (without preventing bacteria, and bacterial debris, from adsorbing). While previous work on GO-functionalized polyamide membranes has shown

that GO coatings may exert dual biocidal/anti-adhesive functions,[20] recent studies have shown that GO nanosheets increase the adhesiveness of inert Si substrates[22] and weakly adhesive polymeric spacer substrates.[23] Here we explain these seemingly contradictory results. Lastly, we elucidate the molecular determinants of adhesion by analyzing the interactions of bacterial adhesin molecules (proteinaceous structures such as pili and outer membrane proteins[50,51]) with the various substrates.

A representative force–distance curve, showing a typical extension–retraction force cycle, is presented in Fig. 8. For each retraction force curve, we recorded the peak adhesion force, F_{Peak}, defined as the binding force with the highest magnitude, and the rupture separation, R, *i.e.*, the separation at which cell–substrate forces vanish (*cf.* Fig. 8). We set the trigger force (F_{Tr}, defined as the force exerted on the bacterium when it contacts the substrate, *cf.* Fig. 8), to 600 pN; this value is of the same order of magnitude as the permeation drag force experienced by similarly-sized colloidal particles during low-pressure membrane filtration.[52]

Fig. 9 (a–c) presents the distribution of *P. fluorescens* peak adhesion forces (F_{Peak}) observed over the different substrates. The "NO" column in the histograms corresponds to measurements in which weak adhesion ($<$ 30 pN, equivalent in magnitude to the noise level in the force) or no adhesion peaks were observed (see Fig. 8 (inset) for a representative non-adhesive force curve).

We observe a broad distribution of peak adhesion forces for all substrates (*cf.* Fig. 9 (a)–(c)), with the majority of adhesion events occurring in the $\approx$ 0 to 0.5 nN range, typical of bacterial adhesion.[51] Further, we observe that adhesion forces are substrate-dependent. Among the surfaces studied,

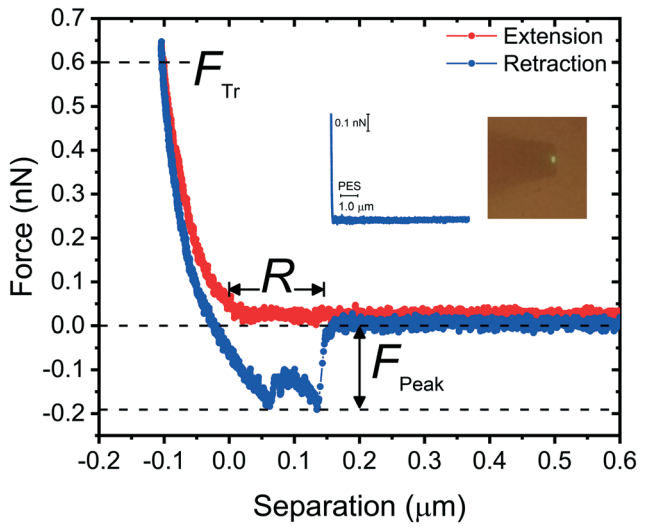

Fig. 8 Representative extension–retraction force cycle recorded over PES with a *P. fluorescens* bacterial probe. The curve shows the definition of the trigger force (F_{Tr}), peak adhesion force (F_{Peak}), and rupture separation (R). The inset shows a representative non-adhesive retraction force curve recorded over PES, and a digital image of a bacterial probe.

PES–GO exhibits the lowest probability of adhesion, with 45.9% of measurements showing no-adhesion events, compared to 22.2% for PES–PAA and 32.3% for PES. We observe three consecutive non-adhesive force curves in 15% (PES–PAA), 21% (PES), and 25% (PES–GO) of the loci probed, *i.e.*, a similar trend to that of the probability of observing non-adhesive events across the whole surface. Consistent with the (quasi-static) AFM measurements, bacterial deposition experiments (Fig. S2†) show that the extent of irreversible adhesion is lowest on PES–GO. Fig. 9 (d), presenting the average of all forces ($\bar{F}_{Peak}$), shows that adhesion is strongest on PES, while PES–GO displays the weakest mean adhesion: $\bar{F}_{Peak}$ = −0.11 (± 0.17) nN for PES–GO *vs.* −0.18 (± 0.18) nN for PES (p = 0.006). PES–PAA substrates also demonstrated weaker adhesions ($\bar{F}_{Peak}$ = −0.13 (± 0.11) nN) compared to PES (p = 0.008), while similar adhesiveness was displayed by PES–PAA and PES–GO (p = 0.6).

A more nuanced adhesion behavior arises when we exclude the non-adhesive measurements from the calculation of the mean. The results, presented in Fig. 9 (e), show that PES substrates still reveal the strongest mean adhesion, *i.e.*, $\bar{F}_{Peak}$ = −0.27 (± 0.15) nN. On the other hand, PES–PAA exhibits the weakest mean adhesion forces with $\bar{F}_{Peak}$ = −0.16 (± 0.10) nN, compared to −0.21 (± 0.18) nN for PES–GO (p = 0.04). Consequently, Fig. 9 shows that, while PES–GO surfaces display the lowest probability of *P. fluorescens* attachment (*i.e.*, highest incidence of non-adhesion events, as shown in Fig. 9 (c)), adhering bacteria engage the GO substrate with forces that are stronger than those observed over PES–PAA, and only somewhat weaker than those observed over PES (Fig. 9 (e)).

The picture emerging from Fig. 9 indicates that edge-tethering GO to a PAA coating decreases the mean adhesion force ($\bar{F}_{Peak}$) of *P. fluorescens* compared to the unmodified PES surface (*cf.* Fig. 9 (d)). However, it is important to note that the lower $\bar{F}_{Peak}$ observed on PES–GO (Fig. 9 (d)) is due to a high incidence of non-adhesive events on the GO-functionalized substrate (*cf.* Fig. 9 (c)), which offsets the relatively strong adhesion forces exhibited by cells that do successfully adhere to the PES–GO surface (Fig. 9 (e)).

Fig. 10 presents the distribution of the rupture separation (R) over the different substrates. R is also distributed broadly, with mean values ($\bar{R}$) around 1 μm that are a reflection of the adhesins, namely pili and flagella, that mediate *P. fluorescens* binding to substrates.[53–55] Fig. 10 further shows that longer ranged interactions are observed over PES ($\bar{R}$ = 1.2 (± 0.9 μm)) compared to PES–PAA ($\bar{R}$ = 0.7 (± 1.0 μm), p = 0.002) and to PES–GO ($\bar{R}$ = 0.8 (± 0.5 μm), p = 0.008), suggesting that more sites along individual adhesins bind to the PES substrate. It is also possible that higher $\bar{R}$ observed on the PES substrate indicates that several adhesins of different contour length mediate attachment on PES.[36] R thus displays behavior in line with the adhesion forces reported in Fig. 9 (d), since longer ranged forces are observed on more adhesion-prone PES substrates. Moreover, in view of the lower $\bar{R}$ observed over PES–GO and PES–PAA, Fig. 10 shows that the

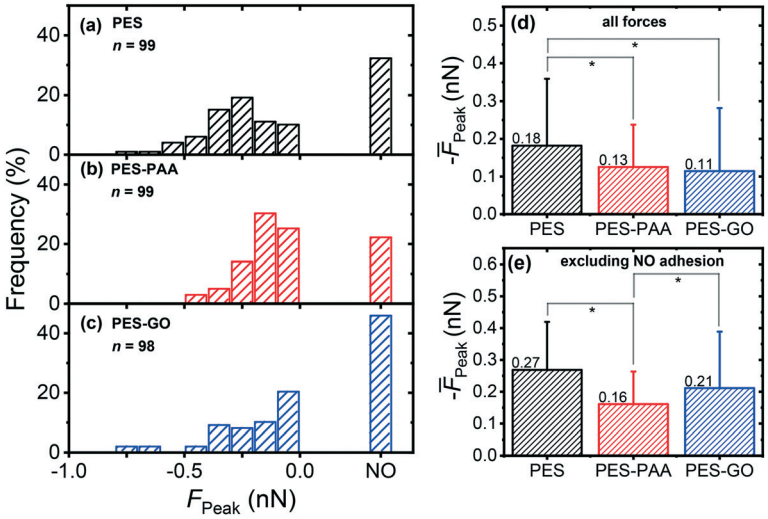

Fig. 9 Distribution of peak adhesion forces (F_{Peak}) of single *P. fluorescens* cells on: (a) pristine PES; (b) poly(acrylic acid) (PAA)-modified PES (PES–PAA); (c) GO-modified PES (PES–GO). The inset shows the number of force measurements (n). Measurements were performed in PBS at pH 7.4. (d) Mean peak adhesion forces ($\bar{F}_{Peak}$) computed from (a)–(c), including non-adhesive events (F_{Peak} = 0 nN). (e) Mean peak adhesion forces excluding non-adhesive events. Error bars in (d) and (e) indicate the standard deviation. Pairwise comparisons denoted by * indicate statistical significance ($p < 0.05$).

range of cell adhesion forces is determined by microbial adhesins, and that extension of poly(acrylic acid) chains during cell pull-off does not contribute significantly to R.

We turn to the interfacial properties presented in Fig. 6 and 7 to explain the differences in adhesive behavior among the three substrate types. Weakening of cell–substrate forces in PES–PAA (*cf.* Fig. 9 (d and e)) compared to PES is due to the PAA coatings resulting in more hydrophilic substrates (*cf.* Fig. 6 (a)), which mitigate adhesion of *P. fluorescens* bacteria reliant on hydrophobic interactions.[36,53,56] In addition, PAA chain compression results in a steric repulsive force that contributes to weaker bioadhesion.[57,58] We note that long-range electrostatic repulsive forces, involving the negatively charged substrate (Fig. 6 (b)) and bacterium, are absent in PBS (Debye length = 0.75 nm). We observe two effects upon functionalization with GO. First, an increase in the frequency of non-adhesive events compared to PES and PES–PAA (*cf.* "NO" column in Fig. 9 (a–c)), which we attribute to the layer of GO nanosheets that is covalently tethered to PES–PAA; this GO coating lowers the roughness of the interface (*cf.* Fig. 7) thus decreasing adsorption surface area, and results in an additional steric barrier that limits binding of the microbe[22] (similarly, higher surface roughness in PES–PAA explains its lower incidence of non-adhesive events compared to PES). Second, we observe an increase in the mean adhesion force relative to PES–PAA (as shown in Fig. 9 (e), which excludes non-adhesive observations). In view of the similar contact angles of PES–PAA and PES–GO (*cf.* Fig. 6 (a)), the stronger adhesion on the GO-coated substrate cannot be explained by a macroscopic view of hydrophobicity. At the nanoscale, however, GO is known to be amphiphilic, possessing hydrophilic sheet edges,[10] and basal surfaces featuring hydrophobic graphenic domains.[10,59] These nanoscale hydrophobic regions embedded in GO serve as sorption sites for hydrophobic molecules,[60–62] and thus can bolster microbial adhesion through interactions with hydrophobic adhesins.[54]

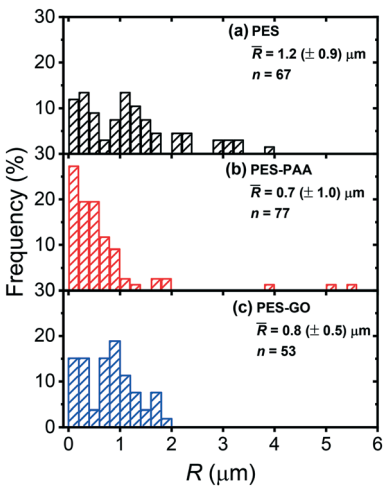

Fig. 10 Distribution of rupture separations (R), defined as the distance at which cell adhesion forces vanish, for various substrates: (a) pristine PES; (b) poly(acrylic acid) (PAA)-modified PES (PES–PAA); (c) GO-modified PES (PES–GO). The inset shows the histogram average ($\bar{R}$ (± standard deviation)), and number of measurements (n). Measurements were performed in PBS at pH 7.4.

Role of adhesin molecules in microbial adhesion. Fig. 11 and 12 discuss the molecular-level determinants of bacterial adhesion. Force measurements on all three substrates exhibit adhesion peaks such as those shown in Fig. 11, whose characteristic shape results from stretching and unfolding of single biopolymer molecules.[63] Examination of these extension events can therefore provide additional insight into the role of adhesin molecules, such as pili, outer membrane proteins

and lipopolysaccharides, in microbial adhesion.[36] Two models are commonly used to describe the elasticity of single biopolymers under force: the worm-like chain (WLC) model, which describes the mechanics of protein domains; and the extended freely-jointed chain (FJC) model, known to describe the elasticity of polysaccharide molecules.[64] In our data only a small fraction of extension events (< 3%) were well described by the FJC model (see Fig. S3† for representative FJC fits on the three substrates); these rare events are due to the extension of polysaccharides on the surface of the bacterial cell, or stretching of PAA chains (known to exhibit FJC mechanics[65]) on the PES–PAA or PES–GO substrate. On the other hand, WLC extension events are far more common, and we analyze them in detail below. We find that 33% of all force measurements collected on PES and PES–PAA substrates, and 26% of measurements collected over PES–GO, exhibit single-molecule extensions that can be quantitatively described by the WLC model. In the WLC model, the elasticity of macromolecules under tension is given by the following force (F)-elongation (z) equation:

$$F(z) = \frac{k_B T}{4L_p}\left[\left(1-\frac{z}{L_c}\right)^{-2} + \frac{4z}{L_c} - 1\right] \quad (1)$$

where L_p is the persistence length (a measure of the flexibility of the polymer chain), L_c is the contour length (*i.e.*, the total length of the unraveled polymer chain), k_B is Boltzmann's constant, and T = 298.15 K is the absolute temperature. Non-linear regression of the force–distance data using the WLC model (carried out with the WLC fitting function in IGOR Pro 6.3) results in best-fit L_p estimates (Fig. 12 (a)) across all substrates with an average value $\bar{L}_p \approx 0.3$ nm, in line with the persistence length of proteins,[63,66,67] thus suggesting outer membrane proteins (such as LapA in *P. fluorescens*[51]) as the adhesins mediating microbial attachment.

We further observe multiple WLC events in a single force measurement (*cf.* Fig. 11), allowing us to calculate the number of WLC extensions per force curve (N_{WLC}), as shown in Fig. 12 (b). While WLC events are observed in fewer PES–GO force curves (26% compared to 33% for the other substrates), the mean values ($\bar{N}_{WLC}$) are similar for PES–GO and PES, *i.e.*, 2.3 ± 2.1 and 2.7 ± 2.2, respectively (p = 0.5). Further PES–PAA exhibits lower $\bar{N}_{WLC}$ (1.4 ± 0.9) compared to PES and PES–GO ($p < 0.05$). Considering that N_{WLC} is proportional to the number of adhesins that attach to the substrate, the values of $\bar{N}_{WLC}$ are consistent with the adhesion properties described previously in Fig. 9 (e), which showed that (provided non-adhesive events are excluded) PES and PES–GO showed similar mean adhesion forces.

The single-molecule extension events presented in Fig. 11 (along with corresponding WLC fits) show the occurrence of consecutive single-molecule extensions. This allows determination of the length scale of the extended biomolecule domains from $\Delta L_c = L_{c,i+1} - L_{c,i}$, where $L_{c,i}$ and $L_{c,i+1}$ denote the contour length of two consecutive WLC fits. As shown in Fig. 12 (c), ΔL_c is narrowly distributed around mean values $\left(\overline{\Delta L_c}\right)$ of 0.10 (± 0.06) μm and 0.11 (± 0.10) μm for PES–PAA and PES–GO, respectively, whereas for PES we observe a much broader distribution with $\overline{\Delta L_c}$ = 0.24 (± 0.18) μm. The tight distribution of ΔL_c around ~100 nm suggests that the WLC events observed on PES–GO and PES–PAA are likely due to proteinaceous adhesins whose domains unravel sequentially in pairs or triplets (the contour length of cell membrane and pilin proteins is 30–60 nm[51,68]), as was recently proposed for *P. fluorescens* adhesins.[51] On the other hand, the much broader distribution observed over PES substrates could be the result of two distinct phenomena. Firstly, desorption of two different adhesin molecules of disparate lengths,[53] resulting in two sequential WLC peaks characterized by a large ΔL_c; the longer rupture separation observed on PES compared to the other two surfaces (see Fig. 10) supports this mechanism. Alternatively, the more hydrophobic character of PES substrates (Fig. 6 (a)) could lead to surface-induced partial unfolding of adhesin molecules,[36] the corresponding change in protein conformation leading to a wider range of ΔL_c values. Finally, Fig. 12 (d) presents the distribution of extension forces (F_{ext}), defined as the force at each peak observed in a single-molecule extension event (*cf.* Fig. 11, top panel). The magnitude of the forces is in the range of 100–300 pN, in agreement with previous reports for unfolding forces of protein domains,[51,63] with the average value ($\bar{F}_{ext}$) being similar for all substrates. This suggests that F_{ext} is primarily due to the elastic response of adhesins to the

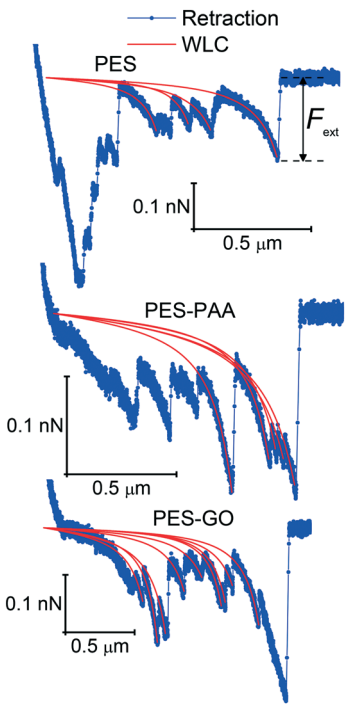

Fig. 11 Enlarged view of retraction force curves, showing single-molecule extension events and corresponding worm-like chain (WLC) fits for various substrates, indicated in the caption.

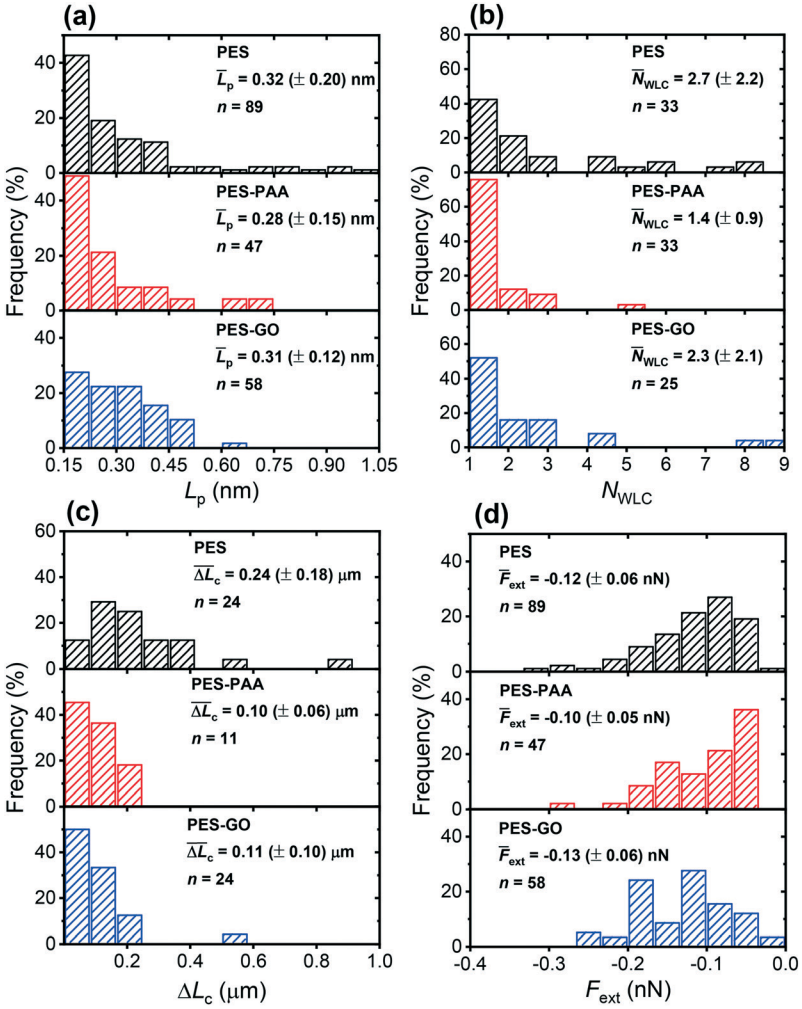

Fig. 12 (a) Distribution of best-fit persistence length values (L_p), obtained from WLC model fits on various substrates (see Fig. 11 for representative fits). (b) Distribution of the number of WLC single-molecule extension events per force curve (N_{WLC}). (c) Distribution of ΔL_c (the difference in contour length (L_c) between two consecutive WLC extension events). (d) Distribution of extension forces (F_{ext}, the force measured at the each WLC extension peak). The caption of each figure indicates the substrate type, histogram average ($\bar{L}_p$, $\bar{N}_{WLC}$, $\overline{\Delta L_c}$, $\bar{F}_{ext}$ (± standard deviation)) and number of measurements (n).

external force, and that desorption from the substrate does not contribute significantly to the extension force.[63]

4. Conclusions

While graphene oxide (GO) has shown strong biocidal activity,[12,13,19,69] there have been conflicting reports as to whether GO can mitigate bacterial adhesion,[22,23] the first step of biofilm formation and biofouling. This paper used single-cell force spectroscopy to show that edge-tethering GO nanosheets to poly(acrylic acid) (PAA) brushes produces GO coatings (formed on polyethersulfone (PES) substrates) characterized by low *P. fluorescens* adhesion forces. Our results show that lower mean adhesion forces observed on GO-functionalized coatings (designated PES–GO) are mainly due to the occurrence of cell–substrate repulsive (non-adhesive) forces; these are in turn derived from the hydrophilicity and steric repulsion afforded by the GO-functionalized PAA layer. A salient observation is that GO is not intrinsically anti-adhesive: its integration into a polymeric brush is essential to achieve a low-adhesion interface. GO-free PAA coatings (termed PES–PAA) also demonstrated lower bacterial adhesion due to their hydrophilicity. In the absence of PAA or GO, PES control substrates exhibited stronger bacterial adhesion due to their hydrophobicity. Analysis of the force spectroscopy data on all substrates shows that adhesion of *P. fluorescens* is driven by proteinaceous adhesins, whose elasticity is well described by the worm-like chain model.

Our results highlight the importance of interfacial properties (*e.g.*, surface roughness, hydrophilicity) in the formulation of GO-based antibacterial interfaces for environmental applications, pointing out possible directions for future study. In the context of water treatment systems, it is necessary to characterize bioadhesion to GO interfaces (such as those in membranes,[19,20] spacers,[23] and adsorbents[7]), under realistic hydrodynamic conditions.

Conflicts of interest

There are no conflicts of interest to declare.

Acknowledgements

This work was supported by the Environment and Natural Resources Trust Fund, as recommended by the Legislative-Citizen Commission on Minnesota Resources. Portions of this work were carried out in the Characterization Facility at UMN, supported by NSF through award DMR-1420013, and at the Minnesota Nano Center, which receives partial support from NSF through the National NanoCoordinated Infrastructure Network (NNCI) (Award Number ECCS-1542202). SRVC is grateful to 3M Co. for a Non-Tenured Faculty Award.

References

1 K. S. Novoselov, A. K. Geim, S. V. Morozov, D. Jiang, Y. Zhang and S. V. Dubonos, *et al.* Electric field in atomically thin carbon films, *Science*, 2004, **306**(5696), 666–669.

2 P. J. J. Alvarez, C. K. Chan, M. Elimelech, N. J. Halas and D. Villagrán, Emerging opportunities for nanotechnology to enhance water security, *Nat. Nanotechnol.*, 2018, **13**(8), 634–641.

3 Y. Zhu, S. Murali, W. Cai, X. Li, J. W. Suk and J. R. Potts, *et al.* Graphene and graphene oxide: Synthesis, properties, and applications, *Adv. Mater.*, 2010, **22**(35), 3906–3924.

4 R. K. Joshi, P. Carbone, F. C. Wang, V. G. Kravets, Y. Su and I. V. Grigorieva, *et al.* Precise and ultrafast molecular sieving through graphene oxide membranes, *Science*, 2014, **343**(6172), 752–754.

5 S. C. O'Hern, M. S. H. Boutilier, J. C. Idrobo, Y. Song, J. Kong and T. Laoui, *et al.* Selective ionic transport through tunable subnanometer pores in single-layer graphene membranes, *Nano Lett.*, 2014, **14**(3), 1234–1241.

6 M. Hu and B. Mi, Enabling graphene oxide nanosheets as water separation membranes, *Environ. Sci. Technol.*, 2013, **47**(8), 3715–3723.

7 N. Yousefi, X. Lu, M. Elimelech and N. Tufenkji, Environmental performance of graphene-based 3D macrostructures, *Nat. Nanotechnol.*, 2019, **14**(2), 107–119, DOI: 10.1038/s41565-018-0325-6.

8 Y. Yang, R. Zhao, T. Zhang, K. Zhao, P. Xiao and Y. Ma, *et al.* Graphene-Based Standalone Solar Energy Converter for Water Desalination and Purification, *ACS Nano*, 2018, **12**(1), 829–835, DOI: 10.1021/acsnano.7b08196.

9 F. Perreault, A. Fonseca De Faria and M. Elimelech, Environmental applications of graphene-based nanomaterials, *Chem. Soc. Rev.*, 2015, **44**(16), 5861–5896.

10 V. C. Sanchez, A. Jachak, R. H. Hurt and A. B. Kane, Biological interactions of graphene-family nanomaterials: An interdisciplinary review, *Chem. Res. Toxicol.*, 2012, **25**(1), 15–34.

11 J. Chen, H. Peng, X. Wang, F. Shao, Z. Yuan and H. Han, Graphene oxide exhibits broad-spectrum antimicrobial activity against bacterial phytopathogens and fungal conidia by intertwining and membrane perturbation, *Nanoscale*, 2014, **6**(3), 1879–1889, Available from: http://xlink.rsc.org/?DOI=C3NR04941H.

12 W. Hu, C. Peng, W. Luo, M. Lv, X. Li and D. Li, *et al.* Graphene-based antibacterial paper, *ACS Nano*, 2010, **4**(7), 4317–4323.

13 F. Perreault, A. F. De Faria, S. Nejati and M. Elimelech, Antimicrobial Properties of Graphene Oxide Nanosheets: Why Size Matters, *ACS Nano*, 2015, **9**(7), 7226–7236.

14 S. Gurunathan, J. W. Han, A. A. Dayem, V. Eppakayala and J. H. Kim, Oxidative stress-mediated antibacterial activity of graphene oxide and reduced graphene oxide in Pseudomonas aeruginosa, *Int. J. Nanomed.*, 2012, **7**, 5901–5914.

15 H. R. Chae, J. Lee, C. H. Lee, I. C. Kim and P. K. Park, Graphene oxide-embedded thin-film composite reverse osmosis membrane with high flux, anti-biofouling, and chlorine resistance, *J. Membr. Sci.*, 2015, **483**, 128–135.

16 M. E. A. Ali, L. Wang, X. Wang and X. Feng, Thin film composite membranes embedded with graphene oxide for water desalination, *Desalination*, 2016, **386**, 67–76.

17 A. Inurria, P. Cay-Durgun, D. Rice, H. Zhang, D. K. Seo and M. L. Lind, *et al.* Polyamide thin-film nanocomposite membranes with graphene oxide nanosheets: Balancing membrane performance and fouling propensity, *Desalination*, 2018, **451**, 139–147.

18 X. Lu, X. Feng, X. Zhang, M. N. Chukwu, C. O. Osuji and M. Elimelech, Fabrication of a Desalination Membrane with Enhanced Microbial Resistance through Vertical Alignment of Graphene Oxide, *Environ. Sci. Technol. Lett.*, 2018, **5**(10), 614–620.

19 F. Perreault, M. E. Tousley and M. Elimelech, Thin-Film Composite Polyamide Membranes Functionalized with Biocidal Graphene Oxide Nanosheets, *Environ. Sci. Technol. Lett.*, 2013, **1**(1), 71–76.

20 F. Perreault, H. Jaramillo, M. Xie, M. Ude, L. D. Nghiem and M. Elimelech, Biofouling Mitigation in Forward Osmosis Using Graphene Oxide Functionalized Thin-Film Composite Membranes, *Environ. Sci. Technol.*, 2016, **50**(11), 5840–5848.

21 Y. F. Dufrene, Sticky microbes: Forces in microbial cell adhesion, *Trends Microbiol.*, 2015, **23**(6), 376–382.

22 J. Xue, S. BinAhmed, Z. Wang, N. G. Karp, B. L. Stottrup and S. Romero-Vargas Castrillón, Bacterial Adhesion to Graphene Oxide (GO)-Functionalized Interfaces Is Determined by Hydrophobicity and GO Sheet Spatial Orientation, *Environ. Sci. Technol. Lett.*, 2018, **5**(1), 14–19.

23 D. Rice, A. C. Barrios, Z. Xiao, A. Bogler, E. Bar-Zeev and F. Perreault, Development of anti-biofouling feed spacers to improve performance of reverse osmosis modules, *Water Res.*, 2018, **145**, 599–607.

24 S. Kang and M. Elimelech, Bioinspired single bacterial cell force spectroscopy, *Langmuir*, 2009, **25**(17), 9656–9659.

25 S. M. Hinsa, M. Espinosa-Urgel, J. L. Ramos and G. A. O'Toole, Transition from reversible to irreversible attachment during biofilm formation by Pseudomonas fluorescens WCS365 requires an ABC transporter and a large secreted protein, *Mol. Microbiol.*, 2003, **49**(4), 905–918.

26 I. E. Ivanov, C. D. Boyd, P. D. Newell, M. E. Schwartz, L. Turnbull and M. S. Johnson, *et al.* Atomic force and super-resolution microscopy support a role for LapA as a cell-surface biofilm adhesin of Pseudomonas fluorescens, *Res. Microbiol.*, 2012, **163**(9–10), 685–691.

27 H. Wang and H. R. Brown, Self-initiated photopolymerization and photografting of acrylic monomers, *Macromol. Rapid Commun.*, 2004, **25**(11), 1095–1099.

28 J. Deng, L. Wang, L. Liu and W. Yang, Developments and new applications of UV-induced surface graft polymerizations, *Prog. Polym. Sci.*, 2009, **34**(2), 156–193.

29 B. Van Der Bruggen, Chemical modification of polyethersulfone nanofiltration membranes: A review, *J. Appl. Polym. Sci.*, 2009, **114**(1), 630–642.

30 E. Igbinigun, Y. Fennell, R. Malaisamy, K. L. Jones and V. Morris, Graphene oxide functionalized polyethersulfone membrane to reduce organic fouling, *J. Membr. Sci.*, 2016, **514**, 518–526.

31 M. Homayoonfal, A. Akbari and M. R. Mehrnia, Preparation of polysulfone nanofiltration membranes by UV-assisted grafting polymerization for water softening, *Desalination*, 2010, **263**(1–3), 217–225.

32 D. Li, M. B. Müller, S. Gilje, R. B. Kaner and G. G. Wallace, Processable aqueous dispersions of graphene nanosheets, *Nat. Nanotechnol.*, 2008, **3**(2), 101–105, Available from: http://www.nature.com/doifinder/10.1038/nnano.2007.451.

33 K. N. Kudin, B. Ozbas, H. C. Schniepp, R. K. Prud'homme, I. A. Aksay and R. Car, Raman spectra of graphite oxide and functionalized graphene sheets, *Nano Lett.*, 2008, **8**(1), 36–41.

34 Z. Grabarek and J. Gergely, Zero-length crosslinking procedure with the use of active esters, *Anal. Biochem.*, 1990, **185**(1), 131–135.

35 S. L. Walker, S. Bhattacharjee, E. M. V. Hoek and M. Elimelech, A novel asymmetric clamping cell for measuring streaming potential of flat surfaces, *Langmuir*, 2002, **18**(6), 2193–2198.

36 S. Binahmed, A. Hasane, Z. Wang, A. Mansurov and S. Romero-Vargas Castrillón, Bacterial Adhesion to Ultrafiltration Membranes: Role of Hydrophilicity, Natural Organic Matter, and Cell-Surface Macromolecules, *Environ. Sci. Technol.*, 2018, **52**(1), 162–172.

37 H. Ma, R. H. Davis and C. N. Bowman, Novel sequential photoinduced living graft polymerization, *Macromolecules*, 2000, **33**(2), 331–335.

38 C. Klaysom, B. P. Ladewig, G. Q. M. Lu and L. Wang, Preparation and characterization of sulfonated polyethersulfone for cation-exchange membranes, *J. Membr. Sci.*, 2011, **368**(1–2), 48–53.

39 E. Pretsch, P. Bühlmann and C. Affolter, *Structure Determination of Organic Compounds*, Springer, 3rd edn, 2000, p. 338.

40 L. Wang, X. Song, T. Wang, S. Wang, Z. Wang and C. Gao, Fabrication and characterization of polyethersulfone/carbon nanotubes (PES/CNTs) based mixed matrix membranes (MMMs) for nanofiltration application, *Appl. Surf. Sci.*, 2015, **330**, 118–125.

41 P. J. Evans, M. R. Bird, A. Pihlajamäki and M. Nyström, The influence of hydrophobicity, roughness and charge upon ultrafiltration membranes for black tea liquor clarification, *J. Membr. Sci.*, 2008, **313**(1–2), 250–262.

42 A. Weis, M. R. Bird, M. Nyström and C. Wright, The influence of morphology, hydrophobicity and charge upon the long-term performance of ultrafiltration membranes fouled with spent sulphite liquor, *Desalination*, 2005, **175**(1 SPEC. ISS), 73–85.

43 H. Susanto and M. Ulbricht, Characteristics, performance and stability of polyethersulfone ultrafiltration membranes prepared by phase separation method using different macromolecular additives, *J. Membr. Sci.*, 2009, **327**(1–2), 125–135.

44 S. Kasemset, Z. He, D. J. Miller, B. D. Freeman and M. M. Sharma, Effect of polydopamine deposition conditions on polysulfone ultrafiltration membrane properties and threshold flux during oil/water emulsion filtration, *Polymer*, 2016, **97**, 247–257.

45 N. Park, B. Kwon, I. S. Kim and J. Cho, Biofouling potential of various NF membranes with respect to bacteria and their soluble microbial products (SMP): Characterizations, flux decline, and transport parameters, *J. Membr. Sci.*, 2005, **258**(1–2), 43–54.

46 M. Pasmore, P. Todd, S. Smith, D. Baker, J. A. Silverstein and D. Coons, *et al.* Effects of ultrafiltration membrane surface properties on Pseudomonas aeruginosa biofilm initiation for the purpose of reducing biofouling, *J. Membr. Sci.*, 2001, **194**(1), 15–32.

47 E. M. Vrijenhoek, S. Hong and M. Elimelech, Influence of membrane surface properties on initial rate of colloidal fouling of reverse osmosis and nanofiltration membranes, *J. Membr. Sci.*, 2001, **188**(1), 115–128.

48 M. Elimelech, X. Zhu, A. E. Childress and S. Hong, Role of membrane surface morphology in colloidal fouling of cellulose acetate and composite aromatic polyamide reverse osmosis membranes, *J. Membr. Sci.*, 1997, **127**(1), 101–109.

49 T. Wu, P. Gong, I. Szleifer, P. Vlček, V. Šubr and J. Genzer, Behavior of surface-anchored poly(acrylic acid) brushes with grafting density gradients on solid substrates: 1. Experiment, *Macromolecules*, 2007, **40**(24), 8756–8764.

50 T. A. Camesano, Y. Liu and M. Datta, Measuring bacterial adhesion at environmental interfaces with single-cell and single-molecule techniques, *Adv. Water Resour.*, 2007, **30**(6–7), 1470–1491.

51 S. El-Kirat-Chatel, A. Beaussart, C. D. Boyd, G. A. O'Toole and Y. F. Dufrêne, Single-cell and single-molecule analysis deciphers the localization, adhesion, and mechanics of the biofilm adhesin LapA, *ACS Chem. Biol.*, 2014, **9**(2), 485–494.

52 A. Ronen, W. Duan, I. Wheeldon, S. Walker and D. Jassby, Microbial Attachment Inhibition through Low-Voltage Electrochemical Reactions on Electrically Conducting Membranes, *Environ. Sci. Technol.*, 2015, **49**(21), 12741–12750.

53 G. Zeng, T. Müller and R. L. Meyer, Single-cell force spectroscopy of bacteria enabled by naturally derived proteins, *Langmuir*, 2014, **30**(14), 4019–4025.

54 S. J. Vesper, Production of Pili (Fimbriae) by Pseudomonas fluorescens and Correlation with Attachment to Corn Roots, *Appl. Environ. Microbiol.*, 1987, **53**(7), 1397–1405, Available from: http://www.ncbi.nlm.nih.gov/pubmed/16347370%5Cnhttp://www.pubmedcentral.nih.gov/articlerender.fcgi?artid=PMC203883.

55 N. Dasgupta, S. K. Arora and R. Ramphal, *The Flagellar System of Pseudomonas aeruginosa BT - Pseudomonas: Volume 1 Genomics, Life Style and Molecular Architecture*, ed. J.-L. Ramos, Springer US, Boston, MA, 2004, pp. 675–698, DOI: 10.1007/978-1-4419-9086-0_22.

56 Y. L. Ong, A. Razatos, G. Georgiou and M. M. Sharma, Adhesion forces between E. coli bacteria and biomaterial surfaces, *Langmuir*, 1999, **15**(8), 2719–2725.

57 S. Pasche, M. Textor, L. Meagher, N. D. Spencer and H. J. Griesser, Relationship between interfacial forces measured by colloid-probe atomic force microscopy and protein resistance of poly(ethylene glycol)-grafted poly(L-lysine) adlayers on niobia surfaces, *Langmuir*, 2005, **21**(14), 6508–6520.

58 S. Gon, K. N. Kumar, K. Nüsslein and M. M. Santore, How bacteria adhere to brushy PEG surfaces: Clinging to flaws and compressing the brush, *Macromolecules*, 2012, **45**(20), 8373–8381.

59 K. Erickson, R. Erni, Z. Lee, N. Alem, W. Gannett and A. Zettl, Determination of the local chemical structure of graphene oxide and reduced graphene oxide, *Adv. Mater.*, 2010, **22**(40), 4467–4472.

60 L. J. Cote, J. Kim, V. C. Tung, J. Luo, F. Kim and J. Huang, Graphene oxide as surfactant sheets, *Pure Appl. Chem.*, 2010, **83**(1), 95–110, Available from: https://www.degruyter.com/view/j/pac.2011.83.issue-1/pac-con-10-10-25/pac-con-10-10-25.xml.

61 J. Kim, L. J. Cote, F. Kim, W. Yuan, K. R. Shull and J. Huang, Graphene oxide sheets at interfaces, *J. Am. Chem. Soc.*, 2010, **132**(23), 8180–8186.

62 Z. Liu, J. T. Robinson, X. Sun and H. Dai, PEGylated nanographene oxide for delivery of water-insoluble cancer drugs, *J. Am. Chem. Soc.*, 2008, **130**(33), 10876–10877.

63 M. Rief, M. Gautel, F. Oesterhelt, J. M. Fernandez and H. E. Gaub, Reversible Unfolding of Individual Titin Immunoglobulin Domains by AFM, *Science*, 1997, **276**(5315), 1109–1112, DOI: 10.1126/science.276.5315.1109.

64 G. Francius, D. Alsteens, V. Dupres, S. Lebeer, S. De Keersmaecker and J. Vanderleyden, *et al.* Stretching polysaccharides on live cells using single molecule force spectroscopy, *Nat. Protoc.*, 2009, **4**(6), 939–946.

65 H. Li, B. Liu, X. Zhang, C. Gao, J. Shen and G. Zou, Single-molecule force spectroscopy on poly(acrylic acid) by AFM, *Langmuir*, 1999, **15**(6), 2120–2124.

66 G. Stirnemann, D. Giganti, J. M. Fernandez and B. J. Berne, Elasticity, structure, and relaxation of extended proteins under force, *Proc. Natl. Acad. Sci. U. S. A.*, 2013, **110**(10), 3847–3852, DOI: 10.1073/pnas.1300596110.

67 M. Carrion-Vazquez, A. F. Oberhauser, S. B. Fowler, P. E. Marszalek, S. E. Broedel and J. Clarke, *et al.* Mechanical and chemical unfolding of a single protein: a comparison, *Proc. Natl. Acad. Sci. U. S. A.*, 1999, **96**(7), 3694–3699, Available from: http://www.ncbi.nlm.nih.gov/pubmed/10097099%0Ahttp://www.pubmedcentral.nih.gov/articlerender.fcgi?artid=PMC22356.

68 A. Filloux, S. de Bentzmann, M. Aurouze, A. Lazdunski and I. Vallet, Fimbrial Genes in *Pseudomonas Aeruginosa* and Pseudomonas Putida, in *Pseudomonas*, ed. J. L. Ramos, 2004, pp. 721–748.

69 O. Akhavan and E. Ghaderi, Toxicity of graphene and graphene oxide nanowalls against bacteria, *ACS Nano*, 2010, **4**(10), 5731–5736.

Electronic Supplementary Material (ESI) for Environmental Science: Nano.

Do Graphene Oxide Nanostructured Coatings Mitigate Bacterial Adhesion?

Electronic Supplementary Information

Karl Wuolo-Journey[1♠], Sara BinAhmed[1♠], Elise Linna[1], Santiago Romero-Vargas Castrillón[1, 2, 3 *]

Environmental Science: Nano

[1] Department of Civil, Environmental, and Geo- Engineering, University of Minnesota, 500 Pillsbury Dr. SE, Minneapolis, MN 55455, USA
[2] Institute for Infrastructure and Environment, School of Engineering, The University of Edinburgh, William Rankine Building, Thomas Bayes Road, Edinburgh EH9 3FG United Kingdom
[3] Institute for Materials and Processes, School of Engineering, The University of Edinburgh, Sanderson Building, Robert Stevenson Road, Edinburgh EH9 3FB United Kingdom

*Corresponding author:
Santiago Romero-Vargas Castrillón, Santiago@ed.ac.uk, sromerov@umn.edu
Tel: +44(0)131 651 3567
♠These authors contributed equally to this work

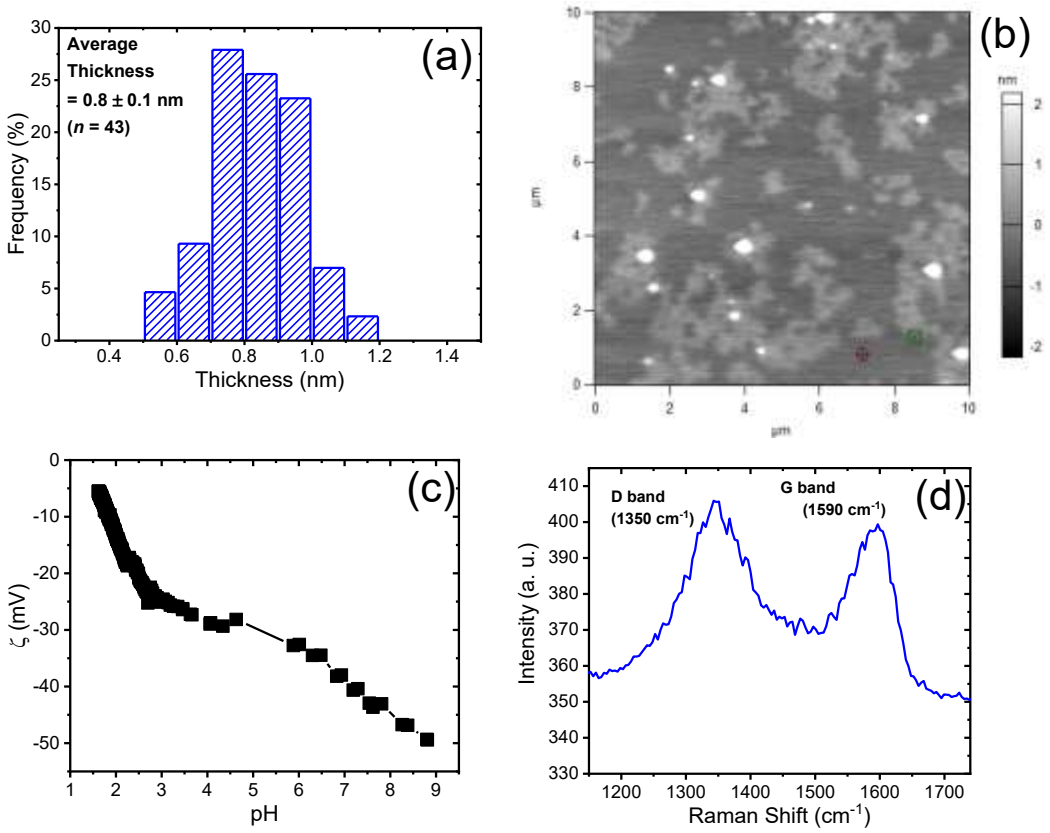

Figure S1. Characterization of graphene oxide (GO) nanosheets: (a) distribution of nanosheet thickness determined by AC mode AFM in air using an AC160TS-R3 Si cantilever (Olympus) with nominal spring constant 26 N m^{-1} and resonance frequency 300 Hz; (b) representative AFM image of GO nanosheets deposited on a Si substrate; (c) ζ-Potential of GO in aqueous dispersion at a concentration of 250 μg mL^{-1}, determined with a Stabino zeta potential analyzer; (d) Raman spectrum of GO nanosheets deposited on a silicon wafer.

Bacterial Deposition Assay. To complement our AFM results, we carried out a bacterial deposition assay to evaluate the bioadhesion propensity of the substrates. The assay entails exposure of the membrane surfaces to a *P. fluorescens* suspension under agitation, followed by colony counting from irreversibly adhered cells.[1] *P. fluorescens* ATCC 13525 was cultured overnight in 50 mL of autoclaved LB broth at 30 °C in an incubator (ThermoScientific MAXQ4450) under stirring (125 rpm). Bacterial suspensions were diluted 1:25 in autoclaved LB broth, and incubated for a further three hours at 175 rpm and 30 °C. Cells were harvested in mid-exponential phase ($OD_{600\ nm} \approx 0.6$) and centrifuged thrice at 5000g (for 1 min), re-suspending the pellet after each centrifugation in 1 mL PBS (pH 7.4). After the final re-suspension, 1-cm^2 substrate coupons were placed at the bottom of scintillation vials and each was immersed in 1 mL of the bacterial suspension, such that the entire coupon was fully covered by the liquid. The scintillation vials were then placed in the incubator (ThermoScientific MAXQ4450) at 30 °C under 175 rpm agitation. After 1 hour, substrates were removed from the suspension, gently rinsed with PBS, and placed in 10 mL of fresh PBS in 50-mL falcon tubes. Following bath sonication for 10 minutes, the resulting suspension was diluted 1:100, and a 50-µL aliquot of the dilution was smeared over an agar plate with a sterilized glass rod. After incubation overnight at 30 °C, the colonies were counted. This experiment was repeated two additional times for each substrate type for a total of three replicates.

The results of the bacterial deposition assay are presented in Fig. S2, showing the number of colony forming units (CFU) normalized by the PES control. Adhesion is significantly mitigated on PES-GO substrates, with the number of colonies on the PES-GO surface being 8.1% of the control PES following a 1-h exposure ($p < 0.05$, one-sided unpaired *t*-test).

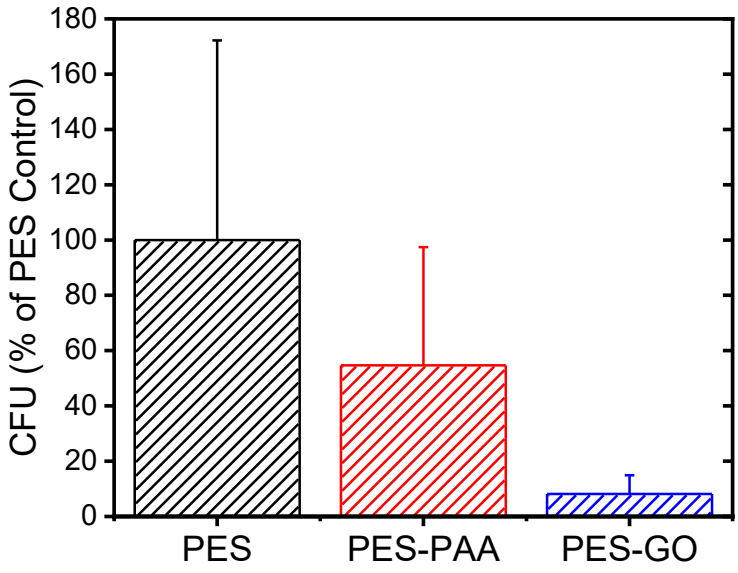

Figure S2. Bacterial deposition assay of pristine PES, poly(acrylic acid) (PAA)-modified PES (PES-PAA), and GO-modified PES (PES-GO) substrates. Colony-forming units (CFU) are shown as % of the PES control. Error bars denote the standard deviation of three experiments.

It is important to note that the CFU data in Fig. S2 are possibly influenced by the cytotoxicity of GO.[1–4] Thus, the precipitous drop in CFU count on PES-GO compared to PES and PES-PAA may be due to a combination of lower adhesion and GO's biocidal activity. However, the relative contributions to the CFU count of adhesion mitigation (due to the interfacial properties of PES-GO) and biocidal activity cannot be disentangled with this simple colony counting assay, and thus would require further investigation.

Characterization of Membrane Transport Properties. The water permeability coefficient (A) of the membranes was determined in a laboratory-scale filtration apparatus equipped with a crossflow cell (CF042D, Sterlitech, with active membrane area, A_m, of 42.1 cm^2), pump (HydraCell M-03S, Wanner Engineering), and temperature-controlled stainless steel feed reservoir. Membranes were compacted with a distilled water feed for 24 hours at a transmembrane

pressure difference (Δp) of 50 psi and crossflow velocity of 0.08 m s^{-1}. Following compaction, measurements of the steady-state permeate flow rate were recorded every second for 1 hour at Δp = 50 psi and 20 °C with a digital flow meter (SLI, Sensirion). The average permeate flow rate, Q_p, was used to compute the water permeability coefficient from $A = Q_p/(A_m \Delta p)$. For control polyethersulfone (PES) membranes, the flux through the membranes was determined by weighing the permeate, since the permeate flow rate exceeded the maximum flow rate measurable with the digital flow meter. Four poly(acrylic acid)-modified (PES-PAA), four GO-modified (PES-GO) and two control PES membranes were characterized.

Effect of Surface Functionalization on Water Permeability and Ion Rejection. Surface modification of the PES membranes resulted in additional hydraulic resistance that decreased the water permeability coefficient (A). For pristine PES we find $A = 102.1 \pm 3.5$ L m^{-2} h^{-1} bar^{-1}. On the other hand, for PES-PAA membranes (prepared by acrylic acid polymerization with 10-s UV exposure), we find $A = 9.0 \pm 1.8$ L m^{-2} h^{-1} bar^{-1}, while for PES-GO, $A = 7.0 \pm 0.7$ L m^{-2} h^{-1} bar^{-1}, i.e., the covalently bonded GO layer further decreases water permeability. We also determined the Na_2SO_4 rejection coefficient (R) at Δp = 50 psi (feed concentration = 10 mM) for the functionalized membranes using a conductivity probe, finding R = 21.4% and 42.7% for PES-GO and PES-PAA, respectively. The A coefficient and ion rejection of PES-PAA and PES-GO materials are similar to those of nanofiltration membranes.[5,6] Additional experiments with PES-PAA membranes prepared with 20-60 sec UV irradiation resulted in steep loss in water permeability (results not shown), due to the formation of a dense PAA layer (observe the prominent carboxyl band at 1700 cm^{-1} when the irradiation time was ≥ 20 s, Fig. 2).

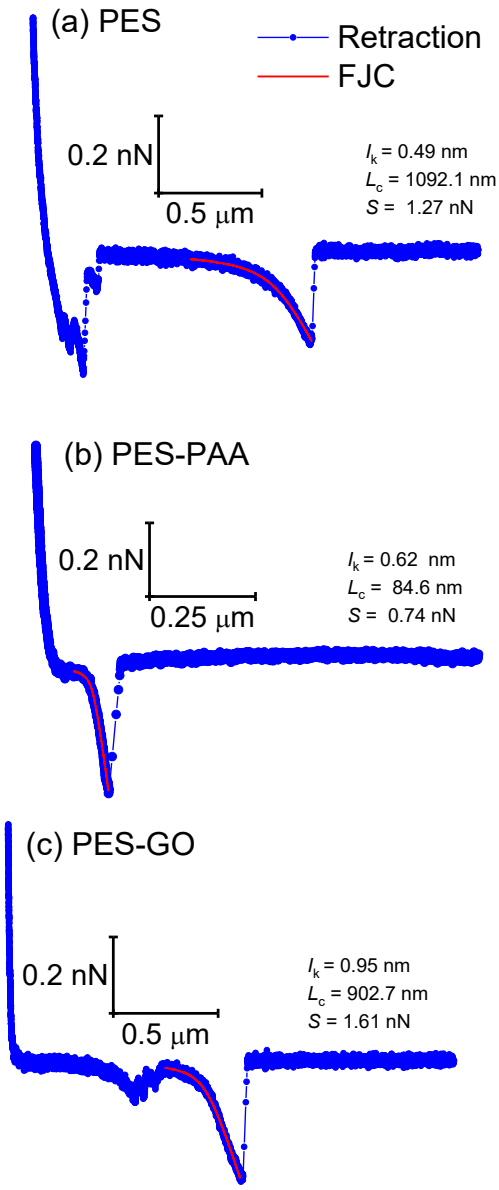

Figure S3. Representative retraction force (F)-elongation (z) curves for different membrane substrates (see caption) recorded with *P. fluorescens* bacterial probes. The data show fits of the extended freely-jointed chain (FJC) model, given by $z(F) = L_c\left[\coth\left(\frac{Fl_k}{k_BT}\right) - \frac{k_BT}{Fl_k}\right]\left(1 + \frac{F}{S}\right)$, where L_c is the contour length, l_k is the Kuhn length, and S is the stretch modulus of the polymer; k_B and T = 298.15 K are Boltzmann's constant and absolute temperature, respectively. Best-fit values of L_c, l_k and S are given in the caption. Due to the thermal noise underlying the measurements (≈ 30 pN), the fitted region of the force-extension curves was smoothed using a locally weighted least-squares smoothing algorithm (loess) implemented in Origin 2018 (Northampton, MA). FJC parameters were obtained by non-linear regression of the smoothed data using the function nlinfit in Matlab R2018a (MathWorks, Natick, MA).

Literature Cited

1. Perreault, F., Tousley, M. E. & Elimelech, M. Thin-Film Composite Polyamide Membranes Functionalized with Biocidal Graphene Oxide Nanosheets. *Environ. Sci. Technol. Lett.* **1**, 71–76 (2013).
2. Perreault, F., De Faria, A. F., Nejati, S. & Elimelech, M. Antimicrobial Properties of Graphene Oxide Nanosheets: Why Size Matters. *ACS Nano* **9**, 7226–7236 (2015).
3. Akhavan, O. & Ghaderi, E. Toxicity of graphene and graphene oxide nanowalls against bacteria. *ACS Nano* **4**, 5731–5736 (2010).
4. Gurunathan, S., Han, J. W., Dayem, A. A., Eppakayala, V. & Kim, J. H. Oxidative stress-mediated antibacterial activity of graphene oxide and reduced graphene oxide in Pseudomonas aeruginosa. *Int. J. Nanomedicine* **7**, 5901–5914 (2012).
5. Bouchoux, A., Roux-de Balmann, H. & Lutin, F. Investigation of nanofiltration as a purification step for lactic acid production processes based on conventional and bipolar electrodialysis operations. *Sep. Purif. Technol.* **52**, 266–273 (2006).
6. Do, V. T., Tang, C. Y., Reinhard, M. & Leckie, J. O. Effects of hypochlorous acid exposure on the rejection of salt, polyethylene glycols, boron and arsenic(V) by nanofiltration and reverse osmosis membranes. *Water Res.* **46**, 5217–5223 (2012).

Environmental Science & Technology Letters

Letter

Cite This: Environ. Sci. Technol. Lett. 2018, 5, 14−19

pubs.acs.org/journal/estlcu

Bacterial Adhesion to Graphene Oxide (GO)-Functionalized Interfaces Is Determined by Hydrophobicity and GO Sheet Spatial Orientation

Jinkai Xue,*[,†,♦] Sara BinAhmed,[†,♦] Zhaoxing Wang,[†] Nathan G. Karp,[†] Benjamin L. Stottrup,[‡] and Santiago Romero-Vargas Castrillón*[,†]

[†]Department of Civil, Environmental, and Geo-Engineering, University of Minnesota, Twin Cities, 500 Pillsbury Dr. SE, Minneapolis, Minnesota 55455, United States

[‡]Department of Physics, Augsburg University, Minneapolis, Minnesota 55454, United States

Supporting Information

ABSTRACT: The potential of graphene oxide (GO) in environmental applications, such as the development of antimicrobial materials and low-fouling membranes, has thus far been hindered by an incomplete understanding of bioadhesion mechanisms on GO interfaces. Using atomic force microscopy (AFM)-based single-cell force spectroscopy, we investigate the adhesion of single *Pseudomonas fluorescens* cells on GO-functionalized interfaces possessing distinct morphologies. Specifically, we investigate Si-GO surfaces, in which Langmuir−Blodgett GO films are transferred to Si wafers by dip-coating, forming an immobilized layer of horizontally arranged GO nanosheets, and PLL-GO surfaces, where GO nanosheets, edge-tethered to poly-L-lysine, form an interface characterized by morphological and conformational disorder. We observe strong adhesion forces on both Si-GO and PLL-GO surfaces; analysis of the pull-off forces in terms of the worm-like chain model reveals that adhesion is driven by hydrophobic interactions between proteinaceous adhesins on *P. fluorescens* and graphenic basal planes. We further show that adhesion forces are significantly stronger on Si-GO surfaces that facilitate interactions with graphenic planes, compared to PLL-GO surfaces, which show weaker adhesion due to steric and electrostatic repulsion. These results therefore demonstrate that the spatial orientation and conformational disorder of GO nanosheets are key factors governing the interfacial properties of graphene nanomaterials.

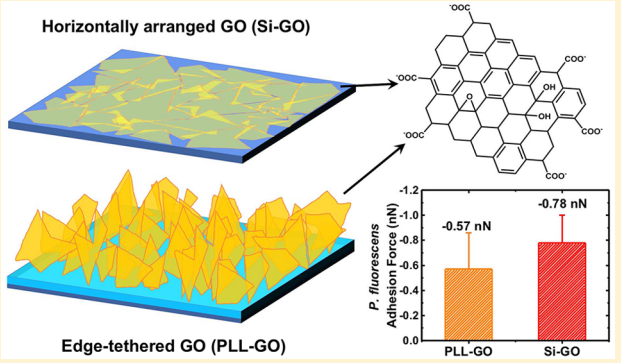

1. INTRODUCTION

The significant interest in graphene nanomaterials is motivated by their unique physical and chemical properties. Graphene is the thinnest, strongest material ever developed.[1] As a 2-D nanomaterial with metallic properties, it is finding applications in electronic and photovoltaic devices.[2] The high surface area and photocatalytic-enhancing properties of graphene hold promise in environmental remediation, adsorption, degradation of organic contaminants, and the development of water purification membranes.[2,3] Furthermore, graphene and graphene oxide (GO) exhibit wide-spectrum antibacterial activity,[4−9] opening new avenues for the development of biocidal materials and interfaces, such a low-biofouling membranes.[10,11] Nonetheless, further deployment of graphene-based biocidal materials has been hindered by an incomplete understanding of the adhesion mechanisms of bacteria on graphenic interfaces. Previous studies have attempted to explain the interactions between cells and individual graphenic sheets in suspension, with contradictory conclusions documented by different investigators. Li et al.[12] and Tu et al.,[13] using a combination of microscopy and simulation, proposed that graphene[12,13] and GO sheets[13] pierce lipid bilayers via sheet asperities or edges; a mechanism for bilayer piercing was provided based on molecular dynamics simulation, which showed spontaneous piercing of the cell membrane when graphene and GO sheets translocate orthogonally to the cell.[12,13] On the other hand, AFM-based force spectroscopy measurements showed that the interactions of a GO-coated AFM probe with *E. coli* cell membranes were predominantly repulsive, possibly due to negatively charged GO sheet edges, which result in electrostatic repulsive forces as the nanosheets impinge on the cell membrane edge-first.[12,14] These studies suggest that GO sheet spatial orientation plays an important role in determining the behavior of interfaces functionalized with GO. The relevance of nanosheet configuration is underscored by reports that nanosheet edge-bacteria contact is a determinant of biocidal activity,[9,15] with a recent

Received: November 12, 2017
Revised: December 7, 2017
Accepted: December 13, 2017
Published: December 13, 2017

DOI: 10.1021/acs.estlett.7b00509
Environ. Sci. Technol. Lett. 2018, 5, 14−19

study reporting higher biocidal activity in GO films comprising, edge-exposed, vertically aligned nanosheets,[16] though this view remains contentious.[17−19] Nonetheless, direct, real-time experimental measurements examining the adhesion forces of bacteria on GO surfaces and the possible role played by GO sheet orientation in GO-cell adhesion forces are still lacking. In this work, we use atomic force microscopy (AFM)-based force spectroscopy to quantitatively evaluate the interactions of single *P. fluorescens* cells, a biofilm forming,[20,21] environmentally relevant bacterium found in soil and drinking water,[22,23] with substrates possessing horizontally oriented or randomly oriented GO surface coatings. We find strong bacterial adhesion on GO-functionalized surfaces, driven by hydrophobic interactions between proteinaceous adhesins and graphenic basal planes in GO. Further, we demonstrate that *P. fluorescens* adhesion is stronger on "flat" GO surface coatings as compared to randomly oriented surface coatings, demonstrating the importance of spatial orientation of GO as a design variable in GO surface coatings.

2. MATERIALS AND METHODS

2.1. Preparation of GO and GO Model Surfaces. GO was prepared following a modification of Hummers' method, as explained in the Supporting Information (SI).[24] Confocal Raman spectroscopy, AFM, and scanning electron microscopy (SEM) were performed to characterize the GO sheets. The characteristic D (∼1350 cm^{-1}) and G (∼1590 cm^{-1}) bands[25] of GO were identified in the Raman spectrum (Figure S1(a)). GO sheets showed an average sheet size (Figure S1(b)) of ∼0.08 μm (SEM images were analyzed with Fiji[26]) and sheet thickness (Figure S1(c, d)) of ∼1 nm, in agreement with previous reports.[14] Zeta potential measurements of GO in aqueous dispersion (Figure S1(e)) showed that the nanosheets are negatively charged, due to deprotonation of carboxylic acid groups at the sheet edges.[27,28]

Two model GO surfaces (i.e., randomly oriented GO sheets and horizontally oriented GO sheets) were prepared. The first class (denoted as PLL-GO surfaces) was prepared by covalently tethering GO sheets to poly-L-lysine (PLL)-coated glass (Poly-Prep slides, Sigma-Aldrich) via amine coupling chemistry.[29] The second class of surfaces (designated Si-GO) was prepared by transferring a GO Langmuir−Blodgett (LB) film[17] to a P-type silicon (Si) wafer via dip-coating.[30] Details on the preparation of GO surfaces can be found in the SI. GO immobilized on the PLL-GO and Si-GO surfaces was confirmed by Raman spectroscopy. Surface roughness, hydrophobicity, and zeta potential were evaluated using AFM, captive bubble contact angle, and streaming current measurements, respectively, as described in the SI.

2.2. AFM-Based Single Cell Force Spectroscopy. *Pseudomonas fluorescens* ATCC 13525 was used in all single-cell force spectroscopy (SCFS) experiments. As in other bacteria of the *Pseudomonas* genus, *P. fluorescens* has high biodhesion and biofilm formation potential, owing to an array of adhesins,[31] including flagella, pili, lipopolysaccharides (LPS), and outer membrane proteins (OMP) that influence its motility and adhesiveness.[32−35] Single *P. fluorescens* cells were adhered to the cantilever using a polydopamine (PDA) wet adhesive.[36,37] Details of the bacterial growth conditions and preparation of bacterial cell AFM probes are given in our recent publication[38] and summarized in the SI.

An MFP-3D-Bio AFM (Asylum Research) integrated to a Zeiss Axio Observer A.1 inverted optical microscope was used for single-cell force measurements at room temperature (25 °C). Extension−retraction cycles were performed at a cantilever speed of 400 nm/s, force distance of 2 μm (longer force distances were used whenever long-range interactions were observed), and trigger force of 600 pN. Force curves were acquired at randomly chosen sites on the specimen surface; only three replicate force curves were recorded over each site to minimize deposition of extracellular polymeric substances. For each model surface, at least three individual cells (from three independent cell cultures) were used to collect a total of ≈100 curves. Raw data (i.e., cantilever deflection versus piezo Z position) were converted into force−separation curves, recording from each pull-off curve the maximum adhesion force (F_{Ad}) and rupture separation (L_R) (i.e., the separation at which surface forces vanish). Cell viability was checked after each experiment by a live/dead assay (Baclight). Only data collected with a live cell that remained at its initial location (such as that shown in Figure S12) are reported and discussed.

3. RESULTS AND DISCUSSION

3.1. Characterization of the Surfaces. Raman spectroscopy maps and AFM topographic images (collected in PBS buffer, pH 7.4) of the GO surfaces are provided in Figure 1.

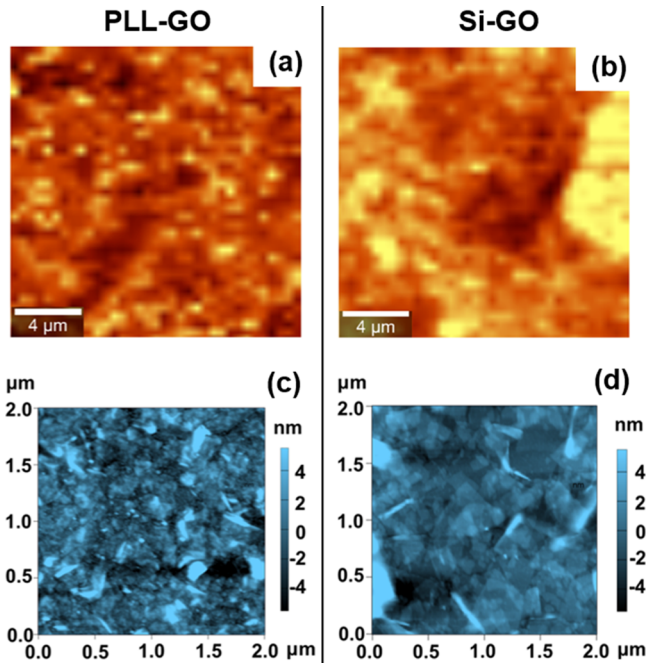

Figure 1. Surface characterization of PLL-GO (left column) and Si-GO surfaces (right column). (a, b) Raman spectroscopy maps of PLL-GO (a) and Si-GO (b) substrates. (c, d) Tapping mode AFM images of PLL-GO (c) and Si-GO (d) substrates. AFM imaging was conducted in PBS buffer, pH 7.4.

The Raman maps (Figure 1(a, b) and Figure S3(a, b)) show regions of high brightness (proportional to the intensity of the D and G peaks of GO), albeit with dissimilar spatial distribution: small (typically <1 μm) regions of high brightness were observed on the PLL-GO surface (Figure 1(a)), whereas the Si-GO surface exhibited larger GO domains (≥1 μm), suggesting the presence of horizontally arranged GO (Figure 1(b)). In control surfaces (GO-free PLL and Si), Raman intensity is significantly attenuated (Figures S3(c, d)). The morphological features of Figure 1(a, b) are consistent with the

DOI: 10.1021/acs.estlett.7b00509
Environ. Sci. Technol. Lett. 2018, 5, 14−19

AFM images (Figure 1(c, d)), showing that two different spatial orientations are realized by these surfaces: GO nanosheets in Si-GO surfaces are stacked horizontally on the Si substrate (Figure 1(d) and Figure S2(b)), whereas a significantly more disordered interface is obtained when GO is tethered to flexible PLL chains (cf. PLL-GO, Figure 1(c) and Figure S2(a)), where horizontally oriented sheets on the substrate are not observed. In accord with the morphological features described in Figure 1, the root-mean-square roughness (R_{RMS}, Figure S4(a)) of PLL-GO (R_{RMS} = 2.78 nm) is higher than that of Si-GO (R_{RMS} = 1.62 nm, which suggests a GO film 1−2 sheets thick on Si). Figure S4(a) further shows that the presence of GO increases the roughness of the unmodified control substrates (note the lower surface roughness of bare PLL and Si surfaces). The orientational disorder of GO nanosheets in PLL-GO is partially due to the roughness of the underlying PLL, and it is also a consequence of bonding GO to primary amines in PLL, which allows edge-tethered solvated nanosheets to undergo thermal agitation. The zeta potential values showed that the four surfaces were negatively charged, exhibiting similar surface potentials (−60 to −90 mV) at pH 7.4 (Figure S4(b)).

The wettability of the surfaces, characterized by the contact angle of captive *n*-decane droplets in PBS (pH 7.4), is presented in Figure S5. Low contact angles (i.e., low *n*-decane wettability) are observed in all surfaces; H-bonding functional groups present in PLL (primary amine groups) and PLL-GO (epoxide, hydroxyl, and carboxylic groups that decorate the GO sheet edges[27,39]) explain the poor wettability with *n*-decane. The similarity of contact angle values observed in Si and Si-GO is consistent with the wetting translucency[40] of graphene films. Given its ultrathin-sheet geometry, a significant fraction of the *n*-decane-Si van der Waals interactions are transmitted through the graphenic planes, resulting in wetting behavior that is relatively unaffected by the graphene coating.[41,42]

3.2. GO Nanosheet Spatial Orientation and Hydrophobicity Are Determining Factors of Bacterial Adhesion. Figure 2(a) presents the mean maximum adhesion force ($\langle F_{Ad} \rangle$, where F_{Ad} is defined in the inset) observed on control and GO surfaces; adhesion force histograms for each system are given in Figure S6. GO functionalization has a significant effect on cell adhesion, as shown by the doubling of $\langle F_{Ad} \rangle$ in PLL-GO compared to PLL substrates and the order-of-magnitude increase in $\langle F_{Ad} \rangle$ observed in Si-GO surfaces compared to the Si control. The mean adhesion forces presented in Figure 2(a) increase as Si (−0.01 nN) < PLL (−0.28 nN) < PLL-GO (−0.57 nN) < Si-GO (−0.78 nN) ($p < 0.01$ from two-sided unpaired *t*-tests); these reflect cell−substrate adhesion forces, as demonstrated by the significantly weaker forces observed in control measurements with bacterium-free PDA-coated cantilevers (Figure S7, $p < 0.01$ except Si, on which weak adhesions are observed with and without cell). To explain the results shown in Figure 2(a), we note that bacterial adhesion is determined by a variety of cell-surface structures, such as pili and outer membrane proteins,[34,35,43] which, owing to the high content of hydrophobic amino acids (in e.g., pilin proteins[43]), mediate attachment to hydrophobic substrates via hydrophobic interactions.[44,45] At the micro- and nanoscales both PLL-GO and Si-GO surfaces present hydrophobic regions embedded in the graphenic planes of the nanosheets,[27,46] which are known to serve as adsorption sites for hydrophobic molecules.[27,47−49] Consequently, the significant increase in $\langle F_{Ad} \rangle$ observed over Si-GO and PLL-GO is ascribed to hydrophobic association of cell-surface adhesins with hydrophobic domains in GO sheets.

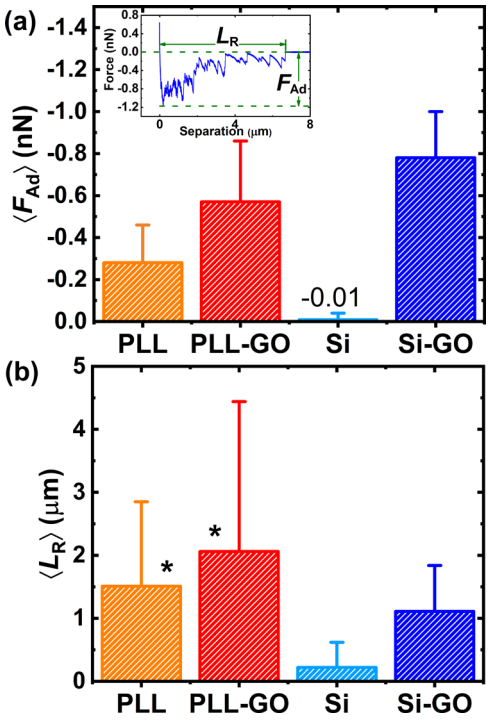

Figure 2. Results of single-cell force spectroscopy. (a) Average maximum adhesion force ($\langle F_{Ad} \rangle$) of *P. fluorescens* cells on the various surfaces. A representative pull-off force curve showing the definition of F_{Ad} and L_R is shown in the inset of panel (a). (b) Mean rupture separation ($\langle L_R \rangle$, the separation at which adhesion forces vanish). All experiments were performed in PBS buffer (pH 7.4). The histograms from which the reported means were computed are given in Figures S6 and S8; $p < 0.01$ (two-tailed unpaired *t*-test) for all pairwise comparisons except when indicated by ∗.

The determining role of hydrophobicity in *P. fluorescens* attachment is underscored by the weak adhesion (∼10 pN, cf. Figure 2(a)) observed on Si substrates, the most hydrophilic surface investigated in this work (cf. Figure S5). Furthermore, we observe stronger ($p < 0.01$) $\langle F_{Ad} \rangle$ over Si-GO than PLL-GO (−0.78 nN vs −0.57 nN, respectively, cf. Figure 2(a)). The different adhesiveness demonstrated by PLL-GO and Si-GO is derived from their respective morphologies. Si-GO surfaces, as shown in Figure 1(d), exhibit horizontally arranged GO sheets, whereas GO sheets tethered to PLL form a rougher and more disordered PLL-GO interface (Figure 1(c) and Figure S4(a)). The flat GO sheet orientation in Si-GO surfaces therefore maximizes the surface area of graphenic planes with which cell biopolymers interact, thereby facilitating bacterial attachment. Low roughness of Si-GO (Figure S4(a)) may also enable bacterial attachment, as observed with pyrolytic graphite.[15] Conversely, bacteria adhering on PLL-GO face negatively charged GO sheet edges,[28] which weaken bacterial attachment due to electrostatic repulsive forces.[14] In addition, GO sheets edge-tethered to PLL create a steric barrier against microbial deposition, akin to that formed by solvated polymers.[50−52] As a bacterium adheres on PLL-GO, GO nanosheets are compressed, the resulting loss of conformational entropy opposing cell adhesion.[50] These data thus demonstrate that nanosheet spatial arrangement (i.e., flat vs randomly oriented) and conformational degrees of freedom play key roles in determining the GO-bacterial cell adhesion forces.

To gain insight into the cell-surface structures mediating adhesion, we analyzed the rupture distance (L_R), defined in

DOI: 10.1021/acs.estlett.7b00509
Environ. Sci. Technol. Lett. 2018, 5, 14−19

Figure 2(a) (inset). The values of the mean rupture distance ($\langle L_R \rangle$) are presented in Figure 2(b), and the distributions of L_R appear in Figure S8. Apart from the Si control, over which no significant adhesion is observed, mean L_R values reported by PLL, PLL-GO, and Si-GO surfaces (1−2 μm) are consistent with bioadhesion mediated by membrane proteins (contour length ≈2 μm[34,35]); a fraction of measurements showing L_R > 2 μm (Figure S8 for PLL, PLL-GO, and Si-GO) is likely due to pili-mediated adhesion, which can extend to several micrometers.[53,54] Long L_R values may also be attributed to stretching of PLL chains on the glass substrates, as shown by the longer-ranged forces exhibited by PLL and PLL-GO compared to Si-GO substrates (Figure 2(b)).

3.3. Proteinaceous Adhesins Mediate *P. fluorescens* Attachment to GO-Functionalized Interfaces. In a subset (~20%) of the pull-off force−separation profiles recorded on PLL, PLL-GO, and Si-GO, we observed the sawtooth pattern (Figure 3(a)) that is associated with force unfolding of protein domains.[44,55] As shown in the inset of Figure 3(a), the peaks are well fitted by the worm-like chain (WLC) model of polymer elasticity[56,57] which describes the force F necessary to unravel a random coil as $F(x) = k_BT/L_P[0.25(1 - x/L_C)^{-2} + x/L_C - 0.25]$, where x is separation, k_B is the Boltzmann constant, T is the absolute temperature (298 K), L_P is the persistence length (a measure of polymer rigidity), and L_C is the contour length (the length of the unfolded macromolecule). Quantitative analysis of the pull-off force curves in terms of the WLC model yielded values of L_P and L_C (in fitting the WLC model, we discarded nonspecific adhesion peaks at short separation, as well as peaks yielding L_P < 0.15 nm, the length of a C−C bond[58]). We find that best-fit L_P values were narrowly distributed with means in the 0.23−0.28 nm range (Figure 3(b) and Figure S9), close to the persistence length of proteins (~0.4−1 nm[34,55,59,60]), and observed that the mean peak force (F_{Unf}, defined in Figure 3(a)) was consistent with the unfolding force of membrane proteins (~300 pN, cf. Figure 3(c) and Figure S10).[34,55] The values of L_P and F_{Unf} suggest that adhesion of *P. fluorescens* is mediated by proteinaceous hydrophobic adhesins, likely to be membrane proteins that interact with hydrophobic graphenic planes in GO nanosheets, and lysyl side chains in PLL. The hydrophobic character of adhesin proteins is manifested by the absence of the sawtooth pattern in all force curves recorded over hydrophilic Si substrates. ΔL_C, the difference in contour lengths between consecutive sawtooth peaks, revealed the length scale of the unfolded domains. As shown in Figures S11(b, c), ΔL_C values for PLL-GO and Si-GO were distributed around means of 66.4 and 80.6 nm, respectively, which suggest that each sawtooth peak is due to unfolding of more than one protein domain (whose repeats are ~30−40 nm for membrane proteins[35] and ~50−60 nm in pilin proteins[53]). The broader distribution of ΔL_C observed over PLL (Figure S11(a)) suggests that adhesins undergo surface-induced unfolding over this substrate.[34]

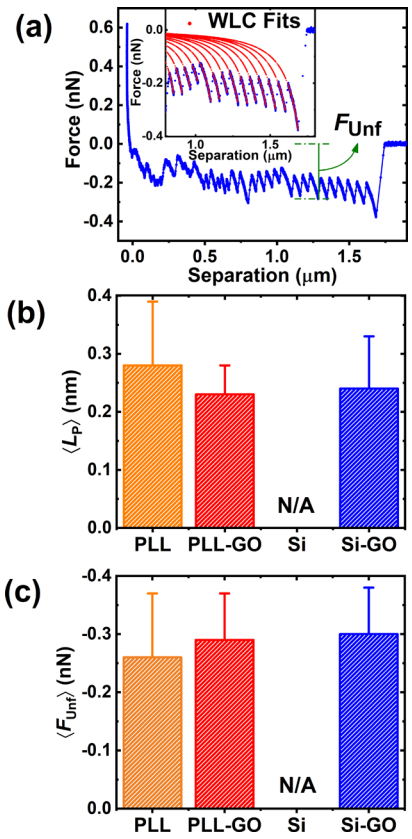

Figure 3. Signatures of macromolecular unfolding observed over different model surfaces. (a) Representative force curve exhibiting the sawtooth pattern characteristic of force-unfolding of macromolecular domains. Representative fits of the worm-like chain (WLC) model to the sawtooth patterns are shown in the inset. (b) Mean persistence length ($\langle L_P \rangle$) obtained from WLC model fits to the pull-off force curve of single *P. fluorescens* cells. (c) Mean unfolding force ($\langle F_{Unf} \rangle$). The definition of F_{Unf} is shown in panel (a). The histograms from which the means in panels (b) and (c) were computed are given in Figures S9 and S10. N/A for Si indicates that no signatures of macromolecular unfolding were observed on this substrate.

In closing, we have demonstrated that the hydrophobic interactions that drive *P. fluorescens* adhesion are stronger in GO interfaces assembled from horizontally arranged nanosheets, as compared to edge-tethered GO sheets where electrostatic and steric repulsion weaken adhesion forces. Our results emphasize the importance of nanosheet hydrophobicity, spatial arrangement, and conformational disorder in determining the interfacial behavior of GO-functionalized substrates, pointing out possible directions for future inquiry. Reactive oxygen species (ROS)-mediated cell oxidation[6,14] is likely to modify cell bioadhesion due to breakdown of the outer membrane. Experiments isolating the competing effect of ROS pose interesting questions that warrant future investigations. Further investigations should also aim to elucidate the mechanism of adhesion of hydrophilic bacteria[61] to graphenic surfaces, perhaps using adhesin-knockout mutants.

■ ASSOCIATED CONTENT

Supporting Information

The Supporting Information is available free of charge on the ACS Publications website at DOI: 10.1021/acs.estlett.7b00509.

Further information on materials and methods (GO synthesis and characterization, preparation and characterization of PLL-GO and Si-GO surfaces, and functionalization of AFM probes with bacterial cells). Results of GO characterization (Figure S1); AFM imaging, Raman spectroscopy images, AFM surface roughness, zeta potential, and contact angle measurements for all surfaces (Figures S2−S5); histograms of adhesion forces (Figures S6 and S7), rupture separations (Figure S8), persistence lengths (Figure S9), unfolding forces (Figure

DOI: 10.1021/acs.estlett.7b00509
Environ. Sci. Technol. Lett. 2018, 5, 14−19

S10), contour lengths (Figure S11); and digital image of bacterial cell AFM probe (Figure S12). (PDF)

AUTHOR INFORMATION

Corresponding Authors

*E-mail: xuexx145@umn.edu. Tel: +1 (226) 505-0458 (Jinkai Xue).

*E-mail: sromerov@umn.edu. Tel: +1 (612) 301-1347 (Santiago Romero-Vargas Castrillón).

ORCID

Santiago Romero-Vargas Castrillón: 0000-0003-3339-7692

Author Contributions

♦J. X. and S. BA. were equal contributors to this work.

Notes

The authors declare no competing financial interest.

ACKNOWLEDGMENTS

This work was supported by grants to S.R.-V.C. from the United States Geological Survey (MN WRC 2015MN362B), 3M Co. (Non-Tenured Faculty Award), and the Environment and Natural Resources Trust Fund, as recommended by the Legislative-Citizen Commission on Minnesota Resources. Portions of this work were carried out in the Characterization Facility and Minnesota Nano Center, University of Minnesota, which receive partial support from NSF through the MRSEC and NNIN programs, respectively. Work at Augsburg University was supported by NSF MRI 1040126.

REFERENCES

(1) Lee, C.; Wei, X.; Kysar, J. W.; Hone, J. Measurement of the elastic properties and intrinsic strength of monolayer graphene. *Science (Washington, DC, U. S.)* **2008**, *321* (5887), 385−388.

(2) Zhu, Y.; Murali, S.; Cai, W.; Li, X.; Suk, J. W.; Potts, J. R.; Ruoff, R. S. Graphene and graphene oxide: Synthesis, properties, and applications. *Adv. Mater.* **2010**, *22* (35), 3906−3924.

(3) Hu, M.; Mi, B. Enabling graphene oxide nanosheets as water separation membranes. *Environ. Sci. Technol.* **2013**, *47* (8), 3715−3723.

(4) Chen, J.; Peng, H.; Wang, X.; Shao, F.; Yuan, Z.; Han, H. Graphene oxide exhibits broad-spectrum antimicrobial activity against bacterial phytopathogens and fungal conidia by intertwining and membrane perturbation. *Nanoscale* **2014**, *6* (3), 1879−1889.

(5) Hu, W.; Peng, C.; Luo, W.; Lv, M.; Li, X.; Li, D.; Huang, Q.; Fan, C. Graphene-based antibacterial paper. *ACS Nano* **2010**, *4* (7), 4317−4323.

(6) Perreault, F.; De Faria, A. F.; Nejati, S.; Elimelech, M. Antimicrobial properties of graphene oxide nanosheets: Why size matters. *ACS Nano* **2015**, *9* (7), 7226−7236.

(7) Gurunathan, S.; Han, J. W.; Dayem, A. A.; Eppakayala, V.; Kim, J. H. Oxidative stress-mediated antibacterial activity of graphene oxide and reduced graphene oxide in *Pseudomonas aeruginosa*. *Int. J. Nanomed.* **2012**, *7*, 5901−5914.

(8) Chen, J.; Wang, X.; Han, H. A new function of graphene oxide emerges: Inactivating phytopathogenic bacterium. *J. Nanopart. Res.* **2013**, *15* (5), 1−14.

(9) Akhavan, O.; Ghaderi, E. Toxicity of graphene and graphene oxide nanowalls against bacteria. *ACS Nano* **2010**, *4* (10), 5731−5736.

(10) Soroush, A.; Ma, W.; Cyr, M.; Rahaman, M. S.; Asadishad, B.; Tufenkji, N. In situ silver decoration on graphene oxide-treated thin film composite forward osmosis membranes: Biocidal properties and regeneration potential. *Environ. Sci. Technol. Lett.* **2016**, *3* (1), 13−18.

(11) Perreault, F.; Jaramillo, H.; Xie, M.; Ude, M.; Nghiem, L. D.; Elimelech, M. Biofouling mitigation in forward osmosis using graphene oxide functionalized thin-film composite membranes. *Environ. Sci. Technol.* **2016**, *50* (11), 5840−5848.

(12) Li, Y.; Yuan, H.; von dem Bussche, A.; Creighton, M.; Hurt, R. H.; Kane, A. B.; Gao, H. Graphene microsheets enter cells through spontaneous membrane penetration at edge asperities and corner sites. *Proc. Natl. Acad. Sci. U. S. A.* **2013**, *110* (30), 12295−12300.

(13) Tu, Y.; Lv, M.; Xiu, P.; Huynh, T.; Zhang, M.; Castelli, M.; Liu, Z.; Huang, Q.; Fan, C.; Fang, H.; et al. Destructive extraction of phospholipids from Escherichia coli membranes by graphene nanosheets. *Nat. Nanotechnol.* **2013**, *8* (8), 594−601.

(14) Romero-Vargas Castrillón, S.; Perreault, F.; De Faria, A. F.; Elimelech, M. Interaction of graphene oxide with bacterial cell membranes: Insights from force spectroscopy. *Environ. Sci. Technol. Lett.* **2015**, *2* (4), 112−117.

(15) Pham, V. T. H.; Truong, V. K.; Quinn, M. D. J.; Notley, S. M.; Guo, Y.; Baulin, V. A.; Al Kobaisi, M.; Crawford, R. J.; Ivanova, E. P. Graphene induces formation of pores that kill spherical and rod-shaped bacteria. *ACS Nano* **2015**, *9* (8), 8458−8467.

(16) Lu, X.; Feng, X.; Werber, J. R.; Chu, C.; Zucker, I.; Kim, J.-H.; Osuji, C. O.; Elimelech, M. Enhanced antibacterial activity through the controlled alignment of graphene oxide nanosheets. *Proc. Natl. Acad. Sci. U. S. A.* **2017**, *114*, E9793.

(17) Mangadlao, J. D.; Santos, C. M.; Felipe, M. J. L.; de Leon, A. C. C.; Rodrigues, D. F.; Advincula, R. C. On the antibacterial mechanism of graphene oxide (GO) Langmuir−Blodgett films. *Chem. Commun.* **2015**, *51* (14), 2886−2889.

(18) Hui, L.; Piao, J. G.; Auletta, J.; Hu, K.; Zhu, Y.; Meyer, T.; Liu, H.; Yang, L. Availability of the basal planes of graphene oxide determines whether it is antibacterial. *ACS Appl. Mater. Interfaces* **2014**, *6* (15), 13183−13190.

(19) Zucker, I.; Werber, J. R.; Fishman, Z. S.; Hashmi, S. M.; Gabinet, U. R.; Lu, X.; Osuji, C. O.; Pfefferle, L. D.; Elimelech, M. Loss of phospholipid membrane integrity induced by two-dimensional nanomaterials. *Environ. Sci. Technol. Lett.* **2017**, *4* (10), 404−409.

(20) O'Toole, G. A.; Kolter, R. Initiation of biofilm formation in *Pseudomonas fluorescens* WCS365 proceeds via multiple, convergent signalling pathways: A genetic analysis. *Mol. Microbiol.* **1998**, *28* (3), 449−461.

(21) Spiers, A. J.; Rainey, P. B. The *Pseudomonas fluorescens* SBW25 wrinkly spreader biofilm requires attachment factor, cellulose fibre and LPS interactions to maintain strength and integrity. *Microbiology* **2005**, *151* (9), 2829−2839.

(22) Haas, D.; Défago, G. Biological control of soil-borne pathogens by fluorescent pseudomonads. *Nat. Rev. Microbiol.* **2005**, *3* (4), 307−319.

(23) Hardalo, C.; Edberg, S. C. *Pseudomonas aeruginosa*: assessment of risk from drinking water. *Crit. Rev. Microbiol.* **1997**, *23* (1), 47−75.

(24) Tung, V. C.; Allen, M. J.; Yang, Y.; Kaner, R. B. High-throughput solution processing of large-scale graphene. *Nat. Nanotechnol.* **2009**, *4* (1), 25−29.

(25) Kudin, K. N.; Ozbas, B.; Schniepp, H. C.; Prud'homme, R. K.; Aksay, I. A.; Car, R. Raman spectra of graphite oxide and functionalized graphene sheets. *Nano Lett.* **2008**, *8* (1), 36−41.

(26) Schindelin, J.; Arganda-Carreras, I.; Frise, E.; Kaynig, V.; Longair, M.; Pietzsch, T.; Preibisch, S.; Rueden, C.; Saalfeld, S.; Schmid, B.; et al. Fiji: an open-source platform for biological-image analysis. *Nat. Methods* **2012**, *9* (7), 676−682.

(27) Sanchez, V. C.; Jachak, A.; Hurt, R. H.; Kane, A. B. Biological interactions of graphene-family nanomaterials: An interdisciplinary review. *Chem. Res. Toxicol.* **2012**, *25*, 15−34.

(28) Li, D.; Müller, M. B.; Gilje, S.; Kaner, R. B.; Wallace, G. G. Processable aqueous dispersions of graphene nanosheets. *Nat. Nanotechnol.* **2008**, *3* (2), 101−105.

(29) Grabarek, Z.; Gergely, J. Zero-length crosslinking procedure with the use of active esters. *Anal. Biochem.* **1990**, *185* (1), 131−135.

(30) Cote, L. J.; Kim, F.; Huang, J. Langmuir-Blodgett assembly of graphite oxide single layers. *J. Am. Chem. Soc.* **2009**, *131* (3), 1043−1049.

(31) Tamber, S.; Hancock, R. E. W. The outer membranes of *Pseudomonas*. In *Pseudomonas*; Ramos, J. L., Ed.; Springer, 2004; pp 575−601.

DOI: 10.1021/acs.estlett.7b00509
Environ. Sci. Technol. Lett. 2018, 5, 14−19

(32) Dasgupta, N.; Arora, S.; Ramphal, R. The flagellar system of *Pseudomonas aeruginosa*. In *Pseudomonas*; Ramos, J. L., Ed.; 2004; Springer, pp 675−698.
(33) Tolker-Nielsen, T.; Molin, S. The biofilm lifestyle of *Pseudomonas*. In *Pseudomonas*; Ramos, J. L., Ed.; Springer, 2004; pp 547−571.
(34) El-Kirat-Chatel, S.; Boyd, C. D.; O'Toole, G. A.; Dufrene, Y. F. Single-molecule analysis of *Pseudomonas fluorescens* footprints. *ACS Nano* **2014**, *8* (2), 1690−1698.
(35) El-Kirat-Chatel, S.; Beaussart, A.; Boyd, C. D.; O'Toole, G. A.; Dufrene, Y. F. Single-cell and single-molecule analysis deciphers the localization, adhesion, and mechanics of the biofilm adhesin LapA. *ACS Chem. Biol.* **2014**, *9* (2), 485−494.
(36) Lee, H.; Dellatore, S. M.; Miller, W. M.; Messersmith, P. B. Mussel-inspired surface chemistry for multifunctional coatings. *Science (Washington, DC, U. S.)* **2007**, *318* (5849), 426−430.
(37) Kang, S.; Elimelech, M. Bioinspired single bacterial cell force spectroscopy. *Langmuir* **2009**, *25* (17), 9656−9659.
(38) BinAhmed, S.; Hasane, A.; Wang, Z.; Mansurov, A.; Romero-Vargas Castrillón, S. Bacterial adhesion to ultrafiltration membranes: Role of hydrophilicity, natural organic matter, and cell-surface macromolecules. *Environ. Sci. Technol.* **2017**, DOI: 10.1021/acs.est.7b03682.
(39) Park, S.; An, J.; Jung, I.; Piner, R. D.; An, S. J.; Li, X.; Velamakanni, A.; Ruoff, R. S. Colloidal suspensions of highly reduced graphene oxide in a wide variety of organic solvents. *Nano Lett.* **2009**, *9* (4), 1593−1597.
(40) Rafiee, J.; Mi, X.; Gullapalli, H.; Thomas, A. V.; Yavari, F.; Shi, Y.; Ajayan, P. M.; Koratkar, N. A. Wetting transparency of graphene. *Nat. Mater.* **2012**, *11* (3), 217−222.
(41) Shih, C.-J.; Strano, M. S.; Blankschtein, D. Wetting translucency of graphene. *Nat. Mater.* **2013**, *12* (10), 866−869.
(42) Shih, C. J.; Wang, Q. H.; Lin, S.; Park, K. C.; Jin, Z.; Strano, M. S.; Blankschtein, D. Breakdown in the wetting transparency of graphene. *Phys. Rev. Lett.* **2012**, *109* (17), 176101.
(43) Vesper, S. J. Production of pili (fimbriae) by *Pseudomonas fluorescens* and correlation with attachment to corn roots. *Appl. Environ. Microbiol.* **1987**, *53* (7), 1397−1405.
(44) Dufrene, Y. F. Sticky microbes: Forces in microbial cell adhesion. *Trends Microbiol.* **2015**, *23*, 376−382.
(45) Ong, Y. L.; Razatos, A.; Georgiou, G.; Sharma, M. M. Adhesion forces between *E. coli* bacteria and biomaterial surfaces. *Langmuir* **1999**, *15* (8), 2719−2725.
(46) Erickson, K.; Erni, R.; Lee, Z.; Alem, N.; Gannett, W.; Zettl, A. Determination of the local chemical structure of graphene oxide and reduced graphene oxide. *Adv. Mater.* **2010**, *22* (40), 4467−4472.
(47) Cote, L. J.; Kim, J.; Tung, V. C.; Luo, J.; Kim, F.; Huang, J. Graphene oxide as surfactant sheets. *Pure Appl. Chem.* **2010**, *83* (1), 95−110.
(48) Kim, J.; Cote, L. J.; Kim, F.; Yuan, W.; Shull, K. R.; Huang, J. Graphene oxide sheets at interfaces. *J. Am. Chem. Soc.* **2010**, *132* (23), 8180−8186.
(49) Liu, Z.; Robinson, J. T.; Sun, X.; Dai, H. PEGylated nanographene oxide for delivery of water-insoluble cancer drugs. *J. Am. Chem. Soc.* **2008**, *130* (33), 10876−10877.
(50) Prime, K. L.; Whitesides, G. M. Adsorption of proteins onto surfaces containing end-attached oligo(ethylene oxide): A model system using self-assembled monolayers. *J. Am. Chem. Soc.* **1993**, *115* (23), 10714−10721.
(51) Prime, K.; Whitesides, G. Self-assembled organic monolayers: model systems for studying adsorption of proteins at surfaces. *Science (Washington, DC, U. S.)* **1991**, *252* (5009), 1164−1167.
(52) Gon, S.; Kumar, K. N.; Nüsslein, K.; Santore, M. M. How bacteria adhere to brushy PEG surfaces: Clinging to flaws and compressing the brush. *Macromolecules* **2012**, *45* (20), 8373−8381.
(53) Filloux, A.; de Bentzmann, S.; Aurouze, M.; Lazdunski, A.; Vallet, I. Fimbrial genes in *Pseudomonas aeruginosa* and *Pseudomonas putida*. In *Pseudomonas*; Ramos, J. L., Ed.; Springer, 2004; pp 721−748.
(54) Whitechurch, C. B. Biogenesis and function of type IV pili in *Pseudomonas* species. In *Pseudomonas*; Ramos, J. L., Ed.; Springer, 2006; pp 139−188.
(55) Rief, M.; Gautel, M.; Oesterhelt, F.; Fernandez, J. M.; Gaub, H. E. Reversible unfolding of individual titin immunoglobulin domains by AFM. *Science (Washington, DC, U. S.)* **1997**, *276* (5315), 1109−1112.
(56) Bustamante, C.; Marko, J.; Siggia, E.; Smith, S. Entropic elasticity of lambda-phage DNA. *Science (Washington, DC, U. S.)* **1994**, *265* (5178), 1599−1600.
(57) Israelachvili, J. N. *Intermolecular and Surface Forces*, Third ed., Academic Press, 2011.
(58) Abu-Lail, N. I.; Camesano, T. A. Elasticity of *Pseudomonas putida* KT2442 surface polymers probed with single-molecule force microscopy. *Langmuir* **2002**, *18* (10), 4071−4081.
(59) Walther, K. A.; Grater, F.; Dougan, L.; Badilla, C. L.; Berne, B. J.; Fernandez, J. M. Signatures of hydrophobic collapse in extended proteins captured with force spectroscopy. *Proc. Natl. Acad. Sci. U. S. A.* **2007**, *104* (19), 7916−7921.
(60) Stirnemann, G.; Giganti, D.; Fernandez, J. M.; Berne, B. J. Elasticity, structure, and relaxation of extended proteins under force. *Proc. Natl. Acad. Sci. U. S. A.* **2013**, *110* (10), 3847−3852.
(61) Krasowska, A.; Sigler, K. How microorganisms use hydrophobicity and what does this mean for human needs? *Front. Cell. Infect. Microbiol.* **2014**, *4*, 1−7.

DOI: 10.1021/acs.estlett.7b00509
Environ. Sci. Technol. Lett. 2018, 5, 14−19

Supporting Information

Bacterial Adhesion to Graphene Oxide (GO)-Functionalized Interfaces is Determined by Hydrophobicity and GO Sheet Spatial Orientation

Jinkai Xue[1,*,♦], Sara BinAhmed[1,♦], Zhaoxing Wang[1], Nathan G. Karp[1], Benjamin L. Stottrup[2], Santiago Romero-Vargas Castrillón[1,*]

Environ. Sci. Technol. Lett.

[1] Department of Civil, Environmental, and Geo- Engineering, University of Minnesota, Twin Cities, Minneapolis, MN 55455, USA

[2] Department of Physics, Augsburg University, Minneapolis, MN 55454

♦J. X. and S. BA. were equal contributors to this work

Contents: 17 pages and 12 figures

*Corresponding authors: Jinkai Xue. Email: xuexx145@umn.edu. Tel: +1 (226) 505-0458. Santiago Romero-Vargas Castrillón. Email: sromerov@umn.edu. Tel: +1 (612) 301-1347.

Supporting Materials and Methods

Synthesis of GO

Graphene oxide (GO) was prepared *via* chemical exfoliation of graphite (Bay Carbon, SP-1, 325 mesh) using a modified Hummers method.[1] First, 2.0 g of graphite was placed in 5 mL of concentrated sulfuric acid at 80 °C. Next, 2.0 g each of $K_2S_2O_8$ and P_2O_5 were added and the suspension was allowed to react at 80 °C for 4.5 hours. After reaction, the mixture was transferred into 320 mL of ultrapure water (18.2 MΩ cm, Barnstead, Thermo Fisher) and allowed to settle overnight. The mixture was subsequently vacuum filtered using PTFE membranes (0.45 μm, Whatman TE 36) and dried overnight at room temperature. Next, the obtained black solid was mixed with 80 mL of concentrated sulfuric acid over an ice bath, and 10.0 g of $KMnO_4$ was slowly added so that the temperature of the mixture did not exceed 10 °C. The mixture was then slowly heated to 35 °C over a period of 2.5 hours. Next, 154 mL of ultrapure water was slowly added, preventing the suspension temperature from exceeding 50 °C, and reacted for 2 hours at room temperature. Lastly, the mixture was transferred to 480 mL of ultrapure water, and 8.4 mL of 30% H_2O_2 was added, causing the mixture to acquire a yellowish-brown color. The suspension was allowed to settle for 2 days, and the precipitate was subsequently recovered by multiple centrifugation steps (12,000 × g, 30 min), initially re-suspending the product in 10% HCl to remove chemical residues and finishing with resuspension in water until the supernatant reached a pH of about 3.5. Finally, the suspended product was purified *via* dialysis (3.5 kDa membranes, Spectrum Labs) for 4 days and lyophilized for 4 days.

Preparation of PLL-GO Surfaces

GO sheets were covalently tethered to poly-L-lysine (PLL, MW = 150-300 kDa) immobilized on glass surfaces (Poly-Prep slides, Sigma Aldrich) *via* amine coupling[2] mediated by EDC (1-ethyl-3-(3-dimethylaminopropyl)carbodiimide hydrochloride) and NHS (*N*-hydroxysuccinimide), following established protocols.[2,3] MES buffer (2-(*N*-morpholino)ethanesulfonic acid, 100 mM, pH 6.0) was mixed with GO aqueous dispersion (250 μg L^{-1}) at a 1:5 volume ratio. Next, EDC (20 mM) and NHS (50 mM) solutions prepared in 10 mM MES buffer were sequentially mixed with the GO suspension. During this step, carboxylic acid groups in GO are converted to amine-reactive esters. The reaction proceeded for 15 min at pH ~5.5. The pH of the suspension was subsequently adjusted to ~7.2 before immersing in the suspension a PLL-coated glass coupon. The suspension was placed on a shaker table (~30 rpm) for 1 h, after which the coupon was rinsed with ultrapure water, and bath-sonicated for ~10 min to remove unbound GO sheets. Prepared PLL-GO coupons were stored in ultrapure water at 4 °C until use.

Preparation of Si-GO Surfaces

Si-GO substrates were prepared *via* dip coating of Langmuir-Blodgett (LB) GO films on P-type silicon wafers (100 orientation, single side polished, test grade, 500-μm thickness). The bare silicon substrate was first soaked in acetone for 15 min, rinsed with copious amounts of ultrapure water, and washed with isopropyl alcohol to eliminate water residues. After air drying, the wafer was placed in a UV/O_3 cleaner for 20 min to eliminate organic residues (ProCleaner™ Plus, Bioforce Nanosciences). The cleaned wafer was stored in a nitrogen-purged desiccator before use.

The LB trough (effective area = 172 cm^2) was cleaned with Alconox solution followed by thorough rinsing with ultrapure water. Thereafter the trough was filled with a sublayer consisting of HCl solution, pH 1.0. The Si wafer was then dipped vertically into the trough well with the upper end clamped on the dipper. Surface pressure was monitored using a Wilhelmy plate positioned parallel to the Si substrate. A mixture of GO dispersion (2 mg mL^{-1}) and methanol (v/v = 1/5) was added to the acidic water sublayer dropwise in 0.5-mL aliquots to a total of 2.5 mL. Five min was allowed between aliquot additions. The setup was left overnight for methanol to completely evaporate. Finally, the Si substrate was pulled up at a constant speed of 0.03 mm/s with a surface pressure of 5 mN/m. More information on GO LB film preparation is documented elsewhere.[4–6]

Confocal Raman Microscopy

Confocal Raman Microscopy (Witec Alpha300R) was performed in the study to confirm the two characteristic bands of GO materials and GO coverage on the model surfaces. Sample surfaces were scanned using a Nikon 100× objective, 532-nm laser excitation and 1800 grooves/mm grating.

The optimal depth for mapping was determined by performing an x-z scan over a 20 × 8 μm^2 (length × depth) cross-section. Next, the x-y Raman map was generated over a 20 × 20 μm^2 scan area at the determined depth, with a resolution of 1 μm. Two spectra were measured per micron. The sum of the area under the D and G peaks of GO (found at ~1350 cm^{-1} and ~1590 cm^{-1}, respectively[7]) was used to generate the signal intensity maps.

AFM Topography and Surface Roughness

An MFP-3D-Bio atomic force microscope (Asylum Research) was used to image the surfaces and measure their nanoscale roughness using tapping (AC) mode AFM in phosphate buffered saline (PBS, pH 7.4). Bruker SNL probes were used (cantilever C, nominal k = 0.24 N/m). Surface images were collected at 0.5 Hz over areas of 20 × 20 μm^2, 5 × 5 μm^2, and 2 × 2 μm^2, on each surface type. Root-mean-square (RMS) roughness was calculated from three randomly selected spots (0.5 μm × 0.5 μm) on each surface type.

Contact Angle Goniometry

Contact angle measurements were performed with a Model 200 contact angle goniometer (Ramé-Hart) equipped with a fluid cell for captive bubble measurements. *n*-Decane drops (2 μL) were injected into the fluid cell (filled with PBS, pH 7.4) and deposited on the surface using a syringe fitted with a J-shaped needle (Type 304 stainless steel, 22 gauge). The left and right contact angles were recorded after 60 s from digital images using the DROPImage Standard software (Ramé-Hart). For each surface, 4 replicate specimens were measured for a total of ~10 deposited droplets.

Surface Charge (ζ-Potential)

The ζ-potential of the surfaces was determined from streaming current measurements using an electrokinetic analyzer (SurPASS, Anton Paar). Two 10 × 20 mm^2 specimen coupons were attached to sample holders using double-sided tape; sample holders were subsequently mounted in an adjustable gap cell, setting the gap size to ≈ 110 μm. The streaming current was measured by flowing the electrolyte solution (1 mM KCl) through the gap (i.e., parallel to the specimen coupons) as the pressure difference was increased to 400 mbar. A linear dependence of the streaming current with the pressure difference was observed, in accordance with the Helmholtz-Smoluchowski equation,[8] and the ζ-potential was determined from the slope. Streaming potential measurements were performed at pH ~5.5 – 10 adding aliquots of 0.05 M NaOH. Two independently prepared samples of each surface type were characterized.

Bacterial Culture Conditions

The as-received freeze-dried bacterial culture powder (*P. fluorescens* ATCC 13525) was used to inoculate 6 mL of LB broth (Miller, Sigma-Aldrich). Following incubation for 2 hours at 30 °C, agar plates were streaked and incubated at 30 °C overnight to grow bacterial colonies. Bacterial suspensions were prepared by transferring a colony with a pipette tip to 50 mL of LB medium. The suspension was incubated overnight at 30 °C and 125 RPM shaking speed, and diluted (1:25) with fresh LB broth. After further incubation for ~3 hours at 30 °C and 175 RPM, cells were harvested in mid-exponential phase ($OD_{600\ nm}$ ≈ 0.4 – 0.6), centrifuged at 5000 × g for 1 min, and re-suspended in PBS, pH 7.4. This step was repeated thrice. All materials and reagents used in cell culture were autoclaved before use.

Sample Preparation and Cantilever Functionalization

A specimen of sample surface with a dimension of ~1 × 0.5 cm^2 was adhered using epoxy (3M Quick Set Epoxy Adhesive) to a piranha- and UV/O_3-cleaned 35-mm circular glass disc (Asylum Research). After a 15-min epoxy curing step, a 20-μL droplet of bacterial suspension was placed on the glass disc beside the specimen. The droplet was let to stand for 30 min to permit bacterial deposition on the glass surface. Afterward, 4 mL of PBS was used to rinse off excess unattached cells, avoiding contact between the specimen surface and the bacterial suspension. The glass disc

was mounted in the AFM fluid cell (Fluid Cell Lite, Asylum Research), which was then filled with 2 mL of PBS buffer (pH 7.4).

Tipless silicon nitride cantilevers with nominal k = 0.01 N/m (Bruker MLCT-O10 probe "C") were used in force spectroscopy experiments. Cantilevers were cleaned in a UV/O_3 chamber for 25 min before use. A self-adherent polydopamine (PDA) coating[9,10] was deposited on the AFM probe to enable attachment of a bacterial cell to the end of the cantilever. PDA deposition was conducted for 15 min (65 RPM shaking speed) from a solution containing 4 mg of dopamine hydrochloride (Sigma-Aldrich) per milliliter of Trizma buffer (10 mM, BioReagent, Sigma-Aldrich) buffered to pH 8.5. Following deposition, the probe was rinsed with ultrapure water and dried in a nitrogen-purged desiccator for 5 min. Prior to bacterial attachment, the cantilever optical lever sensitivity was measured over the bare glass surface, and the spring constant (k) was calibrated using the thermal noise method[11] (the values of k were within the range specified by the manufacturer). The AFM probe was mounted onto the AFM probe holder, and the AFM head was thereafter lowered into the fluid cell, allowing ~40 min for the cantilever deflection signal to reach a stable value. To prepare a single-cell AFM probe, the PDA-coated cantilever was engaged at a 1 nN loading force on a single bacterial cell identified using the 63× objective of the inverted optical microscope (Zeiss Axio Observer A.1). After 5 min, the cantilever (functionalized with the bacterial cell) was withdrawn.

Supporting Results

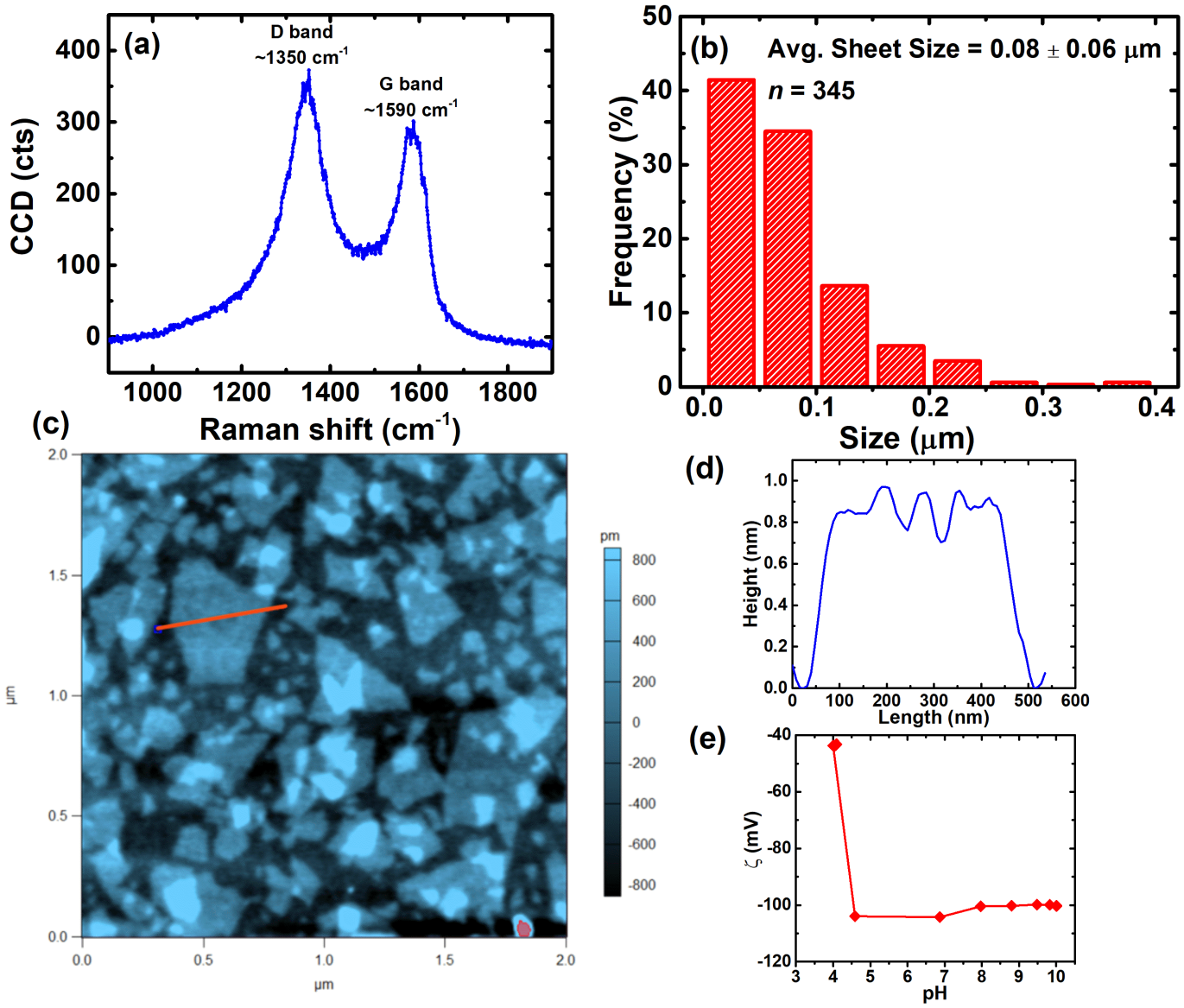

Figure S1: Characterization of graphene oxide (GO): (a) Raman spectrum; (b) sheet size (equivalent radius) distribution; (c) tapping mode AFM image of GO sheets deposited on silicon; (d) GO sheet height profile (determined along the red line in panel c); (e) zeta potential of GO in aqueous dispersion at a concentration of 250 µg mL^{-1}.

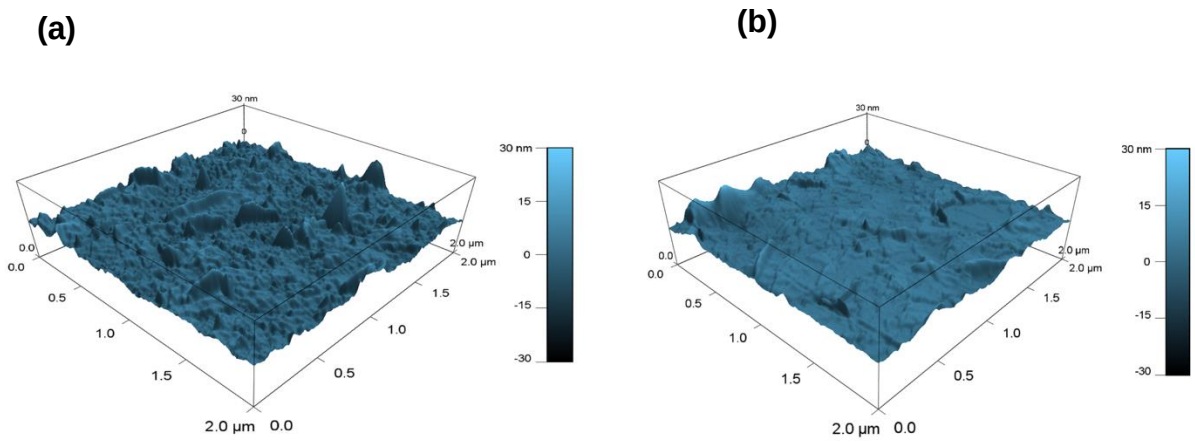

Figure S2: Surface topography visualized by tapping mode AFM: (a) PLL-GO and (b) Si-GO.

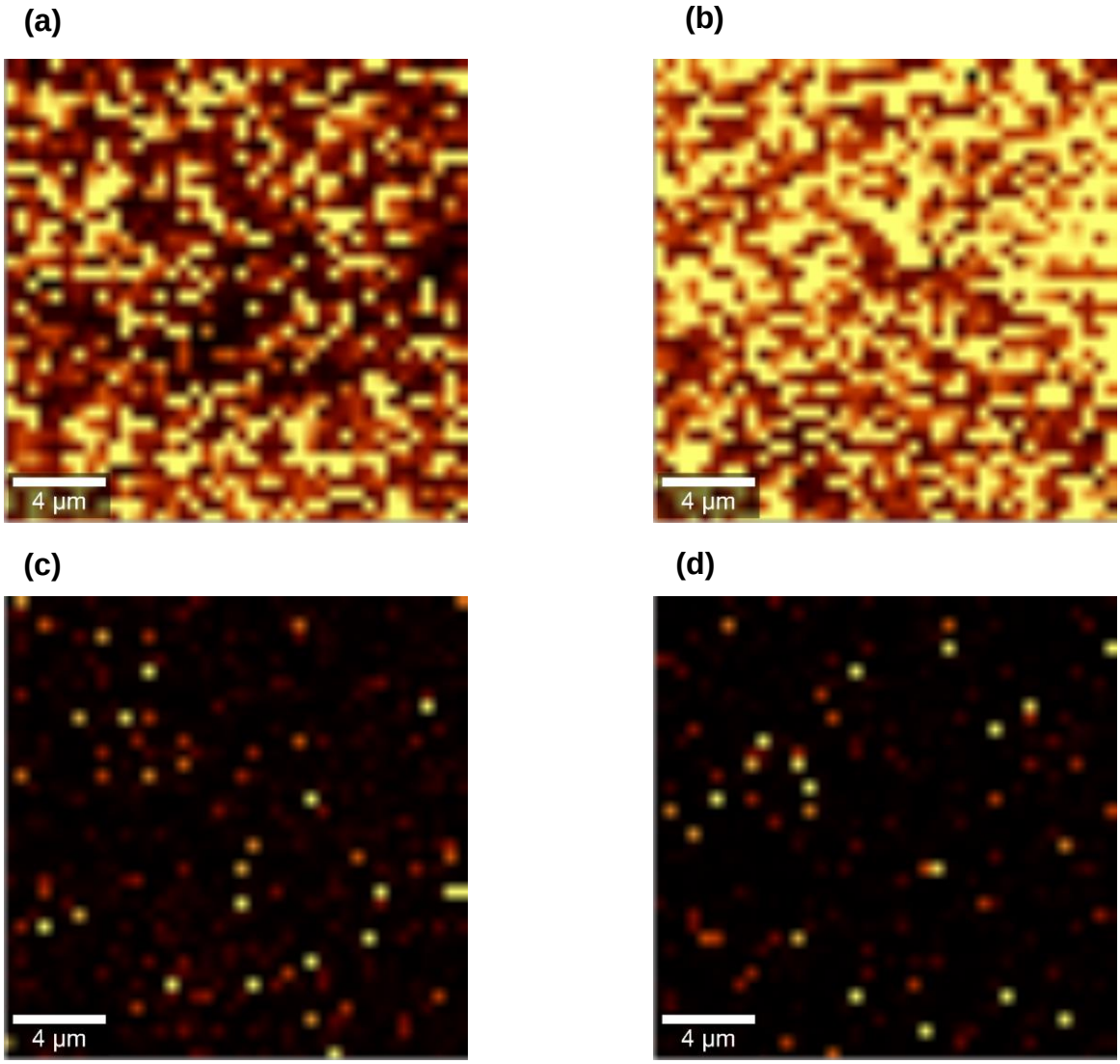

Figure S3: Raman spectroscopy images of (a) PLL-GO, (b) Si-GO, (c) PLL, and (d) Si surfaces.

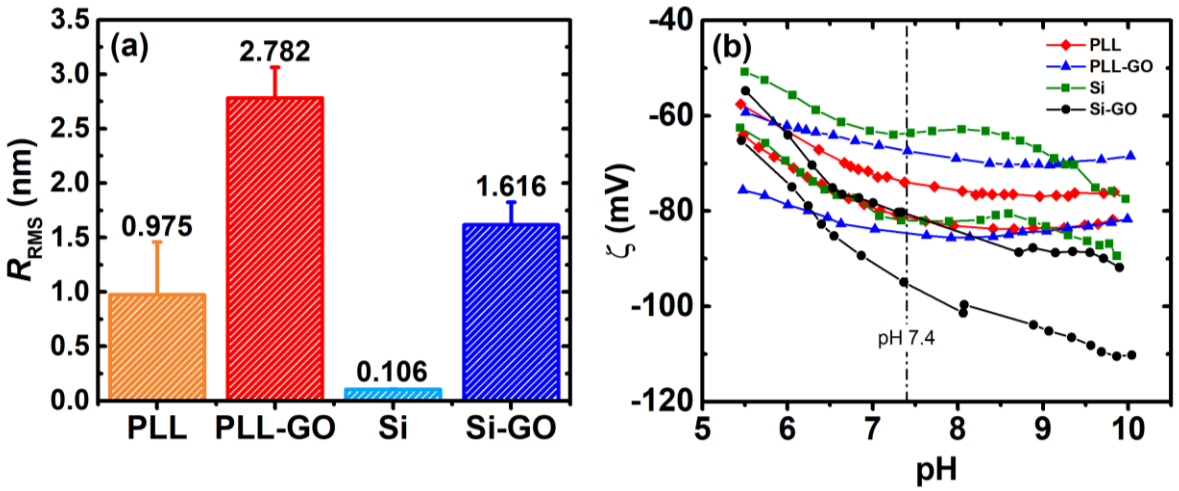

Figure S4: RMS roughness values (a) and ζ-potential as a function of pH (b) for the different surfaces.

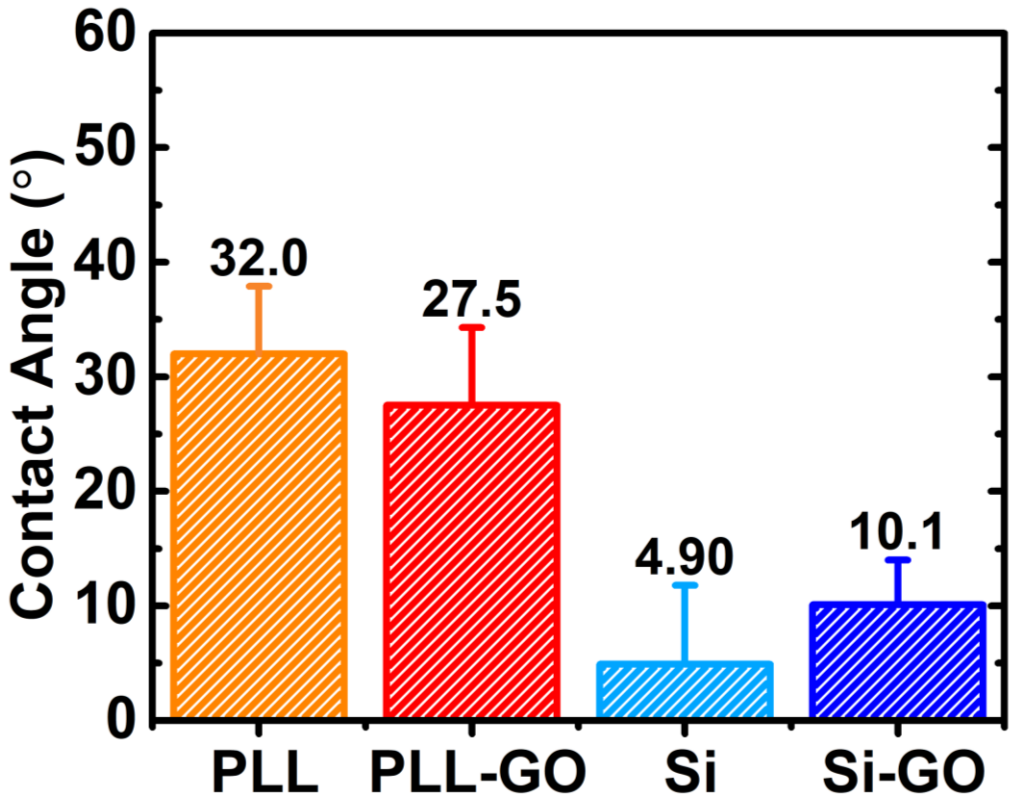

Figure S5: Contact angles obtained through the captive bubble method using *n*-decane droplets in PBS buffer (pH 7.4).

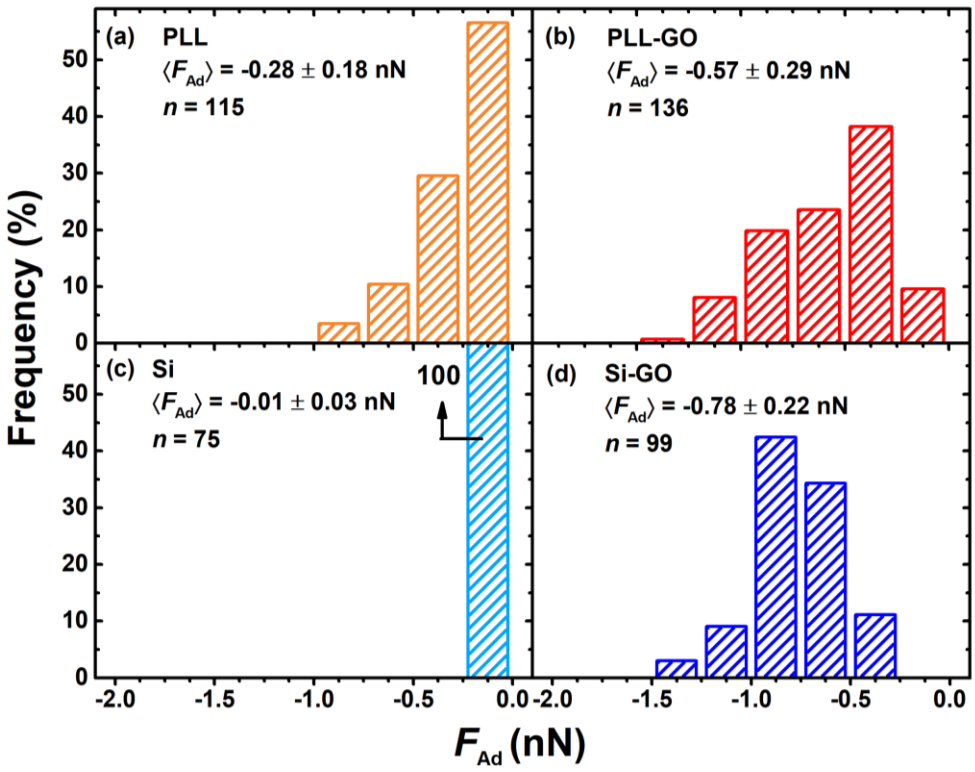

Figure S6: Distribution of maximum adhesion forces (F_{Ad}) of single *P. fluorescens* cells on: (a) poly-L-lysine-coated glass (PLL); (b) graphene oxide (GO)-functionalized PLL surfaces (PLL-GO); (c) Si wafers; (d) Langmuir-Blodgett GO films deposited on Si wafers by dip-coating (Si-GO). The inset shows the histogram average ($\langle F_{Ad} \rangle$), standard deviation, and number of measurements (n). Measurements were performed in PBS buffer (pH 7.4).

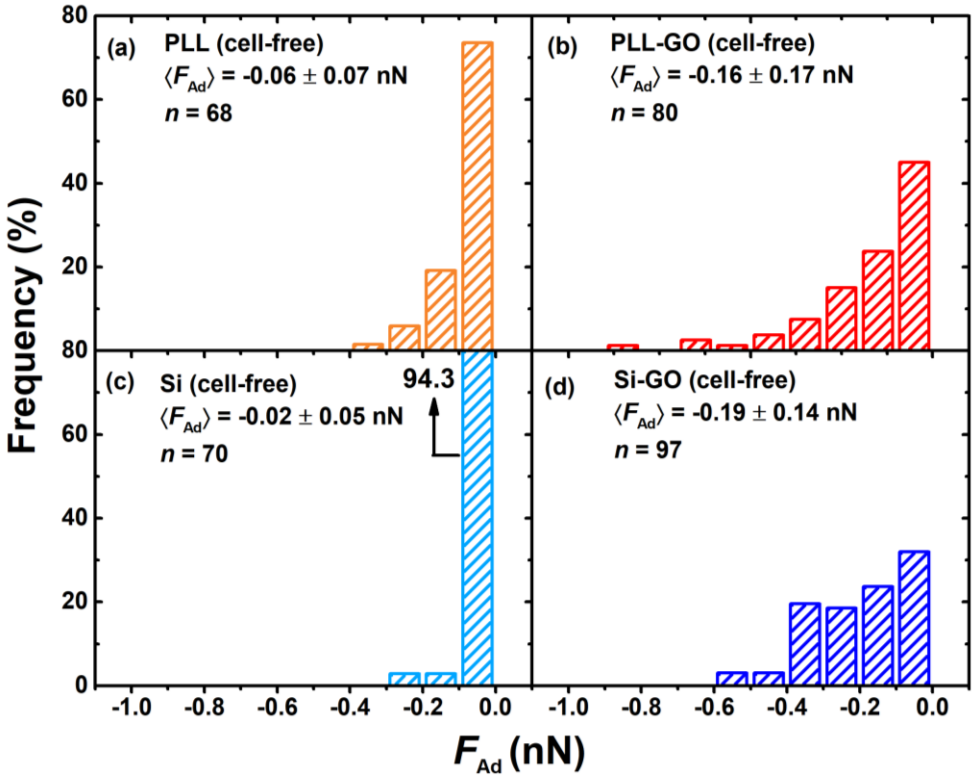

Figure S7: Distribution of maximum adhesion forces (F_{Ad}) of cell-free polydopamine-coated cantilevers on: (a) poly-L-lysine-coated glass (PLL); (b) graphene oxide (GO)-functionalized PLL surfaces (PLL-GO); (c) Si wafers; (d) Langmuir-Blodgett GO films deposited on Si wafers by dip-coating (Si-GO). The inset shows the histogram average ($\langle F_{Ad} \rangle$), standard deviation, and number of measurements (n). Experiments were performed in PBS buffer (pH 7.4).

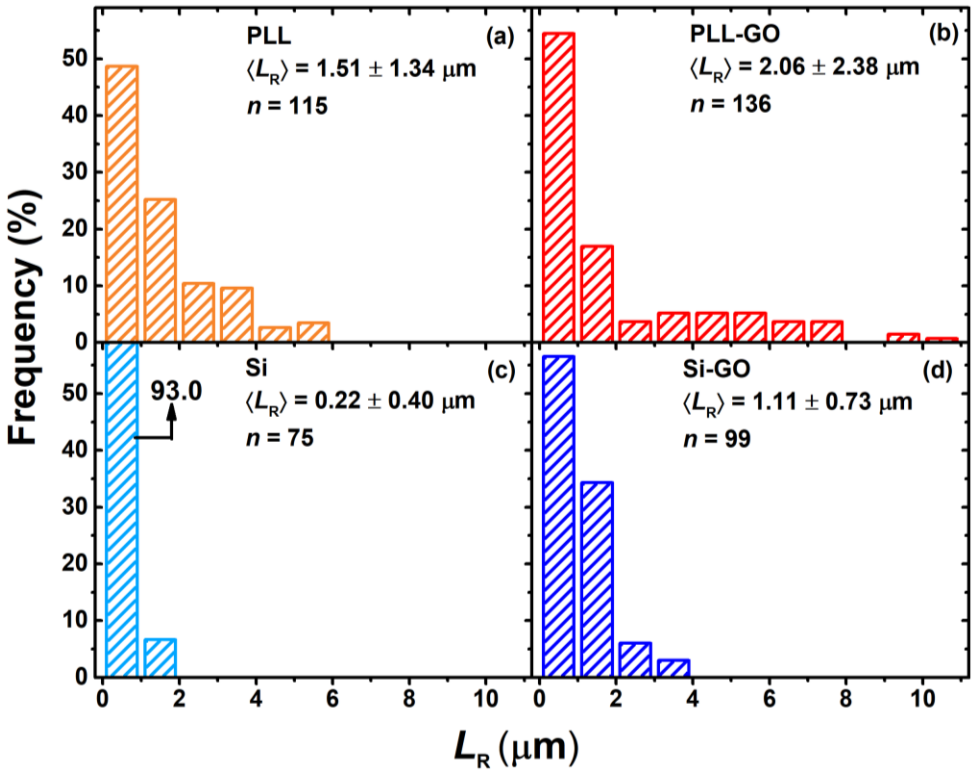

Figure S8: Distribution of rupture separation (L_R: distance from the surface at which adhesion forces vanish) for single *P. fluorescens* cells on: (a) poly-L-lysine-coated glass (PLL); (b) graphene oxide (GO)-functionalized PLL surfaces (PLL-GO); (c) Si wafers; (d) Langmuir-Blodgett GO films deposited on Si wafers by dip-coating (Si-GO). The inset shows the histogram average ($\langle L_R \rangle$), standard deviation, and number of measurements (n). Experiments were performed in PBS buffer (pH 7.4).

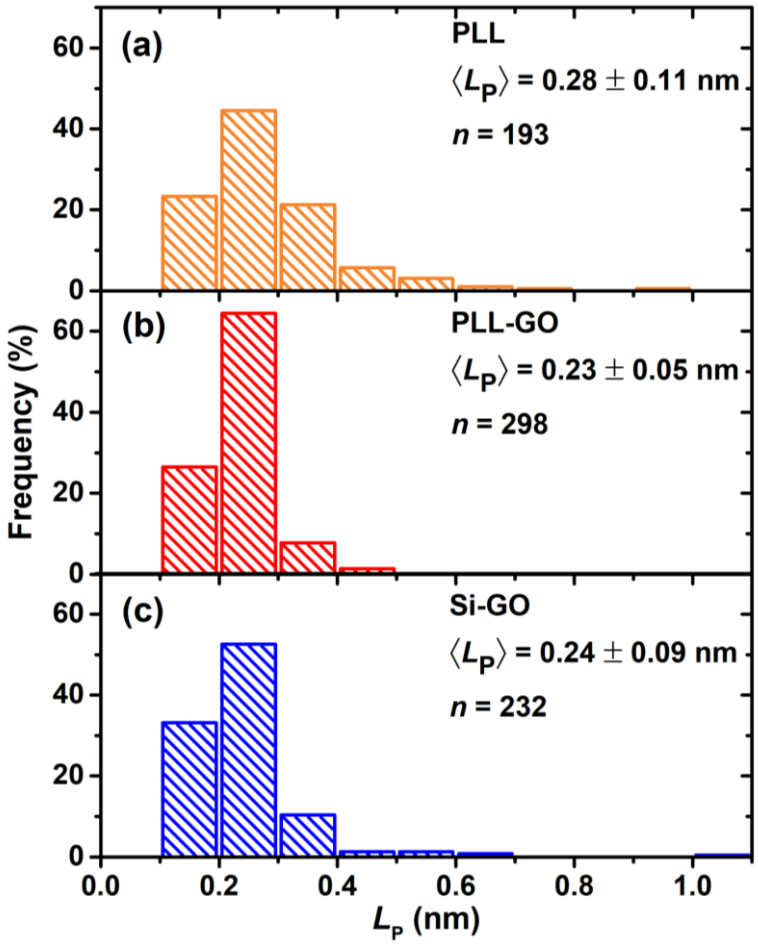

Figure S9: Distribution of best-fit persistence length values (L_P), obtained from WLC model fits to the pull-off force curve of single *P. fluorescens* cells on: (a) poly-L-lysine-coated glass (PLL); (b) graphene oxide (GO)-functionalized PLL surfaces (PLL-GO); (c) Langmuir-Blodgett GO films deposited on Si wafers by dip-coating (Si-GO). The inset shows the histogram average (⟨L_P⟩), standard deviation, and number of measurements (n). Experiments were performed in PBS buffer (pH 7.4).

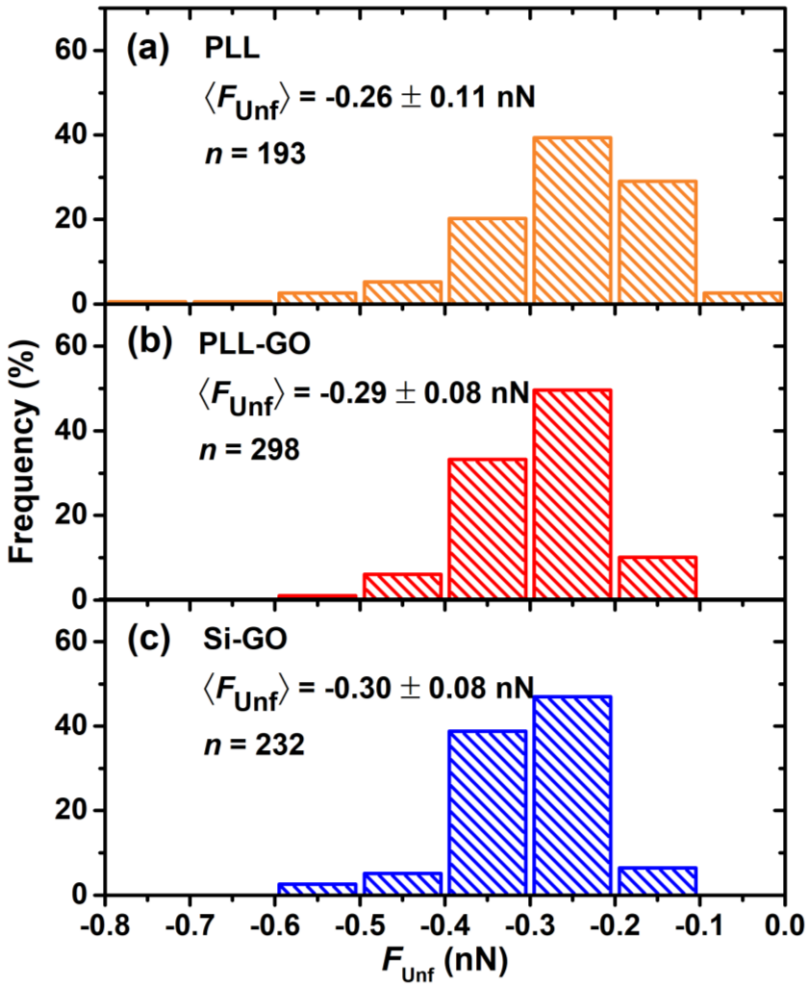

Figure S10: Distribution of the unfolding forces (F_{Unf}, the force measured at the sawtooth peak, cf. Figure 3(a)), obtained from the pull-off force curve of single *P. fluorescens* cells on: (a) poly-L-lysine-coated glass (PLL); (b) graphene oxide (GO)-functionalized PLL surfaces (PLL-GO); (c) Langmuir-Blodgett GO films deposited on Si wafers by dip-coating (Si-GO). The inset shows the histogram average ($\langle F_{Unf} \rangle$), standard deviation, and number of measurements (n). Experiments were performed in PBS buffer (pH 7.4).

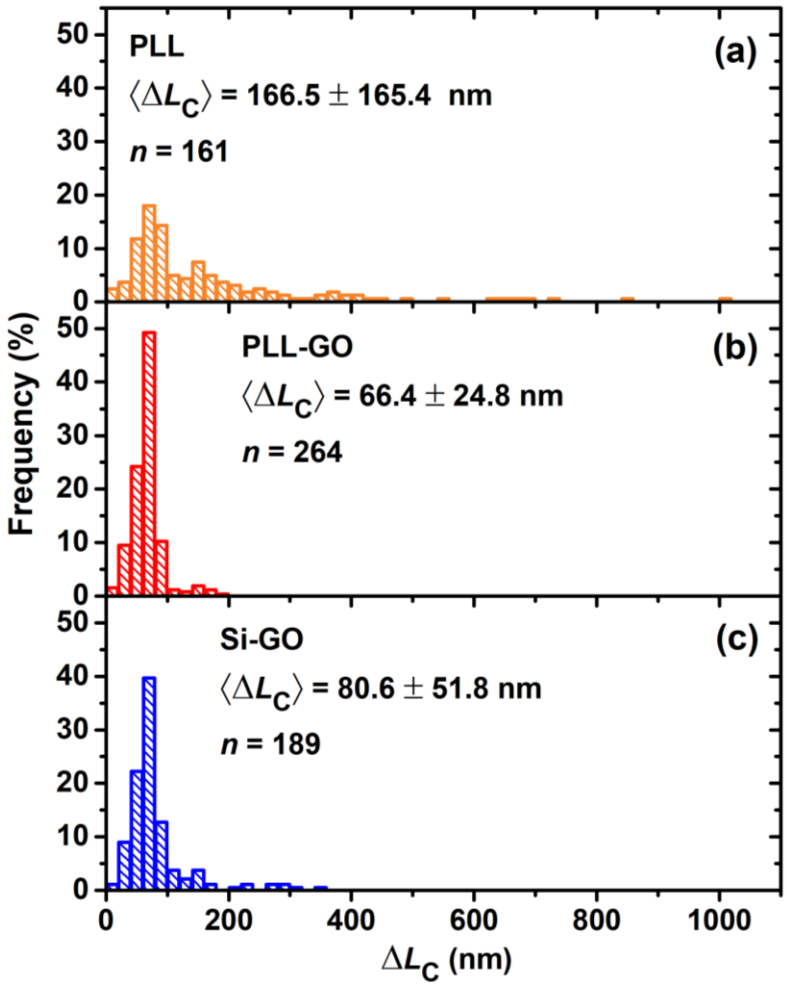

Figure S11: Distribution of ΔL_C (the difference in contour length between two consecutive sawtooth peaks), obtained from the pull-off force curve of single *P. fluorescens* cells on: (a) poly-L-lysine-coated glass (PLL); (b) graphene oxide (GO)-functionalized PLL surfaces (PLL-GO); (c) Langmuir-Blodgett GO films deposited on Si wafers by dip-coating (Si-GO). The inset shows the histogram average ($\langle \Delta L_C \rangle$), standard deviation, and number of measurements (n). Experiments were performed in PBS buffer (pH 7.4).

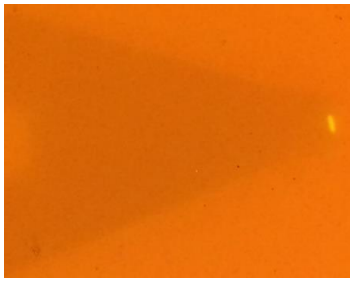

Figure S12: Bacterial cell probe imaged after force measurements. The bacterial cell (*P. fluorescens*) was attached to the front edge of a tipless AFM cantilever using polydopamine wet adhesive. The observed green fluorescence indicates that the cell remained viable throughout the experiment.

Supporting References

(1) Tung, V. C.; Allen, M. J.; Yang, Y.; Kaner, R. B. High-throughput solution processing of large-scale graphene. *Nat. Nanotechnol.* **2009**, *4* (1), 25–29.

(2) Grabarek, Z.; Gergely, J. Zero-length crosslinking procedure with the use of active esters. *Anal. Biochem.* **1990**, *185* (1), 131–135.

(3) Hermanson, G. T. *Bioconjugate Techniques: Third Edition*; 2013, 259–266.

(4) Valtierrez-Gaytan, C.; Ismail, I.; Macosko, C.; Stottrup, B. L. Interfacial activity of graphene oxide. *Colloids Surfaces A Physicochem. Eng. Asp.* **2017**, *529*, 434–442.

(5) Cote, L. J.; Kim, F.; Huang, J. Langmuir-Blodgett assembly of graphite oxide single layers. *J. Am. Chem. Soc.* **2009**, *131* (3), 1043–1049.

(6) Kim, F.; Cote, L. J.; Huang, J. Graphene oxide: Surface activity and two-dimensional assembly. *Adv. Mater.* **2010**, *22* (17), 1954–1958.

(7) Kudin, K. N.; Ozbas, B.; Schniepp, H. C.; Prud'homme, R. K.; Aksay, I. A.; Car, R. Raman spectra of graphite oxide and functionalized graphene sheets. *Nano Lett.* **2008**, *8* (1), 36–41.

(8) Werner, C.; Körber, H.; Zimmermann, R.; Dukhin, S.; Jacobasch, H. Extended electrokinetic characterization of flat solid surfaces. *J. Colloid Interface Sci.* **1998**, *208* (1), 329–346.

(9) Lee, H.; Dellatore, S. M.; Miller, W. M.; Messersmith, P. B. Mussel-inspired surface chemistry for multifunctional coatings. *Science (80-.).* **2007**, *318* (5849), 426–430.

(10) Kang, S.; Elimelech, M. Bioinspired single bacterial cell force spectroscopy. *Langmuir* **2009**, *25* (17), 9656–9659.

(11) Hutter, J. L.; Bechhoefer, J. Calibration of atomic-force microscope tips. *Rev. Sci. Instrum.* **1993**, *64* (7), 1868–1873.